Numerical simulation of immiscible incompressible viscous, viscoelastic and elastic multiphase flows

Léo Aurélio DISERENS

La plus grande gloire n'est pas de ne jamais tomber,
mais de se relever à chaque chute.
— Nelson Mandela

A ma maman,
mon papa et mon frère

Remerciements

Comme une thèse de doctorat ne peut pas être considérée comme une réussite uniquement personelle, je tiens ici à remercier les gens qui m'ont permis d'atteindre cet objectif.

Tout d'abord, je tiens à remercier mes superviseurs de thèse, Marco Picasso et Alexandre Caboussat, qui ont permis que ces années de doctorats se passent dans les meilleures conditions. Merci énormément pour votre soutien dans les moments difficiles, notamment durant le covid. Merci Marco pour les ballades à ce moment-là, mais aussi tous les repas de midi que tu as partagé avec nous. Que ça soit à ces occasions ou lors des discussions scientifiques, tu t'es montré très proche de nous et c'était très agréable. Merci Alexandre pour votre rigueur dans le cadre scientifique et professionel, mais aussi humain. Nos discussions hebdomadaires m'ont permis de garder un bon cadre de travail, mais étaient aussi simplement de très bon moments et j'en garde un excellent souvenir.

Je remercie les membres de mon jury de thèse, Simone Deparis, Emmanuel Audusse et Alexei Lozinski, pour leur lecture attentive de ma thèse et leurs questions et remarques très pertinentes, qui ont considérablement amélioré mon ouvrage. Cette thèse n'aurait pas abouti sans l'aide d'Alexandre Masserey et surtout Julien Hess d'Ycoor Systems SA. Ton aide et ta patience ont été très précieux à mes yeux, merci énormément. Je tiens à remercier aussi Ariane Cordonnier pour son super travail, son aide et son amitié dans les moments importants. J'ai aussi eu les meilleurs collègues de bureau: merci énormément à Samuel Dubuis, pour son amitié et sa super intronisation au travail et à l'ambiance d'un PhD. Merci aussi pour les discussions et apports scientifiques, qu'un passage à la Bavaria un 19 Juin n'a pu que sublimer. Merci Emile pour les matchs de volley et pour tous ses super moments, ça a été un immense plaisir que de partager le bureau avec toi. Le Jean, tu es arrivé à la fin mais on s'est tout de suite super bien entendu, merci à toi pour ton soutien et ton amitié. Merci aussi à Antonin qui a partagé mon bureau un semestre. Merci aussi à Arwa et Dimitrios. Je tiens finalement à remercier celui et celle avec qui j'ai passé le plus de temps. Maude et Paride, merci énormément pour tout ces super moments, ces ballades, ces vacances, ces multiples verres et ses super souvenirs. Vous m'avez permis de passer la meilleure fin de thèse possible. Merci finalement à Boris, adopté du groupe Picasso, pour tous ces super moments et les superbes parties d'échecs. Merci aussi aux vieux et gros docteurs Jonathan et Vil pour les barres de rire.

Remerciements

Je tiens aussi à remercier tous les collègues du batiments de math. Virginie et Guillaume, vous êtes des fous au grand coeur, merci pour tout. Merci aussi à Simone, Orane et toutes les secrétaires pour leurs aides, soutien et amitiées. Merci aux jeunes topologues Adélie, Célia et Lyne pour les multiples café, ainsi qu'à David, Quentin, Gauthier, Bruno et tous les autres gens cool que j'oublie. Thanks also to all old and new MATHICSE members, Giac, Giacommino, Fabian, Riccardo, Eva, Gonzalo; and Axel, David, Riccardo, Andrea, both Fabios, Matteo and everyone else for the great discussions, retreats and all the laughter. Merci encore à Samuel, Emile, Adélie, Tanguy, Katie et Maude, anciens et nouveaux représentants des doctorants, pour les importantes discussions et réunions et pour votre aide. I also want to thank the SIAM chapter of the EPFL for the great interest in providing the link between academic and industry, and for all the great talk and conferences we have had.

Je tiens finalement à remercier tous mes amis, les Harrys et compagnie, les Pranginois, les matheux, les nyonnais-e-s, les gens de Paléo, le LVBC et tous les autres pour votre soutien et amitié durant ces cinq dernières années et les précédentes. Ces moments sont très importants pour moi. J'ai eu l'immense chance de partager une collocation avec deux différentes mais incroyables personnes pendant quatre ans. Merci énormément Louis pour m'avoir accueilli chez toi. Ces moments ensembles à la colloc' sont gravés dans mon coeur à jamais. Tu as rendu la vie d'un doctorant plus facile et plus marrante que jamais. Merci beaucoup aussi à Lucie, pour les discussions, les rires et le soutien. Vous avez rendu les années covid plus que supportables. Finalement, merci beaucoup Chloé pour cette super année de collocation. C'était super agréable de t'avoir à la maison, on a passé de super moments. Merci aussi beaucoup pour ton soutien et ta compréhension.

Je terminerai ces remerciements par ma famille, qui m'ont toujours apporté tout leur soutien. Merci aux Diserens de Confignon pour tout votre amour, c'est toujours un plaisir de vous voir. Merci aussi à mes grands-parents, je vous aime fort. J'ai terminé chaque semaine de mon doctorat au 16 rue de la Pontaise à Prangins, chez les gens pour qui cette thèse est dédiée. Merci maman, papa, Marius, pour tout votre amour et tout votre soutien. Quand nous sommes ensemble, rien ne me semble impossible. Je ne serai jamais ici sans vous, merci de tout mon coeur.

Lausanne, February 10, 2023   Léo Aurélio Diserens

◼ Abstract

A unified numerical framework is presented for the modelling of multiphasic viscoelastic and elastic flows. The rheologies considered range from incompressible Newtonian or Oldroyd-B viscoelastic fluids to Neo-Hookean elastic solids. The model is formulated in Eulerian coordinates. The unknowns are the volume fraction of each phase (liquid, viscoelastic or solid), the velocity, pressure and the stress in each phase.

A time splitting strategy is applied in order to decouple the advection operators and the diffusion operators. The numerical approximation in space consists of a two-grid method. The advection equations are solved with a method of characteristics on a structured grid of small cells and the diffusion step uses an unstructured coarser finite element mesh. An implicit time scheme is suggested for the time discretisation of the diffusion step. Estimates for the time and space discretisation of a simplified model are presented, which proves unconditional stability.

Several numerical experiments are presented, first for the simulation of one phase flows with free surfaces. The implicit time scheme is shown to be more efficient than the explicit one. Then, the model for the deformation of an elastic material is validated for several test cases. Finally, Signorini boundary conditions are implemented and presented for the simulation of the bouncing of an elastic ball.

The multiphase model is validated through different test cases. Collisions between Neo-Hookean elastic solids are explored. Simulations of multiple viscoelastic flows are presented: an immersed viscoelastic droplet and a Newtonian fluid in a constricted cavity. The fall of an immersed Neo-Hookean elastic solid into an incompressible Newtonian or viscoelastic fluid is also presented.

Finally, the one phase model is extended to compressible flows. The method of characteristics is updated in order to solve the advection equations, when the velocity is not divergence-free. A numerical scheme is proposed and a numerical experiment is presented.

Keywords: computational fluid dynamics, continuum mechanics, Eulerian framework, free-surface flows, multiphase flows, time-splitting, two-grids, method of characteristics, finite elements, fluid-structure interactions, weakly compressible flows.

Résumé

Un modèle numérique unifié est présenté afin de modéliser l'écoulement multiphasique de fluides viscoélastiques et de solides élastiques avec une surface libre. Les différents types de rhéologies comprennent les fluides incompressibles Newtoniens, les fluides viscoélastiques avec un modèle de type Oldroyd-B incompressible et les solides élastiques avec un modèle de type Neo-Hookéen incompressible. Une formulation Eulerienne est utilisée pour la modélisation du problème, où les inconnues sont les fractions de volumes de chaque phase (liquide ou solide), ainsi que la vitesse, la pression et le tenseur de contraintes pour chaque phase.

Les termes de transport et de diffusion sont découplés à l'aide d'une méthode à pas fractionnaires (splitting). L'approximation numérique du système d'équations utilise deux maillages. Une méthode des caractéristiques est utilisée pour résoudre les équations de transport sur une grille structurée de petites cellules, tandis que les termes de diffusion sont résolus sur un maillage éléments finis non-structuré plus grossier. Un schéma implicite en temps est proposé pour la discrétisation en temps de l'opérateur de diffusion. Des résultats de stabilité pour la discrétisation en temps puis en espace sont présentés pour un modèle simplifié.

Le modèle est validé par différents cas-tests, dans un premier temps en considérant une unique phase. Nous montrons que notre schéma implicite est plus précis que le schéma explicite. Ensuite, le modèle de déformation élastique est validé pour différents cas-tests. Finalement, les conditions de bord de Signorini sont implémentées afin de reproduire le rebond d'une balle élastique.

Le modèle multiphase est validé à travers différents cas-tests. La simulation de la collision de deux sphères solides est abordée. L'interaction entre plusieurs fluides viscoélatiques est étudiée pour une simulation d'écoulement d'une goutte de fluide viscoélastique immergée dans un fluide newtonien. La simulation de déformation d'un solide Neo-Hookean immergé dans un fluide incompressible Newtonien ou viscoélastique est aussi présentée.

Finalement, le modèle numérique unifié est étendu aux écoulement faiblement compressibles. La méthode des caractéristiques est adaptée afin de résoudre les équations de transport, lorsque la divergence de la vitesse ne vaut plus zéro. Une expérience numérique est présentée.

Résumé

Mots-clés : mécanique des fluides, mécanique des milieux continus, coordonnées Eule-riennes, surfaces libres, écoulements multiphase, pas de temps fractionnaire, méthode à deux grilles, méthodes des caractéristiques, éléments finis, interaction fluide-structure, écoulement faiblement compressible.

∎ Contents

Contents

■ Introduction

The goal of this thesis is to present a unified model for the simulation of the interactions between fluids and structures with free surfaces. A multiphase formulation is proposed to model three different types of interactions: fluid-fluid, fluid-structure or structure-structure. The rheology of the fluids considered are Newtonian and viscoelastic liquids. Their interaction with multiple elastic solids is formulated in Eulerian coordinates.

This introduction contains four parts. A state-of-the-art of viscoelastic fluids is first discussed. A quick introduction to continuum mechanics is then presented, emphasizing the difference between Lagrangian and Eulerian formulations. Multiphase and free surfaces flows problem are then discussed. Finally, an overview of the present thesis is described.

Fluid mechanics: viscoelastic fluids

Rheology pertains to the study of material flows and deformations under mechanical forces. This concerns gas, liquids or solids. However, complex fluids [OP02] exhibit a different behaviour than the three phases of matter [BAH87, Lar99, CGR16]. As mentioned in [Lar99], "Specification of a viscosity or an elastic modulus does not even begin to describe the mechanical properties of such a substance." Examples of such materials range from different foods like mayonnaise, chocolate but also ice cream, blood or even computer screens, containing liquid crystals.

Newtonian fluids exhibit a linear relation between the stress and the gradient of the flow velocity. A fluid is called non-Newtonian when this relation is nonlinear. These relations can involve high or very low temperature as in glassy liquids or electrorheological fluids, which can become very viscous under electrical currents. This relation between stress and strain in the flow implies a change in the viscosity of the fluid. For example, the viscosity of shear-thinning and thickening fluids respectively decreases or increases under large velocity gradients. The class of viscoelastic fluids exhibit a non-Newtonian behaviour in the sense that their relaxation time - the time for the stress to return to zero under constant-strain condition - is strictly positive. For instance, polymeric fluids, made of polymer chains, are exhibiting elastic properties.

The mathematical modelling of viscoelastic flows at the macroscopic level uses Navier-Stokes equation coupled with a constitutive equation for the extra-stress tensor [LL89, OP02]. This last equation models the elastic behaviour of the material. The Navier-Stokes equations are based on the principles of the mass and momentum equations, which read

$$\frac{\partial \rho}{\partial t} + \nabla \cdot (\rho \boldsymbol{u}) = 0,$$
$$\rho \left(\frac{\partial \boldsymbol{u}}{\partial t} + (\boldsymbol{u} \cdot \nabla) \cdot \boldsymbol{u} \right) - \nabla \cdot \boldsymbol{T} = \boldsymbol{F}_e,$$

where ρ denotes the density of the fluid, $\boldsymbol{u}$ the velocity of the fluid, $\boldsymbol{T}$ is the tensor of internal body forces and $\boldsymbol{F}_e$ the external forces. A fluid is said to be incompressible if its density is constant in time and space. In this case, the velocity of the flow satisfies $\nabla \cdot \boldsymbol{u} = 0$ [TELB06]. However, this is a mathematical simplification, since all fluids exhibit compressible behaviour at a certain scale. In this case, the relation between the density and the pressure in the fluid is defined by an equation of state. Compressible flows are discussed in chapter 5.

In the case of an incompressible Newtonian fluid, the stress contains the pressure of the fluid p and is linear with respect to the strain tensor $\boldsymbol{\epsilon}(\boldsymbol{u}) = \frac{1}{2}(\nabla \boldsymbol{u} + \nabla \boldsymbol{u}^T)$:

$$\boldsymbol{T} = -p\boldsymbol{I} + 2\eta_s \boldsymbol{\epsilon}(\boldsymbol{u}),$$

where η_s is called the solvent viscosity. For viscoelastic fluids, the following definition of the stress tensor $\boldsymbol{T}$ is considered

$$\boldsymbol{T} = -p\boldsymbol{I} + 2\eta_s \boldsymbol{\epsilon}(\boldsymbol{u}) + \boldsymbol{\sigma},$$

where $\boldsymbol{\sigma}$ is an extra-stress tensor due to the viscoelastic effect. At the microscopic level, considering polymeric fluids, mathematical models arising from kinetic theories can be considered [BCP06, LOP11]. In the dumbbells model, polymer chains are modelled as beads linked by an elastic string. They are not interacting with each other. At the macroscopic level, this kinetic theory coincides with the so-called Oldroyd-B constitutive equation

$$\boldsymbol{\sigma} + \lambda \left(\frac{\partial \boldsymbol{\sigma}}{\partial t} + (\boldsymbol{u} \cdot \nabla) \boldsymbol{\sigma} - \nabla \boldsymbol{u} \boldsymbol{\sigma} - \boldsymbol{\sigma} \nabla \boldsymbol{u}^T \right) = 2\eta_p \boldsymbol{\epsilon}(\boldsymbol{u}),$$

where $\eta_p, \lambda > 0$ respectively denotes the polymer viscosity and the relaxation time of the viscoelastic fluid [CGR16]. More realistic is the so-called Finitely Extensible Nonlinear Elastic (FENE) microscopic model, in which dumbells have finite extensions

[Lar99, OP02]. At the macroscopic level, the Oldroyd-B model can be generalised:

$$f(\boldsymbol{\sigma})\boldsymbol{\sigma} + \lambda \left(\frac{\partial \boldsymbol{\sigma}}{\partial t} + (\boldsymbol{u} \cdot \nabla)\boldsymbol{\sigma} - \nabla \boldsymbol{u}\boldsymbol{\sigma} - \boldsymbol{\sigma}\nabla \boldsymbol{u}^T \right) = 2\eta_p \boldsymbol{\epsilon}(\boldsymbol{u}),$$

where f can be a function of $\boldsymbol{\sigma}$ and yields more complex models, such as the Giesekus or Phan-Thien-Tanner (PTT) models [BAH87, Lar99, BCP11], which allow shear-thinning behaviour.

In viscoelastic flows, the nonlinear terms $\nabla \boldsymbol{u}\boldsymbol{\sigma} + \boldsymbol{\sigma}\nabla \boldsymbol{u}^T$ in the Oldroyd-B equation gives rise to unstabilities in various cases. The most famous one is of contraction $4:1$, where a viscoelastic fluid flows into a contracted domain [TCM05, HFK05, KKK$^+$05]. The non-dimensional Weissenberg number $We = \lambda V/L$, where V is a characteristic velocity and L a characteristic length, plays a major role, as instabilities arise when this number is high. Different methods have been proposed to deal with this problem [BCP11], but this is not addressed in this thesis. A complete review of the instability problem arising from the Oldroyd-B model can be found in [SJK$^+$22].

When $\eta_s = 0$, even in the absence of the non linear terms $\nabla \boldsymbol{u}\boldsymbol{\sigma} + \boldsymbol{\sigma}\nabla \boldsymbol{u}^T$, stability issues may be encountered depending on the finite element spaces used for velocity and extra-stress [FGP97, BPS01]. A remedy is to use the Elastic Viscous Split Stress (EVSS), which adds an extra-component $\boldsymbol{D} = \boldsymbol{\epsilon}(\boldsymbol{u})$ [FGP00, BPS01, PR01, BPL06].

Continuum mechanics

The analysis of a structure has a major role in engineering. Balance principles are the state of the art from principles of physics, as they allow the mathematical formulation of continuum mechanics problems [BL19, BC09, Hol02]. In these balance principles, the relation between the stress and the relative deformation of the material, called strain, is derived from Newton's second law of motion and already gives important tools for the modelling. As examples of different problems, a beam buckles if the applied force reaches a certain threshold, see Figure 1. For material testing like tensile test, where the material is loaded until failure, a nonlinear relation between these two quantities can be observed as a viscoplastic behaviour arises at a strain threshold. Indeed, past a certain strain, the tensile specimen will not recover its original form as predicted by Hooke's law and thus nonlinearity appears. Finally, necking (shrinking of the material under tension) and failure behaviours are dependent of the material, which could be either ductile (undergo large strain rates before failing) or brittle (fails quickly at viscoplastic point).

The motion of any given object can be described in Lagrangian and Eulerian coordinates [Hol02]. Consider Ω_0 being the initial configuration of a given material and $\boldsymbol{X} \in \Omega_0$, the Lagrangian formulation of displacement is $\boldsymbol{D}(\boldsymbol{X}, t) = \boldsymbol{x}(\boldsymbol{X}, t) - \boldsymbol{X}$ for $\boldsymbol{x}$ being the
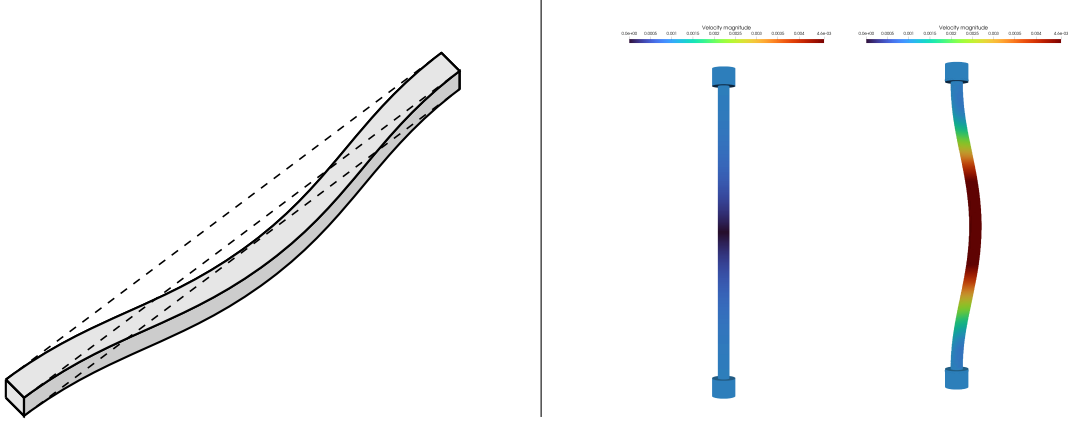
Figure 1 – Buckling of a beam. Left: sketch of beam buckling. Right: Numerical experiment.

deformation of $\boldsymbol{X}$ at time t. Here a particle in position $\boldsymbol{X} \in \Omega_0$ is monitored through time and space. The Cauchy's first equation of motion in Lagrangian formulation is described by:

$$\frac{\partial}{\partial t}\boldsymbol{U} - \nabla \cdot \tilde{\boldsymbol{C}} = \boldsymbol{b}, \qquad \text{where} \qquad \frac{\partial}{\partial t}\boldsymbol{D} = \boldsymbol{U},$$

where $\boldsymbol{D}$ is the deformation, $\boldsymbol{U}$ is the velocity, $\tilde{\boldsymbol{C}}$ is the Cauchy stress tensor and $\boldsymbol{b}$ is a vector of external forces. Different models of constitutive laws allow to determine the material response [Hol02, Ogd97]. The hyperelastic materials are derived from a so-called Helmholtz free-energy function Ψ of the deformation gradient tensor $\tilde{\boldsymbol{F}}$ [RBJ97]. Indeed, the stress $\tilde{\boldsymbol{C}}$ is then given as a function of the deformation gradient tensor $\tilde{\boldsymbol{F}}$, defined as

$$\tilde{\boldsymbol{F}}(\boldsymbol{X}, t) = \frac{\partial \boldsymbol{x}}{\partial \boldsymbol{X}}(\boldsymbol{X}, t),$$

so that

$$\frac{\partial \tilde{\boldsymbol{F}}}{\partial t}(\boldsymbol{X}, t) = \nabla_{\boldsymbol{X}} \boldsymbol{U}(\boldsymbol{X}, t).$$

One of the most basic constitutive equation shows a linear relation between stress and strain, similarly as in Hooke's law, and is called Neo-Hookean model:

$$\tilde{\boldsymbol{C}} = -p\boldsymbol{I} + \mu(\tilde{\boldsymbol{F}}\tilde{\boldsymbol{F}}^T - \boldsymbol{I}),$$

where μ is the Lamé parameter of the material. For small deformations, the compressible version of the Neo-Hookean model reduces to the linear elasticity equation $\tilde{\boldsymbol{C}} = 2\mu\boldsymbol{\epsilon}(\boldsymbol{D}) + \lambda(\nabla \cdot \boldsymbol{D})\boldsymbol{I}$, where λ is called the first Lamé parameter. A widely applied constitutive model for compressible materials is the Saint-Venant Kirchhoff model [Hol02, DR06, Ric13] and reads

$$\tilde{\boldsymbol{C}} = J^{-1}\tilde{\boldsymbol{F}}(\lambda \text{tr}(\tilde{\boldsymbol{E}})\boldsymbol{I} + 2\mu\tilde{\boldsymbol{E}})\tilde{\boldsymbol{F}}^T,$$

where $J = \det(\tilde{\boldsymbol{F}})$ and the tensor $\tilde{\boldsymbol{E}} = \frac{1}{2}(\tilde{\boldsymbol{F}}^T\tilde{\boldsymbol{F}} - \boldsymbol{I})$ is called the Green-Lagrange strain

tensor. This model is often used for the simulation of metal deformation [Hol02].

In the Eulerian formulation, the corresponding Eulerian fields are defined as

$$\boldsymbol{u}(\boldsymbol{x}(\boldsymbol{X},t),t) = \boldsymbol{U}(\boldsymbol{X},t)$$
$$\boldsymbol{C}(\boldsymbol{x}(\boldsymbol{X},t),t) = \tilde{\boldsymbol{C}}(\boldsymbol{X},t)$$
$$\boldsymbol{d}(\boldsymbol{x}(\boldsymbol{X},t),t) = \boldsymbol{D}(\boldsymbol{X},t),$$
$$\boldsymbol{F}(\boldsymbol{x}(\boldsymbol{X},t),t) = \tilde{\boldsymbol{F}}(\boldsymbol{X},t),$$

so that the Cauchy's first equation of motion reads for the Eulerian formulation:

$$\frac{\partial}{\partial t}\boldsymbol{u} + (\boldsymbol{u} \cdot \nabla)\boldsymbol{u} - \nabla \cdot \boldsymbol{C} = \boldsymbol{b}.$$

Similarly as in fluid dynamics, for incompressible deformation, the velocity $\boldsymbol{u}$ satisfies $\nabla \cdot \boldsymbol{u} = 0$. The constitutive equations previously introduced for the Lagrangian coordinates can be equally formulated in Eulerian coordinates [DR06, Pic16]. This is further described in chapter 1.

The Eulerian formulation of continuum mechanics has interests for large deformations of the structure and when changes of topology of the structure are expected [DD05, Ric13, TBMG20]. The use of a finite element (FE) method allows to solve the mathematical problem in complex geometries and high-order FE methods allows to obtain accurate results [DD05]. It has been widely applied to classical engineering numerical simulations, such as buckling [TK17, TOG16] and deforming beam [NLCH21]. The use of isogeometric analysis has also gain in popularity for its ability to reproduce exactly complex geometries in computational mechanics [TBMG20]. In order to use Lagrangian coordinates for large deformations, an alternative method has been found by [GM77] to apply fully Lagrangian formulation using the Smooth Particle Hydrodynamics (SPH) for astrophysics simulation. It has recently gained popularity for fluid flows or computational mechanics [ZL18, IGP22], but the enforcement of boundary conditions is difficult and has a large computational cost.

Multiphase and free-surface flows

The interaction of multiple bodies is ubiquitous in nature, whether they correspond to fluids and/or solids. The interactions between fluids and structures are of great interest in different applications. A classical example is the blood flow through veins or the air flowing into elastic media [DDFQ06, DGN04]. On a larger level we can mention the lifting effect of air pressure on planes wings or the water effect on immersed part of a sailing boat, and the wind flow along the sail [PQ05]. Concerning the interactions between fluids, the behaviour of bubbles in liquids can greatly modify its flow and effects like

capillarity and are also important to take into account. A difference of densities between immiscible fluids induces gravity currents and implies for instance the Kelvin-Helmholtz effect [TCM11]. It happens in a wide range of events in nature, such as meteorology, wave in oceans, or avalanches. Free-surface flows involve an interface between the fluid and its surrounding medium, which can be modelled as void and thus implies no force on the interface. It proves useful when the impact of surrounding air is small enough to be neglected, as in dam-break simulations [Mar00, ABD08, CBM11]

The numerical simulation of free surface flows allows to model fluid flow and elastic deformation with reduced computational time. Thus it is nowadays used in a large range of domains but especially in fluid flows and structure deformations. The numerical simulation of free surfaces flows is difficult because tracking the interface comes with issues, such as numerical diffusion, mass conservation or topology changes. Lagrangian coordinates of the interface or the so-called front-tracking method can be used [TBE$^+$01]. The use of SPH method has also increased in popularity for free surface flows [FPRA09, XOJL12]. Hybrid method between Lagrangian and Eulerian coordinates like the marker and cell method allows to obtain advantages of both approaches [MTF$^+$08]. Using Eulerian coordinates, two methods are mainly used to model free-surface flows. The Volume of Fluid (VOF) method has been introduced in [HN81]. Here, the fluid is described by a volume fraction of liquid φ, which is the characteristic function of the fluid, and is thus discontinuous across the interface. The function is transported by the fluid and hence solves the following equation in the sense of distributions:

$$\frac{\partial \varphi}{\partial t} + \boldsymbol{u} \cdot \nabla \varphi = 0.$$

Since the characteristic function is tracked in the whole fluid domain, the VOF method induces a conservation of the mass of the fluid. However, the lack of regularity of φ is the main drawback of the method and hence the level set method was introduced by [Set96]. The interface corresponds to the zero level set of a smooth level-set function. Mass conservation is the main challenge of the method. The VOF approach is used here because of its ability to limit fluid mass loss and thus is of particular interest for mould filling, glacier flow or jet buckling experiments [Mar00, MPR03, BPL06, Jou10], as illustrated in Figure 2. In these articles, the SLIC algorithm [NW76] together with a two grid approach were used to lower the numerical diffusion of the method. Alternative interface reconstruction methods have been proposed in literature in order to have more accuracy, see for instance [SZ99, PZ99].

The VOF and level set methods can also be applied to interactions between multiple fluids. The VOF method remains popular with its ability to conserve mass and with the relative ease to avoid numerical diffusion [JBCP14, IZN18]. The level set method can also be applied for multiphase formulations as in [VdPSVW05, MBY22] or coupled with VOF method [SLSO08]. Multiple Newtonian and viscoelastic phases flows allow
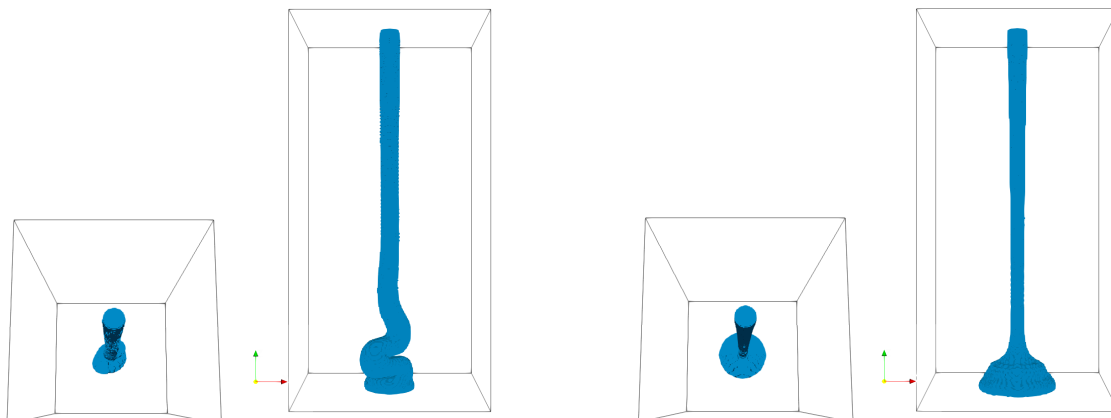
Figure 2 – Jet-buckling experiment. A Newtonian (left) and a viscoelastic (right) fluid are injected in a cavity and buckle when touching the bottom of the cavity. The elastic effect due to extra-stress term yields a bouncing of the viscoelastic fluid.

the modelling of complex natural relations which are of particular interest in industries but also to medical applications and the use of the VOF method conserving the total mass of the fluids is the main argument [FOA$^+$16, LHPCP19]. Numerical models for the simulation of the interactions between Newtonian fluids are nowadays widely known and used in multiple applications. Incorporating viscoelastic fluids is less frequent, but has already been seen in literature [SLSO08, FOA$^+$16, XAX19, LHPCP19, VG20].

Fluid-structure interactions

Fluid-structure interactions (FSI) have also been widely studied [STD$^+$96, CGN05, NGA$^+$19, OR21] using different numerical methods. The Arbitrary Lagrangian Eulerian method (ALE) is used for its ability to enlighten the advantages of both Lagrangian and Eulerian framework [DDFQ06] [HLZ81, AÖ10]. The mesh is moved as particles with the fluid velocity in Lagrangian coordinates, while it is fixed in Eulerian coordinates. In ALE method, the mesh is moving arbitrarily with a different speed than the flow velocity. Using this method, the interface between the fluid and the structure follows the mesh velocity, which enhances the precision at the interface [DGN04].

The immersed boundary method allows to model large deformations of thin structure as flags or filaments [RHC15, LHS15, MWY$^+$20], which is a major drawback of fully Eulerian formulation for multiphase model. The simulation of more than two phases is of greater complexity and hence is rarely seen in literature. Some examples can be found in [dNKM07, JBCP14]. The interaction between viscoelastic fluids and elastic solids (VFSI) also has been studied [MWY$^+$20, He21]. The Eulerian formulation of the problem is less frequent but is efficiently simulating large deformations of the structures [DR06, Ric13].

Interactions between structures

Simulation for the contact between elastic bodies in order to capture, e.g., friction, lubrication, fretting fatigue and wear is of high importance and is referred to tribology. An overview can be found in [HPMR04, VYS$^+$18] and, for example, FE simulations of tight elastic knots [BJS$^+$21, JGB$^+$21]. The traditional way to deal with FE simulations in tribology is to use Lagrangian coordinates and the elastic structure theory. Microscopically, big disparities at the surface between the bodies appear in friction problems. The discretisation of these disparities using Eulerian finite element methods can lead to large errors and require a huge accuracy. Thus this family of numerical methods is of proper usage when applied to large deformations and under the hypothesis of relatively flat surfaces.

Overview of the thesis

In this thesis, we further analyse the unified model suggested in [Pic16], where we can consider incompressible Newtonian and viscoelastic flows, or the deformation of incompressible Neo-Hookean material. The numerical scheme developed in [MPR03, BPL06] is advocated. It consists in a time-splitting algorithm for the time discretisation and a two-grid approach for the space discretisation. A novel time discretisation is proposed, taking advantage of the unified model. The model is validated for different test-cases.

The model of [JBCP14] for the simulation of multiple immiscible incompressible Newtonian phases is then extended in order to model phases which can be either an incompressible Newtonian or viscoelastic fluids, or an incompressible Neo-Hookean elastic solid. The model is then applied to different numerical experiments. The thesis is structured in the following manner.

In chapter 1, the unified mathematical model of [Pic16] is presented and the numerical framework is explained. The numerical scheme is based on a splitting strategy for the system of equations [Glo03] and a two-grid approach, as in [MPR03, Bon06]. An original time discretisation is suggested in order to increase the accuracy and obtain the unconditional stability of the scheme. A stability analysis is performed on a simplified model in order to compare the original EVSS scheme used in [BPL06] with the proposed alternative.

In chapter 2, both time discretisations described earlier are compared for viscoelastic flows and in different engineering validation test cases. The validation of the elastic model for incompressible Neo-Hookean material is presented through different test cases. The use and implementation of the Signorini boundary conditions is detailed.

In chapter 3, a multiple phase model for multiple viscoelastic fluids flows and elastic solid

deformations with free surfaces is presented. The approach presented in [JBCP14] is adapted to the unified model, where multiple different phases interact with each other. A VOF method with several volume fraction of liquids is adopted, with adapted numerical algorithms to reduce numerical diffusion.

In chapter 4, various numerical simulations obtained using our multiphase model are presented. Convergence of our numerical scheme is presented for different type of interactions, being either fluid-fluid, fluid-structure or structure-structure interactions.

Finally in chapter 5, the unified model is extended in order to model weakly compressible free surfaces flows for viscoelastic fluids and including compressible Neo-Hookean materials.

1 Numerical modelling of incompressible viscoelastic free-surface flows: from Newtonian fluids to elastic solids

In [BPL06], a model for the simulation of incompressible viscoelastic free surface flows has been presented. In [Pic16], the model is extended to include the flow of an incompressible Neo-Hookean elastic solid in Eulerian coordinates. In this chapter, this unified model is presented and its numerical approximation is studied. The order one splitting algorithm and the space discretisation using the two-grid approach studied in [BPL06] is applied. An original implicit time discretisation of the diffusion operator is presented as well as the numerical analysis of a simplified problem.

1.1 The mathematical model

Let Λ be a cavity of $\mathbb{R}^3$ in which a fluid is contained and let $T > 0$ be the final time of the simulation. Let $\varphi : \Lambda \times [0, T] \to \{0, 1\}$ be the volume fraction of fluid, i.e. φ equals 1 in the fluid and 0 in what is modelled as the surrounding vacuum. Thus the function $\varphi(\cdot, t)$ denotes the characteristic function of the liquid region, which is defined by $\Omega(t) = \{\boldsymbol{x} \in \Lambda; \varphi(\boldsymbol{x}, t) = 1\}$ for $0 \le t \le T$. Finally let $\mathcal{Q}_T$ be the space-time domain containing the fluid

$$\mathcal{Q}_T = \{(\boldsymbol{x}, t) \in \Lambda \times (0, T); \ \boldsymbol{x} \in \Omega(t)\}.$$

The function φ is transported with the fluid velocity $\boldsymbol{u}$ and is solution of the following equation in the weak sense [Mar00]:

$$\frac{\partial \varphi}{\partial t} + \boldsymbol{u} \cdot \nabla \varphi = 0, \quad \text{in } \Lambda \times [0, T]. \tag{1.1a}$$

In the fluid region, the velocity field $\boldsymbol{u} : \mathcal{Q}_T \to \mathbb{R}^3$, the pressure field $p : \mathcal{Q}_T \to \mathbb{R}$ and

the extra-stress tensor field $\boldsymbol{\sigma} : \mathcal{Q}_T \to \mathbb{R}^{3\times3}$ satisfy:

$$\rho \left(\frac{\partial \boldsymbol{u}}{\partial t} + (\boldsymbol{u} \cdot \nabla)\boldsymbol{u} \right) - 2\eta_s \nabla \cdot \boldsymbol{\epsilon}(\boldsymbol{u}) + \nabla p - \nabla \cdot \boldsymbol{\sigma} = \rho \boldsymbol{g}, \qquad \text{in } \mathcal{Q}_T, \qquad (1.1b)$$

$$\nabla \cdot \boldsymbol{u} = 0, \qquad \text{in } \mathcal{Q}_T, \qquad (1.1c)$$

$$\alpha \boldsymbol{\sigma} + \lambda \left(\frac{\partial \boldsymbol{\sigma}}{\partial t} + (\boldsymbol{u} \cdot \nabla)\boldsymbol{\sigma} - \nabla \boldsymbol{u} \boldsymbol{\sigma} - \boldsymbol{\sigma} \nabla \boldsymbol{u}^T \right) = 2\eta_p \boldsymbol{\epsilon}(\boldsymbol{u}), \qquad \text{in } \mathcal{Q}_T. \qquad (1.1d)$$

Here ρ is the density, $\boldsymbol{g}$ is the gravity, $\eta_s \geq 0$ is the solvent viscosity, $\eta_p > 0$ and λ are respectively the polymer viscosity and the relaxation time, and $\boldsymbol{\epsilon}(\boldsymbol{u}) = \frac{1}{2}(\nabla \boldsymbol{u} + \nabla \boldsymbol{u}^T)$. The additional parameter $\alpha \in \{0,1\}$ allows the system of equations (1.1) to model different problems:

1. Setting $\alpha = 1$ and $\lambda = 0$, the system of equations reduces to a system of Navier-Stokes equations for incompressible Newtonian flow with viscosity $\eta_s + \eta_p$.

2. Setting $\alpha = 1$ and $\lambda > 0$, the equation (1.1d) is the standard Oldroyd-B equation modelling the extra-stress of a viscoelastic fluid.

3. When $\alpha = 0$, $\lambda > 0$ and $\eta_s = 0$, the equation (1.1d) allows to model an elastic incompressible solid in Eulerian coordinates.

In order to justify point 3., let us introduce the Cauchy stress tensor of an elastic solid. Consider $\Omega_0 = \Omega(0)$ being the initial configuration of a given material and $\boldsymbol{X} \in \Omega_0$. First, the Lagrangian formulation of displacement is

$$\boldsymbol{x}(\boldsymbol{X}, t) - \boldsymbol{X} = \int_0^t \boldsymbol{u}(\boldsymbol{x}(\boldsymbol{X}, s), s) \, \mathrm{d}s \qquad (1.2)$$

where $\boldsymbol{x}$ is the deformation of $\boldsymbol{X}$ at time t and $\boldsymbol{u}(\boldsymbol{x}, t)$ the velocity at position $\boldsymbol{x}$ and time t. From equations (1.1a) and (1.2), the characteristic function φ satisfies

$$\varphi(\boldsymbol{x}(\boldsymbol{X}, t), t) = \varphi(\boldsymbol{X}, 0), \qquad (1.3)$$

for $\boldsymbol{X} \in \Omega_0$. The deformation gradient tensor in Lagrangian coordinates $\tilde{\boldsymbol{F}} : \Omega_0 \times [0, T] \to \mathbb{R}^{3\times3}$ is defined for all $\boldsymbol{X} \in \Omega_0$ by

$$\tilde{\boldsymbol{F}}_{ij}(\boldsymbol{X}, t) = \frac{\partial \boldsymbol{x}_i}{\partial \boldsymbol{X}_j}(\boldsymbol{X}, t), \quad i, j = 1, 2, 3.$$

By deriving in space and time the displacement equation (1.2), it yields

$$\frac{\partial \tilde{\boldsymbol{F}}}{\partial t}(\boldsymbol{X}, t) = \nabla \boldsymbol{u}(\boldsymbol{x}(\boldsymbol{X}, t), t) \tilde{\boldsymbol{F}}(\boldsymbol{X}, t). \qquad (1.4)$$

We now define $\boldsymbol{F} : \mathcal{Q}_T \to \mathbb{R}^{3\times3}$ to be the deformation gradient tensor in Eulerian

coordinates as $\boldsymbol{F}(\boldsymbol{x}(\boldsymbol{X},t),t) = \tilde{\boldsymbol{F}}(\boldsymbol{X},t)$, so that (1.4) becomes

$$\frac{\partial \boldsymbol{F}}{\partial t} + \boldsymbol{u} \cdot \nabla \boldsymbol{F} = \nabla \boldsymbol{u} \boldsymbol{F}. \tag{1.5a}$$

Now let $\boldsymbol{\sigma}$ be the Neo-Hookean elastic stress tensor, as defined in [DR06]:

$$\boldsymbol{\sigma} = \frac{\eta_p}{\lambda}(\boldsymbol{F}\boldsymbol{F}^T - \boldsymbol{I}), \tag{1.5b}$$

where $\boldsymbol{I}$ is the identity tensor. The modified Oldroyd-B equation (1.1d) for $\alpha = 0$, $\lambda > 0$ then arises from (1.5a) and (1.5b). Indeed, taking the convected derivative $\left(\frac{\partial}{\partial t} + \boldsymbol{u} \cdot \nabla\right)$ of (1.5b) we find

$$\frac{\partial \boldsymbol{\sigma}}{\partial t} + (\boldsymbol{u} \cdot \nabla)\boldsymbol{\sigma} = \frac{\eta_p}{\lambda}\left(\left(\frac{\partial \boldsymbol{F}}{\partial t} + (\boldsymbol{u} \cdot \nabla)\boldsymbol{F}\right)\boldsymbol{F}^T + \boldsymbol{F}\left(\frac{\partial \boldsymbol{F}^T}{\partial t} + (\boldsymbol{u} \cdot \nabla)\boldsymbol{F}^T\right)\right)$$

so that using (1.5a), we obtain

$$\frac{\partial \boldsymbol{\sigma}}{\partial t} + (\boldsymbol{u} \cdot \nabla)\boldsymbol{\sigma} - \nabla \boldsymbol{u}\boldsymbol{\sigma} - \boldsymbol{\sigma}\nabla \boldsymbol{u}^T = \frac{2\eta_p}{\lambda}\boldsymbol{\epsilon}(\boldsymbol{u}). \tag{1.6}$$

Hence, when the parameter $\alpha = 0$, the tensor $\boldsymbol{\sigma}$ models the Cauchy stress tensor of an incompressible Neo-Hookean elastic solid. Notice that the ratio η_p/λ denotes here the Lamé parameter for an incompressible solid.

The initial and boundary conditions added to (1.1) are the following. At initial time, both the velocity $\boldsymbol{u}_0 = \boldsymbol{u}(\cdot,0)$ and extra-stress $\boldsymbol{\sigma}_0 = \boldsymbol{\sigma}(\cdot,0)$ are prescribed in Ω_0. For $0 \le t \le T$, the free surface at time t is defined as $\partial\Omega(t)\backslash\partial\Lambda$. It is assumed that no force apply at the free surface: $(-p\boldsymbol{I} + 2\eta_s\boldsymbol{\epsilon}(\boldsymbol{u})) + \boldsymbol{\sigma})\boldsymbol{n} = 0$, where $\boldsymbol{n}$ is the unit outer normal of $\partial\Omega(t)\backslash\partial\Lambda$. On $\partial\Lambda$ either zero tangent force (free slip), zero normal force or no slip boundary conditions can be prescribed. The free slip condition writes on $\partial\Lambda$:

$$((-p\boldsymbol{I} + 2\eta_s\boldsymbol{\epsilon}(\boldsymbol{u}) + \boldsymbol{\sigma})\boldsymbol{n}) \cdot \boldsymbol{t} = 0,$$
$$\boldsymbol{u} \cdot \boldsymbol{n} = 0,$$

where $\boldsymbol{t}$ denotes any vector tangent to $\partial\Lambda$. Signorini boundary conditions can also be applied on $\partial\Lambda$, see section 2.3.1. Finally in the case of inflow boundary conditions the velocity and extra stress must be prescribed at the inflow boundary: $\boldsymbol{u} = \boldsymbol{u}_{\mathbf{in}}$ and $\boldsymbol{\sigma} = \boldsymbol{\sigma}_{\mathbf{in}}$ on $\Gamma_{\mathrm{in}} = \{\boldsymbol{x} \in \partial\Lambda; (\boldsymbol{u} \cdot \boldsymbol{n})(\boldsymbol{x},t) < 0\}$. A sketch of the main features of the mathematical model is shown in Figure 1.1.
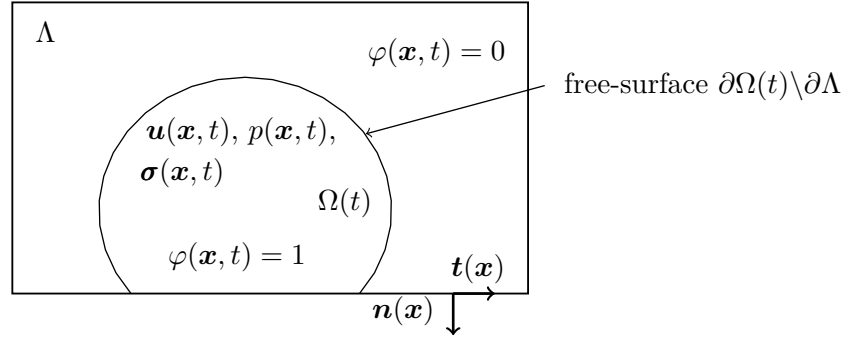
Figure 1.1 – Sketch of the mathematical model at time t. The characteristic function φ determines the position $\Omega(t)$ of the material. The free-surface corresponds to the set where the function φ exhibits a discontinuity. The smooth variables $\boldsymbol{u}$, p and $\boldsymbol{\sigma}$ take values in the material domain $\Omega(t)$.

1.2   An a priori estimate

Consider the momentum equation (1.1b). Since $\boldsymbol{u}$ is not defined on the whole domain Λ, we define in a formal way the product of (1.1b) with $\varphi\boldsymbol{u}$, integrated on Λ, as:

$$\int_\Lambda \varphi\rho\boldsymbol{u}\cdot\left(\frac{\partial\boldsymbol{u}}{\partial t}+(\boldsymbol{u}\cdot\nabla)\boldsymbol{u}\right)\,\mathrm{d}\boldsymbol{x}=\int_{\Omega(t)}\boldsymbol{u}\rho\cdot\left(\frac{\partial\boldsymbol{u}}{\partial t}+(\boldsymbol{u}\cdot\nabla)\boldsymbol{u}\right)\,\mathrm{d}\boldsymbol{x}.$$

From Reynold's transport Theorem A.0.1 in Appendix A, since the normal component of the velocity of the interface equals that of the fluid [Mar00], we find:

$$\begin{aligned}
\frac{\mathrm{d}}{\mathrm{d}t}\int_\Lambda \varphi\rho|\boldsymbol{u}|^2\,\mathrm{d}\boldsymbol{x}=\frac{\mathrm{d}}{\mathrm{d}t}\int_{\Omega(t)}\rho|\boldsymbol{u}|^2\,\mathrm{d}\boldsymbol{x}&=\int_{\Omega(t)}2\rho\frac{\partial\boldsymbol{u}}{\partial t}\cdot\boldsymbol{u}\,\mathrm{d}\boldsymbol{x}+\int_{\partial\Omega(t)}\rho|\boldsymbol{u}|^2(\boldsymbol{u}\cdot\boldsymbol{n})\,\mathrm{d}\boldsymbol{S}\\
&=\int_{\Omega(t)}2\rho\frac{\partial\boldsymbol{u}}{\partial t}\cdot\boldsymbol{u}\,\mathrm{d}\boldsymbol{x}+\int_{\Omega(t)}\nabla\cdot(\rho|\boldsymbol{u}|^2\boldsymbol{u})\,\mathrm{d}\boldsymbol{x}\quad(1.7)\\
&=\int_{\Omega(t)}\left(2\rho\boldsymbol{u}\cdot\left(\frac{\partial\boldsymbol{u}}{\partial t}+(\boldsymbol{u}\cdot\nabla)\boldsymbol{u}\right)+\rho|\boldsymbol{u}|^2(\nabla\cdot\boldsymbol{u})\right)\,\mathrm{d}\boldsymbol{x}.
\end{aligned}$$

Similarly:

$$\begin{aligned}
-\int_\Lambda \varphi\left(2\eta_s\nabla\cdot\boldsymbol{\epsilon}(\boldsymbol{u})-\nabla p+\nabla\cdot\boldsymbol{\sigma}\right)\cdot\boldsymbol{u}\,\mathrm{d}\boldsymbol{x}&=-\int_{\Omega(t)}\left(2\eta_s\nabla\cdot\boldsymbol{\epsilon}(\boldsymbol{u})-\nabla p+\nabla\cdot\boldsymbol{\sigma}\right)\cdot\boldsymbol{u}\,\mathrm{d}\boldsymbol{x}\\
&=\int_{\Omega(t)}\left(2\eta_s\boldsymbol{\epsilon}(\boldsymbol{u})-p\boldsymbol{I}+\boldsymbol{\sigma}\right):\boldsymbol{\epsilon}(\boldsymbol{u})\,\mathrm{d}\boldsymbol{x}\\
&\quad-\int_{\partial\Omega(t)}\boldsymbol{u}\cdot\left(2\eta_s\boldsymbol{\epsilon}(\boldsymbol{u})-p\boldsymbol{I}+\boldsymbol{\sigma}\right)\boldsymbol{n}\,\mathrm{d}\boldsymbol{S}\quad(1.8)\\
&=\int_{\Omega(t)}2\eta_s|\boldsymbol{\epsilon}(\boldsymbol{u})|^2-p(\nabla\cdot\boldsymbol{u})+\boldsymbol{\sigma}:\boldsymbol{\epsilon}(\boldsymbol{u})\,\mathrm{d}\boldsymbol{x}\\
&=\int_\Lambda\left(2\eta_s|\boldsymbol{\epsilon}(\boldsymbol{u})|^2+\boldsymbol{\sigma}:\boldsymbol{\epsilon}(\boldsymbol{u})\right)\varphi\,\mathrm{d}\boldsymbol{x},
\end{aligned}$$

since $\boldsymbol{u} = 0$ on $\partial\Lambda$ and free-surfaces interface condition $(2\eta_s\boldsymbol{\epsilon}(\boldsymbol{u}) + \boldsymbol{\sigma})\boldsymbol{n} - p\boldsymbol{n} = 0$ on $\partial\Omega(t)\backslash\partial\Lambda$. Finally from (1.1c), we obtain with formal computations:

$$\frac{\mathrm{d}}{\mathrm{d}t}\int_\Lambda \varphi\frac{\rho}{2}|\boldsymbol{u}|^2 \ \mathrm{d}\boldsymbol{x} + \int_\Lambda \left(2\eta_s|\boldsymbol{\epsilon}(\boldsymbol{u})|^2 + \boldsymbol{\sigma}:\boldsymbol{\epsilon}(\boldsymbol{u})\right)\varphi \ \mathrm{d}\boldsymbol{x} = \int_\Lambda \varphi\rho\boldsymbol{g}\cdot\boldsymbol{u} \ \mathrm{d}\boldsymbol{x}. \qquad (1.9)$$

Consider now the equation (1.1d). Using the same formal computation we find

$$\int_\Lambda \alpha\varphi|\boldsymbol{\sigma}|^2 \ \mathrm{d}\boldsymbol{x} + \int_\Lambda \lambda\varphi\left(\frac{\partial\boldsymbol{\sigma}}{\partial t} + (\boldsymbol{u}\cdot\nabla)\boldsymbol{\sigma}\right):\boldsymbol{\sigma} \ \mathrm{d}\boldsymbol{x} - \int_\Lambda 2\eta_p\varphi\boldsymbol{\epsilon}(\boldsymbol{u}):\boldsymbol{\sigma} \ \mathrm{d}\boldsymbol{x} - \lambda S(\boldsymbol{u},\boldsymbol{\sigma},\varphi)$$

$$= \int_{\Omega(t)} \alpha|\boldsymbol{\sigma}|^2 \ \mathrm{d}\boldsymbol{x} + \int_{\Omega(t)} \lambda\left(\frac{\partial\boldsymbol{\sigma}}{\partial t} + (\boldsymbol{u}\cdot\nabla)\boldsymbol{\sigma}\right):\boldsymbol{\sigma} \ \mathrm{d}\boldsymbol{x} - \int_{\Omega(t)} 2\eta_p\boldsymbol{\epsilon}(\boldsymbol{u}):\boldsymbol{\sigma} \ \mathrm{d}\boldsymbol{x} - \lambda S(\boldsymbol{u},\boldsymbol{\sigma},\varphi)$$

with $S(\boldsymbol{u},\boldsymbol{\sigma},\varphi) = \int_\Lambda \varphi\left(\nabla\boldsymbol{u}\boldsymbol{\sigma} + \boldsymbol{\sigma}\nabla\boldsymbol{u}^T\right):\boldsymbol{\sigma} \ \mathrm{d}\boldsymbol{x}$. Hence, using the same computations than for (1.7) and using (1.1c), it yields:

$$\frac{\mathrm{d}}{\mathrm{d}t}\int_\Lambda \varphi|\boldsymbol{\sigma}|^2 \ \mathrm{d}\boldsymbol{x} = \int_\Lambda 2\varphi\boldsymbol{\sigma}:\left(\frac{\partial\boldsymbol{\sigma}}{\partial t} + (\boldsymbol{u}\cdot\nabla)\boldsymbol{\sigma}\right) \ \mathrm{d}\boldsymbol{x}.$$

And we obtain:

$$\int_\Lambda \frac{\alpha}{2\eta_p}\varphi|\boldsymbol{\sigma}|^2 \ \mathrm{d}\boldsymbol{x} + \frac{\mathrm{d}}{\mathrm{d}t}\int_\Lambda \frac{\lambda}{4\eta_p}\varphi|\boldsymbol{\sigma}|^2 \ \mathrm{d}\boldsymbol{x} - \int_\Lambda \varphi\boldsymbol{\epsilon}(\boldsymbol{u}):\boldsymbol{\sigma} \ \mathrm{d}\boldsymbol{x} = \frac{\lambda}{2\eta_p}S(\boldsymbol{u},\boldsymbol{\sigma},\varphi). \qquad (1.10)$$

Summing (1.7) and (1.10), it yields:

$$\frac{\mathrm{d}}{\mathrm{d}t}\int_\Lambda \left(\rho|\boldsymbol{u}|^2 + \frac{\lambda}{2\eta_p}|\boldsymbol{\sigma}|^2\right)\varphi \ \mathrm{d}\boldsymbol{x} + \int_\Lambda \left(\frac{\alpha}{\eta_p}|\boldsymbol{\sigma}|^2 + 4\eta_s|\boldsymbol{\epsilon}(\boldsymbol{u})|^2\right)\varphi \ \mathrm{d}\boldsymbol{x}$$

$$= \int_\Lambda 2\rho\varphi\boldsymbol{g}\cdot\boldsymbol{u} \ \mathrm{d}\boldsymbol{x} + \frac{\lambda}{\eta_p}S(\boldsymbol{u},\boldsymbol{\sigma},\varphi) \qquad (1.11)$$

The nonlinear terms expressed by $S(\boldsymbol{u},\boldsymbol{\sigma},\varphi)$ do not allow the energy of the system to be conserved [BPL06]. The term $S(\boldsymbol{u},\boldsymbol{\sigma},\varphi)$ disappear when applied to co-rotational Oldroyd-B model [LM00]. Finally, results on energy estimates for the Oldroyd-B model can be found in [LO03].

1.3 An order one splitting scheme for the time discretisation

The splitting scheme considered in [Glo03, MPR03, BPL06] is used. Let Δt be the time step, N be the number of time steps, $\Delta t = T/N$ and $t^n = n\Delta t$, $n = 0, 1, \ldots, N$. Let $n \geq 1$ and assume that at time t^{n-1}, the approximated volume fraction $\varphi^{n-1} : \Lambda \to \mathbb{R}$ is known. The approximated material domain is then defined by $\Omega^{n-1} = \{\boldsymbol{x} \in \Lambda; \varphi^{n-1}(\boldsymbol{x}) = 1\}$. Let $\boldsymbol{u}^{n-1} : \Omega^{n-1} \to \mathbb{R}^3$ and $\boldsymbol{\sigma}^{n-1} : \Omega^{n-1} \to \mathbb{R}^{3\times3}$ respectively be the approximations of the velocity $\boldsymbol{u}(t^{n-1})$ and extra-stress tensor $\boldsymbol{\sigma}(t^{n-1})$. During the prediction step, the set

of advection equations from t^{n-1} to t^n is solved:

$$\frac{\partial \boldsymbol{v}}{\partial t} + (\boldsymbol{v} \cdot \nabla)\boldsymbol{v} = \boldsymbol{0}, \tag{1.12a}$$

$$\frac{\partial \boldsymbol{\tau}}{\partial t} + (\boldsymbol{v} \cdot \nabla)\boldsymbol{\tau} = \boldsymbol{0}, \tag{1.12b}$$

$$\frac{\partial \psi}{\partial t} + (\boldsymbol{v} \cdot \nabla)\psi = 0, \tag{1.12c}$$

with initial conditions

$$\boldsymbol{v}(t^{n-1}) = \boldsymbol{u}^{n-1}, \quad \boldsymbol{\tau}(t^{n-1}) = \boldsymbol{\sigma}^{n-1}, \quad \psi(t^{n-1}) = \varphi^{n-1}.$$

Dirichlet boundary conditions for the system of equations (1.12) are only prescribed if inflow boundary conditions apply on Γ_{in}. The system of equations (1.12) can be solved exactly using the method of characteristics. Indeed, for $\boldsymbol{x} : \Omega^{n-1} \times [t^{n-1}, t^n] \to \Lambda$, we have $\dfrac{\partial}{\partial t}\boldsymbol{x}(\boldsymbol{X}, t) = \boldsymbol{v}(\boldsymbol{x}(\boldsymbol{X}, t), t)$ (similar as in (1.2)) and from (1.12a), $\boldsymbol{v}$ is constant along the characteristic line:

$$\frac{\mathrm{d}}{\mathrm{d}t}\boldsymbol{v}(\boldsymbol{x}(\boldsymbol{X}, t), t) = \frac{\partial}{\partial t}\boldsymbol{v}(\boldsymbol{x}(\boldsymbol{X}, t), t) + \left(\frac{\partial}{\partial t}\boldsymbol{x}(\boldsymbol{X}, t) \cdot \nabla\right)\boldsymbol{v}(\boldsymbol{x}(\boldsymbol{X}, t), t) = 0.$$

This yields $\boldsymbol{v}(\boldsymbol{x}(\boldsymbol{X}, t), t) = \boldsymbol{v}(\boldsymbol{X}, t^{n-1}) = \boldsymbol{u}^{n-1}(\boldsymbol{X}, t^{n-1}), \quad t^{n-1} \le t \le t^n$. But from equation (1.2), we find

$$\boldsymbol{x}(\boldsymbol{X}, t) = \boldsymbol{X} + \int_{t^{n-1}}^{t} \boldsymbol{v}(\boldsymbol{x}(\boldsymbol{X}, s), s) \, \mathrm{d}s = \boldsymbol{X} + (t - t^{n-1})\boldsymbol{u}^{n-1}(\boldsymbol{X}, t^{n-1}).$$

Thus $\boldsymbol{v}(\boldsymbol{X} + (t - t^{n-1})\boldsymbol{u}^{n-1}(\boldsymbol{X}, t^{n-1}), t) = \boldsymbol{u}^{n-1}(\boldsymbol{X}, t^{n-1})$. Let us denote by $\boldsymbol{u}^{n-\frac{1}{2}}, \boldsymbol{\sigma}^{n-\frac{1}{2}}, \varphi^n$ the solutions at time t^n of (1.12). We thus have for all $\boldsymbol{X} \in \Omega^{n-1}$:

$$\boldsymbol{u}^{n-\frac{1}{2}}(\boldsymbol{X} + \Delta t \boldsymbol{u}^{n-1}(\boldsymbol{X})) = \boldsymbol{u}^{n-1}(\boldsymbol{X}), \tag{1.13a}$$

$$\boldsymbol{\sigma}^{n-\frac{1}{2}}(\boldsymbol{X} + \Delta t \boldsymbol{u}^{n-1}(\boldsymbol{X})) = \boldsymbol{\sigma}^{n-1}(\boldsymbol{X}), \tag{1.13b}$$

$$\varphi^n(\boldsymbol{X} + \Delta t \boldsymbol{u}^{n-1}(\boldsymbol{X})) = \varphi^{n-1}(\boldsymbol{X}). \tag{1.13c}$$

The computational domain is then updated, $\Omega^n = \{\boldsymbol{x} \in \Lambda; \varphi^n(\boldsymbol{x}) = 1\}$ and the correction step consists in finding $\boldsymbol{v} : \Omega^n \times [t^{n-1}, t^n] \to \mathbb{R}^3$, $q : \Omega^n \times [t^{n-1}, t^n] \to \mathbb{R}$ and $\boldsymbol{\tau} : \Omega^n \times [t^{n-1}, t^n] \to \mathbb{R}^{3\times 3}$ which satisfy

$$\rho\frac{\partial \boldsymbol{v}}{\partial t} - 2\eta_s \nabla \cdot \boldsymbol{\epsilon}(\boldsymbol{v}) + \nabla q - \nabla \cdot \boldsymbol{\tau} = \rho\boldsymbol{g}, \tag{1.14a}$$

$$\nabla \cdot \boldsymbol{v} = 0, \tag{1.14b}$$

$$\alpha\boldsymbol{\tau} + \lambda\left(\frac{\partial \boldsymbol{\tau}}{\partial t} - \nabla\boldsymbol{v}\boldsymbol{\tau} - \boldsymbol{\tau}\nabla\boldsymbol{v}^T\right) = 2\eta_p\boldsymbol{\epsilon}(\boldsymbol{v}), \tag{1.14c}$$

with initial conditions $\boldsymbol{v}(t^{n-1}) = \boldsymbol{u}^{n-\frac{1}{2}}$ and $\boldsymbol{\tau}(t^{n-1}) = \boldsymbol{\sigma}^{n-\frac{1}{2}}$. On the interface $\partial\Omega^n$, the boundary conditions are similar to those discussed at the end of section 1.1 (no-slip, zero normal force, zero tangential force). The approximation of velocity, pressure and extra-stress at time t^n are then updated by $\boldsymbol{u}^n = \boldsymbol{v}(t^n)$, $p^n = q(t^n)$ and $\boldsymbol{\sigma}^n = \boldsymbol{\tau}(t^n)$. A sketch of both steps of the splitting algorithm is shown in Figure 1.2.
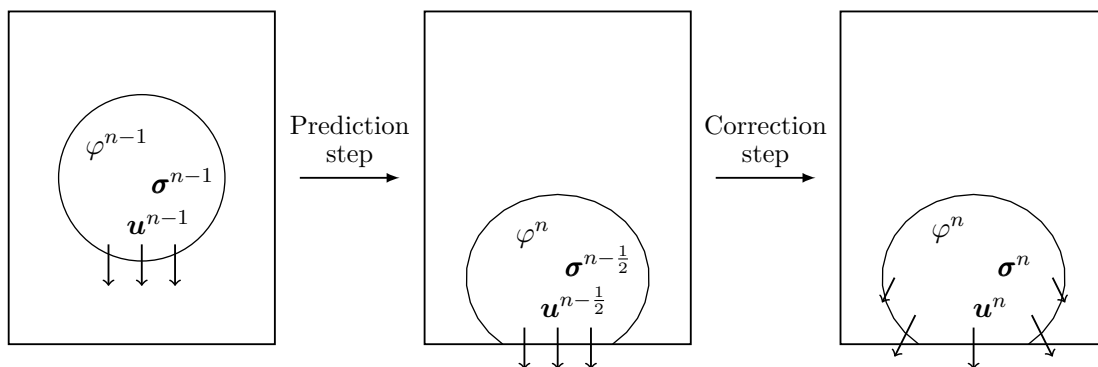
Figure 1.2 – Sketch of the main steps of splitting algorithm. In the prediction step, the fluid domain is updated with (1.13c) for the characteristic function φ^n. The velocity and extra-stress tensor are first transported with (1.13a) and (1.13b), then updated to $\boldsymbol{u}^n$ and $\boldsymbol{\sigma}^n$ during the correction step, by solving (1.14).

1.4 Space discretisation: two-grid approach and algorithms

The systems (1.12) and (1.14) are of very different nature, hyperbolic and parabolic respectively. A two-grid approach is used to solve them with different methods. The method of characteristics used to solve (1.12) is implemented on a structured grid of small cubic cells of size h, whereas (1.14) is solved on a tetrahedral unstructured mesh using finite elements of larger size H, see Figure 1.3.

The choice h small and H large is motivated as follows. First, a high accuracy is needed to track the interface, since φ is discontinuous (1 in the liquid, 0 in the vaccum). A grid of small size h allows to reduce the numerical diffusion on φ and have enough precision on the free-surface. Finally, the method of characteristics is easily implemented on a structured grid, without having to solve a linear system. Since the velocity and stress are smooth inside the material domain, the use of finite elements with a coarser grid of size H allows to save computational time. Moreover, cavities with complex topologies can be considered and the boundary conditions can be easily enforced. In [MPR03, BPL06], numerical experiments have shown that the ratio between H and h should be between 3 and 5.

<div align="center">Prediction step   Correction step</div>
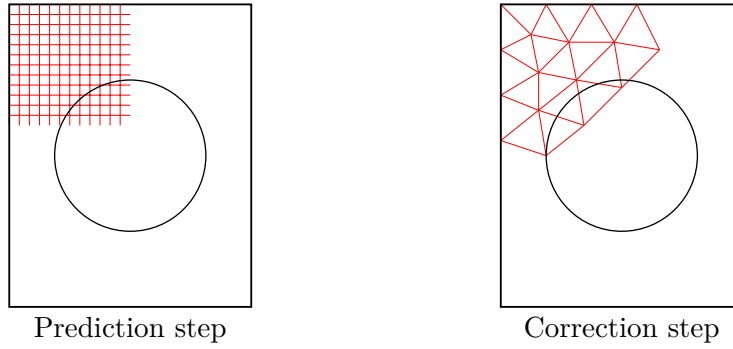
Figure 1.3 – Two-grid approach. The two grids are the same for all time steps. Left: fine structured grid of small cells to solve the prediction step (1.12). Right: coarse unstructured finite element mesh to solve the correction step (1.14).

1.4.1 Prediction step: structured grid

Consider a grid of cubic cells C_{ijk} with center $\boldsymbol{x}_{ijk}$. Let $\varphi_{ijk}^{n-1} \in [0,1]$ be the approximated value of the characteristic function $\varphi \in \{0,1\}$ at time t^{n-1} in each cell C_{ijk}, for all indices i,j,k. Also, we define $\boldsymbol{u}_{ijk}^{n-1}$ and $\boldsymbol{\sigma}_{ijk}^{n-1}$ to be the approximation of respectively the velocity $\boldsymbol{u}$ and the extra-stress tensor $\boldsymbol{\sigma}$. The prediction step consists now in implementing (1.13) on the grid. For (1.13c), the value φ_{ijk}^{n-1} of the cells is shifted by the distance $\Delta t \boldsymbol{u}_{ijk}^{n-1}$ and its content is redistributed between the intersected cells. The Figure 1.4 illustrates an example in two space dimensions. The values of $\varphi_{ijk}^{n-1}\boldsymbol{u}_{ijk}^{n-1}$ and $\varphi_{ijk}^{n-1}\boldsymbol{\sigma}_{ijk}^{n-1}$ are also advected according to (1.13a) and (1.13b).
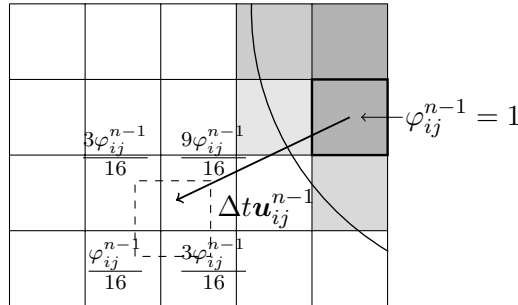
Figure 1.4 – Advection of characteristic function. The value in φ_{ij}^{n-1} is redistributed with respect to the intersecting cells.

In order to reduce the numerical diffusion at the interface, a SLIC (Simple Linear Interface Calculator) procedure is applied. Introduced by [NW76], the algorithm is applied before the advection of the characteristic function φ_{ijk}^{n-1}. For each cell where $0 < \varphi_{ijk}^{n} < 1$, its initial volume h^3 is reduced in a smaller parallelepiped of volume $\varphi_{ijk}^{n-1}h^3$, which dimensions depend on the value of φ^{n-1} in the surrounding neighbour cells [MPR03]. It is then pushed on the boundary of the cell which is common to another fully filled

cell, see an example in Figure 1.6 and 1.5. Thus the volume does not spread during the advection and numerical diffusion is lowered [MPR03], see Figure 1.6 for a 2D illustration.
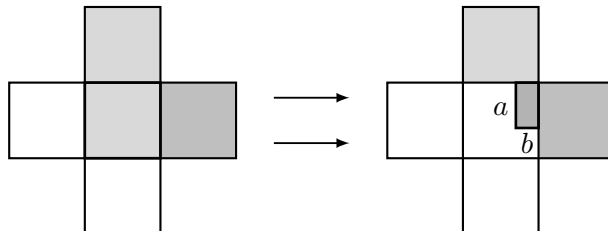
Figure 1.5 – In this example, the cell in the middle has a value $0 < \varphi_{ij}^{n-1} < 1$. We have $0 < \varphi_{i+1,j}^{n-1}, \varphi_{i,j+1}^{n-1} < 1$ and $\varphi_{i-1,j}^{n-1}, \varphi_{i,j-1}^{n-1} = 0$. In this case, the interface in the cell C_{ij} is defined as a rectangle $a \times b$, with $\dfrac{a}{b} = \dfrac{\varphi_{i+1,j}^{n-1}}{\varphi_{i,j+1}^{n-1}}$ and $ab = h^2 \varphi_{ij}^{n-1}$, see [MPR03] for details.
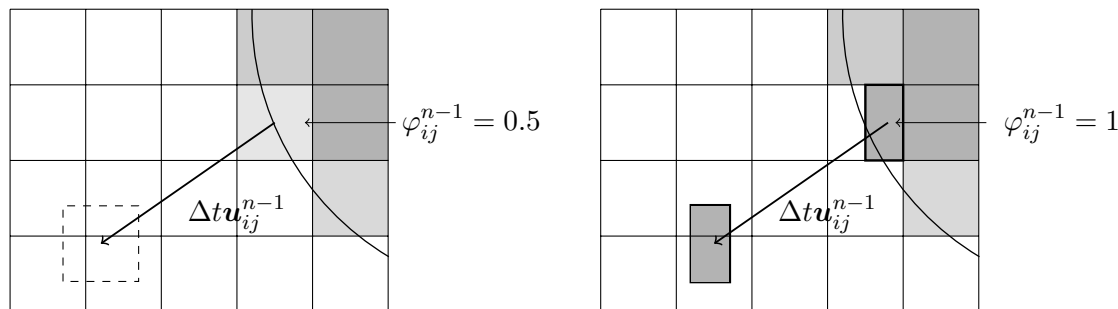
Figure 1.6 – Left: Illustration of numerical diffusion during the prediction step. Right: A sketch of SLIC algorithm to reduce numerical diffusion. Rather than advecting a cell half filled, half of the cell is completely filled, then the half cell is advected.

It may occur that $\varphi_{ijk}^{n} > 1$, although the flow is divergence-free. Furthermore, the prediction step can send liquid cells outside the cavity Λ and hence those must be redistributed into the cavity. The decompression algorithm proposed in [MPR03, BPL06] is applied. The procedure is the following: for all cells such that $\varphi_{ijk}^{n} > 1$ or which are advected out of the domain, the leftovers are stored in a buffer. This buffer is used to fill the cells which are not completely filled after advection and the SLIC procedure ($0 < \varphi_{ijk}^{n} < 1$). If the buffer is not empty, the remaining value is stored until the next time step.

The CFL number at time t^n is defined as

$$\text{CFL} = \frac{\max_{i,j,k} |\boldsymbol{u}_{ijk}^{n}| \cdot \Delta t}{h}. \tag{1.15}$$

The method of characteristics has the important property to remain stable, even for a CFL number larger than 1. However, if the time step is too large, the splitting error

increases. In practice, the CFL number is taken between 1 and 10.

In Figure 1.7, a sketch of the implementation of inflow boundary condition is displayed. In order to let the material flow into the cavity, cells are created in a volume (a surface in the 2D sketch of Figure 1.7) outside the cavity Λ of depth $\Delta t\boldsymbol{u}_{\mathbf{in}}$ and of width and length corresponding to the inflow surface. The values of the velocity $\boldsymbol{u}_{ijk}$ and the extra-stress $\boldsymbol{\sigma}_{ijk}$ in these inflow cells corresponds to the inflow values $\boldsymbol{u}_{\mathbf{in}}$ and $\boldsymbol{\sigma}_{\mathbf{in}}$ respectively. They are then transported using the method of characteristics during the prediction step, as described previously.
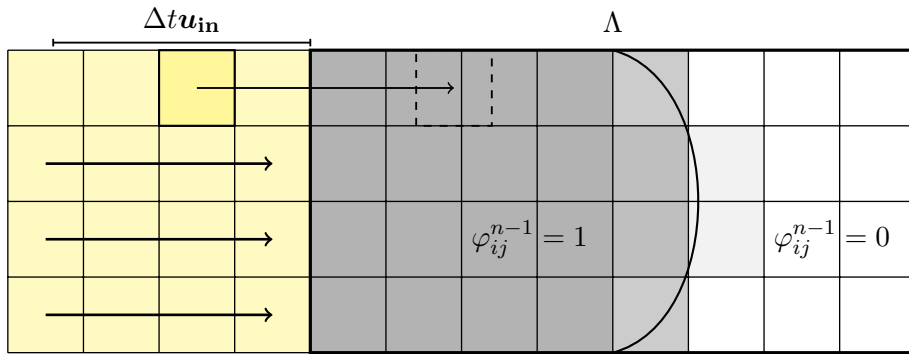
Figure 1.7 – Implementation of inflow boundary conditions. A zone of fully filled cells of length $\Delta t\boldsymbol{u}_{\mathbf{in}}$ is created on the other side of the inflow surface. The cells are then transported using the method of characteristics during the prediction step.

1.4.2   Interpolation between cells and FE mesh

Let $H > 0$ and $\mathcal{T}_H$ be a mesh of the cavity Λ, with tetrahedron having maximum diameter H. In order to compute the correction step, $\varphi_{ijk}^n, \boldsymbol{u}_{ijk}^{n-\frac{1}{2}}, \boldsymbol{\sigma}_{ijk}^{n-\frac{1}{2}}$ are then interpolated from the grid to the FE mesh. The interpolation algorithm is based on inverse distance weighted method introduced in [Fra82] and has already been used in, i.e., [LPS+18]. In the latter, the distance is taken to be the squared distance, thus giving less weight to the most distant cells. Thus the VOF value at node P of the mesh is computed as

$$\varphi_H^n(P) = \frac{\displaystyle\sum_{\substack{K \in \mathcal{T}_H \\ P \in K}} \sum_{\boldsymbol{x}_{ijk} \in K} \frac{\varphi_{ijk}^n}{\left\| P - \boldsymbol{x}_{ijk} \right\|^2}}{\displaystyle\sum_{\substack{K \in \mathcal{T}_H \\ P \in K}} \sum_{\boldsymbol{x}_{ijk} \in K} \frac{1}{\left\| P - \boldsymbol{x}_{ijk} \right\|^2}}. \tag{1.16}$$

We can now define the set of active elements and the computational domain as:

$$\Omega_H^n = \{K \in \mathcal{T}_H : \text{ there is a vertex of } K \text{ such that } \varphi_H^n(P) \geq 0.5\}. \tag{1.17}$$

The predicted velocity is then interpolated as

$$
\boldsymbol{u}_H^{n-\frac{1}{2}}(P) = \frac{\displaystyle\sum_{\substack{K\in\mathcal{T}_H \\ P\in K}} \sum_{\boldsymbol{x}_{ijk}\in K} \frac{\varphi_{ijk}^n \boldsymbol{u}_{ijk}^{n-\frac{1}{2}}}{\left\|P-\boldsymbol{x}_{ijk}\right\|^2}}{\displaystyle\sum_{\substack{K\in\mathcal{T}_H \\ P\in K}} \sum_{\boldsymbol{x}_{ijk}\in K} \frac{\varphi_{ijk}^n}{\left\|P-\boldsymbol{x}_{ijk}\right\|^2}} .
\tag{1.18}
$$

A similar formula as (1.18) is applied to interpolate the extra-stress.

Remark 1.4.1. In [Mar00], the characteristic function, the velocity and extra-stress tensor are interpolated using an approximate L^2 projection as follows:

$$
\varphi_H^n(P) = \frac{\displaystyle\sum_{\substack{K\in\mathcal{T}_H \\ P\in K}} \sum_{\boldsymbol{x}_{ijk}\in K} \phi_P(\boldsymbol{x}_{ijk})\varphi_{ijk}^n}{\displaystyle\sum_{\substack{K\in\mathcal{T}_H \\ P\in K}} \sum_{\boldsymbol{x}_{ijk}\in K} \phi_P(\boldsymbol{x}_{ijk})} ,
\tag{1.19}
$$

where ϕ_P is the finite element basis function corresponding to vertex P and

$$
\boldsymbol{u}_H^{n-\frac{1}{2}}(P) = \frac{\displaystyle\sum_{\substack{K\in\mathcal{T}_H \\ P\in K}} \sum_{\boldsymbol{x}_{ijk}\in K} \phi_P(\boldsymbol{x}_{ijk})\varphi_{ijk}^n \boldsymbol{u}_{ijk}^{n-\frac{1}{2}}}{\displaystyle\sum_{\substack{K\in\mathcal{T}_H \\ P\in K}} \sum_{\boldsymbol{x}_{ijk}\in K} \phi_P(\boldsymbol{x}_{ijk})\varphi_{ijk}^n}
\tag{1.20}
$$

and similarly as (1.20) for the extra-stress. A numerical experiment in Appendix B shows that both interpolation methods have the same convergence rate but the inverse distance weighted method is more precise. Thus this method has been preferred over the classical L^2 projection (1.20). $\qquad\square$

After the correction step (see section 1.4.3 hereafter), interpolation of the velocity and extra-stress from the FE mesh to the grid is performed. Here, the inverse distance weighted method yields:

$$
\boldsymbol{u}_{ijk}^n = \frac{\displaystyle\sum_{\substack{P\in K \\ \boldsymbol{x}_{ijk}\in K}} \frac{\boldsymbol{u}_H^n(P)}{\left\|P-\boldsymbol{x}_{ijk}\right\|^2}}{\displaystyle\sum_{\substack{P\in K \\ \boldsymbol{x}_{ijk}\in K}} \frac{1}{\left\|P-\boldsymbol{x}_{ijk}\right\|^2}}
\tag{1.21}
$$

and similarly as (1.21) for the extra-stress. The interpolation formula (1.21) is only applied to the active cells, that is those such that $\varphi_{ijk}^n > 0$.

1.4.3 Correction step: finite elements

In order to save computational time, equations (1.14a) and (1.14b) are decoupled from equation (1.14c). A possible order one scheme corresponding to (1.14) which enables the decoupling between the velocity-pressure variables and the extra-stress consists in

finding $\boldsymbol{u}^n : \Omega^n \to \mathbb{R}^3$ and $p^n : \Omega^n \to \mathbb{R}$ such that

$$\rho\frac{\boldsymbol{u}^n - \boldsymbol{u}^{n-\frac{1}{2}}}{\Delta t} - 2\eta_s \nabla \cdot \boldsymbol{\epsilon}(\boldsymbol{u}^n) + \nabla p^n - \nabla \cdot \boldsymbol{\sigma}^{n-\frac{1}{2}} = \rho\boldsymbol{g}, \qquad \text{in } \Omega^n, \qquad (1.22a)$$

$$\nabla \cdot \boldsymbol{u}^n = 0, \qquad \text{in } \Omega^n, \qquad (1.22b)$$

and then $\boldsymbol{\sigma}^n : \Omega^n \to \mathbb{R}^{3\times 3}$ such that

$$\alpha\boldsymbol{\sigma}^n + \lambda\left(\frac{\boldsymbol{\sigma}^n - \boldsymbol{\sigma}^{n-\frac{1}{2}}}{\Delta t} - \nabla\boldsymbol{u}^n\boldsymbol{\sigma}^{n-\frac{1}{2}} - \boldsymbol{\sigma}^{n-\frac{1}{2}}(\nabla\boldsymbol{u}^n)^T\right) = 2\eta_p\boldsymbol{\epsilon}(\boldsymbol{u}^n), \quad \text{in } \Omega^n. \quad (1.22c)$$

This scheme is unfortunately unstable when $\eta_s = 0$. The EVSS scheme was introduced for the stationary case in the context of Oldroyd-B system of equations ($\alpha = 1$)[RAB90]. It has been widely studied [FGP00, BPS01, BPL06] and consists in adding

$$\boldsymbol{D}^{n-\frac{1}{2}} = \boldsymbol{\epsilon}(\boldsymbol{u}^{n-\frac{1}{2}}) \qquad (1.23)$$

to equation (1.22a) for stability purposes. It then leads to finding $\boldsymbol{u}^n : \Omega^n \to \mathbb{R}^3$ and $p^n : \Omega^n \to \mathbb{R}$ such that

$$\rho\frac{\boldsymbol{u}^n - \boldsymbol{u}^{n-\frac{1}{2}}}{\Delta t} - 2(\eta_s + \eta_p)\nabla \cdot \boldsymbol{\epsilon}(\boldsymbol{u}^n) + \nabla p^n - \nabla \cdot \left(\boldsymbol{\sigma}^{n-\frac{1}{2}} - 2\eta_p\boldsymbol{D}^{n-\frac{1}{2}}\right) = \rho\boldsymbol{g}, \quad (1.24a)$$

$$\nabla \cdot \boldsymbol{u}^n = 0, \qquad (1.24b)$$

then finding $\boldsymbol{\sigma}^n : \Omega^n \to \mathbb{R}^{3\times 3}$ to solving (1.22c).

The tensor $\boldsymbol{D}^{n-\frac{1}{2}}$ requires to store 6 additional variables during computations. Furthermore, we can expect a conditional stability of the numerical scheme when the extra-stress tensor is taken explicitly in (1.24a). An alternative scheme is presented here. We start from the semi-implicit scheme

$$\rho\frac{\boldsymbol{u}^n - \boldsymbol{u}^{n-\frac{1}{2}}}{\Delta t} - 2\eta_s\nabla \cdot \boldsymbol{\epsilon}(\boldsymbol{u}^n) + \nabla p^n - \nabla \cdot \boldsymbol{\sigma}^n = \rho\boldsymbol{g}, \qquad \text{in } \Omega^n, \quad (1.25a)$$

$$\nabla \cdot \boldsymbol{u}^n = 0, \qquad \text{in } \Omega^n, \quad (1.25b)$$

$$\alpha\boldsymbol{\sigma}^n + \lambda\left(\frac{\boldsymbol{\sigma}^n - \boldsymbol{\sigma}^{n-\frac{1}{2}}}{\Delta t} - \nabla\boldsymbol{u}^{n-\frac{1}{2}}\boldsymbol{\sigma}^{n-\frac{1}{2}} - \boldsymbol{\sigma}^{n-\frac{1}{2}}(\nabla\boldsymbol{u}^{n-\frac{1}{2}})^T\right) = 2\eta_p\boldsymbol{\epsilon}(\boldsymbol{u}^n), \quad \text{in } \Omega^n. \quad (1.25c)$$

A major drawback of (1.25) is that the equations for $\boldsymbol{u}^n$, p^n and $\boldsymbol{\sigma}^n$ are now coupled. Fortunately, we can explicit $\boldsymbol{\sigma}^n$ from (1.25c) and substitute it in (1.25a) to decouple the computation of $\boldsymbol{u}^n$, p^n from that of $\boldsymbol{\sigma}^n$. Thus, we first find $\boldsymbol{u}^n : \Omega^n \to \mathbb{R}^3$ and

$p^n : \Omega^n \to \mathbb{R}$ such that

$$\rho \frac{\boldsymbol{u}^n - \boldsymbol{u}^{n-\frac{1}{2}}}{\Delta t} - 2\left(\eta_s + \frac{\eta_p \Delta t}{\lambda + \alpha \Delta t}\right) \nabla \cdot \boldsymbol{\epsilon}(\boldsymbol{u}^n) + \nabla p^n = \frac{\lambda}{\lambda + \alpha \Delta t} \nabla \cdot \boldsymbol{\sigma}^{n-\frac{1}{2}}$$

$$+ \frac{\lambda \Delta t}{\lambda + \alpha \Delta t} \nabla \cdot (\nabla \boldsymbol{u}^{n-\frac{1}{2}} \boldsymbol{\sigma}^{n-\frac{1}{2}} + \boldsymbol{\sigma}^{n-\frac{1}{2}} (\nabla \boldsymbol{u}^{n-\frac{1}{2}})^T) + \rho \boldsymbol{g}, \qquad \text{in } \Omega^n. \tag{1.25d}$$

and then $\boldsymbol{\sigma}^n : \Omega^n \to \mathbb{R}^{3 \times 3}$ satisfying (1.22c) instead of (1.25c), since the velocity has been updated.

Consider now the finite element discretization of the systems of equations (1.24) and (1.25) for a discretisation $\mathcal{T}_H$. The active domain Ω_H^n is defined in (1.17). For the sake of simplicity, the FE spaces are described when no-slip boundary conditions apply on $\partial \Lambda \cap \partial \Omega_H^n$ and when $\partial \Omega^n \neq \partial \Lambda$, so that the pressure is not defined up to a constant. The piecewise linear finite element spaces read:

$$\boldsymbol{V}_H^n = \{\boldsymbol{v} \in (\mathcal{C}^0(\overline{\Omega_H^n}))^3; \boldsymbol{v}_{|K} \in (\mathbb{P}_1(K))^3, \forall K \in \mathcal{T}_H, K \subset \Omega_H^n; \; \boldsymbol{v}_{|\partial \Lambda \cap \Omega_H^n} = \boldsymbol{0}\}, \tag{1.26a}$$

$$Q_H^n = \{q \in \mathcal{C}^0(\overline{\Omega_H^n}); q_{|K} \in \mathbb{P}_1(K), \forall K \in \mathcal{T}_H, K \subset \Omega_H^n\}, \tag{1.26b}$$

$$\boldsymbol{T}_H^n = \{\boldsymbol{\tau} \in (\mathcal{C}^0(\overline{\Omega_H^n}))^{3 \times 3}; \boldsymbol{\tau}_{|K} \in (\mathbb{P}_1(K))^{3 \times 3}, \forall K \in \mathcal{T}_H, K \subset \Omega_H^n\}. \tag{1.26c}$$

We consider $\boldsymbol{u}_H^{n-\frac{1}{2}} \in \boldsymbol{V}_H^n$ and $\boldsymbol{\sigma}_H^{n-\frac{1}{2}} \in \boldsymbol{T}_H^n$ computed by using the method of characteristics after the prediction step, see 1.4.2. For the explicit EVSS time discretisation scheme (1.24), we first compute the EVSS stabilization tensor by projection of the strain tensor onto $\boldsymbol{T}_H^n$:

Find $\boldsymbol{D}_H^{n-\frac{1}{2}} \in \boldsymbol{T}_H^n$ such that

$$\int_{\Omega_H^n} \boldsymbol{D}_H^{n-\frac{1}{2}} : \boldsymbol{\tau}_H \, \mathrm{d}\boldsymbol{x} = \int_{\Omega_H^n} \boldsymbol{\epsilon}(\boldsymbol{u}_H^{n-\frac{1}{2}}) : \boldsymbol{\tau}_H \, \mathrm{d}\boldsymbol{x}, \quad \forall \boldsymbol{\tau}_H \in \boldsymbol{T}_H^n. \tag{1.27a}$$

Then we recover the velocity $\boldsymbol{u}_H^n$ and the pressure p_H^n by solving the following system of equations:

Find $\boldsymbol{u}_H^n \in \boldsymbol{V}_H^n$, $p_H^n \in Q_H^n$ such that

$$
\int_{\Omega_H^n} \rho \frac{\boldsymbol{u}_H^n - \boldsymbol{u}_H^{n-\frac{1}{2}}}{\Delta t} \cdot \boldsymbol{v}_H \, \mathrm{d}\boldsymbol{x} + \int_{\Omega_H^n} 2(\eta_s + \eta_p)\boldsymbol{\epsilon}(\boldsymbol{u}_H^n) : \boldsymbol{\epsilon}(\boldsymbol{v}_H) \, \mathrm{d}\boldsymbol{x} - \int_{\Omega_H^n} p_H^n \nabla \cdot \boldsymbol{v}_H \, \mathrm{d}\boldsymbol{x}
$$

$$
= \int_{\Omega_H^n} (2\eta_p \boldsymbol{D}_H^{n-\frac{1}{2}} - \boldsymbol{\sigma}_H^{n-\frac{1}{2}}) : \boldsymbol{\epsilon}(\boldsymbol{v}_H) \, \mathrm{d}\boldsymbol{x} + \int_{\Omega_H^n} \rho \boldsymbol{g} \cdot \boldsymbol{v}_H \, \mathrm{d}\boldsymbol{x}, \qquad \forall \boldsymbol{v}_H \in \boldsymbol{V}_H^n, \quad (1.27\mathrm{b})
$$

$$
\int_{\Omega_H^n} (\nabla \cdot \boldsymbol{u}_H^n) q_H \, \mathrm{d}\boldsymbol{x} \tag{1.27c}
$$

$$
+ \sum_{\substack{K \in \mathcal{T}_H \\ K \subset \Omega_H^n}} \alpha_K \int_K \left(\nabla p_H^n - \nabla \cdot \boldsymbol{\sigma}_H^{n-\frac{1}{2}} - \rho \boldsymbol{g} \right) \cdot \nabla q_H \, \mathrm{d}\boldsymbol{x} = 0, \qquad \forall q_H \in Q_H^n.
$$

The local stabilization coefficients α_k are defined by

$$
\alpha_K = \begin{cases} \dfrac{|K|^{\frac{2}{3}}}{12(\eta_s + \eta_p)} & \text{if } Re_K \leq 3, \\[3mm] \dfrac{|K|^{\frac{2}{3}}}{4Re_K(\eta_s + \eta_p)} & \text{otherwise,} \end{cases}
$$

where the local Reynolds number Re_K is defined by

$$
Re_K = \frac{\rho |K|^{\frac{1}{3}} \max_{\boldsymbol{x} \in K} |\boldsymbol{u}_H^{n-\frac{1}{2}}(\boldsymbol{x})|}{2(\eta_s + \eta_p)}.
$$

This stabilization parameter has been studied in the context of stationary Stokes problems with GLS stabilization, see, e.g., [FH93]. Alternative stabilisation methods could be used for evolutionary problems [TS03]. Then the extra-stress tensor $\boldsymbol{\sigma}_H^n \in \boldsymbol{T}_H^n$ is computed by solving:

$$
\int_{\Omega_H^n} \boldsymbol{\sigma}_H^n : \boldsymbol{\tau}_H \, \mathrm{d}\boldsymbol{x} = \int_{\Omega_H^n} \frac{\lambda}{\lambda + \alpha \Delta t} \boldsymbol{\sigma}_H^{n-\frac{1}{2}} : \boldsymbol{\tau}_H \, \mathrm{d}\boldsymbol{x}
$$

$$
+ \int_{\Omega_H^n} \frac{\lambda \Delta t}{\lambda + \alpha \Delta t} (\nabla \boldsymbol{u}_H^n \boldsymbol{\sigma}_H^{n-\frac{1}{2}} + \boldsymbol{\sigma}_H^{n-\frac{1}{2}} (\nabla \boldsymbol{u}_H^n)^T) : \boldsymbol{\tau}_H \, \mathrm{d}\boldsymbol{x} \tag{1.27d}
$$

$$
+ \int_{\Omega_H^n} \frac{2\eta_p \Delta t}{\lambda + \alpha \Delta t} \boldsymbol{\epsilon}(\boldsymbol{u}_H^n) : \boldsymbol{\tau}_H \, \mathrm{d}\boldsymbol{x}, \qquad \forall \boldsymbol{\tau}_H \in \boldsymbol{T}_H^n.
$$

Consider now the semi-implicit scheme (1.25). The decoupling strategy applied in (1.25d) is now applied here to obtain an explicit formulation with respect to the extra-stress tensor. So the implicit fully discrete formulation of the problem (1.25d) is the following:

Find $\boldsymbol{u}_H^n \in \boldsymbol{V}_H^n$, $p_H^n \in Q_H^n$ such that

$$\int_{\Omega_H^n} \rho \frac{\boldsymbol{u}_H^n - \boldsymbol{u}_H^{n-\frac{1}{2}}}{\Delta t} \cdot \boldsymbol{v}_H \, \mathrm{d}\boldsymbol{x} + \int_{\Omega_H^n} 2 \left(\eta_s + \frac{\eta_p \Delta t}{\lambda + \alpha \Delta t} \right) \boldsymbol{\epsilon}(\boldsymbol{u}_H^n) : \boldsymbol{\epsilon}(\boldsymbol{v}_H) \, \mathrm{d}\boldsymbol{x}$$

$$- \int_{\Omega_H^n} p_H^n \nabla \cdot \boldsymbol{v}_H \, \mathrm{d}\boldsymbol{x} = \int_{\Omega_H^n} \rho \boldsymbol{g} \cdot \boldsymbol{v}_H \, \mathrm{d}\boldsymbol{x} - \int_{\Omega_H^n} \frac{\lambda}{\lambda + \alpha \Delta t} \boldsymbol{\sigma}_H^{n-\frac{1}{2}} : \boldsymbol{\epsilon}(\boldsymbol{v}_H) \, \mathrm{d}\boldsymbol{x} \qquad (1.28\text{a})$$

$$- \int_{\Omega_H^n} \frac{\lambda \Delta t}{\lambda + \alpha \Delta t} (\nabla \boldsymbol{u}_H^{n-\frac{1}{2}} \boldsymbol{\sigma}_H^{n-\frac{1}{2}} + \boldsymbol{\sigma}_H^{n-\frac{1}{2}} (\nabla \boldsymbol{u}_H^{n-\frac{1}{2}})^T) : \boldsymbol{\epsilon}(\boldsymbol{v}_H) \, \mathrm{d}\boldsymbol{x}, \qquad \forall \boldsymbol{v}_H \in \boldsymbol{V}_H^n,$$

$$\int_{\Omega_H^n} (\nabla \cdot \boldsymbol{u}_H^n) q_H \, \mathrm{d}\boldsymbol{x} \qquad\qquad\qquad (1.28\text{b})$$

$$+ \sum_{\substack{K \in \mathcal{T}_H \\ K \subset \Omega_H^n}} \alpha_K \int_K \left(\nabla p_H^n - \frac{\lambda}{\lambda + \alpha \Delta t} \nabla \cdot \boldsymbol{\sigma}_H^{n-\frac{1}{2}} - \rho \boldsymbol{g} \right) \cdot \nabla q_H \, \mathrm{d}\boldsymbol{x} = 0, \qquad \forall q_H \in Q_H^n.$$

The stabilisation terms in the equation (1.28b) do not fully correspond to the diffusion terms in (1.25d), introducing a lack of consistency. However, numerical results show empirically that these additional terms do not improve stability of the results, and were thus removed. In the next step, we solve the weak formulation of the Oldroyd-B equation (1.27d) to recover the extra-stress tensor $\boldsymbol{\sigma}_H^n \in \boldsymbol{T}_H^n$. The coefficient α_K in (1.28b) becomes:

$$\alpha_K = \begin{cases} \dfrac{|K|^{\frac{2}{3}}}{12 \left(\eta_s + \eta_p \frac{\Delta t}{\lambda + \alpha \Delta t} \right)} & \text{if } Re_K \leq 3 \\[4ex] \dfrac{|K|^{\frac{2}{3}}}{4 Re_K \left(\eta_s + \eta_p \frac{\Delta t}{\lambda + \alpha \Delta t} \right)} & \text{otherwise,} \end{cases}$$

where the local Reynolds number Re_K is defined by

$$Re_K = \frac{\rho |K|^{\frac{1}{3}} \max_{\boldsymbol{x} \in K} |\boldsymbol{u}_H^{n-\frac{1}{2}}(\boldsymbol{x})|}{2 \left(\eta_s + \eta_p \frac{\Delta t}{\lambda + \alpha \Delta t} \right)}.$$

Indeed, this definition for the coefficients α_K is motivated by the modification of the viscosity in (1.25d) and (1.28a), by the modified viscosity $\eta_s + \eta_p \frac{\Delta t}{\lambda + \alpha \Delta t}$. Numerical experiments have shown that the system is better stabilized using this definition.

The linear systems corresponding to (1.27b), (1.27c) or (1.28a), (1.28b) are solved using a Generalised minimal residual (GMRES) algorithm with an incomplete LU preconditioner. The mass matrix is approximated using mass lumping, thus the linear systems (1.27a) and (1.27d) are diagonal.

1.5 Analysis of a simplified model for the time discretisation

Stability and convergence of the time discretisation schemes for a simplified system of equations are now studied. The domain is considered entirely filled with liquid ($\varphi = 1$ in Λ and thus $\Lambda = \Omega(t) = \Omega$, for $0 \leq t \leq T$). The system (1.1) is considered, where all convective and nonlinear terms are removed:

$$\rho \frac{\partial \boldsymbol{u}}{\partial t} - 2\eta_s \nabla \cdot \boldsymbol{\epsilon}(\boldsymbol{u}) + \nabla p - \nabla \cdot \boldsymbol{\sigma} = \boldsymbol{0}, \qquad \text{in } \Omega \times [0, T], \qquad (1.29a)$$

$$\nabla \cdot \boldsymbol{u} = 0, \qquad \text{in } \Omega \times [0, T], \qquad (1.29b)$$

$$\alpha \boldsymbol{\sigma} + \lambda \frac{\partial \boldsymbol{\sigma}}{\partial t} = 2\eta_p \boldsymbol{\epsilon}(\boldsymbol{u}), \qquad \text{in } \Omega \times [0, T], \qquad (1.29c)$$

$$\boldsymbol{u} = 0, \qquad \text{on } \partial\Omega \times [0, T]. \qquad (1.29d)$$

Formal calculations are now used to prove a priori estimates for this model. Multiplying (1.29a)-(1.29c) respectively by $\boldsymbol{u}$, p, $\boldsymbol{\sigma}$ and integrating over space yields

$$\frac{\mathrm{d}}{\mathrm{d}t} \int_\Omega \left(\rho |\boldsymbol{u}|^2 + \frac{\lambda}{2\eta_p} |\boldsymbol{\sigma}|^2 \right) \, \mathrm{d}\boldsymbol{x} + \int_\Omega \left(4\eta_s |\boldsymbol{\epsilon}(\boldsymbol{u})|^2 + \frac{\alpha}{\eta_p} |\boldsymbol{\sigma}|^2 \right) \, \mathrm{d}\boldsymbol{x} = 0. \qquad (1.30)$$

When $\eta_s = 0$, the $\boldsymbol{\epsilon}(\boldsymbol{u})$ term vanishes in the above equality; thus we need another estimate. Let us take the time derivative of (1.29a):

$$\rho \frac{\partial^2 \boldsymbol{u}}{\partial t^2} - 2\eta_s \nabla \cdot \boldsymbol{\epsilon} \left(\frac{\partial \boldsymbol{u}}{\partial t} \right) + \nabla \frac{\partial p}{\partial t} - \nabla \cdot \frac{\partial \boldsymbol{\sigma}}{\partial t} = \boldsymbol{0}.$$

Then adding λ times the above equation to α times (1.29a) and eliminating $\boldsymbol{\sigma}$ using (1.29c) yields

$$\rho \lambda \frac{\partial^2 \boldsymbol{u}}{\partial t^2} + \rho \alpha \frac{\partial \boldsymbol{u}}{\partial t} - 2\eta_s \lambda \nabla \cdot \boldsymbol{\epsilon} \left(\frac{\partial \boldsymbol{u}}{\partial t} \right) + \lambda \nabla \frac{\partial p}{\partial t} + \alpha \nabla p - 2(\alpha \eta_s + \eta_p) \nabla \cdot \boldsymbol{\epsilon}(\boldsymbol{u}) = \boldsymbol{0}. \quad (1.31)$$

Multiplying by $\dfrac{\partial \boldsymbol{u}}{\partial t}$ and integrating on Ω yields

$$\frac{1}{2} \frac{\mathrm{d}}{\mathrm{d}t} \int_\Omega \left(\rho \lambda \left| \frac{\partial \boldsymbol{u}}{\partial t} \right|^2 + 2(\alpha \eta_s + \eta_p) |\boldsymbol{\epsilon}(\boldsymbol{u})|^2 \right) \, \mathrm{d}\boldsymbol{x}$$

$$+ \int_\Omega \left(\rho \alpha \left| \frac{\partial \boldsymbol{u}}{\partial t} \right|^2 + 2\eta_s \lambda \left| \boldsymbol{\epsilon} \left(\frac{\partial \boldsymbol{u}}{\partial t} \right) \right|^2 \right) \, \mathrm{d}\boldsymbol{x} = 0.$$

Integrating from $t = 0$ to $t = T$ yields

$$
\int_\Omega \left(\rho\lambda \left| \frac{\partial \boldsymbol{u}}{\partial t}(T) \right|^2 + 2(\alpha\eta_s + \eta_p)|\boldsymbol{\epsilon}(\boldsymbol{u})(T)|^2 \right) \, \mathrm{d}\boldsymbol{x}
$$

$$
+ \int_0^T \int_\Omega \left(2\rho\alpha \left| \frac{\partial \boldsymbol{u}}{\partial t} \right|^2 + 4\eta_s\lambda \left| \boldsymbol{\epsilon}\left(\frac{\partial \boldsymbol{u}}{\partial t} \right) \right|^2 \right) \, \mathrm{d}\boldsymbol{x} \, \mathrm{d}t \qquad (1.32)
$$

$$
= \int_\Omega \left(\rho\lambda \left| \frac{\partial \boldsymbol{u}}{\partial t}(0) \right|^2 + 2(\alpha\eta_s + \eta_p)|\boldsymbol{\epsilon}(\boldsymbol{u})(0)|^2 \right) \, \mathrm{d}\boldsymbol{x}.
$$

Hence we are able to bound the $\boldsymbol{\epsilon}(\boldsymbol{u})$ term even when $\alpha = \eta_s = 0$. Such a stability estimate is usually dedicated to wave equations, where the control is made on the time derivative of $\boldsymbol{u}$. This is not surprising, since the simplified unified model (1.29) is hyperbolic when $\alpha = \eta_s = 0$ and describes wave propagation, whereas it is parabolic when either α or η_s are not 0. Note that (1.31) corresponds to a modified fluid dynamics equation, first derived in [CR81, CM72] for $\alpha = 1$ and with the additional convective terms. Some convergence results were proven in [RS12a, RS12b].

Let Δt be the time step, N be the number of time steps such that $\Delta t = T/N$ and $t^n = n\Delta t$, $n = 0, 1, \ldots, N$. The two different numerical schemes (1.24) and (1.25) for the time discretisations are considered here for the reduced system (1.29), and stability estimates analogous to (1.32) are obtained for each of them. The EVSS scheme consists in finding $\boldsymbol{u}^n$ and p^n in Ω such that

$$
\rho \frac{\boldsymbol{u}^n - \boldsymbol{u}^{n-1}}{\Delta t} - 2(\eta_s + \eta_p)\nabla \cdot \boldsymbol{\epsilon}(\boldsymbol{u}^n) + \nabla p^n = \nabla \cdot (\boldsymbol{\sigma}^{n-1} - 2\eta_p \boldsymbol{D}^{n-1}), \qquad (1.33\text{a})
$$

$$
\nabla \cdot \boldsymbol{u}^n = 0, \qquad (1.33\text{b})
$$

then $\boldsymbol{\sigma}^n$ and $\boldsymbol{D}^n$ such that

$$
\alpha\boldsymbol{\sigma}^n + \lambda \left(\frac{\boldsymbol{\sigma}^n - \boldsymbol{\sigma}^{n-1}}{\Delta t} \right) = 2\eta_p \boldsymbol{\epsilon}(\boldsymbol{u}^n), \qquad (1.33\text{c})
$$

$$
\boldsymbol{D}^n = \boldsymbol{\epsilon}(\boldsymbol{u}^n) \qquad (1.33\text{d})
$$

Given $\boldsymbol{u}^0 \in H_0^1(\Omega)^3$ and $\boldsymbol{\sigma}^0 \in L^2(\Omega)^{3\times3}$, for $n = 1, \ldots, N$, let $\boldsymbol{u}^n, p^n$ and $\boldsymbol{\sigma}^n$ to be the unique weak solution of (1.33) and further assume that $\boldsymbol{u}^n \in H_0^1(\Omega)^3$, $p^n \in L_0^2(\Omega)$ and $\boldsymbol{\sigma}^n \in L^2(\Omega)^{3\times3}$. The following Proposition shows the conditional stability of the EVSS scheme (1.33), which corresponds to the discrete counterpart of (1.30) and (1.32).

Proposition 1.5.1. Consider the EVSS scheme (1.33). For $\eta_s, \eta_p > 0$, if $\Delta t \leq \lambda$, we

have

$$
\int_\Omega \left(\rho |\boldsymbol{u}^N|^2 + \frac{\lambda}{4\eta_p} |\boldsymbol{\sigma}^N|^2 \right) \mathrm{d}\boldsymbol{x} \tag{1.34}
$$

$$
\leq \int_\Omega \left(\rho |\boldsymbol{u}^0|^2 + \frac{\lambda}{2\eta_p} |\boldsymbol{\sigma}^0|^2 \right) \mathrm{d}\boldsymbol{x} + \Delta t \int_\Omega \left(3\eta_p |\boldsymbol{\epsilon}(\boldsymbol{u}^0)|^2 + \frac{\alpha+1}{4\eta_p} |\boldsymbol{\sigma}^0| \right) \mathrm{d}\boldsymbol{x}.
$$

Furthermore, if $\alpha = 1$, we have for all $\Delta t > 0$

$$
\int_\Omega \left(\frac{\rho\lambda}{2} \left| \frac{\boldsymbol{u}^N - \boldsymbol{u}^{N-1}}{\Delta t} \right|^2 + 2\eta_p\lambda\Delta t \left| \boldsymbol{\epsilon}\left(\frac{\boldsymbol{u}^N - \boldsymbol{u}^{N-1}}{\Delta t} \right) \right|^2 + 2(\eta_s + \eta_p)|\boldsymbol{\epsilon}(\boldsymbol{u}^N)|^2 \right) \mathrm{d}\boldsymbol{x}
$$

$$
+ \sum_{n=1}^{N-1} \Delta t \int_\Omega \left(\rho \left| \frac{\boldsymbol{u}^n - \boldsymbol{u}^{n-1}}{\Delta t} \right|^2 + 2\eta_s\lambda \left| \boldsymbol{\epsilon}\left(\frac{\boldsymbol{u}^n - \boldsymbol{u}^{n-1}}{\Delta t} \right) \right|^2 \right) \mathrm{d}\boldsymbol{x} \tag{1.35}
$$

$$
\leq \int_\Omega \left(\frac{\rho\lambda}{2} \left| \frac{\boldsymbol{u}^1 - \boldsymbol{u}^0}{\Delta t} \right|^2 + 2\eta_p\lambda\Delta t \left| \boldsymbol{\epsilon}\left(\frac{\boldsymbol{u}^1 - \boldsymbol{u}^0}{\Delta t} \right) \right|^2 + 2(\eta_s + \eta_p)|\boldsymbol{\epsilon}(\boldsymbol{u}^1)|^2 \right) \mathrm{d}\boldsymbol{x}.
$$

If $\alpha = 0$ and $\Delta t \leq \lambda(\eta_s + 2\eta_p)/\eta_p$, we have

$$
\int_\Omega \left(\rho\lambda \left| \frac{\boldsymbol{u}^N - \boldsymbol{u}^{N-1}}{\Delta t} \right|^2 + \eta_p |\boldsymbol{\epsilon}(\boldsymbol{u}^N)|^2 + \eta_p |\boldsymbol{\epsilon}(\boldsymbol{u}^{N-1})|^2 \right) \mathrm{d}\boldsymbol{x} \tag{1.36}
$$

$$
\leq \int_\Omega \left(\rho\lambda \left| \frac{\boldsymbol{u}^1 - \boldsymbol{u}^0}{\Delta t} \right|^2 + \eta_p |\boldsymbol{\epsilon}(\boldsymbol{u}^1)|^2 + \eta_p |\boldsymbol{\epsilon}(\boldsymbol{u}^0)|^2 + (2\eta_p + \eta_s)\lambda\Delta t \left| \boldsymbol{\epsilon}\left(\frac{\boldsymbol{u}^1 - \boldsymbol{u}^0}{\Delta t} \right) \right|^2 \right) \mathrm{d}\boldsymbol{x}.
$$

Proof. The weak formulation of the system of equations (1.33) yields for $n = 1, \ldots, N$: Find $\boldsymbol{u}^n \in H_0^1(\Omega)^3$, $p^n \in L_0^2(\Omega)$ and $\boldsymbol{\sigma}^n \in L^2(\Omega)^{3\times 3}$ such that:

$$
\int_\Omega \rho \frac{\boldsymbol{u}^n - \boldsymbol{u}^{n-1}}{\Delta t} \cdot \boldsymbol{v} \, \mathrm{d}\boldsymbol{x} + 2(\eta_s + \eta_p) \int_\Omega \boldsymbol{\epsilon}(\boldsymbol{u}^n) : \boldsymbol{\epsilon}(\boldsymbol{v}) \, \mathrm{d}\boldsymbol{x} \tag{1.37a}
$$

$$
- \int_\Omega p^n (\nabla \cdot \boldsymbol{v}) \, \mathrm{d}\boldsymbol{x} + \int_\Omega (\boldsymbol{\sigma}^{n-1} - 2\eta_p \boldsymbol{D}^{n-1}) : \boldsymbol{\epsilon}(\boldsymbol{v}) \, \mathrm{d}\boldsymbol{x} = 0, \quad \forall \boldsymbol{v} \in H_0^1(\Omega)^3,
$$

$$
\int_\Omega (\nabla \cdot \boldsymbol{u}^n) q \, \mathrm{d}\boldsymbol{x} = 0, \quad \forall q \in L_0^2(\Omega), \tag{1.37b}
$$

$$
\int_\Omega \alpha\boldsymbol{\sigma}^n : \boldsymbol{\tau} \, \mathrm{d}\boldsymbol{x} + \int_\Omega \lambda \frac{\boldsymbol{\sigma}^n - \boldsymbol{\sigma}^{n-1}}{\Delta t} : \boldsymbol{\tau} \, \mathrm{d}\boldsymbol{x} \tag{1.37c}
$$

$$
- \int_\Omega 2\eta_p \boldsymbol{\epsilon}(\boldsymbol{u}^n) : \boldsymbol{\tau} \, \mathrm{d}\boldsymbol{x} = 0, \quad \forall \boldsymbol{\tau} \in L^2(\Omega)^{3\times 3}
$$

$$
\int_\Omega \boldsymbol{D}^n : \boldsymbol{\tau} \, \mathrm{d}\boldsymbol{x} - \int_\Omega \boldsymbol{\epsilon}(\boldsymbol{u}^n) : \boldsymbol{\tau} \, \mathrm{d}\boldsymbol{x} = 0, \quad \forall \boldsymbol{\tau} \in L^2(\Omega)^{3\times 3}. \tag{1.37d}
$$

By choosing $\boldsymbol{v} = \boldsymbol{u}^n + \boldsymbol{u}^{n-1}$ in (1.37a) and $\boldsymbol{\tau} = \boldsymbol{\sigma}^n + \boldsymbol{\sigma}^{n-1}$ in (1.37c), we obtain:

$$\int_\Omega \frac{\rho}{\Delta t}(|\boldsymbol{u}^n|^2 - |\boldsymbol{u}^{n-1}|^2) \ \mathrm{d}\boldsymbol{x} + 2(\eta_s + \eta_p) \int_\Omega \left(|\boldsymbol{\epsilon}(\boldsymbol{u}^n)|^2 + \boldsymbol{\epsilon}(\boldsymbol{u}^n) : \boldsymbol{\epsilon}(\boldsymbol{u}^{n-1}) \right) \ \mathrm{d}\boldsymbol{x}$$

$$- \int_\Omega p^n \nabla \cdot (\boldsymbol{u}^n + \boldsymbol{u}^{n-1}) \ \mathrm{d}\boldsymbol{x} + \int_\Omega \boldsymbol{\sigma}^{n-1} : (\boldsymbol{\epsilon}(\boldsymbol{u}^n) + \boldsymbol{\epsilon}(\boldsymbol{u}^{n-1})) \ \mathrm{d}\boldsymbol{x}$$

$$- \int_\Omega 2\eta_p \boldsymbol{\epsilon}(\boldsymbol{u}^{n-1}) : (\boldsymbol{\epsilon}(\boldsymbol{u}^n) + \boldsymbol{\epsilon}(\boldsymbol{u}^{n-1})) \ \mathrm{d}\boldsymbol{x} = 0$$

$$\int_\Omega \frac{\alpha}{2\eta_p}(|\boldsymbol{\sigma}^n|^2 + \boldsymbol{\sigma}^n : \boldsymbol{\sigma}^{n-1}) \ \mathrm{d}\boldsymbol{x} + \int_\Omega \frac{\lambda}{2\eta_p \Delta t}(|\boldsymbol{\sigma}^n|^2 - |\boldsymbol{\sigma}^{n-1}|^2) \ \mathrm{d}\boldsymbol{x} = \int_\Omega \boldsymbol{\epsilon}(\boldsymbol{u}^n) : (\boldsymbol{\sigma}^n + \boldsymbol{\sigma}^{n-1}) \ \mathrm{d}\boldsymbol{x},$$

where the EVSS tensor $\boldsymbol{D}^{n-1}$ is eliminated using (1.33d). The pressure terms are eliminated using (1.37b) for $q = p^n$; and summing both equations yields

$$\int_\Omega \left(\rho|\boldsymbol{u}^n|^2 + \frac{\lambda}{2\eta_p}|\boldsymbol{\sigma}^n|^2 \right) \ \mathrm{d}\boldsymbol{x} + \frac{\alpha \Delta t}{2\eta_p} \int_\Omega \left(|\boldsymbol{\sigma}^n|^2 + \boldsymbol{\sigma}^n : \boldsymbol{\sigma}^{n-1} \right) \ \mathrm{d}\boldsymbol{x}$$

$$+ \Delta t \int_\Omega \left(2(\eta_s + \eta_p)|\boldsymbol{\epsilon}(\boldsymbol{u}^n)|^2 + 2\eta_s \boldsymbol{\epsilon}(\boldsymbol{u}^n) : \boldsymbol{\epsilon}(\boldsymbol{u}^{n-1}) \ \mathrm{d}\boldsymbol{x} + \boldsymbol{\sigma}^{n-1} : \boldsymbol{\epsilon}(\boldsymbol{u}^{n-1}) \right) \ \mathrm{d}\boldsymbol{x}$$

$$= \int_\Omega \left(\rho|\boldsymbol{u}^{n-1}|^2 + \frac{\lambda}{2\eta_p}|\boldsymbol{\sigma}^{n-1}|^2 \right) \ \mathrm{d}\boldsymbol{x} + \Delta t \int_\Omega \left(2\eta_p|\boldsymbol{\epsilon}(\boldsymbol{u}^{n-1})|^2 + \boldsymbol{\sigma}^n : \boldsymbol{\epsilon}(\boldsymbol{u}^n) \right) \ \mathrm{d}\boldsymbol{x}.$$

Using Young's inequality, we obtain

$$\int_\Omega 2(\eta_s + \eta_p)|\boldsymbol{\epsilon}(\boldsymbol{u}^n)|^2 + 2\eta_s \boldsymbol{\epsilon}(\boldsymbol{u}^n) : \boldsymbol{\epsilon}(\boldsymbol{u}^{n-1}) \ \mathrm{d}\boldsymbol{x} \geq \int_\Omega (\eta_s + 2\eta_p)|\boldsymbol{\epsilon}(\boldsymbol{u}^n)|^2 - \eta_s|\boldsymbol{\epsilon}(\boldsymbol{u}^{n-1})|^2 \ \mathrm{d}\boldsymbol{x}$$

and

$$\frac{\alpha}{2\eta_p} \int_\Omega |\boldsymbol{\sigma}^n|^2 + \boldsymbol{\sigma}^n : \boldsymbol{\sigma}^{n-1} \ \mathrm{d}\boldsymbol{x} \geq \frac{\alpha}{4\eta_p} \int_\Omega |\boldsymbol{\sigma}^n|^2 - |\boldsymbol{\sigma}^{n-1}|^2 \ \mathrm{d}\boldsymbol{x}.$$

This yields

$$\int_\Omega \left(\rho|\boldsymbol{u}^n|^2 + \frac{\lambda}{2\eta_p}|\boldsymbol{\sigma}^n|^2 \right) \ \mathrm{d}\boldsymbol{x} + \Delta t \int_\Omega \left(\frac{\alpha}{4\eta_p}|\boldsymbol{\sigma}^n|^2 + (\eta_s + 2\eta_p)|\boldsymbol{\epsilon}(\boldsymbol{u}^n)|^2 - \boldsymbol{\sigma}^n : \boldsymbol{\epsilon}(\boldsymbol{u}^n) \right) \ \mathrm{d}\boldsymbol{x}$$

$$\leq \int_\Omega \left(\rho|\boldsymbol{u}^{n-1}|^2 + \frac{\lambda}{2\eta_p}|\boldsymbol{\sigma}^{n-1}|^2 \right) \ \mathrm{d}\boldsymbol{x}$$

$$+ \Delta t \int_\Omega \left(\frac{\alpha}{4\eta_p}|\boldsymbol{\sigma}^{n-1}|^2 + (\eta_s + 2\eta_p)|\boldsymbol{\epsilon}(\boldsymbol{u}^{n-1})|^2 - \boldsymbol{\sigma}^{n-1} : \boldsymbol{\epsilon}(\boldsymbol{u}^{n-1}) \right) \ \mathrm{d}\boldsymbol{x} \leq \cdots \leq$$

$$\int_\Omega \left(\rho|\boldsymbol{u}^0|^2 + \frac{\lambda}{2\eta_p}|\boldsymbol{\sigma}^0|^2 \right) \ \mathrm{d}\boldsymbol{x} + \Delta t \int_\Omega \left(\frac{\alpha}{4\eta_p}|\boldsymbol{\sigma}^0|^2 + (\eta_s + 2\eta_p)|\boldsymbol{\epsilon}(\boldsymbol{u}^0)|^2 - \boldsymbol{\sigma}^0 : \boldsymbol{\epsilon}(\boldsymbol{u}^0) \right) \ \mathrm{d}\boldsymbol{x}.$$

From

$$\Delta t \int_\Omega \boldsymbol{\sigma}^n : \boldsymbol{\epsilon}(\boldsymbol{u}^n) \ \mathrm{d}\boldsymbol{x} \leq \frac{\Delta t}{4\eta_p} \|\boldsymbol{\sigma}^n\|^2_{L^2(\Omega)^{3\times3}} + \Delta t \eta_p \|\boldsymbol{\epsilon}(\boldsymbol{u}^n)\|^2_{L^2(\Omega)^{3\times3}},$$

we find for $n = N$:

$$\int_\Omega \left(\rho |\boldsymbol{u}^N|^2 + \frac{2\lambda - \Delta t}{4\eta_p} |\boldsymbol{\sigma}^N|^2 \right) \, \mathrm{d}\boldsymbol{x} + \Delta t \int_\Omega \left(\frac{\alpha}{4\eta_p} |\boldsymbol{\sigma}^N|^2 + (\eta_s + \eta_p)|\boldsymbol{\epsilon}(\boldsymbol{u}^N)|^2 \right) \, \mathrm{d}\boldsymbol{x}$$

$$\leq \int_\Omega \left(\rho |\boldsymbol{u}^0|^2 + \frac{\lambda}{2\eta_p} |\boldsymbol{\sigma}^0|^2 \right) \, \mathrm{d}\boldsymbol{x} + \Delta t \int_\Omega \left(\frac{\alpha + 1}{4\eta_p} |\boldsymbol{\sigma}^0|^2 + (\eta_s + 3\eta_p)|\boldsymbol{\epsilon}(\boldsymbol{u}^0)|^2 \right) \, \mathrm{d}\boldsymbol{x}.$$

which, for $\Delta t \leq \lambda$, yields (1.34).

For the second result, the goal is to get rid of the extra-stress tensor $\boldsymbol{\sigma}^n$ by using (1.33c). Taking λ times the difference between two steps of (1.37a) plus α times (1.37a) gives:

$$\int_\Omega \rho\lambda \frac{\boldsymbol{u}^{n+1} - 2\boldsymbol{u}^n + \boldsymbol{u}^{n-1}}{\Delta t^2} \cdot \boldsymbol{v} \, \mathrm{d}\boldsymbol{x} + \int_\Omega 2(\eta_s + \eta_p)\lambda\boldsymbol{\epsilon}\left(\frac{\boldsymbol{u}^{n+1} - \boldsymbol{u}^n}{\Delta t} \right) : \boldsymbol{\epsilon}(\boldsymbol{v}) \, \mathrm{d}\boldsymbol{x}$$

$$- \int_\Omega \left(\lambda\frac{p^{n+1} - p^n}{\Delta t} + \alpha p^{n+1} \right) (\nabla \cdot \boldsymbol{v}) \, \mathrm{d}\boldsymbol{x}$$

$$+ \int_\Omega \lambda \left(\frac{\boldsymbol{\sigma}^n - \boldsymbol{\sigma}^{n-1}}{\Delta t} - 2\eta_p\frac{\boldsymbol{D}^n - \boldsymbol{D}^{n-1}}{\Delta t} \right) : \boldsymbol{\epsilon}(\boldsymbol{v}) \, \mathrm{d}\boldsymbol{x} + \int_\Omega \rho\alpha\frac{\boldsymbol{u}^{n+1} - \boldsymbol{u}^n}{\Delta t} \cdot \boldsymbol{v} \, \mathrm{d}\boldsymbol{x}$$

$$+ \int_\Omega 2(\eta_s + \eta_p)\alpha\boldsymbol{\epsilon}(\boldsymbol{u}^{n+1}) : \boldsymbol{\epsilon}(\boldsymbol{v}) \, \mathrm{d}\boldsymbol{x} + \int_\Omega \alpha(\boldsymbol{\sigma}^n - 2\eta_p\boldsymbol{D}^n) : \boldsymbol{\epsilon}(\boldsymbol{v}) \, \mathrm{d}\boldsymbol{x} = 0.$$

Using $\boldsymbol{\tau} = \boldsymbol{\epsilon}(\boldsymbol{v})$ in (1.37c) and (1.37d) to eliminate respectively $\boldsymbol{\sigma}^n, \boldsymbol{\sigma}^{n-1}$ and $\boldsymbol{D}^n, \boldsymbol{D}^{n-1}$, we find:

$$\int_\Omega \rho\lambda \frac{\boldsymbol{u}^{n+1} - 2\boldsymbol{u}^n + \boldsymbol{u}^{n-1}}{\Delta t^2} \cdot \boldsymbol{v} \, \mathrm{d}\boldsymbol{x} + \int_\Omega 2(\eta_s + \eta_p)\lambda\boldsymbol{\epsilon}\left(\frac{\boldsymbol{u}^{n+1} - \boldsymbol{u}^n}{\Delta t} \right) : \boldsymbol{\epsilon}(\boldsymbol{v}) \, \mathrm{d}\boldsymbol{x}$$

$$- \int_\Omega \left(\lambda\frac{p^{n+1} - p^n}{\Delta t} + \alpha p^{n+1} \right) (\nabla \cdot \boldsymbol{v}) \, \mathrm{d}\boldsymbol{x} \qquad (1.38)$$

$$- \int_\Omega 2\lambda\eta_p\boldsymbol{\epsilon}\left(\frac{\boldsymbol{u}^n - \boldsymbol{u}^{n-1}}{\Delta t} \right) : \boldsymbol{\epsilon}(\boldsymbol{v}) \, \mathrm{d}\boldsymbol{x} + \int_\Omega \rho\alpha\frac{\boldsymbol{u}^{n+1} - \boldsymbol{u}^n}{\Delta t} \cdot \boldsymbol{v} \, \mathrm{d}\boldsymbol{x}$$

$$+ \int_\Omega 2(\eta_s + \eta_p)\alpha\boldsymbol{\epsilon}(\boldsymbol{u}^{n+1}) : \boldsymbol{\epsilon}(\boldsymbol{v}) \, \mathrm{d}\boldsymbol{x} + \int_\Omega 2\eta_p(1 - \alpha)\boldsymbol{\epsilon}(\boldsymbol{u}^n) : \boldsymbol{\epsilon}(\boldsymbol{v}) \, \mathrm{d}\boldsymbol{x} = 0.$$

If $\alpha = 1$, setting $\boldsymbol{v} = \boldsymbol{u}^{n+1} - \boldsymbol{u}^n$ in (1.38) and using $a(a-b) = \frac{1}{2}a^2 - \frac{1}{2}b^2 + \frac{1}{2}(a-b)^2$, we find:

$$\int_\Omega \frac{\rho\lambda}{2}\left|\frac{\boldsymbol{u}^{n+1}-\boldsymbol{u}^n}{\Delta t}\right|^2 + \frac{\rho\lambda}{2}\left|\frac{\boldsymbol{u}^{n+1}-2\boldsymbol{u}^n+\boldsymbol{u}^{n-1}}{\Delta t}\right|^2$$

$$+\,(\eta_s+\eta_p)|\boldsymbol{\epsilon}(\boldsymbol{u}^{n+1})|^2 + (\eta_s+\eta_p)|\boldsymbol{\epsilon}(\boldsymbol{u}^{n+1}-\boldsymbol{u}^n)|^2$$

$$+\,2\eta_p\lambda\Delta t\left|\boldsymbol{\epsilon}\left(\frac{\boldsymbol{u}^{n+1}-\boldsymbol{u}^n}{\Delta t}\right)\right|^2 + 2\eta_p\lambda\Delta t\left|\boldsymbol{\epsilon}\left(\frac{\boldsymbol{u}^{n+1}-2\boldsymbol{u}^n+\boldsymbol{u}^{n-1}}{\Delta t}\right)\right|^2\,\mathrm{d}\boldsymbol{x}$$

$$+\,\Delta t\int_\Omega \rho\left|\frac{\boldsymbol{u}^{n+1}-\boldsymbol{u}^n}{\Delta t}\right|^2 + 2\eta_s\lambda\left|\boldsymbol{\epsilon}\left(\frac{\boldsymbol{u}^{n+1}-\boldsymbol{u}^n}{\Delta t}\right)\right|^2\,\mathrm{d}\boldsymbol{x}$$

$$=\int_\Omega \left(\frac{\rho\lambda}{2}\left|\frac{\boldsymbol{u}^n-\boldsymbol{u}^{n-1}}{\Delta t}\right|^2 + (\eta_s+\eta_p)|\boldsymbol{\epsilon}(\boldsymbol{u}^n)|^2\right.$$

$$\left.+2\eta_p\lambda\Delta t\left|\boldsymbol{\epsilon}\left(\frac{\boldsymbol{u}^n-\boldsymbol{u}^{n-1}}{\Delta t}\right)\right|^2\right)\,\mathrm{d}\boldsymbol{x}.$$

The pressure terms cancel out by use of the equation (1.37b) for $q=\{p^{n+1},p^n\}$. Summing from $n=1$ to $n=N-1$, we obtain (1.35).

If $\alpha=0$, setting $\boldsymbol{v}=\boldsymbol{u}^{n+1}-\boldsymbol{u}^{n-1}$ in (1.38), we obtain:

$$\int_\Omega \frac{\rho\lambda}{2}\left|\frac{\boldsymbol{u}^{n+1}-\boldsymbol{u}^n}{\Delta t}\right|^2 + 2\eta_p\lambda\Delta t\left|\boldsymbol{\epsilon}\left(\frac{\boldsymbol{u}^{n+1}-\boldsymbol{u}^n}{\Delta t}\right)\right|^2 + 2\eta_p\boldsymbol{\epsilon}(\boldsymbol{u}^n):\boldsymbol{\epsilon}(\boldsymbol{u}^{n+1}-\boldsymbol{u}^{n-1})$$

$$+\,2\eta_s\lambda\Delta t\boldsymbol{\epsilon}\left(\frac{\boldsymbol{u}^{n+1}-\boldsymbol{u}^n}{\Delta t}\right):\boldsymbol{\epsilon}\left(\frac{\boldsymbol{u}^{n+1}-\boldsymbol{u}^{n-1}}{\Delta t}\right)\,\mathrm{d}\boldsymbol{x}$$

$$=\int_\Omega \frac{\rho\lambda}{2}\left|\frac{\boldsymbol{u}^n-\boldsymbol{u}^{n-1}}{\Delta t}\right|^2 + 2\eta_p\lambda\Delta t\left|\boldsymbol{\epsilon}\left(\frac{\boldsymbol{u}^n-\boldsymbol{u}^{n-1}}{\Delta t}\right)\right|^2\,\mathrm{d}\boldsymbol{x}.$$

Since $a^2-b^2\leq 2a(a+b)$ we have

$$\left|\boldsymbol{\epsilon}\left(\frac{\boldsymbol{u}^{n+1}-\boldsymbol{u}^n}{\Delta t}\right)\right|^2 - \left|\boldsymbol{\epsilon}\left(\frac{\boldsymbol{u}^n-\boldsymbol{u}^{n-1}}{\Delta t}\right)\right|^2 \leq 2\boldsymbol{\epsilon}\left(\frac{\boldsymbol{u}^{n+1}-\boldsymbol{u}^n}{\Delta t}\right):\boldsymbol{\epsilon}\left(\frac{\boldsymbol{u}^{n+1}-\boldsymbol{u}^{n-1}}{\Delta t}\right)$$

and

$$2\boldsymbol{\epsilon}(\boldsymbol{u}^n):\boldsymbol{\epsilon}(\boldsymbol{u}^{n+1}-\boldsymbol{u}^{n-1}) = 2\boldsymbol{\epsilon}(\boldsymbol{u}^n):\boldsymbol{\epsilon}(\boldsymbol{u}^{n+1}-\boldsymbol{u}^n) + \boldsymbol{\epsilon}(\boldsymbol{u}^n):\boldsymbol{\epsilon}(\boldsymbol{u}^n-\boldsymbol{u}^{n-1})$$

$$=\left|\boldsymbol{\epsilon}(\boldsymbol{u}^{n+1})\right|^2 - |\boldsymbol{\epsilon}(\boldsymbol{u}^n)|^2 - \left|\boldsymbol{\epsilon}(\boldsymbol{u}^{n+1}-\boldsymbol{u}^n)\right|^2$$

$$+\,|\boldsymbol{\epsilon}(\boldsymbol{u}^n)|^2 - \left|\boldsymbol{\epsilon}(\boldsymbol{u}^{n-1})\right|^2 + \left|\boldsymbol{\epsilon}(\boldsymbol{u}^n-\boldsymbol{u}^{n-1})\right|^2.$$

It yields

$$\int_\Omega \frac{\rho\lambda}{2}\left|\frac{\boldsymbol{u}^{n+1}-\boldsymbol{u}^n}{\Delta t}\right|^2 + (2\eta_p+\eta_s)\lambda\Delta t\left|\boldsymbol{\epsilon}\left(\frac{\boldsymbol{u}^{n+1}-\boldsymbol{u}^n}{\Delta t}\right)\right|^2$$

$$+ \eta_p|\boldsymbol{\epsilon}(\boldsymbol{u}^{n+1})|^2 + \eta_p|\boldsymbol{\epsilon}(\boldsymbol{u}^n)|^2 - \Delta t^2\eta_p\left|\boldsymbol{\epsilon}\left(\frac{\boldsymbol{u}^{n+1}-\boldsymbol{u}^n}{\Delta t}\right)\right|^2\,\mathrm{d}\boldsymbol{x}$$

$$\leq \int_\Omega \frac{\rho\lambda}{2}\left|\frac{\boldsymbol{u}^n-\boldsymbol{u}^{n-1}}{\Delta t}\right|^2 + (2\eta_p+\eta_s)\lambda\Delta t\left|\boldsymbol{\epsilon}\left(\frac{\boldsymbol{u}^n-\boldsymbol{u}^{n-1}}{\Delta t}\right)\right|^2$$

$$+ \eta_p|\boldsymbol{\epsilon}(\boldsymbol{u}^n)|^2 + \eta_p|\boldsymbol{\epsilon}(\boldsymbol{u}^{n-1})|^2 - \Delta t^2\eta_p\left|\boldsymbol{\epsilon}\left(\frac{\boldsymbol{u}^n-\boldsymbol{u}^{n-1}}{\Delta t}\right)\right|^2\,\mathrm{d}\boldsymbol{x}.$$

Summing from $n=1$ to $n=N-1$ and assuming $\Delta t \leq \lambda(2\eta_s+\eta_s)/\eta_p$ yields (1.36). ∎

Let us now consider the implicit scheme (1.25) for the linearized system (1.29):
Find $\boldsymbol{u}^n$, p^n and $\boldsymbol{\sigma}^n$ in Ω such that

$$\rho\frac{\boldsymbol{u}^n-\boldsymbol{u}^{n-1}}{\Delta t} - 2\eta_s\nabla\cdot\boldsymbol{\epsilon}(\boldsymbol{u}^n) + \nabla p^n - \nabla\cdot\boldsymbol{\sigma}^n = \boldsymbol{0}, \tag{1.39a}$$

$$\nabla\cdot\boldsymbol{u}^n = 0, \tag{1.39b}$$

$$\alpha\boldsymbol{\sigma}^n + \lambda\left(\frac{\boldsymbol{\sigma}^n-\boldsymbol{\sigma}^{n-1}}{\Delta t}\right) = 2\eta_p\boldsymbol{\epsilon}(\boldsymbol{u}^n). \tag{1.39c}$$

Similarly as for the EVSS scheme (1.33), given $\boldsymbol{u}^0 \in H_0^1(\Omega)^3$ and $\boldsymbol{\sigma}^0 \in L^2(\Omega)^{3\times3}$, for $n=1,\ldots,N$, let $\boldsymbol{u}^n, p^n$ and $\boldsymbol{\sigma}^n$ to be the unique weak solution of (1.39) and further assume that $\boldsymbol{u}^n \in H_0^1(\Omega)^3$, $p^n \in L_0^2(\Omega)$ and $\boldsymbol{\sigma}^n \in L^2(\Omega)^{3\times3}$. In this case, the following Proposition proves the unconditional stability of the scheme. Unlike the Proposition (1.5.1) for the EVSS scheme, it corresponds to the exact discrete counterpart of (1.30) and (1.32):

Proposition 1.5.2. Consider the implicit scheme (1.39). For all $\Delta t > 0, \eta_s \geq 0, \eta_p > 0, \alpha = \{0,1\}$, we have:

$$\int_\Omega \left(\rho|\boldsymbol{u}^N|^2 + \frac{\lambda}{2\eta_p}|\boldsymbol{\sigma}^N|^2\right)\,\mathrm{d}\boldsymbol{x} + \sum_{n=1}^N \Delta t\int_\Omega\left(4\eta_s|\boldsymbol{\epsilon}(\boldsymbol{u}^n)|^2 + \frac{\alpha}{\eta_p}|\boldsymbol{\sigma}^n|^2\right)\,\mathrm{d}\boldsymbol{x} \tag{1.40}$$

$$\leq \int_\Omega \left(\rho|\boldsymbol{u}^0|^2 + \frac{\lambda}{2\eta_p}|\boldsymbol{\sigma}^0|^2\right)\,\mathrm{d}\boldsymbol{x}.$$

and

$$\int_\Omega \left(\rho\lambda \left| \frac{\boldsymbol{u}^N - \boldsymbol{u}^{N-1}}{\Delta t} \right|^2 + 2(\eta_s\alpha + \eta_p)|\boldsymbol{\epsilon}(\boldsymbol{u}^N)|^2 \right) \, \mathrm{d}\boldsymbol{x} \tag{1.41}$$

$$\leq \int_\Omega \left(\rho\lambda \left| \frac{\boldsymbol{u}^1 - \boldsymbol{u}^0}{\Delta t} \right|^2 + 2(\eta_s\alpha + \eta_p)|\boldsymbol{\epsilon}(\boldsymbol{u}^1)|^2 \right) \, \mathrm{d}\boldsymbol{x}.$$

Proof. The weak formulation of the system of equations (1.39) yields for $n = 1, \ldots, N$:

$$\int_\Omega \rho \frac{\boldsymbol{u}^n - \boldsymbol{u}^{n-1}}{\Delta t} \cdot \boldsymbol{v} \, \mathrm{d}\boldsymbol{x} + \int_\Omega 2\eta_s\boldsymbol{\epsilon}(\boldsymbol{u}^n) : \boldsymbol{\epsilon}(\boldsymbol{v}) \, \mathrm{d}\boldsymbol{x} \tag{1.42a}$$

$$- \int_\Omega p^n(\nabla \cdot \boldsymbol{v}) \, \mathrm{d}\boldsymbol{x} + \int_\Omega \boldsymbol{\sigma}^n : \boldsymbol{\epsilon}(\boldsymbol{v}) \, \mathrm{d}\boldsymbol{x} = 0, \quad \forall \boldsymbol{v} \in H_0^1(\Omega)^3,$$

$$\int_\Omega (\nabla \cdot \boldsymbol{u}^n)q \, \mathrm{d}\boldsymbol{x} = 0, \quad \forall q \in L_0^2(\Omega), \tag{1.42b}$$

$$\int_\Omega \alpha\boldsymbol{\sigma}^n : \boldsymbol{\tau} \, \mathrm{d}\boldsymbol{x} + \int_\Omega \lambda\frac{\boldsymbol{\sigma}^n - \boldsymbol{\sigma}^{n-1}}{\Delta t} : \boldsymbol{\tau} \, \mathrm{d}\boldsymbol{x} \tag{1.42c}$$

$$- \int_\Omega 2\eta_p\boldsymbol{\epsilon}(\boldsymbol{u}^n) : \boldsymbol{\tau} \, \mathrm{d}\boldsymbol{x} = 0, \quad \forall \boldsymbol{\tau} \in L^2(\Omega)^{3\times3}.$$

By substituting the test functions in the system of equations (1.42) respectively by $\boldsymbol{v} = \boldsymbol{u}^n$, $q = p^n$ and $\boldsymbol{\tau} = \boldsymbol{\sigma}^n$, we obtain using the formula $2(a-b)a = a^2 - b^2 + (a-b)^2$:

$$\int_\Omega \frac{\rho}{2\Delta t} \cdot (|\boldsymbol{u}^n|^2 - |\boldsymbol{u}^{n-1}|^2 + |\boldsymbol{u}^n - \boldsymbol{u}^{n-1}|^2) \, \mathrm{d}\boldsymbol{x} + 2\eta_s \int_\Omega |\boldsymbol{\epsilon}(\boldsymbol{u}^n)|^2 \, \mathrm{d}\boldsymbol{x} - \int_\Omega p^n(\nabla \cdot \boldsymbol{u}^n) \, \mathrm{d}\boldsymbol{x}$$

$$+ \int_\Omega \boldsymbol{\sigma}^n : \boldsymbol{\epsilon}(\boldsymbol{u}^n) \, \mathrm{d}\boldsymbol{x} = 0, \tag{1.43a}$$

$$\int_\Omega (\nabla \cdot \boldsymbol{u}^n)p^n \, \mathrm{d}\boldsymbol{x} = 0, \tag{1.43b}$$

$$\int_\Omega \alpha|\boldsymbol{\sigma}^n|^2 \, \mathrm{d}\boldsymbol{x} + \int_\Omega \frac{\lambda}{2\Delta t} \cdot (|\boldsymbol{\sigma}^n|^2 - |\boldsymbol{\sigma}^{n-1}|^2 + |\boldsymbol{\sigma}^n - \boldsymbol{\sigma}^{n-1}|^2) \, \mathrm{d}\boldsymbol{x}$$

$$- \int_\Omega 2\eta_p\boldsymbol{\epsilon}(\boldsymbol{u}^n) : \boldsymbol{\sigma}^n \, \mathrm{d}\boldsymbol{x} = 0. \tag{1.43c}$$

Substituting (1.43b), (1.43c) into (1.43a), it yields:

$$\int_\Omega \rho\frac{|\boldsymbol{u}^n|^2 - |\boldsymbol{u}^{n-1}|^2}{\Delta t} + \frac{\lambda}{2\eta_p}\frac{|\boldsymbol{\sigma}^n|^2 - |\boldsymbol{\sigma}^{n-1}|^2}{\Delta t} \, \mathrm{d}\boldsymbol{x} + \int_\Omega 4\eta_s|\boldsymbol{\epsilon}(\boldsymbol{u}^n)|^2 + \frac{\alpha}{\eta_p}|\boldsymbol{\sigma}^n|^2 \, \mathrm{d}\boldsymbol{x}$$

$$+ \Delta t \int_\Omega \left(\rho \left| \frac{\boldsymbol{u}^n - \boldsymbol{u}^{n-1}}{\Delta t} \right|^2 + \frac{\lambda}{2\eta_p} \left| \frac{\boldsymbol{\sigma}^n - \boldsymbol{\sigma}^{n-1}}{\Delta t} \right|^2 \right) \, \mathrm{d}\boldsymbol{x} = 0.$$

The first result is obtained by summing for $n = 1$ to N.

For the second result, we proceed as in the previous Proposition. Let us take the scalar product of (1.39a) with a test function $\boldsymbol{v} \in H_0^1(\Omega)^3$, integrate over Ω and take the difference between two consecutive time steps. We obtain

$$\int_\Omega \rho \frac{\boldsymbol{u}^{n+1} - 2\boldsymbol{u}^n + \boldsymbol{u}^{n-1}}{\Delta t} \cdot \boldsymbol{v} \, \mathrm{d}\boldsymbol{x} + \int_\Omega 2\eta_s \boldsymbol{\epsilon} \left(\boldsymbol{u}^{n+1} - \boldsymbol{u}^n \right) : \boldsymbol{\epsilon}(\boldsymbol{v}) \, \mathrm{d}\boldsymbol{x}$$
$$- \int_\Omega \left(p^{n+1} - p^n \right) (\nabla \cdot \boldsymbol{v}) \, \mathrm{d}\boldsymbol{x} + \int_\Omega (\boldsymbol{\sigma}^{n+1} - \boldsymbol{\sigma}^n) : \boldsymbol{\epsilon}(\boldsymbol{v}) \, \mathrm{d}\boldsymbol{x} = 0. \qquad (1.44)$$

Then we take $\lambda/\Delta t$ times the above equation, add it to α times the weak formulation of (1.39a):

$$\int_\Omega \rho\lambda \frac{\boldsymbol{u}^{n+1} - 2\boldsymbol{u}^n + \boldsymbol{u}^{n-1}}{\Delta t^2} \cdot \boldsymbol{v} \, \mathrm{d}\boldsymbol{x} + \int_\Omega 2\eta_s \lambda \boldsymbol{\epsilon} \left(\frac{\boldsymbol{u}^{n+1} - \boldsymbol{u}^n}{\Delta t} \right) \cdot \boldsymbol{\epsilon}(\boldsymbol{v}) \, \mathrm{d}\boldsymbol{x}$$
$$- \int_\Omega \left(\lambda \frac{p^{n+1} - p^n}{\Delta t} + \alpha \nabla p^{n+1} \right) (\nabla \cdot \boldsymbol{v}) \, \mathrm{d}\boldsymbol{x} + \int_\Omega \rho\alpha \frac{\boldsymbol{u}^{n+1} - \boldsymbol{u}^n}{\Delta t} \cdot \boldsymbol{v} \, \mathrm{d}\boldsymbol{x} \qquad (1.45)$$
$$+ \int_\Omega 2\eta_s \alpha \boldsymbol{\epsilon}(\boldsymbol{u}^{n+1}) : \boldsymbol{\epsilon}(\boldsymbol{v}) \, \mathrm{d}\boldsymbol{x} + \int_\Omega \left(\alpha \boldsymbol{\sigma}^{n+1} + \lambda \frac{\boldsymbol{\sigma}^{n+1} - \boldsymbol{\sigma}^n}{\Delta t} \right) : \boldsymbol{\epsilon}(\boldsymbol{v}) \, \mathrm{d}\boldsymbol{x} = 0.$$

The pressure terms are cancelled out by equation (1.42b). Using $\boldsymbol{v} = \boldsymbol{u}^{n+1} - \boldsymbol{u}^n$ in (1.45) and $\boldsymbol{\tau} = \boldsymbol{\epsilon}(\boldsymbol{u}^{n+1} - \boldsymbol{u}^n)$ in (1.42c), we can also eliminate the extra-stress terms, and applying the formulas $(a - b)a = \frac{1}{2}a^2 - \frac{1}{2}b^2 + \frac{1}{2}(a - b)^2$, it yields:

$$\int_\Omega \frac{\rho\lambda}{2} \left| \frac{\boldsymbol{u}^{n+1} - \boldsymbol{u}^n}{\Delta t} \right|^2 + \frac{\rho\lambda}{2} \left| \frac{\boldsymbol{u}^{n+1} - 2\boldsymbol{u}^n + \boldsymbol{u}^{n-1}}{\Delta t} \right|^2 + (\eta_s \alpha + \eta_p)|\boldsymbol{\epsilon}(\boldsymbol{u}^{n+1})|^2$$
$$+ (\eta_s \alpha + \eta_p)|\boldsymbol{\epsilon}(\boldsymbol{u}^{n+1}) - \boldsymbol{\epsilon}(\boldsymbol{u}^n)|^2 \, \mathrm{d}\boldsymbol{x}$$
$$+ \Delta t \int_\Omega \rho\alpha \left| \frac{\boldsymbol{u}^{n+1} - \boldsymbol{u}^n}{\Delta t} \right|^2 + 2\eta_s \lambda \left| \boldsymbol{\epsilon} \frac{\boldsymbol{u}^{n+1} - \boldsymbol{u}^n}{\Delta t} \right|^2 \, \mathrm{d}\boldsymbol{x}$$
$$\leq \int_\Omega \frac{\rho\lambda}{2} \left| \frac{\boldsymbol{u}^n - \boldsymbol{u}^{n-1}}{\Delta t} \right|^2 + (\eta_s \alpha + \eta_p)|\boldsymbol{\epsilon}(\boldsymbol{u}^n)|^2 \, \mathrm{d}\boldsymbol{x}.$$

Summing from $n = 1$ to $n = N - 1$ we obtain the result. ∎

Remark 1.5.1. The results obtained from Propositions 1.5.1 and 1.5.2 do not give stability estimates only related to data, but estimates also involving the first iterate of the solution at time t^1. To obtain those estimates, using more formal computation, we start from the strong momentum equation (1.39a) that we multiply by $\dfrac{\boldsymbol{u}^n - \boldsymbol{u}^{n-1}}{\Delta t}$, integrate on Ω and use (1.39c):

$$\int_\Omega \rho \left| \frac{\boldsymbol{u}^n - \boldsymbol{u}^{n-1}}{\Delta t} \right|^2 \mathrm{d}\boldsymbol{x} - 2 \left(\eta_s + \frac{\eta_p \Delta t}{\lambda + \alpha \Delta t} \right) \int_\Omega (\nabla \cdot \boldsymbol{\epsilon}\,(\boldsymbol{u}^n)) \cdot \left(\frac{\boldsymbol{u}^n - \boldsymbol{u}^{n-1}}{\Delta t} \right) \mathrm{d}\boldsymbol{x}$$

$$+ \int_\Omega \nabla p^n \cdot \left(\frac{\boldsymbol{u}^n - \boldsymbol{u}^{n-1}}{\Delta t} \right) \mathrm{d}\boldsymbol{x}$$

$$= \left(\frac{\lambda}{\lambda + \alpha \Delta t} \right) \int_\Omega (\nabla \cdot \boldsymbol{\sigma}^{n-1}) \cdot \left(\frac{\boldsymbol{u}^n - \boldsymbol{u}^{n-1}}{\Delta t} \right) \mathrm{d}\boldsymbol{x}$$

Using the no-slip boundary conditions and the incompressibility condition, we obtain for $n = 1$

$$\int_\Omega \rho \left| \frac{\boldsymbol{u}^1 - \boldsymbol{u}^0}{\Delta t} \right|^2 \mathrm{d}\boldsymbol{x} + \left(\frac{2\eta_s}{\Delta t} + \frac{2\eta_p}{\lambda + \alpha \Delta t} \right) \int_\Omega \boldsymbol{\epsilon}\left(\boldsymbol{u}^1\right) : \boldsymbol{\epsilon}\left(\boldsymbol{u}^1 - \boldsymbol{u}^0\right) \mathrm{d}\boldsymbol{x}$$

$$= \left(\frac{\lambda}{\lambda + \alpha \Delta t} \right) \int_\Omega (\nabla \cdot \boldsymbol{\sigma}^0) \cdot \left(\frac{\boldsymbol{u}^1 - \boldsymbol{u}^0}{\Delta t} \right) \mathrm{d}\boldsymbol{x}.$$

Using the formula $2(a - b)a = a^2 - b^2 + (a - b)^2$ and the Cauchy-Schwarz and Young inequalites, we obtain for $n = 1$

$$\int_\Omega \frac{\rho}{2} \left| \frac{\boldsymbol{u}^1 - \boldsymbol{u}^0}{\Delta t} \right|^2 \mathrm{d}\boldsymbol{x} + \int_\Omega \left(\frac{\eta_s}{\Delta t} + \frac{\eta_p}{\lambda + \alpha \Delta t} \right) |\boldsymbol{\epsilon}(\boldsymbol{u}^1)|^2 \, \mathrm{d}\boldsymbol{x}$$

$$\leq \int_\Omega \left(\frac{\eta_s}{\Delta t} + \frac{\eta_p}{\lambda + \alpha \Delta t} \right) |\boldsymbol{\epsilon}(\boldsymbol{u}^0)|^2 \, \mathrm{d}\boldsymbol{x} \qquad (1.46)$$

$$+ \int_\Omega \left(\frac{\lambda}{\lambda + \alpha \Delta t} \right)^2 \frac{1}{2\rho} |\nabla \cdot \boldsymbol{\sigma}^0|^2 \, \mathrm{d}\boldsymbol{x}.$$

This stability estimate blow off when Δt goes to 0, except in the case of $\eta_s = 0$. Thus we can formulate the final estimate, which depends on the parameter η_s: when $\eta_s > 0$, the estimate (1.40) gives control on the L^2 norm of the velocity, the extra-stress tensor and the gradient of the velocity.

In the case of $\eta_s = 0$, then we obtain using the estimates (1.41) and (1.46):

$$\int_\Omega \left(\rho\lambda \left| \frac{\boldsymbol{u}^N - \boldsymbol{u}^{N-1}}{\Delta t} \right|^2 + 2\eta_p |\boldsymbol{\epsilon}(\boldsymbol{u}^N)|^2 \right) \mathrm{d}\boldsymbol{x} \overset{(1.41)}{\leq} \int_\Omega \left(\rho\lambda \left| \frac{\boldsymbol{u}^1 - \boldsymbol{u}^0}{\Delta t} \right|^2 + 2\eta_p |\boldsymbol{\epsilon}(\boldsymbol{u}^1)|^2 \right) \mathrm{d}\boldsymbol{x}$$

$$\leq \int_\Omega \left(\rho(\lambda + \alpha \Delta t) \left| \frac{\boldsymbol{u}^1 - \boldsymbol{u}^0}{\Delta t} \right|^2 + 2\eta_p |\boldsymbol{\epsilon}(\boldsymbol{u}^1)|^2 \right) \mathrm{d}\boldsymbol{x}$$

$$\overset{(1.46)}{\leq} \int_\Omega \left(2\eta_p |\boldsymbol{\epsilon}(\boldsymbol{u}^0)|^2 + \frac{\lambda^2}{\rho(\lambda + \alpha \Delta t)} |\nabla \cdot \boldsymbol{\sigma}^0|^2 \right) \mathrm{d}\boldsymbol{x}.$$

We can obtain a similar result for the EVSS scheme, which is a conditionally stable scheme in time. Take the scalar product of (1.33a) with $(\boldsymbol{u}^n - \boldsymbol{u}^{n-1})/\Delta t$, integrate over Ω and use homogeneous Dirichlet boundary conditions. From Proposition 1.5.1 and using analogous computations as for the implicit scheme, we have for $\Delta t \leq \lambda$ and $\alpha \in \{0,1\}$:

$$\int_\Omega \left(\rho\lambda \left| \frac{\boldsymbol{u}^N - \boldsymbol{u}^{N-1}}{\Delta t} \right|^2 + 2(\alpha\eta_s + \eta_p)|\boldsymbol{\epsilon}(\boldsymbol{u}^N)|^2 \right) \mathrm{d}\boldsymbol{x}$$
$$\leq \int_\Omega \left(2\lambda\frac{\eta_s + \eta_p}{\Delta t} + 1 \right) \left| \boldsymbol{\epsilon}(\boldsymbol{u}^0) \right|^2 \mathrm{d}\boldsymbol{x} + \int_\Omega \frac{\lambda}{\rho} \left| \nabla \cdot (\boldsymbol{\sigma}^0 - \boldsymbol{\epsilon}(\boldsymbol{u}^0)) \right|^2 \mathrm{d}\boldsymbol{x}.$$

$\square$

The two following Propositions prove some convergence results for the implicit time discretisation solution of (1.39). First, the convergence for the time approximation of $\boldsymbol{u}$ and $\boldsymbol{\sigma}$ is proved.

Proposition 1.5.3. Assume that the weak solution of the problem (1.29)
$\boldsymbol{u} \in L^2((0,T); H_0^1(\Omega)^3) \cap H^2((0,T); L^2(\Omega)^3)$, $p \in L^2((0,T); L_0^2(\Omega))$
and $\boldsymbol{\sigma} \in H^2((0,T); L^2(\Omega)^{3\times3})$. Let $n > 0$, $\Delta t > 0$, $t^n = n\Delta t$ and $\boldsymbol{u}^n, p^n, \boldsymbol{\sigma}^n$ be the unique weak solution of the implicit time scheme (1.39). Then, $\exists C > 0$ independent of the time step Δt such that:

$$\rho \left\| \boldsymbol{u}(t^N) - \boldsymbol{u}^N \right\|_{L^2(\Omega)^3}^2 + \frac{\lambda}{2\eta_p} \left\| \boldsymbol{\sigma}(t^N) - \boldsymbol{\sigma}^N \right\|_{L^2(\Omega)^{3\times3}}^2 \qquad (1.47)$$
$$+ \Delta t \sum_{n=1}^N \left(4\eta_s \left\| \boldsymbol{\epsilon}(\boldsymbol{u}(t^n) - \boldsymbol{u}^n) \right\|_{L^2(\Omega)^{3\times3}}^2 + \frac{\alpha}{2\eta_p} \left\| \boldsymbol{\sigma}(t^N) - \boldsymbol{\sigma}^N \right\|_{L^2(\Omega)^{3\times3}}^2 \right) \leq C\Delta t^2.$$

Proof in Appendix C.1

In the case of $\eta_s = 0$, a convergence result for $\frac{\partial \boldsymbol{u}}{\partial t}$ and $\boldsymbol{\epsilon}(\boldsymbol{u})$ is proven for the implicit scheme (1.39).

Proposition 1.5.4. Assume that the weak solution of the problem (1.29)
$\boldsymbol{u} \in L^2((0,T); H_0^1(\Omega)^3) \cap H^3((0,T); L^2(\Omega)^3)$, $p \in L^2((0,T); L_0^2(\Omega))$
and $\boldsymbol{\sigma} \in H^2((0,T); H(\mathrm{div})(\Omega)^{3\times3})$. Let $n > 0$, $t^n = n\Delta t$ and $\boldsymbol{u}^n, p^n, \boldsymbol{\sigma}^n$ be the unique weak solution of the implicit time scheme (1.39). Then, $\exists C > 0$ independent of the time step Δt such that:

$$\rho\lambda \left\| \frac{(\boldsymbol{u}(t^N) - \boldsymbol{u}(t^{N-1}))}{\Delta t} - \frac{\boldsymbol{u}^N - \boldsymbol{u}^{N-1}}{\Delta t} \right\|_{L^2(\Omega)^3}^2 + 2(\eta_s\alpha + \eta_p) \left\| \boldsymbol{\epsilon}(\boldsymbol{u}(t^N) - \boldsymbol{u}^N) \right\|_{L^2(\Omega)^{3\times3}}^2$$

$$+ \Delta t \sum_{n=1}^{N} \left(\rho\alpha \left\| \frac{(\boldsymbol{u}(t^n) - \boldsymbol{u}(t^{n-1}))}{\Delta t} - \frac{\boldsymbol{u}^n - \boldsymbol{u}^{n-1}}{\Delta t} \right\|_{L^2(\Omega)^3}^2 \right. \tag{1.48}$$

$$\left. + 4\eta_s \left\| \boldsymbol{\epsilon} \left(\frac{(\boldsymbol{u}(t^n) - \boldsymbol{u}(t^{n-1}))}{\Delta t} - \frac{\boldsymbol{u}^n - \boldsymbol{u}^{n-1}}{\Delta t} \right) \right\|_{L^2(\Omega)^{3\times3}}^2 \right)$$

$$\leq \rho\lambda \left\| \frac{\boldsymbol{u}(t^1) - \boldsymbol{u}^1}{\Delta t} \right\|_{L^2}^2 + 2(\eta_s\alpha + \eta_p) \left\| \boldsymbol{\epsilon}(\boldsymbol{u}(t^1) - \boldsymbol{u}^1) \right\|_{L^2}^2 + C\Delta t^2 + h.o.t.,$$

where *h.o.t.* denote higher order terms. *Proof in Appendix C.2*

The results proved in both Propositions (1.5.3) and (1.5.4) are the convergence counterpart of the results (1.40) and (1.41) of Proposition (1.5.2). The equation (1.48) however relies on the error on the first step, which can be eliminated using an analogous computation as in Remark 1.5.1.

Remark 1.5.2. Numerical experiments show that the EVSS scheme is less accurate when $\alpha = 0$, $\eta_s = 0$ and the η_p/λ is very large (recall that η_p/λ is the Lamé coefficient for an incompressible material). To understand this, consider the simplified model (1.29) and the set of parameters for the incompressible Neo-Hookean elastic solid ($\eta_s = 0, \lambda > 0$ and $\alpha = 0$). It yields by applying this set of parameter to (1.31):

$$\rho\frac{\partial^2 \boldsymbol{u}}{\partial t^2} + \nabla\frac{\partial p}{\partial t} - \frac{2\eta_p}{\lambda}\nabla\cdot\boldsymbol{\epsilon}(\boldsymbol{u}) = \boldsymbol{0}. \tag{1.49}$$

This equation corresponds to a wave equation for the wave displacement $\boldsymbol{u}$. Consider the EVSS scheme (1.33) in the case $\eta_s = \alpha = 0$:

$$\rho\frac{\boldsymbol{u}^{n+1} - 2\boldsymbol{u}^n + \boldsymbol{u}^{n-1}}{\Delta t^2} - 2\eta_p\Delta t\nabla\cdot\left(\boldsymbol{\epsilon}\left(\frac{\boldsymbol{u}^{n+1} - 2\boldsymbol{u}^n + \boldsymbol{u}^{n-1}}{\Delta t^2} \right) \right)$$

$$+ \nabla\left(\frac{p^{n+1} - p^n}{\Delta t} \right) - \frac{2\eta_p}{\lambda}\nabla\cdot\boldsymbol{\epsilon}(\boldsymbol{u}^n) = \boldsymbol{0}.$$

and compare to the implicit scheme (1.45) in the case $\eta_s = \alpha = 0$ it yields:

$$\rho\frac{\boldsymbol{u}^{n+1} - 2\boldsymbol{u}^n + \boldsymbol{u}^{n-1}}{\Delta t^2} + \nabla\left(\frac{p^{n+1} - p^n}{\Delta t} \right) - \frac{2\eta_p}{\lambda}\nabla\cdot\boldsymbol{\epsilon}(\boldsymbol{u}^{n+1}) = \boldsymbol{0}. \tag{1.50}$$

Therefore, the EVSS scheme carries an extra term corresponding to the time discretisation of $-2\eta_p\Delta t\nabla\cdot\boldsymbol{\epsilon}\left(\frac{\partial^2 \boldsymbol{u}}{\partial t^2}\right)$, thus we can anticipate that the implicit scheme should be more accurate than the EVSS scheme when η_p is large. This will be confirmed by numerical

experiments. $\square$

1.6 Analysis of the free-surface flow model for the time discretisation

In this section, we compute the discrete counterpart of the a priori estimate (1.11). Let $N \in \mathbb{R}^*$, $\Delta t = T/N$ and $t^n = n\Delta t$. Let $n > 0$ and consider the implicit time discretisation scheme (1.25) of the diffusive system of equation (1.14) the correction step. Let φ^n at time t^n and $\Omega^n = \{\boldsymbol{x} \in \Lambda; \varphi^n(\boldsymbol{x}) = 1\}$. The initial and boundary conditions are similar as described at the end of sections 1.1 and 1.3. The velocity $\boldsymbol{u}^{n-\frac{1}{2}}$ and extra-stress $\boldsymbol{\sigma}^{n-\frac{1}{2}}$ were previously computed together with φ^n in the prediction step (1.12). For $t^{n-1} \le t \le t^n$, the free surface is defined as $\partial\Omega^n \backslash \partial\Lambda$. It is assumed that no force apply at the free surface: $(-p^n \boldsymbol{I} + 2\eta_s \boldsymbol{\epsilon}(\boldsymbol{u}) + \boldsymbol{\sigma}^n)\boldsymbol{n} = 0$, where $\boldsymbol{n}$ is the unit outer normal of $\partial\Omega^n \backslash \partial\Lambda$. On $\partial\Lambda$, no slip boundary conditions ($\boldsymbol{u} = 0$) are prescribed. Similarly as in section 1.2, since $\boldsymbol{u}^n$ is not defined on the whole domain Λ, we define in a formal way the product of (1.1b) with $\varphi\boldsymbol{u}$, then integrate on Λ, as:

$$\int_\Lambda \rho\varphi^n \frac{\boldsymbol{u}^n - \boldsymbol{u}^{n-\frac{1}{2}}}{\Delta t} \cdot \boldsymbol{u}^n \ \mathrm{d}\boldsymbol{x} = \int_{\Omega(t)} \rho \frac{\boldsymbol{u}^n - \boldsymbol{u}^{n-\frac{1}{2}}}{\Delta t} \cdot \boldsymbol{u}^n \ \mathrm{d}\boldsymbol{x}.$$

Hence, taking the scalar product of (1.25a) with $\varphi^n \boldsymbol{u}^n$, (1.25b) with $\varphi^n p^n$, (1.25c) with $\varphi^n \boldsymbol{\sigma}^n$ and integrating over the whole domain Λ yields

$$-\int_\Lambda \varphi^n \boldsymbol{u}^n \cdot (\nabla \cdot (2\eta_s \boldsymbol{\epsilon}(\boldsymbol{u}^n) - p^n \boldsymbol{I} - \boldsymbol{\sigma}^n)) \ \mathrm{d}\boldsymbol{x} + \int_\Lambda \rho\varphi^n \frac{\boldsymbol{u}^n - \boldsymbol{u}^{n-\frac{1}{2}}}{\Delta t} \cdot \boldsymbol{u}^n \ \mathrm{d}\boldsymbol{x}$$
$$= \int_\Lambda \rho\varphi^n \boldsymbol{g} \cdot \boldsymbol{u}^n \ \mathrm{d}\boldsymbol{x}, \qquad (1.51a)$$

$$\int_\Lambda \varphi^n (\nabla \cdot \boldsymbol{u}^n) p^n \ \mathrm{d}\boldsymbol{x} = 0 \qquad (1.51b)$$

$$\int_\Lambda \frac{\alpha}{2\eta_p} \varphi^n |\boldsymbol{\sigma}^n|^2 \ \mathrm{d}\boldsymbol{x} + \int_\Lambda \frac{\lambda\varphi^n}{2\eta_p \Delta t} \left(\boldsymbol{\sigma}^n - \boldsymbol{\sigma}^{n-\frac{1}{2}}\right) : \boldsymbol{\sigma}^{n-\frac{1}{2}} \ \mathrm{d}\boldsymbol{x} - \int_\Lambda \varphi^n \boldsymbol{\epsilon}(\boldsymbol{u}^n) : \boldsymbol{\sigma}^n \ \mathrm{d}\boldsymbol{x}$$
$$= \frac{\lambda}{2\eta_p} S(\boldsymbol{u}^{n-\frac{1}{2}}, \boldsymbol{\sigma}^{n-\frac{1}{2}}, \varphi^n).$$
$$(1.51c)$$

The variables $\boldsymbol{u}^n$, p^n and $\boldsymbol{\sigma}^n$ are not defined on the whole domain Λ and thus the same formal convention as previously has been applied for the integration. From free-surfaces boundary conditions and $\boldsymbol{u} = \boldsymbol{0}$ on $\partial\Lambda$ we find

$$-\int_\Lambda \varphi^n \boldsymbol{u}^n \cdot (\nabla \cdot (2\eta_s \boldsymbol{\epsilon}(\boldsymbol{u}^n) - p^n \boldsymbol{I} - \boldsymbol{\sigma}^n)) \ \mathrm{d}\boldsymbol{x} = -\int_{\Omega^n} \boldsymbol{u}^n \cdot (\nabla \cdot (2\eta_s \boldsymbol{\epsilon}(\boldsymbol{u}^n) - p^n \boldsymbol{I} - \boldsymbol{\sigma}^n)) \ \mathrm{d}\boldsymbol{x}$$
$$= \int_\Lambda \varphi^n \left(2\eta_s |\boldsymbol{\epsilon}(\boldsymbol{u}^n)|^2 - p^n \nabla \cdot \boldsymbol{u}^n + \boldsymbol{\sigma}^n : \boldsymbol{\epsilon}(\boldsymbol{u}^n)\right) \ \mathrm{d}\boldsymbol{x}.$$

Using the formula $2a(a - b) = a^2 - b^2 + (a - b)^2$ and divergence theorem, we obtain

$$\int_\Lambda \varphi^n \left(2\eta_s |\boldsymbol{\epsilon}(\boldsymbol{u}^n)|^2 - p^n \nabla \cdot \boldsymbol{u}^n + \boldsymbol{\sigma}^n : \boldsymbol{\epsilon}(\boldsymbol{u}^n) \right) \, \mathrm{d}\boldsymbol{x}$$

$$+ \int_\Lambda \frac{\rho}{2\Delta t} \varphi^n \left(|\boldsymbol{u}^n|^2 - |\boldsymbol{u}^{n-\frac{1}{2}}|^2 + \left| \boldsymbol{u}^n - \boldsymbol{u}^{n-\frac{1}{2}} \right|^2 \right) \, \mathrm{d}\boldsymbol{x} = \int_\Lambda \rho \varphi^n \boldsymbol{g} \cdot \boldsymbol{u}^n \, \mathrm{d}\boldsymbol{x},$$

$$\int_\Lambda \varphi^n (\nabla \cdot \boldsymbol{u}^n) p^n \, \mathrm{d}\boldsymbol{x} = 0.$$

and

$$\int_\Lambda \frac{\alpha}{2\eta_p} \varphi^n |\boldsymbol{\sigma}^n|^2 \, \mathrm{d}\boldsymbol{x} + \int_\Lambda \frac{\lambda \varphi^n}{2\eta_p \Delta t} \left(|\boldsymbol{\sigma}^n|^2 - |\boldsymbol{\sigma}^{n-\frac{1}{2}}|^2 + \left| \boldsymbol{\sigma}^n - \boldsymbol{\sigma}^{n-\frac{1}{2}} \right|^2 \right) \, \mathrm{d}\boldsymbol{x}$$

$$- \int_\Lambda \varphi^n \boldsymbol{\epsilon}(\boldsymbol{u}^n) : \boldsymbol{\sigma}^n \, \mathrm{d}\boldsymbol{x} = \frac{\lambda}{2\eta_p} S(\boldsymbol{u}^{n-\frac{1}{2}}, \boldsymbol{\sigma}^{n-\frac{1}{2}}, \varphi^n).$$

It finally yields

$$\int_\Lambda \left(\rho |\boldsymbol{u}^n|^2 + \frac{\lambda}{2\eta_p} |\boldsymbol{\sigma}^n|^2 \right) \varphi^n \, \mathrm{d}\boldsymbol{x} + \Delta t \int_\Lambda \left(4\eta_s |\boldsymbol{\epsilon}(\boldsymbol{u}^n)|^2 + \frac{\alpha}{\eta_p} |\boldsymbol{\sigma}^n|^2 \right) \varphi^n \, \mathrm{d}\boldsymbol{x}$$

$$+ \Delta t^2 \int_\Lambda \left(\rho \left| \frac{\boldsymbol{u}^n - \boldsymbol{u}^{n-\frac{1}{2}}}{\Delta t} \right|^2 + \frac{\lambda}{2\eta_p} \left| \frac{\boldsymbol{\sigma}^n - \boldsymbol{\sigma}^{n-\frac{1}{2}}}{\Delta t} \right|^2 \right) \varphi^n \, \mathrm{d}\boldsymbol{x}$$

$$= \int_\Lambda \left(\rho |\boldsymbol{u}^{n-\frac{1}{2}}|^2 + \frac{\lambda}{2\eta_p} |\boldsymbol{\sigma}^{n-\frac{1}{2}}|^2 \right) \varphi^n \, \mathrm{d}\boldsymbol{x}$$

$$+ \Delta t \left(\int_\Lambda 2\rho \varphi^n \boldsymbol{g} \cdot \boldsymbol{u}^n \, \mathrm{d}\boldsymbol{x} + \frac{\lambda}{\eta_p} S(\boldsymbol{u}^{n-\frac{1}{2}}, \boldsymbol{\sigma}^{n-\frac{1}{2}}, \varphi^n) \right).$$

Following chapter 3.4 in [Pir88], we find with the change of variables (1.13):

$$\int_\Lambda \left(\rho |\boldsymbol{u}^{n-\frac{1}{2}}|^2 + \frac{\lambda}{2\eta_p} |\boldsymbol{\sigma}^{n-\frac{1}{2}}|^2 \right) \varphi^n \, \mathrm{d}\boldsymbol{x}$$

$$= \int_\Lambda \left(\rho |\boldsymbol{u}^{n-1}|^2 + \frac{\lambda}{2\eta_p} |\boldsymbol{\sigma}^{n-1}|^2 \right) \varphi^{n-1} \left| \det \left(\boldsymbol{I} + \Delta t \nabla \boldsymbol{u}^{n-1} \right)^{-1} \right| \, \mathrm{d}\boldsymbol{x}.$$

From incompressibility condition, we have

$$\det \left(\boldsymbol{I} - \Delta t \nabla \boldsymbol{u}^{n-1} \right)^{-1} = 1 / \left(1 - \Delta t (\nabla \cdot \boldsymbol{u}^{n-1}) + \Delta t^2 |\nabla \boldsymbol{u}^{n-1}|^2 - \mathcal{O}(\Delta t^3) \right)$$

$$= 1 / \left(1 + \Delta t^2 |\nabla \boldsymbol{u}^{n-1}|^2 - \mathcal{O}(\Delta t^3) \right)$$

$$= 1 + C^{n-1} \Delta t^2 + \mathcal{O}(\Delta t^3).$$

Here, the value C^{m-1} is dependent on the gradient of the velocity, hence not constant. Additional analysis is needed to obtain a priori estimate for this problem and will not be addressed here. The interested reader can refer, for instance, to [Rav85, Sül88] for the

Newtonian case without free-surface.

1.7 Analysis of a simplified model for the fully discretized scheme

We address now the full discretisation of the system (1.29). Consider a domain entirely filled with a liquid or solid ($\varphi = 1$ in Λ and thus $\Lambda = \Omega(t) = \Omega$, for $0 \leq t \leq T$). The FE discretisation of the implicit scheme (1.39) is:

Find $\boldsymbol{u}_H^n \in \boldsymbol{V}_H$, $p_H^n \in Q_H$

$$\int_\Omega \rho \frac{\boldsymbol{u}_H^n - \boldsymbol{u}_H^{n-1}}{\Delta t} \cdot \boldsymbol{v}_H \, \mathrm{d}\boldsymbol{x} + \int_\Omega 2 \left(\eta_s + \frac{\eta_p \Delta t}{\lambda + \alpha \Delta t} \right) \boldsymbol{\epsilon}(\boldsymbol{u}_H^n) : \boldsymbol{\epsilon}(\boldsymbol{v}_H) \, \mathrm{d}\boldsymbol{x} \tag{1.52a}$$

$$- \int_\Omega p_H^n \nabla \cdot \boldsymbol{v}_H \, \mathrm{d}\boldsymbol{x} + \int_\Omega \frac{\lambda}{\lambda + \alpha \Delta t} \boldsymbol{\sigma}_H^{n-1} : \boldsymbol{\epsilon}(\boldsymbol{v}_H) \, \mathrm{d}\boldsymbol{x} = \boldsymbol{0}, \qquad \forall \boldsymbol{v}_H \in \boldsymbol{V}_H,$$

$$\int_\Omega (\nabla \cdot \boldsymbol{u}_H^n) q_H \, \mathrm{d}\boldsymbol{x} + \sum_{K \in \mathcal{T}_H} \alpha_K \int_K \nabla p_H^n \cdot \nabla q_H \, \mathrm{d}\boldsymbol{x} = 0, \qquad \forall q_H \in Q_H, \tag{1.52b}$$

and then find $\boldsymbol{\sigma}_H^n \in \boldsymbol{T}_H$ such that

$$\int_\Omega \boldsymbol{\sigma}_H^n : \boldsymbol{\tau}_H \, \mathrm{d}\boldsymbol{x} = \int_\Omega \frac{\lambda}{\lambda + \alpha \Delta t} \boldsymbol{\sigma}_H^{n-1} : \boldsymbol{\tau}_h \, \mathrm{d}\boldsymbol{x} \tag{1.52c}$$

$$+ \int_\Omega \frac{2\eta_p \Delta t}{\lambda + \alpha \Delta t} \boldsymbol{\epsilon}(\boldsymbol{u}_H^n) : \boldsymbol{\tau}_H \, \mathrm{d}\boldsymbol{x}, \quad \forall \boldsymbol{\tau}_H \in \boldsymbol{T}_H,$$

where $\boldsymbol{V}_H$, Q_H and $\boldsymbol{T}_H$ are the spaces of piecewise linear finite elements (1.26) for the full domain, when $\Omega_H^n = \Omega = \Lambda$. Here, the stabilisation coefficient α_K is defined similarly as in section 1.4.3 for the implicit scheme (1.28). The terms $-\frac{\lambda}{\lambda + \Delta t} \nabla \cdot \boldsymbol{\sigma}_H^{n-\frac{1}{2}} - \rho \boldsymbol{g}$ are removed to simplify the computations.

The equation (1.52a) is not equivalent to the finite element formulation of the implicit scheme (1.25), which would yield

$$\int_\Omega \rho \frac{\boldsymbol{u}_H^n - \boldsymbol{u}_H^{n-1}}{\Delta t} \cdot \boldsymbol{v}_H \, \mathrm{d}\boldsymbol{x} + \int_\Omega 2\eta_s \boldsymbol{\epsilon}(\boldsymbol{u}_H^n) : \boldsymbol{\epsilon}(\boldsymbol{v}_H) \, \mathrm{d}\boldsymbol{x} - \int_\Omega p_H^n (\nabla \cdot \boldsymbol{v}_H) \, \mathrm{d}\boldsymbol{x} \tag{1.53}$$

$$+ \int_\Omega \boldsymbol{\sigma}_H^n : \boldsymbol{\epsilon}(\boldsymbol{v}_H) \, \mathrm{d}\boldsymbol{x} = \boldsymbol{0}, \quad \forall \boldsymbol{v}_H \in \boldsymbol{V}_H,$$

Since $\boldsymbol{v}_H \in \boldsymbol{V}_H$, $\boldsymbol{\epsilon}(\boldsymbol{v}_H) \notin \boldsymbol{T}_H$; rather we have $\boldsymbol{\epsilon}(\boldsymbol{v}_H) \in \boldsymbol{W}_H = \{\boldsymbol{w} \in L^2(\Omega_H)^{3 \times 3}; \boldsymbol{w}_{|K} \in \mathbb{P}_0(K), \forall K \in \mathcal{T}_H\}$. Thus, the equation (1.53) cannot be retrieved from (1.52a). We are going to prove that the implicit formulation (1.52) does not impact the stability of the numerical scheme.

To do so, we introduce the continuous L^2-projection operator onto $\boldsymbol{T}_H$. Let π_H :

$(L^2(\Omega))^{3\times3} \to \boldsymbol{T}_H$ be the projection operator onto $\boldsymbol{T}_H$, defined for all $\boldsymbol{w} \in (L^2(\Omega))^{3\times3}$ by $\pi_H(\boldsymbol{w}) \in \boldsymbol{T}_H$ and:

$$\int_\Omega \pi_H(\boldsymbol{w}) : \boldsymbol{\tau}_H \, \mathrm{d}\boldsymbol{x} = \int_\Omega \boldsymbol{w} : \boldsymbol{\tau}_H \, \mathrm{d}\boldsymbol{x}, \quad \forall \boldsymbol{\tau}_H \in \boldsymbol{T}_H. \tag{1.54}$$

We have the following result:

Proposition 1.7.1. Consider the numerical scheme (1.52). For all $\Delta t > 0, \eta_s \geq 0, \eta_p > 0$ and $\alpha = \{0, 1\}$, we have:

$$\int_\Omega \left(\rho |\boldsymbol{u}_H^N|^2 + \frac{\lambda}{2\eta_p} |\boldsymbol{\sigma}_H^N|^2 \right) \mathrm{d}\boldsymbol{x} + \Delta t \sum_{n=1}^N \int_\Omega \left(4\eta_s |\boldsymbol{\epsilon}(\boldsymbol{u}_H^n)|^2 + \frac{\alpha}{\eta_p} |\boldsymbol{\sigma}_H^n|^2 \right) \mathrm{d}\boldsymbol{x} \tag{1.55}$$

$$\leq \int_\Omega \left(\rho |\boldsymbol{u}_H^0|^2 + \frac{\lambda}{2\eta_p} |\boldsymbol{\sigma}_H^0|^2 \right) \mathrm{d}\boldsymbol{x}.$$

and

$$\int_\Omega \left(\rho\lambda \left| \frac{\boldsymbol{u}_H^N - \boldsymbol{u}_H^{N-1}}{\Delta t} \right|^2 + 2\eta_s \alpha |\boldsymbol{\epsilon}(\boldsymbol{u}_H^N)|^2 + 2\eta_p |\pi_H(\boldsymbol{\epsilon}(\boldsymbol{u}_H^N))|^2 \right) \mathrm{d}\boldsymbol{x} + \sum_{K \in \mathcal{T}_H} \alpha_K \int_K \alpha |\nabla p_H^N|^2 \, \mathrm{d}\boldsymbol{x}$$

$$+ \Delta t^2 \int_\Omega \frac{\alpha\eta_p}{\lambda + \alpha\Delta t} \left| \boldsymbol{\epsilon}(\boldsymbol{u}_H^N) - \pi_H(\boldsymbol{\epsilon}(\boldsymbol{u}_H^N)) \right|^2 \mathrm{d}\boldsymbol{x}$$

$$\leq \int_\Omega \left(\rho\lambda \left| \frac{\boldsymbol{u}_H^1 - \boldsymbol{u}_H^0}{\Delta t} \right|^2 + 2\eta_s \alpha |\boldsymbol{\epsilon}(\boldsymbol{u}_H^1)|^2 + 2\eta_p |\pi_H(\boldsymbol{\epsilon}(\boldsymbol{u}_H^1))|^2 \right) \mathrm{d}\boldsymbol{x} \tag{1.56}$$

$$+ \sum_{K \in \mathcal{T}_H} \alpha_K \int_K \alpha |\nabla p_H^1|^2 \, \mathrm{d}\boldsymbol{x} + \Delta t^2 \int_\Omega \frac{\alpha\eta_p}{\lambda + \alpha\Delta t} \left| \boldsymbol{\epsilon}(\boldsymbol{u}_H^1) - \pi_H(\boldsymbol{\epsilon}(\boldsymbol{u}_H^1)) \right|^2 \mathrm{d}\boldsymbol{x}.$$

Proof. Let $\boldsymbol{\tau}_H = \pi_H(\boldsymbol{\epsilon}(\boldsymbol{v}_H))$ in (1.52c) and from (1.54) it yields

$$\int_\Omega \boldsymbol{\sigma}_H^n : \boldsymbol{\epsilon}(\boldsymbol{v}_H) \, \mathrm{d}\boldsymbol{x} = \int_\Omega \frac{\lambda}{\lambda + \alpha\Delta t} \boldsymbol{\sigma}_H^{n-1} : \boldsymbol{\epsilon}(\boldsymbol{v}_H) \, \mathrm{d}\boldsymbol{x} + \int_\Omega \frac{2\eta_p \Delta t}{\lambda + \alpha\Delta t} \boldsymbol{\epsilon}(\boldsymbol{u}_H^n) : \pi_H(\boldsymbol{\epsilon}(\boldsymbol{v}_H)) \, \mathrm{d}\boldsymbol{x}.$$

Plugging this expression back into (1.52a) yields

$$\int_\Omega \rho \frac{\boldsymbol{u}_H^n - \boldsymbol{u}_H^{n-1}}{\Delta t} \cdot \boldsymbol{v}_h \, \mathrm{d}\boldsymbol{x} + \int_\Omega 2\eta_s \boldsymbol{\epsilon}(\boldsymbol{u}_H^n) : \boldsymbol{\epsilon}(\boldsymbol{v}_H) \, \mathrm{d}\boldsymbol{x} - \int_\Omega p_H^n \nabla \cdot \boldsymbol{v}_h \, \mathrm{d}\boldsymbol{x} + \int_\Omega \boldsymbol{\sigma}_H^n : \boldsymbol{\epsilon}(\boldsymbol{v}_H) \, \mathrm{d}\boldsymbol{x}$$

$$+ \int_\Omega \frac{2\eta_p \Delta t}{\lambda + \alpha\Delta t} \boldsymbol{\epsilon}(\boldsymbol{u}_H^n) : (\boldsymbol{\epsilon}(\boldsymbol{v}_H) - \pi_H(\boldsymbol{\epsilon}(\boldsymbol{v}_H))) \, \mathrm{d}\boldsymbol{x} = 0. \tag{1.57}$$

From the L^2-projection operator π_H definition (1.54), we have

$$\int_\Omega \frac{2\eta_p \Delta t}{\lambda + \alpha\Delta t} \pi_H(\boldsymbol{\epsilon}(\boldsymbol{u}_H^n)) : (\boldsymbol{\epsilon}(\boldsymbol{u}_H^n) - \pi_H(\boldsymbol{\epsilon}(\boldsymbol{u}_H^n))) \, \mathrm{d}\boldsymbol{x} = 0. \tag{1.58}$$

Notice that multiplying (1.52c) by $\dfrac{\lambda + \alpha \Delta t}{\Delta t}$ yields

$$\int_{\Omega} \alpha \boldsymbol{\sigma}_H^n : \boldsymbol{\tau}_H \, \mathrm{d}\boldsymbol{x} + \int_{\Omega} \lambda \frac{\boldsymbol{\sigma}_H^n - \boldsymbol{\sigma}_H^{n-1}}{\Delta t} : \boldsymbol{\tau}_H \, \mathrm{d}\boldsymbol{x} = \int_{\Omega} 2\eta_p \boldsymbol{\epsilon}(\boldsymbol{u}_H^n) : \boldsymbol{\tau}_H \, \mathrm{d}\boldsymbol{x}. \qquad (1.59)$$

Let $\boldsymbol{v}_H = \boldsymbol{u}_H^n$ in (1.57), $q_H = p_H^n$ in (1.52b) and $\boldsymbol{\tau}_H = \boldsymbol{\sigma}_H^n$ in (1.59). Using (1.58) and the identity $a(a - b) = \frac{1}{2}(a^2 - b^2 + (a - b)^2)$, we find

$$\int_{\Omega} \rho(|\boldsymbol{u}_H^n|^2 + |\boldsymbol{u}_H^n - \boldsymbol{u}_H^{n-1}|^2) + \frac{\lambda}{2\eta_p}(|\boldsymbol{\sigma}_H^n|^2 + |\boldsymbol{\sigma}_H^n - \boldsymbol{\sigma}_H^{n-1}|^2) \, \mathrm{d}\boldsymbol{x}$$

$$+ \Delta t \int_{\Omega} \left(4\eta_s |\boldsymbol{\epsilon}(\boldsymbol{u}_H^n)|^2 + \frac{\alpha}{\eta_p}|\boldsymbol{\sigma}_H^n|^2 \right) \, \mathrm{d}\boldsymbol{x}$$

$$+ \Delta t \sum_{K \in \mathcal{T}_H} \alpha_K \int_K |\nabla p_H^n|^2 \, \mathrm{d}\boldsymbol{x} + \Delta t^2 \int_{\Omega} \frac{4\eta_p}{\lambda + \alpha \Delta t} |\boldsymbol{\epsilon}(\boldsymbol{u}_H^n) - \pi_H(\boldsymbol{\epsilon}(\boldsymbol{u}_H^n))|^2 \, \mathrm{d}\boldsymbol{x}$$

$$= \int_{\Omega} \rho|\boldsymbol{u}_H^{n-1}|^2 + \frac{\lambda}{2\eta_p}|\boldsymbol{\sigma}_H^{n-1}|^2 \, \mathrm{d}\boldsymbol{x}.$$

Summing from $n = 1$ to N yields

$$\int_{\Omega} \left(\rho|\boldsymbol{u}_H^N|^2 + \frac{\lambda}{2\eta_p}|\boldsymbol{\sigma}_H^N|^2 \right) \, \mathrm{d}\boldsymbol{x} + \Delta t \sum_{i=1}^{N} \int_{\Omega} \left(4\eta_s|\boldsymbol{\epsilon}(\boldsymbol{u}_H^i)|^2 + \frac{\alpha}{\eta_p}|\boldsymbol{\sigma}_H^i|^2 \right) \, \mathrm{d}\boldsymbol{x}$$

$$+ \Delta t^2 \sum_{i=1}^{N} \int_{\Omega} \left(\rho \left| \frac{\boldsymbol{u}_H^i - \boldsymbol{u}_H^{i-1}}{\Delta t} \right|^2 + \frac{\lambda}{2\eta_p} \left| \frac{\boldsymbol{\sigma}_H^i - \boldsymbol{\sigma}_H^{i-1}}{\Delta t} \right|^2 \right) \, \mathrm{d}\boldsymbol{x} \qquad (1.60)$$

$$+ \Delta t \sum_{i=1}^{N} \sum_{K \in \mathcal{T}_H} \alpha_K \int_K |\nabla p_H^i|^2 \, \mathrm{d}\boldsymbol{x} + \Delta t^2 \sum_{i=1}^{N} \int_{\Omega} \left(\frac{4\eta_p}{\lambda + \alpha \Delta t} |\boldsymbol{\epsilon}(\boldsymbol{u}_H^i) - \pi_H(\boldsymbol{\epsilon}(\boldsymbol{u}_H^i))|^2 \right) \, \mathrm{d}\boldsymbol{x}$$

$$= \int_{\Omega} \left(\rho|\boldsymbol{u}_H^0|^2 + \frac{\lambda}{2\eta_p}|\boldsymbol{\sigma}_H^0|^2 \right) \, \mathrm{d}\boldsymbol{x},$$

which yields (1.55).

For the second result, we proceed as in Proposition 1.5.2. Let us take the difference between two consecutive time steps of the modified momentum equation (1.57), and divide the result by Δt to obtain

$$\int_{\Omega} \left(\frac{\boldsymbol{u}_H^{n+1} - 2\boldsymbol{u}_H^n + \boldsymbol{u}_H^{n-1}}{\Delta t^2} \right) \cdot \boldsymbol{v}_H \, \mathrm{d}\boldsymbol{x} + \int_{\Omega} 2\eta_s \boldsymbol{\epsilon} \left(\frac{\boldsymbol{u}_H^{n+1} - \boldsymbol{u}_H^n}{\Delta t} \right) : \boldsymbol{\epsilon}(\boldsymbol{v}_H) \, \mathrm{d}\boldsymbol{x}$$

$$- \int_{\Omega} \left(\frac{p_H^{n+1} - p_H^n}{\Delta t} \right) (\nabla \cdot \boldsymbol{v}_H) \, \mathrm{d}\boldsymbol{x} + \int_{\Omega} \left(\frac{\boldsymbol{\sigma}_H^{n+1} - \boldsymbol{\sigma}_H^n}{\Delta t} \right) : \boldsymbol{\epsilon}(\boldsymbol{v}_H) \, \mathrm{d}\boldsymbol{x}$$

$$+ \int_{\Omega} \frac{2\eta_p \Delta t}{\lambda + \alpha \Delta t} \boldsymbol{\epsilon} \left(\frac{\boldsymbol{u}_H^{n+1} - \boldsymbol{u}_H^n}{\Delta t} \right) : (\boldsymbol{\epsilon}(\boldsymbol{v}_H) - \pi_H(\boldsymbol{\epsilon}(\boldsymbol{v}_H))) \, \mathrm{d}\boldsymbol{x} = 0.$$

Then we take λ times the above equation and add it to α times (1.57):

$$\int_\Omega \rho \left(\alpha \frac{\boldsymbol{u}_H^{n+1} - \boldsymbol{u}_H^n}{\Delta t} + \lambda \frac{\boldsymbol{u}_H^{n+1} - 2\boldsymbol{u}_H^n + \boldsymbol{u}_H^{n-1}}{\Delta t^2} \right) \cdot \boldsymbol{v}_H \ \mathrm{d}\boldsymbol{x}$$

$$+ \int_\Omega 2\eta_s \left(\alpha \boldsymbol{\epsilon}(\boldsymbol{u}_H^{n+1}) + \lambda \boldsymbol{\epsilon} \left(\frac{\boldsymbol{u}_H^{n+1} - \boldsymbol{u}_H^n}{\Delta t} \right) \right) : \boldsymbol{\epsilon}(\boldsymbol{v}_H) \ \mathrm{d}\boldsymbol{x} \qquad (1.61)$$

$$- \int_\Omega \left(\alpha p_H^{n+1} + \lambda \frac{p_H^{n+1} - p_H^n}{\Delta t} \right) (\nabla \cdot \boldsymbol{v}_H) \ \mathrm{d}\boldsymbol{x} + \int_\Omega \left(\alpha \boldsymbol{\sigma}_H^{n+1} + \lambda \frac{\boldsymbol{\sigma}_H^{n+1} - \boldsymbol{\sigma}_H^n}{\Delta t} \right) : \boldsymbol{\epsilon}(\boldsymbol{v}_H) \ \mathrm{d}\boldsymbol{x}$$

$$+ \int_\Omega \frac{2\eta_p \Delta t}{\lambda + \alpha \Delta t} \left(\alpha \boldsymbol{\epsilon} \left(\boldsymbol{u}_H^{n+1} \right) + \lambda \boldsymbol{\epsilon} \left(\frac{\boldsymbol{u}_H^{n+1} - \boldsymbol{u}_H^n}{\Delta t} \right) \right) : (\boldsymbol{\epsilon}(\boldsymbol{v}_H) - \pi_H(\boldsymbol{\epsilon}(\boldsymbol{v}_H))) \ \mathrm{d}\boldsymbol{x} = 0.$$

Take the difference between two time steps in (1.52b) gives

$$\int_\Omega \nabla \cdot (\boldsymbol{u}_H^{n+1} - \boldsymbol{u}_H^n) q_H \ \mathrm{d}\boldsymbol{x} + \sum_{K \in \mathcal{T}_H} \alpha_K \int_K \nabla(p_H^{n+1} - p_H^n) \cdot \nabla q_H \ \mathrm{d}\boldsymbol{x} = 0. \qquad (1.62)$$

Let $\boldsymbol{v}_H = \boldsymbol{u}_H^{n+1} - \boldsymbol{u}_H^n$ in (1.61) and $q_H = \alpha p_H^{n+1} + \lambda \frac{p_H^{n+1} - p_H^n}{\Delta t}$ in (1.62). It yields

$$\int_\Omega \frac{\rho\lambda}{2} \left| \frac{\boldsymbol{u}_H^{n+1} - \boldsymbol{u}_H^n}{\Delta t} \right|^2 + \frac{\rho\lambda}{2} \left| \frac{\boldsymbol{u}_H^{n+1} - 2\boldsymbol{u}_H^n + \boldsymbol{u}_H^{n-1}}{\Delta t} \right|^2 \ \mathrm{d}\boldsymbol{x} + \Delta t \int_\Omega \rho\alpha \left| \frac{\boldsymbol{u}_H^{n+1} - \boldsymbol{u}_H^n}{\Delta t} \right|^2 \ \mathrm{d}\boldsymbol{x}$$

$$+ \int_\Omega 2\eta_s \left(\alpha \boldsymbol{\epsilon}(\boldsymbol{u}_H^{n+1}) + \lambda \boldsymbol{\epsilon} \left(\frac{\boldsymbol{u}_H^{n+1} - \boldsymbol{u}_H^n}{\Delta t} \right) \right) : \boldsymbol{\epsilon}(\boldsymbol{u}_H^{n+1} - \boldsymbol{u}_H^n) \ \mathrm{d}\boldsymbol{x}$$

$$+ \sum_{K \in \mathcal{T}_H} \alpha_K \int_K \nabla(p_H^{n+1} - p_H^n) \cdot \nabla \left(\alpha p_H^{n+1} + \lambda \frac{p_H^{n+1} - p_H^n}{\Delta t} \right) \ \mathrm{d}\boldsymbol{x}$$

$$+ \int_\Omega \frac{2\eta_p \Delta t}{\lambda + \alpha \Delta t} \left(\alpha \boldsymbol{\epsilon} \left(\boldsymbol{u}_H^{n+1} \right) + \lambda \boldsymbol{\epsilon} \left(\frac{\boldsymbol{u}_H^{n+1} - \boldsymbol{u}_H^n}{\Delta t} \right) \right) : (\boldsymbol{\epsilon}(\boldsymbol{u}_H^{n+1} - \boldsymbol{u}_H^n) - \pi_H(\boldsymbol{\epsilon}(\boldsymbol{u}_H^{n+1} - \boldsymbol{u}_H^n))) \ \mathrm{d}\boldsymbol{x}$$

$$+ \int_\Omega \left(\alpha \boldsymbol{\sigma}_H^{n+1} + \lambda \frac{\boldsymbol{\sigma}_H^{n+1} - \boldsymbol{\sigma}_H^n}{\Delta t} \right) : \boldsymbol{\epsilon}(\boldsymbol{u}_H^{n+1} - \boldsymbol{u}_H^n) \ \mathrm{d}\boldsymbol{x} = \int_\Omega \frac{\rho\lambda}{2} \left| \frac{\boldsymbol{u}_H^n - \boldsymbol{u}_H^{n-1}}{\Delta t} \right|^2 \ \mathrm{d}\boldsymbol{x}.$$

Now we take $\boldsymbol{\tau}_H = \pi_H(\boldsymbol{\epsilon}(\boldsymbol{u}_H^{n+1} - \boldsymbol{u}_H^n))$ in (1.59) and using (1.54) we obtain

$$\int_\Omega \left(\alpha \boldsymbol{\sigma}_H^{n+1} + \lambda \frac{\boldsymbol{\sigma}_H^{n+1} - \boldsymbol{\sigma}_H^n}{\Delta t} \right) : \boldsymbol{\epsilon}(\boldsymbol{u}_H^{n+1} - \boldsymbol{u}_H^n) \ \mathrm{d}\boldsymbol{x}$$

$$\overset{(1.59)}{=} \int_\Omega 2\eta_p \boldsymbol{\epsilon}(\boldsymbol{u}_H^{n+1}) : (\pi_H(\boldsymbol{\epsilon}(\boldsymbol{u}_H^{n+1} - \boldsymbol{u}_H^n))) \ \mathrm{d}\boldsymbol{x}$$

$$\overset{(1.54)}{=} \int_\Omega 2\eta_p \pi_H(\boldsymbol{\epsilon}(\boldsymbol{u}_H^{n+1})) : (\pi_H(\boldsymbol{\epsilon}(\boldsymbol{u}_H^{n+1} - \boldsymbol{u}_H^n))) \ \mathrm{d}\boldsymbol{x}.$$

Using the equality $(\alpha a + \beta(a-b))(a-b) = \frac{\alpha}{2}(a^2 - b^2) + (\beta + \frac{\alpha}{2})(a-b)^2$, we find

$$
\int_\Omega \rho\lambda \left| \frac{\boldsymbol{u}_H^{n+1} - \boldsymbol{u}_H^n}{\Delta t} \right|^2 + \rho\lambda \left| \frac{\boldsymbol{u}_H^{n+1} - 2\boldsymbol{u}_H^n + \boldsymbol{u}_H^{n-1}}{\Delta t} \right|^2
$$

$$
+ 2\eta_s\alpha(|\boldsymbol{\epsilon}(\boldsymbol{u}_H^{n+1})|^2 + |\boldsymbol{\epsilon}(\boldsymbol{u}_H^{n+1}) - \boldsymbol{\epsilon}(\boldsymbol{u}_H^n)|^2) \ \mathrm{d}\boldsymbol{x}
$$

$$
+ \int_\Omega 2\eta_p(|\pi_H(\boldsymbol{\epsilon}(\boldsymbol{u}_H^{n+1}))|^2 + |\pi_H(\boldsymbol{\epsilon}(\boldsymbol{u}_H^{n+1}) - \boldsymbol{\epsilon}(\boldsymbol{u}_H^n))|^2) \ \mathrm{d}\boldsymbol{x}
$$

$$
+ \Delta t \int_\Omega \rho\alpha \left| \frac{\boldsymbol{u}_H^{n+1} - \boldsymbol{u}_H^n}{\Delta t} \right|^2 + 4\eta_s\lambda \left| \boldsymbol{\epsilon}\left(\frac{\boldsymbol{u}_H^{n+1} - \boldsymbol{u}_H^n}{\Delta t} \right) \right|^2 \ \mathrm{d}\boldsymbol{x}
$$

$$
+ \sum_{K \in \mathcal{T}_H} \alpha_K \int_K \alpha|\nabla p_H^{n+1}|^2 + \left(\frac{2\lambda}{\Delta t} + \alpha \right) |\nabla(p_H^{n+1} - p_H^n)|^2 \ \mathrm{d}\boldsymbol{x}
$$

$$
+ \Delta t \int_\Omega \frac{2\alpha\eta_p\Delta t}{\lambda + \alpha\Delta t} |\boldsymbol{\epsilon}(\boldsymbol{u}_H^{n+1}) - \pi_H(\boldsymbol{\epsilon}(\boldsymbol{u}_H^{n+1}))|^2 \ \mathrm{d}\boldsymbol{x}
$$

$$
+ \Delta t \int_\Omega \frac{2\eta_p\Delta t}{\lambda + \alpha\Delta t} \left(\alpha + \frac{2\lambda}{\Delta t} \right) |\boldsymbol{\epsilon}(\boldsymbol{u}_H^{n+1} - \boldsymbol{u}_H^n) - \pi_H(\boldsymbol{\epsilon}(\boldsymbol{u}_H^{n+1} - \boldsymbol{u}_H^n))|^2 \ \mathrm{d}\boldsymbol{x}
$$

$$
= \int_\Omega \frac{\rho\lambda}{2} \left| \frac{\boldsymbol{u}_H^n - \boldsymbol{u}_H^{n-1}}{\Delta t} \right|^2 + 2\eta_s\alpha|\boldsymbol{\epsilon}(\boldsymbol{u}_H^n)|^2 + 2\eta_p|\pi_H(\boldsymbol{\epsilon}(\boldsymbol{u}_H^n))|^2 \ \mathrm{d}\boldsymbol{x}
$$

$$
+ \sum_{K \in \mathcal{T}_H} \alpha_K \int_K \frac{\alpha}{2}|\nabla p_H^n|^2 \ \mathrm{d}\boldsymbol{x} + \Delta t \int_\Omega \frac{2\alpha\eta_p\Delta t}{\lambda + \alpha\Delta t} |\boldsymbol{\epsilon}(\boldsymbol{u}_H^n) - \pi_H(\boldsymbol{\epsilon}(\boldsymbol{u}_H^n))|^2 \ \mathrm{d}\boldsymbol{x}.
$$

Summing from $n = 1$ to $n = N - 1$ we obtain (1.56). ∎

A similar result can be obtained for the following EVSS numerical scheme for the linearized system (1.29), using the stabilisation coefficient α_K defined similarly as in section 1.4.3 for the EVSS scheme (1.27):

$$
\int_\Omega \boldsymbol{D}_H^{n-1} : \boldsymbol{\tau}_H \ \mathrm{d}\boldsymbol{x} = \int_{\Omega^n} \boldsymbol{\epsilon}(\boldsymbol{u}_H^{n-1}) : \boldsymbol{\tau}_H \ \mathrm{d}\boldsymbol{x}, \qquad \forall \boldsymbol{\tau}_H \in \boldsymbol{T}_H, \qquad (1.63\mathrm{a})
$$

$$
\int_\Omega \rho \frac{\boldsymbol{u}_H^n - \boldsymbol{u}_H^{n-1}}{\Delta t} \cdot \boldsymbol{v}_H \ \mathrm{d}x + \int_\Omega 2(\eta_s + \eta_p)\boldsymbol{\epsilon}(\boldsymbol{u}_H^n) : \boldsymbol{\epsilon}(\boldsymbol{v}_H) \ \mathrm{d}\boldsymbol{x} \qquad (1.63\mathrm{b})
$$

$$
- \int_\Omega p_H^n \nabla \cdot \boldsymbol{v}_H \ \mathrm{d}\boldsymbol{x} = \int_\Omega (2\eta_p\boldsymbol{D}_H^{n-1} - \boldsymbol{\sigma}_H^{n-1}) : \boldsymbol{\epsilon}(\boldsymbol{v}_H) \ \mathrm{d}x, \qquad \forall \boldsymbol{v}_H \in \boldsymbol{V}_H,
$$

$$
\int_\Omega (\nabla \cdot \boldsymbol{u}_H^n)q_H \ \mathrm{d}\boldsymbol{x} + \sum_{K \in \mathcal{T}_H} \alpha_K \int_K \nabla p_H^n \cdot \nabla q_H \ \mathrm{d}\boldsymbol{x} = 0, \qquad \forall q_H \in Q_H, \qquad (1.63\mathrm{c})
$$

$$
\int_\Omega \boldsymbol{\sigma}_H^n : \boldsymbol{\tau}_H \ \mathrm{d}\boldsymbol{x} = \int_\Omega \frac{\lambda}{\lambda + \alpha\Delta t}\boldsymbol{\sigma}_H^{n-1} : \boldsymbol{\tau}_H \ \mathrm{d}\boldsymbol{x} \qquad (1.63\mathrm{d})
$$

$$
+ \int_\Omega \frac{2\eta_p\Delta t}{\lambda + \alpha\Delta t}\boldsymbol{\epsilon}(\boldsymbol{u}_H^n) : \boldsymbol{\tau}_H \ \mathrm{d}\boldsymbol{x}, \qquad \forall \boldsymbol{\tau}_H \in \boldsymbol{T}_H.
$$

Proposition 1.7.2. Consider the numerical scheme (1.63). For all $\Delta t \leq \lambda$, $\eta_s \geq 0$, $\eta_p > 0$: and $\alpha = \{0, 1\}$, we have:

$$\int_\Omega \left(\rho |\boldsymbol{u}_H^N|^2 + \frac{\lambda}{4\eta_p} |\boldsymbol{\sigma}_H^N|^2 \right) \, \mathrm{d}\boldsymbol{x} \leq \int_\Omega \left(\rho |\boldsymbol{u}_H^0|^2 + \frac{\lambda}{2\eta_p} |\boldsymbol{\sigma}_H^0|^2 \right) \, \mathrm{d}\boldsymbol{x} \tag{1.64}$$

$$+ \Delta t \int_\Omega \left((\eta_s + 3\eta_p) |\boldsymbol{\epsilon}(\boldsymbol{u}_H^0)|^2 + \frac{\alpha+1}{4\eta_p} |\boldsymbol{\sigma}_H^0|^2 \right) \, \mathrm{d}\boldsymbol{x} + \Delta t \sum_{K \in \mathcal{T}_H} \frac{\alpha_K}{2} \int_K |\nabla p_H^0|^2 \, \mathrm{d}\boldsymbol{x}.$$

Furthermore, for $\alpha = 1$, we have for $\Delta t > 0$, with $\eta_s \geq 0$, $\eta_p > 0$:

$$\int_\Omega \left(\rho \lambda \left| \frac{\boldsymbol{u}_H^N - \boldsymbol{u}_H^{N-1}}{\Delta t} \right|^2 + (\eta_s + \eta_p) |\boldsymbol{\epsilon}(\boldsymbol{u}_H^N)|^2 \right) \, \mathrm{d}\boldsymbol{x}$$

$$+ \sum_{K \in \mathcal{T}_H} \alpha_K \int_K |\nabla p_H^N|^2 \, \mathrm{d}\boldsymbol{x} + \int_\Omega 2\eta_p \lambda \left| \pi_H \left(\boldsymbol{\epsilon} \left(\frac{\boldsymbol{u}_H^N - \boldsymbol{u}_H^{N-1}}{\Delta t} \right) \right) \right|^2 \, \mathrm{d}\boldsymbol{x} \tag{1.65}$$

$$\leq \int_\Omega \left(\rho \lambda \left| \frac{\boldsymbol{u}_H^1 - \boldsymbol{u}_H^0}{\Delta t} \right|^2 + (\eta_s + \eta_p) |\boldsymbol{\epsilon}(\boldsymbol{u}_H^1)|^2 \right) \, \mathrm{d}\boldsymbol{x} + \sum_{K \in \mathcal{T}_H} \alpha_K \int_K \frac{\alpha}{2} |\nabla p_H^1|^2 \, \mathrm{d}\boldsymbol{x}$$

$$+ \int_\Omega 2\eta_p \lambda \left| \pi_H \left(\boldsymbol{\epsilon} \left(\frac{\boldsymbol{u}_H^1 - \boldsymbol{u}_H^0}{\Delta t} \right) \right) \right|^2 \, \mathrm{d}\boldsymbol{x}$$

and for $\alpha = 0$ and $\Delta t \leq \lambda$ we have:

$$\int_\Omega \frac{\rho \lambda}{2} \left| \frac{\boldsymbol{u}_H^N - \boldsymbol{u}_H^{N-1}}{\Delta t} \right|^2 + \int_\Omega \eta_p (|\pi_H(\boldsymbol{\epsilon}(\boldsymbol{u}_H^N))|^2 + |\pi_H(\boldsymbol{\epsilon}(\boldsymbol{u}_H^{N-1}))|^2) \, \mathrm{d}\boldsymbol{x}$$

$$+ \Delta t \int_\Omega (\eta_s + \eta_p) \lambda \left| \boldsymbol{\epsilon} \left(\frac{\boldsymbol{u}_H^N - \boldsymbol{u}_H^{N-1}}{\Delta t} \right) \right|^2 \, \mathrm{d}\boldsymbol{x} + \Delta t \sum_{K \in \mathcal{T}_H} \frac{\alpha_k \lambda}{2} \int_K \left| \nabla \left(\frac{p_H^N - p_H^{N-1}}{\Delta t} \right) \right|^2 \, \mathrm{d}\boldsymbol{x}$$

$$\leq \int_\Omega \frac{\rho \lambda}{2} \left| \frac{\boldsymbol{u}_H^1 - \boldsymbol{u}_H^0}{\Delta t} \right|^2 \, \mathrm{d}\boldsymbol{x} + \int_\Omega \eta_p (|\pi_H(\boldsymbol{\epsilon}(\boldsymbol{u}_H^1))|^2 + |\pi_H(\boldsymbol{\epsilon}(\boldsymbol{u}_H^0))|^2) \, \mathrm{d}\boldsymbol{x} \tag{1.66}$$

$$+ \Delta t \int_\Omega (\eta_s + 2\eta_p) \lambda \left| \boldsymbol{\epsilon} \left(\frac{\boldsymbol{u}_H^1 - \boldsymbol{u}_H^0}{\Delta t} \right) \right|^2 \, \mathrm{d}\boldsymbol{x} + \Delta t \sum_{K \in \mathcal{T}_H} \frac{\alpha_k \lambda}{2} \int_K \left| \nabla \left(\frac{p_H^1 - p_H^0}{\Delta t} \right) \right|^2 \, \mathrm{d}\boldsymbol{x}.$$

Proof in Appendix C.3

Similarly to the stability estimates proofs for the analytical solution, the implicit scheme is proved to be unconditionally stable, whereas it is not the case for the EVSS scheme. However, even if the first stability estimates shows no control on $\boldsymbol{\sigma}_H^n$ for $\eta_s = 0$, the velocity and its gradient are controlled and thus $\boldsymbol{\sigma}_H^n$ as well.

The projection operator π_H shows similarity to the ZZ error estimator introduced in [ZZ95] in the 1D case. Indeed, the projection π_H is equivalent to the projector of the gradient $\nabla \boldsymbol{u}_h \in \boldsymbol{W}_H$ onto the space of piecewise linear finite element function

$\boldsymbol{T}_H$. It is proved in [ZZ98] that, for a Laplace problem with enough regularity, this quantity converges to the norm of the gradient of the error. However in our case, no proofs of convergence could be obtained for the quantity $\|\boldsymbol{\epsilon}(\boldsymbol{u}_H^n) - \pi_H(\boldsymbol{\epsilon}(\boldsymbol{u}_H^n))\|$, but it can be bounded. Indeed, we have $\|\boldsymbol{\epsilon}(\boldsymbol{u}_H^n) - \pi_H(\boldsymbol{\epsilon}(\boldsymbol{u}_H^n))\|_{L^2(\Omega)^{3\times3}} \leq \|\boldsymbol{\epsilon}(\boldsymbol{u}_H^n)\|_{L^2(\Omega)^{3\times3}}$ and $\|\pi_H(\boldsymbol{\epsilon}(\boldsymbol{u}_H^n))\|_{L^2(\Omega)^{3\times3}} \leq \|\boldsymbol{\epsilon}(\boldsymbol{u}_H^n)\|_{L^2(\Omega)^{3\times3}}$. Finally, the proposition 1.7.1 shows that $\|\boldsymbol{\epsilon}(\boldsymbol{u}_H^n)\|_{L^2(\Omega)^{3\times3}} < \infty$ for $\eta_s > 0$ and $\|\pi_H(\boldsymbol{\epsilon}(\boldsymbol{u}_H^n))\|_{L^2(\Omega)^{3\times3}} < \infty$ for $\eta_s = 0$.

Consider the quantity at time t^n, $n = 1, \ldots, N$

$$E^n = \int_\Omega \left(\rho|\boldsymbol{u}_H^n|^2 + \frac{\lambda}{2\eta_p}|\boldsymbol{\sigma}_H^n|^2 \right)\,\mathrm{d}\boldsymbol{x} + \sum_{i=1}^n \Delta t \int_\Omega \left(4\eta_s|\boldsymbol{\epsilon}(\boldsymbol{u}_H^i)|^2 + \frac{\alpha}{\eta_p}|\boldsymbol{\sigma}_H^i|^2 \right)\,\mathrm{d}\boldsymbol{x}, \quad (1.67)$$

with its initial value for $n = 0$

$$E^0 = \int_\Omega \left(\rho|\boldsymbol{u}_H^0|^2 + \frac{\lambda}{2\eta_p}|\boldsymbol{\sigma}_H^0|^2 \right)\,\mathrm{d}\boldsymbol{x}. \quad (1.68)$$

The inequality (1.55) in the proposition 1.7.1 shows that (1.67) is bounded by (1.68). Note that, for $n = 1, \ldots, N$:

$$\int_\Omega \frac{\lambda}{2\eta_p} \left| \frac{\boldsymbol{\sigma}_H^n - \boldsymbol{\sigma}_H^{n-1}}{\Delta t} \right|^2\,\mathrm{d}\boldsymbol{x} = \int_\Omega \boldsymbol{\epsilon}(\boldsymbol{u}_H^n) : \frac{\boldsymbol{\sigma}_H^n - \boldsymbol{\sigma}_H^{n-1}}{\Delta t}\,\mathrm{d}\boldsymbol{x} - \int_\Omega \frac{\alpha}{2\eta_p}\boldsymbol{\sigma}_H^n : \frac{\boldsymbol{\sigma}_H^n - \boldsymbol{\sigma}_H^{n-1}}{\Delta t}\,\mathrm{d}\boldsymbol{x}$$

$$\leq \|\boldsymbol{\epsilon}(\boldsymbol{u}_H^n)\|_{L^2(\Omega)^{3\times3}} \left\| \frac{\boldsymbol{\sigma}_H^n - \boldsymbol{\sigma}_H^{n-1}}{\Delta t} \right\|_{L^2(\Omega)^{3\times3}}$$

$$+ \frac{\alpha}{2\eta_p} \|\boldsymbol{\sigma}_H^n\|_{L^2(\Omega)^{3\times3}} \left\| \frac{\boldsymbol{\sigma}_H^n - \boldsymbol{\sigma}_H^{n-1}}{\Delta t} \right\|_{L^2(\Omega)^{3\times3}}.$$

Hence, we find that

$$\left\| \frac{\boldsymbol{\sigma}_H^n - \boldsymbol{\sigma}_H^{n-1}}{\Delta t} \right\|_{L^2(\Omega)^{3\times3}} \leq \|\boldsymbol{\epsilon}(\boldsymbol{u}_H^n)\|_{L^2(\Omega)^{3\times3}} + \frac{\alpha}{2\eta_p} \|\boldsymbol{\sigma}_H^n\|_{L^2(\Omega)^{3\times3}}.$$

Thus, the remaining terms in (1.60) without the stabilisation term $\sum_{K \in \mathcal{T}_H} \alpha_K \int_K |\nabla p_H^i|^2\,\mathrm{d}\boldsymbol{x}$ yields:

$$\Delta t^2 \sum_{i=1}^N \int_\Omega \left(\rho \left| \frac{\boldsymbol{u}_H^i - \boldsymbol{u}_H^{i-1}}{\Delta t} \right|^2 + \frac{\lambda}{2\eta_p} \left| \frac{\boldsymbol{\sigma}_H^i - \boldsymbol{\sigma}_H^{i-1}}{\Delta t} \right|^2 \right)\,\mathrm{d}\boldsymbol{x}$$

$$+ \Delta t^2 \sum_{i=1}^N \int_\Omega \left(\frac{4\eta_p}{\lambda + \alpha\Delta t}|\boldsymbol{\epsilon}(\boldsymbol{u}_H^i) - \pi_H(\boldsymbol{\epsilon}(\boldsymbol{u}_H^i))|^2 \right)\,\mathrm{d}\boldsymbol{x} = \mathcal{O}(\Delta t).$$

This means that, if we further assume that

$$\sum_{K \in \mathcal{T}_H} \alpha_K \int_K |\nabla p_H^i|^2 \, \mathrm{d}\boldsymbol{x} = \mathcal{O}(H^2), \quad i = 1, \ldots, N, \tag{1.69}$$

the equation (1.60) in the proof of the proposition shows that the energy E^n (1.67) converges in order one in time and space to the initial energy E^0 (1.68). Unfortunately, no evidence shows that (1.69) is true. If the gradient of the pressure can be bounded, this convergence result can be confirmed numerically, as presented in the next chapter.

2 Numerical experiments of incompressible viscoelastic free surface flows

In this chapter, numerical results obtained using the model described in chapter 1 are presented. First we present the advantages of the newly introduced implicit scheme over the EVSS scheme in a context of viscoelastic or elastic free surfaces flows. Finally the model for elastic flows with free surfaces is validated for several test cases. This allows to show the advantages of our model, mainly for large deformations and topology changes.

More precisely, we present a simulation in a full domain ($\varphi \equiv 1$) with an explicit solution to show the advantages of implicit scheme, then a Poiseuille flow simulation is presented in the next section. Three different problems have then been chosen for validation: a traction or tensile testing, an Euler-Bernoulli beam oscillations and a buckling experiment. Finally, the bouncing of an elastic material and a machining experiment is presented, the latter demonstrating large deformations of steel-simulated material and tearing piece. The numerical scheme is implemented in C++ and run on a system equipped with a 3.60GHz Intel Core i7-7820X processor and 128 GB RAM.

2.1 Validation of numerical scheme on exact solutions

In these two first numerical experiments, we focus on the comparison between the EVSS and the implicit schemes for both the simplified model (1.29) and the complete model (1.1).

2.1.1 Exact solution in a square domain for simplified model

In this problem, we address the simplified model (1.29). The cavity is fully filled ($\varphi = 1$), and the nonlinear terms $\nabla \boldsymbol{u}\boldsymbol{\sigma} + \boldsymbol{\sigma}\nabla \boldsymbol{u}^T$ as well as the convective terms are removed. Consider a rectangular domain in two dimensions $\Lambda = [0, 1]^2$ m^2 containing a viscoelastic fluid ($\alpha = 1$) or an elastic solid ($\alpha = 0$) with an initial velocity $\boldsymbol{u}_0$ and an initial extra-stress tensor $\boldsymbol{\sigma}_0$. The set of parameters for this simulation is $\lambda = 1$ s, $\rho = 1$ kg/m^3, $\eta_s = 0$ Pa s, $\eta_p = 10$ Pa s and $T = 0.112$ s. We perform the simulations with $\alpha \in \{0, 1\}$

respectively for elastic and viscoelastic simulations. Using such a set of parameters, initial and Dirichlet boundary conditions are chosen so that the exact solution in the viscoelastic case ($\alpha = 1$) is

$$\boldsymbol{u}(\boldsymbol{x}, t) = \begin{pmatrix} -\sin(\pi x)\cos(\pi y) \\ \cos(\pi x)\sin(\pi y) \end{pmatrix} e^{-t/2} \left(\cos\left(\frac{\omega t}{2}\right) + \sin\left(\frac{\omega t}{2}\right) / \omega \right),$$

$$p(\boldsymbol{x}, t) = 0,$$

$$\boldsymbol{\sigma}(\boldsymbol{x}, t) = \begin{pmatrix} -40\pi \cos(\pi x)\cos(\pi y) & 0 \\ 0 & 40\pi\cos(\pi x)\cos(\pi y) \end{pmatrix} e^{-t/2} \sin\left(\frac{\omega t}{2}\right) / \omega,$$

where $\boldsymbol{x} = (x, y)$ and $\omega = \sqrt{80\pi^2 - 1}$. Similarly, the exact solution in the elastic case ($\alpha = 0$) is:

$$\boldsymbol{u}(\boldsymbol{x}, t) = \begin{pmatrix} -\sin(\pi x)\cos(\pi y) \\ \cos(\pi x)\sin(\pi y) \end{pmatrix} \cos(\sqrt{20}\pi t),$$

$$p(\boldsymbol{x}, t) = 0,$$

$$\boldsymbol{\sigma}(\boldsymbol{x}, t) = \begin{pmatrix} -\sqrt{20}\pi \cos(\pi x)\cos(\pi y) & 0 \\ 0 & \sqrt{20}\pi \cos(\pi x)\cos(\pi y) \end{pmatrix} \sin(\sqrt{20}\pi t).$$

Denoting by H the maximum diameter of the FE mesh, the coarse discretisation corresponds to $H = 0.1$ m, $\Delta t = 0.0005$ s, the middle discretisation to $H = 0.05$ m, $\Delta t = 0.00025$ s, the fine discretisation to $H = 0.025$ m, $\Delta t = 0.000125$ s and even the finer one with $H = 0.0125$ m, $\Delta t = 0.0000625$ s. Since the prediction step is not included in this experiment, the parameter h corresponding to the size of the grid cells is not involved. Dirichlet boundary conditions apply on $\partial\Lambda$ for $\boldsymbol{u}$ and the pressure p is set to 0 on the boundary. The simulation results obtained with the EVSS scheme (1.63) and the implicit scheme (1.52) are displayed in Figure 2.1, where we compare exact and computed solutions along the diagonal $y = x$ at final time T. In Figure 2.2, convergence graphs are plotted by computing the L^2-error of the velocity $\boldsymbol{u}$ and extra-stress components $\boldsymbol{\sigma}_{xx}$ and $\boldsymbol{\sigma}_{yy}$ for both numerical methods and physical cases (viscoelastic fluid and elastic solid). An order one convergence can be observed for both schemes, although the implicit scheme is more precise.

Let us show numerically the results of the a priori estimates in chapter 1, i.e. the convergence of the discrete energy system (1.67)

$$E^n = \int_\Omega \left(\rho |\boldsymbol{u}_H^n|^2 + \frac{\lambda}{2\eta_p} |\boldsymbol{\sigma}_H^n|^2 \right) \, \mathrm{d}\boldsymbol{x} + \sum_{i=1}^n \Delta t \int_\Omega \left(4\eta_s |\boldsymbol{\epsilon}(\boldsymbol{u}_H^i)|^2 + \frac{\alpha}{\eta_p} |\boldsymbol{\sigma}_H^i|^2 \right) \, \mathrm{d}\boldsymbol{x} \quad (2.1)$$
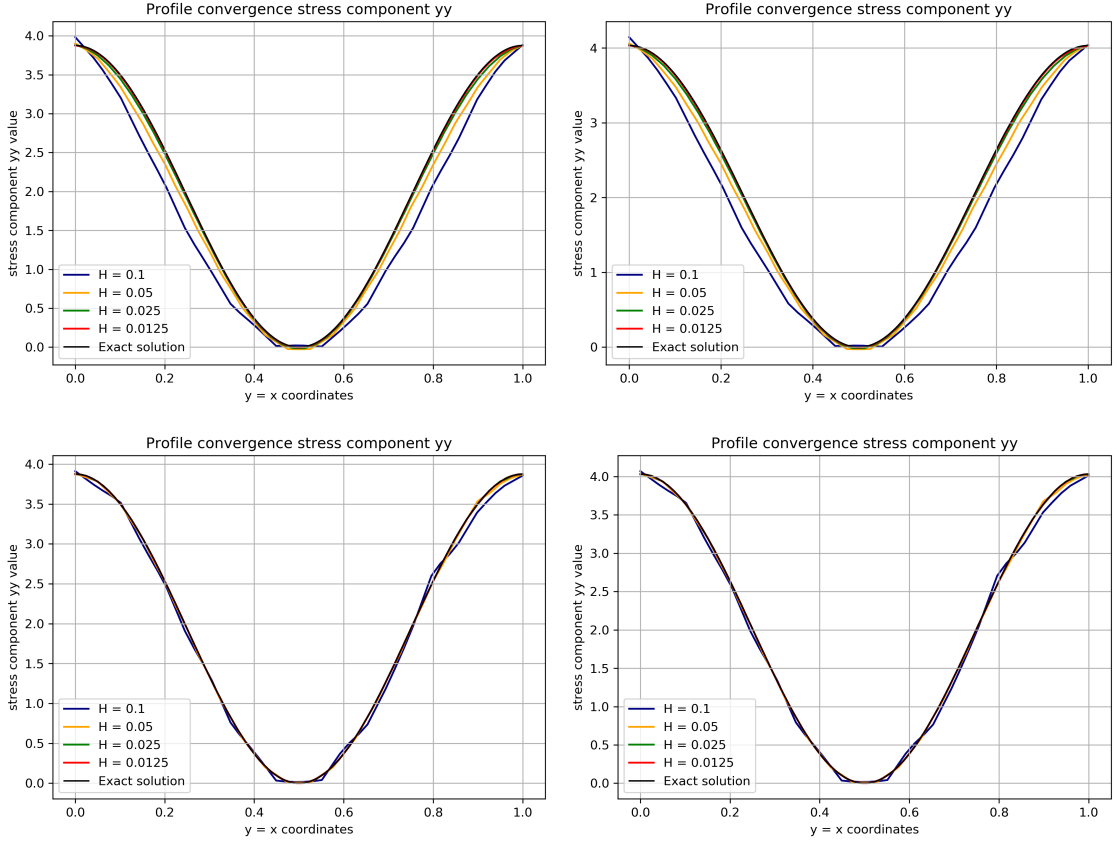
Figure 2.1 – Exact solution in a square domain. Simulation of a viscoelastic flow and an elastic solid deformation in a square domain. The coefficient $\sigma_{yy,H}$ of the stress tensor is shown along the diagonal of the domain for various mesh sizes at final time $T = 0.112$. Top: explicit EVSS scheme, Bottom: implicit scheme. Left: the viscoelastic experiment ($\alpha = 1$), Right: the elastic experiment ($\alpha = 0$).

to the initial system energy (1.68)

$$E^0 = \int_\Omega \left(\rho |\boldsymbol{u}_H^0|^2 + \frac{\lambda}{2\eta_p} |\boldsymbol{\sigma}_H^0|^2 \right) \, \mathrm{d}\boldsymbol{x}. \tag{2.2}$$

In Proposition 1.7.1, an order one convergence is proved in space and time of the discrete system energy (1.67). In Figure 2.3, the evolution of the discrete system energy E^n is presented for $0 \le t \le T$, where $T = 0.17$ s. The coarser parameters here are $H = 0.1$ m, $\Delta t = 0.01$ s. Convergence graph shows order one convergence of the error $\left| E^n - E^0 \right|$ for both viscoelastic ($\alpha = 1$) and elastic ($\alpha = 0$) cases. In the last case, since $\eta_s = 0$, the remaining terms are the kinetic $\rho \left\| \boldsymbol{u}_H^n \right\|_{L^2(\Omega)^3}$ and elastic $\frac{\lambda}{2\eta_p} \left\| \boldsymbol{\sigma}_H^n \right\|_{L^2(\Omega)^{3\times3}}$ energy. Hence, although the implicit scheme does not preserve the total kinetic and elastic energy, we have convergence to the initial energy.
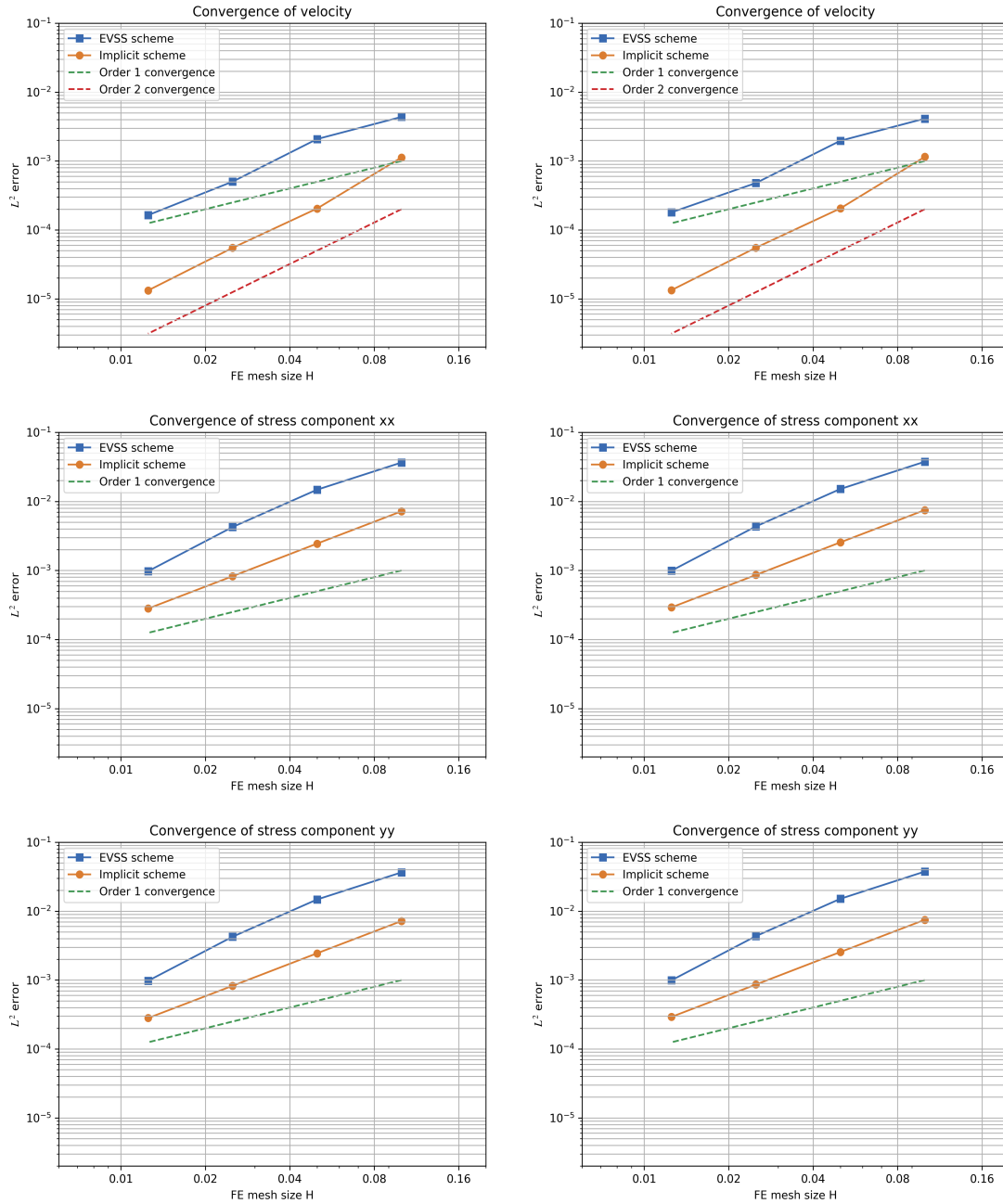
Figure 2.2 – Exact solution in a square domain. Convergence graphs. Top: L^2 norm of the error for velocity $\left\| \boldsymbol{u}(T) - \boldsymbol{u}_H^N \right\|_{L^2(\Omega)}$. Middle: L^2 norm of the error for extra-stress component xx $\left\| \boldsymbol{\sigma}_{xx}(T) - \boldsymbol{\sigma}_{xx,H}^N \right\|_{L^2(\Omega)}$. Bottom: L^2 norm of the error for extra-stress component yy $\left\| \boldsymbol{\sigma}_{yy}(T) - \boldsymbol{\sigma}_{yy,H}^N \right\|_{L^2(\Omega)}$. Left: the viscoelastic experiment ($\alpha = 1$), Right: the elastic experiment ($\alpha = 0$).
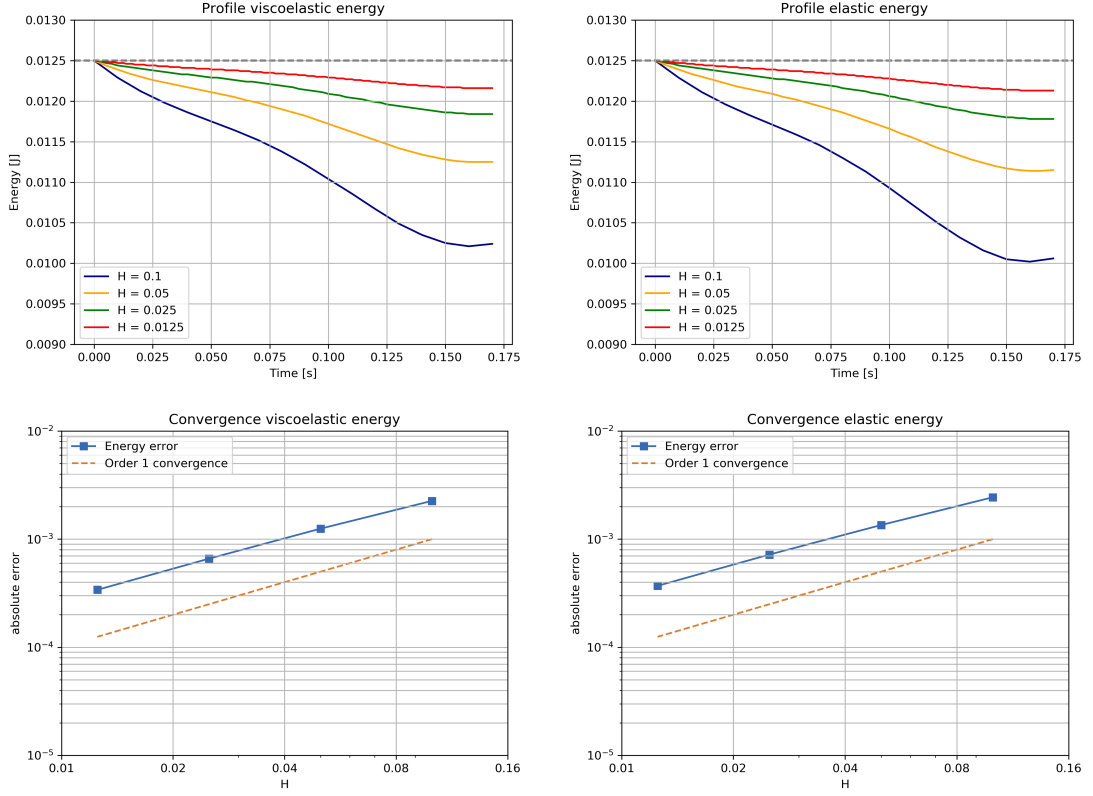
Figure 2.3 – Exact solution in a square domain. Convergence graphs of the discretized system energy (1.67) for implicit scheme. Top: evolution of (1.67) in time. Bottom: Absolute value of the error with initial value $|E^n - E^0|$. Left: viscoelastic experiment ($\alpha = 1$). Right: elastic experiment (right) ($\alpha = 0$).

2.1.2 Poiseuille flow for the free surface problem

The Poiseuille flow is a typical experiment for viscoelastic fluids [SJK$^+$22]. Here the goal is to compare both schemes (1.22) and (1.25) using the complete model, with a free surface, the nonlinear terms $\nabla \boldsymbol{u}\boldsymbol{\sigma} + \boldsymbol{\sigma}\nabla\boldsymbol{u}^T$ and transport terms. The same numerical experiment has been used in [BPL06] for validation of the model using the EVSS scheme, with values from [TMC$^+$02].

A rectangular domain $\Lambda = [0, L_1]$ m$\times[0, L_2]$ m$\times[0, L_3]$ m is considered, with $L_1 = 4$, $L_2 = 1$ and $L_3 = 0.2$. Starting from an empty domain, an inflow on the left boundary ($\{x = 0\}$) of a viscoelastic fluid fills the domain with the following values for the velocity field and the extra-stress tensor:

$$\boldsymbol{u}(x, y, z, t) = \begin{pmatrix} u_x \\ 0 \\ 0 \end{pmatrix} \quad \boldsymbol{\sigma}(x, y, z, t) = \begin{pmatrix} \sigma_{xx} & \sigma_{xy} & 0 \\ \sigma_{xy} & 0 & 0 \\ 0 & 0 & 0 \end{pmatrix},$$

with

$$u_x(y) = 6y(L_2 - y), \quad \sigma_{xx}(y) = 72\eta_s\lambda(2y - L_2)^2, \quad \sigma_{xy}(y) = -6\eta_p(2y - L_2).$$

No-slip boundary condition ($\boldsymbol{u} = \boldsymbol{0}$) are imposed at the top and bottom boundaries of Λ, free-slip ($\boldsymbol{u} \cdot \boldsymbol{n} = 0$) at front and back, and an outflow with an imposed velocity is enforced on the right end. The set of parameters for this simulation is $\rho = 1$ kg/m^3, $\eta_s = 0.5$ Pa s, $\eta_p = 0.5$ Pa s, $\lambda = 0.5$ s and $T = 9$ s. The viscoelastic flow is laminar, hence the velocity and extra-stress imposed at the inflow are recovered in the whole domain. The domain is eventually filled with fluid, as seen in Figure 2.4.
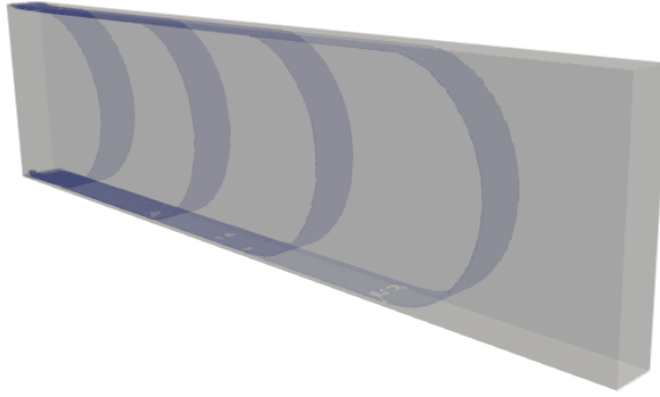
Figure 2.4 – Poiseuille flow. Evolution of the free surface in a numerical simulation of Poiseuille flow in an initially empty cavity at times $t = 0.8, 1.6, 2.4, 3.2$ s.

The CFL constant (1.15) in this numerical experiment can be quite large. Hence, we choose it to be equal to 6. Interpolation errors between the FE mesh are then lowered. Unconditional stability was proved for the implicit scheme when nonlinear terms are not considered. The value of λ is equal to 1. It corresponds to a Weissenberg number of $Wi = \lambda L_2/U = 1$, where U is the average velocity, as studied in [BPL06]. Convergence of the implicit scheme towards a steady state solution could not be obtained for a higher Weissenberg number.

Convergence with respect to $\Delta t, h$ and H is studied starting with a full domain to speed up the computations. The coarse setting corresponds to $H = 0.1$ m, $h = 0.025$ m and $\Delta t = 0.1$ s. Finer meshes are then obtained by dividing the discretisation parameters $\Delta t, h$ and H by two. In Figure 2.5 the order one convergence is recovered. Similarly as in the previous numerical experiment, the error of the implicit scheme is smaller than the one of the EVSS scheme. The profile of velocity and extra-stress components xx and xy on the line $(x, z) = (2, 0.1)$ are shown in Figure 2.6. Boundary layers can be observed

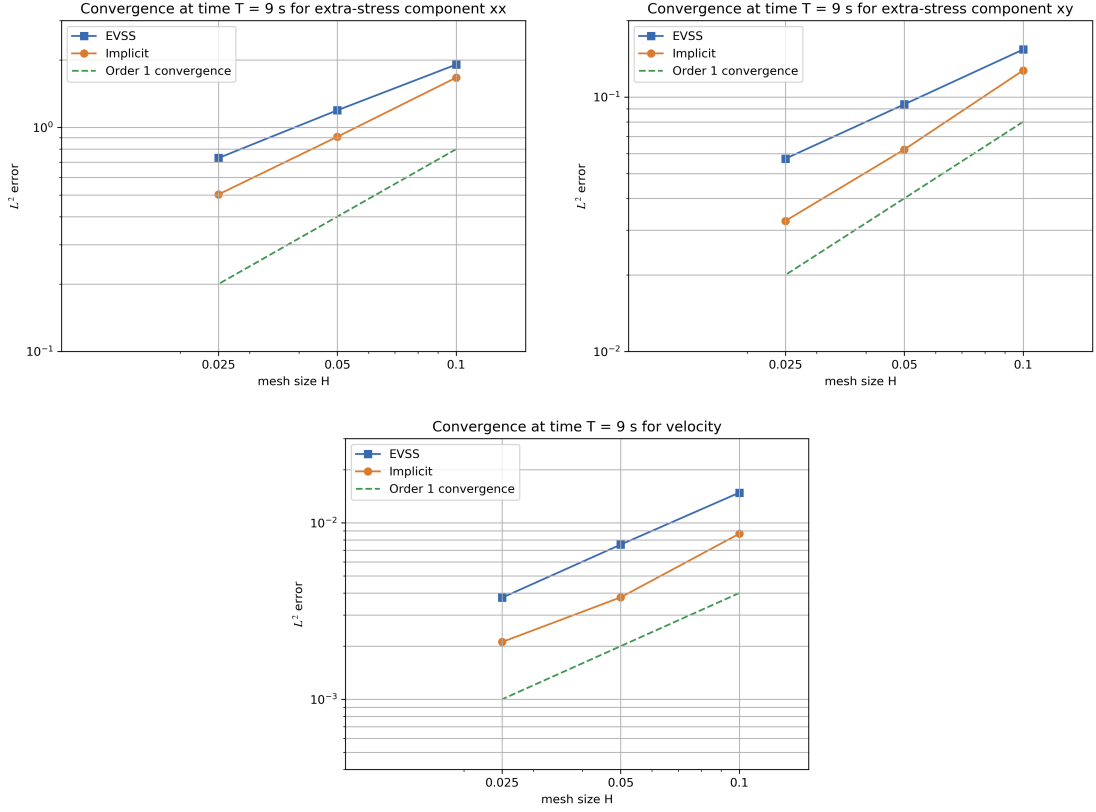for the extra-stress as already reported in [BPL06].

Figure 2.5 – Poiseuille flow. Convergence graphs for the stationary Poiseuille flow for EVSS and implicit schemes. Top: L^2 norm of the error for the extra-stress components $\left\|\boldsymbol{\sigma}_{xx}(T) - \boldsymbol{\sigma}_{xx,h}^N\right\|_{L^2(\Omega)}$ (left) and $\left\|\boldsymbol{\sigma}_{xy}(T) - \boldsymbol{\sigma}_{xy,h}^N\right\|_{L^2(\Omega)}$ (right). Bottom: L^2 norm of the error for the velocity $\left\|\boldsymbol{u}(T) - \boldsymbol{u}_h^N\right\|_{L^2(\Omega)}$.

In these numerical experiments, the order one convergence of the numerical scheme presented in chapter 1 has been verified for both viscoelastic flows ($\alpha = 1$) and elastic deformations ($\alpha = 0$). Furthermore, the newly introduced implicit time discretisation (1.28) proved to be more accurate than the EVSS scheme (1.27). The latter only proved to be more stable in the case of a high Weissenberg number.

2.2 Numerical simulation of more realistic test cases

In the next simulations, the model for solid elastic deformations ($\alpha = 0$ and $\eta_s = 0$) is studied on more realistic test cases. The implicit scheme (1.28) is applied in this section due to its improved accuracy.
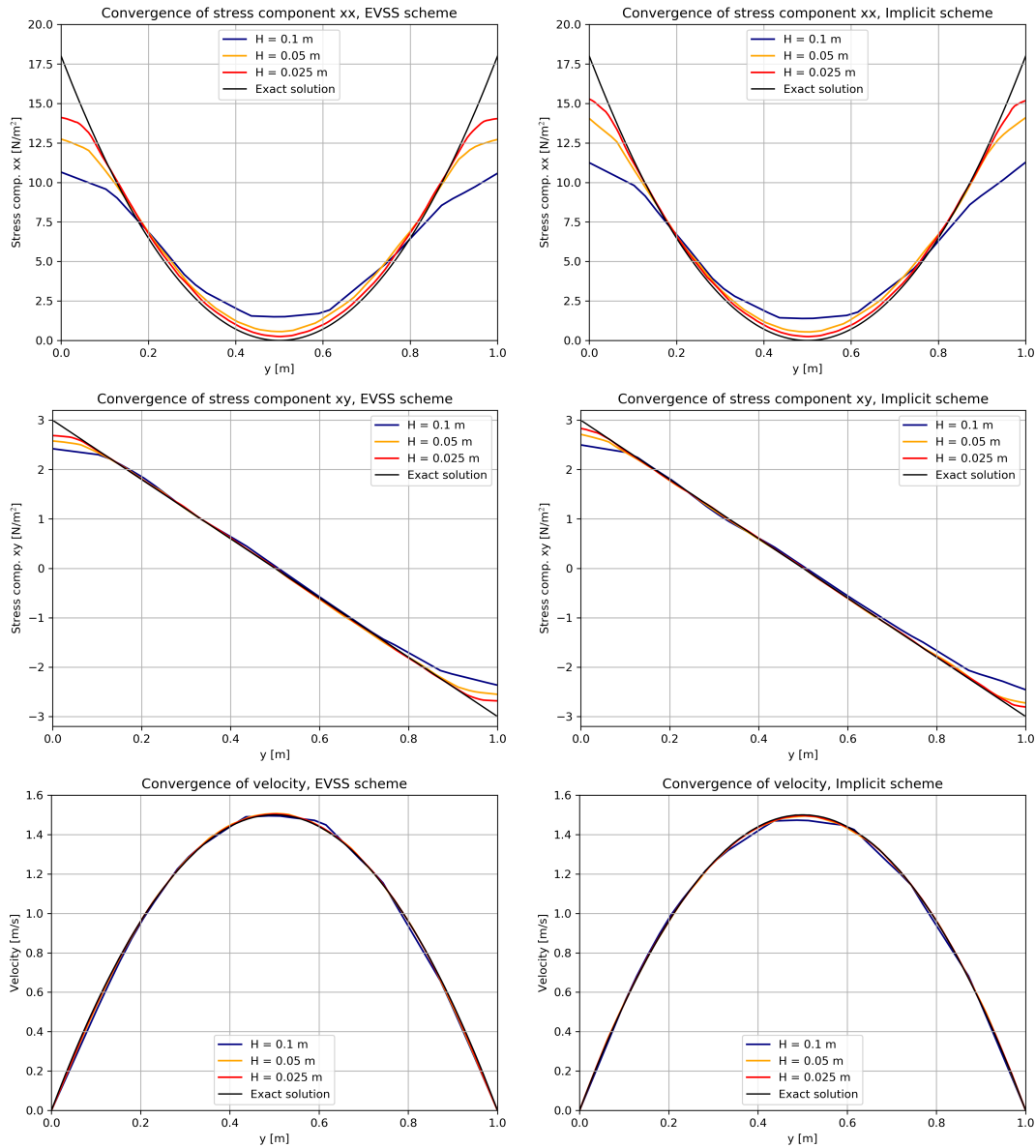
Figure 2.6 – Poiseuille flow. Convergence profile along the line $(x, z) = (2, 0.1)$ for EVSS scheme (left) and implicit scheme (right). Top: Extra-stress component $\boldsymbol{\sigma}_{xx}$. Middle: Extra-stress component $\boldsymbol{\sigma}_{xy}$. Bottom: Velocity $\boldsymbol{u}_x$.

2.2.1   Tensile test

Traction tests are used to determine the physical properties of a material (Young Modulus, elongation, failure point, ...) [JCEL07, JEL08, CC04, POV+12]. In a so-called tensile test, a specimen is subject to a longitudinal load and elongated until failure. The specimen is usually composed of two shoulders and a gage section, see Figure 2.7. A phenomenon called necking takes place, where the center cross section of the tensile

specimen shrinks before failing. We want to model a traction experiment and obtain the stress-strain curve of a given material. This curve yields the stress on the material with respect to the relative elongation imposed on the tensile specimen.

The data for the tensile specimens and stress-strain curves are extracted from [CC04]. It corresponds to a SAE 1045 steel material. We consider the two different shapes of tensile specimen in [CC04], as illustrated in Figure 2.7 (top row). The first specimen is cylindrical and the gage section has length 68 mm. The second specimen is rectangular (sheet sample) and has length 60 mm. More details on the dimensions of the tensile specimens are listed in [CC04]. The corresponding set of parameters are $\rho = 7800$ kg/m^3, $\eta_s = 0$ Pa s, $\eta_p = 3.7 \cdot 10^{10}$ Pa s, $\lambda = 0.5$ s and $\alpha = 0$, corresponding to a Young modulus of $E = 222000$ MPa. Hence, the goal is to show the accuracy and the convergence of our model using a stress strain curve. However, the Neo-Hookean model for incompressible material is only allows to describe the stress-strain curve of a given material for small strains. Thus, only the elastic property of the material can be approximated, not the plastic ones. The latter describes the state where the deformations are not revertible anymore, which is opposed to the elastic deformations. At this point, larger deformations are obtained for a smaller loading force, which flatten the stress-strain curve.
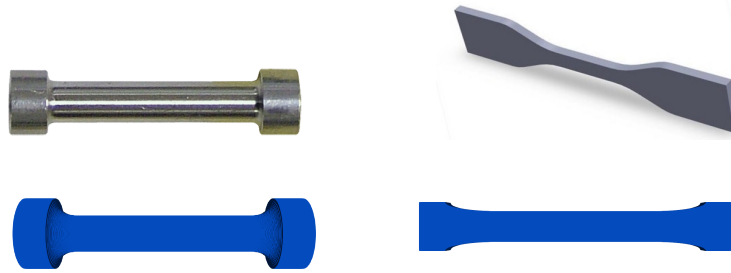

Figure 2.7 – Tensile test. Up: Tensile specimen example (sources: https://www.tecquipment.com/ and https://www.3dcontentcentral.com/). Bottom: Elastic domain Ω_0 on cells grid. Left: cylindrical section. Right: sheet sample.

The cavity Λ is a cylinder of radius 0.008 m and length 0.1 m for the cylindrical specimen. For the sheet sample, we use $\Lambda = [-0.013, 0.013]$ m$\times[-0.005, 0.005]$ m$\times[-0.066, 0.066]$ m. The initial elastic domain $\Omega_0 = \{\boldsymbol{x} \in \Lambda; \varphi(\boldsymbol{x}, 0) = 1\}$ is displayed in Figure 2.7 (bottom row). As in [BPL06], the axial force applied on the shoulders (both ends) of the specimen is simulated using an imposed velocity. Shoulders are moved vertically along the $\mathcal{O}z$ axis in opposite directions in order to stretch the specimen, at constant speed $\boldsymbol{u}_{\text{imp}} = (0, 0, \pm 0.5)$ mm/s. It is applied by imposing velocity at the nodes of the FE mesh inside the domain corresponding to shoulders locations. The convergence study consists in using three different mesh sizes and time steps. In the coarse settings, the time step is $\Delta t = 0.4$ s

with final time $T = 2$ s, the cell grid size is $h = 0.5$ mm and the average finite element diameter is $H = 2$ mm, aiming at a CFL number (1.15) on the cells grid of 0.5. The RAM memory and CPU time to compute the simulations are summarised in the following table:

	Cylindrical section			Sheet sample	
h [mm]	memory [GB]	CPU time [h]	h [mm]	memory [GB]	CPU time [h]
0.5	0.525	$2.11 \cdot 10^{-2}$	0.5	0.364	$8.32 \cdot 10^{-3}$
0.25	3.259	$3.03 \cdot 10^{-1}$	0.25	2.23	$8.25 \cdot 10^{-2}$
0.125	24.36	9.15	0.125	16.76	1.56

The memory usage and CPU running time are multiplied respectively by 8 and 16 when h, H and Δt are divided by 2, which are the expected proportions for 3D numerical simulations. Two gauge marks at the end of the tensile bodies monitor the strain during elongation. Here the total stress $\tilde{\boldsymbol{\sigma}} = -p\boldsymbol{I} + \boldsymbol{\sigma}$ is taken into account for the computations of the stress-strain curve, from the definition of an incompressible Neo-Hookean model [DR06, Hol02]. The results are shown in Figure 2.8. As predicted, incompressible Neo-Hookean model do not allow to follow the experimental stress-strain curve. Hence the necking observed at $t = 0.2$ s does not occur in the simulations. However, the elastic behaviour of the specimen is close to the experimental one. Since the parameter η_p is very big, the EVSS scheme applied to traction experiment hardly converges, see remark 1.5.2 in section 1.5. However the implicit scheme does not deal with large elongation and fails for $t > 2$ s.
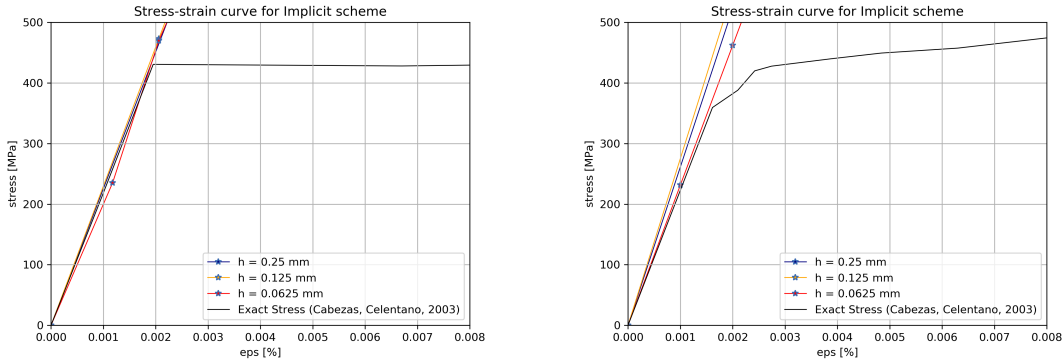

Figure 2.8 – Tensile test. Stress-strain curve for experimental data and convergence of implicit scheme. The horizontal axis eps[%] corresponds to the relative elongation $(L - L_0)/L$, where L_0 is the initial length of the gage section. Left: cylindrical specimen. Right: sheet sample. Zoom on elastic deformation.

The stress component $\boldsymbol{\sigma}_{zz}$ and pressure p are monitored in the center of the specimen and in Figure 2.9 the quantity $\tilde{\boldsymbol{\sigma}}_{zz} = -p + \boldsymbol{\sigma}_{zz}$ is displayed at a given time $t = 0.4$ s along the line $(x, y) = (0, 0)$, which correspond to axial symmetry line of the cylinder.

The profile for the sheet sample is taken along the line $(x, y) = (0, 0)$ on the longest symmetry axis. During the elastic stretch of the tensile experiment, we expect the stress to be equally spread along the two gauge marks of the tensile specimen. Oscillations can be observed for coarser meshes, when the complex behaviour of tensile test cannot be approximated with enough precision. The use of a finer mesh and the implicit scheme allow a better approximation.
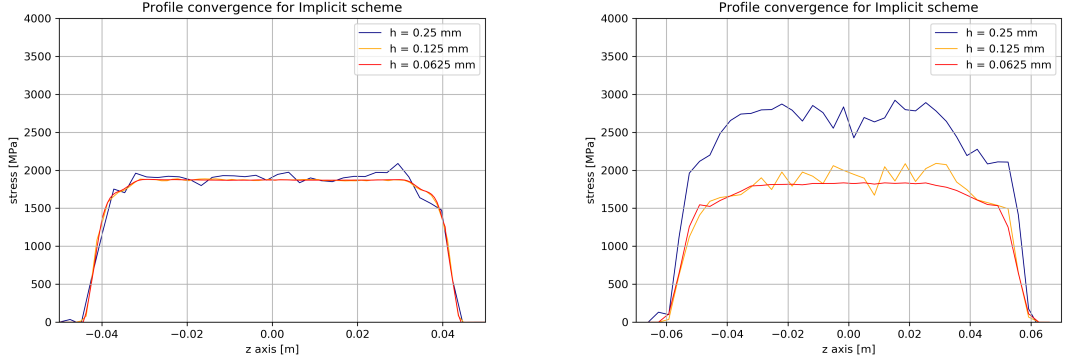

Figure 2.9 – Tensile test. Axial profile of stress tensor component $\boldsymbol{\sigma}_{zz}$. Left: cylindrical specimen. Right: sheet sample.

To compute the viscoplastic phenomenon, the incompressible Neo-Hookean model must be modified in order to take into account the nonlinear behaviour of the Cauchy stress tensor. Alternative models as St-Venant Kirchhoff model could be applied, but the compressible effect must be tackled, which is the topic of chapter 5. Nonlinear relations could be applied to stress-strain relation [Leb02, CC04, JEL08]. The modified Oldroyd-B equation (1.1d) for nonlinear strain yields

$$\frac{\partial}{\partial t}\boldsymbol{\sigma} + (\boldsymbol{u} \cdot \nabla)\boldsymbol{\sigma} - \nabla\boldsymbol{u}\boldsymbol{\sigma} - \boldsymbol{\sigma}\nabla\boldsymbol{u}^T = \frac{2\eta_p}{\lambda}\frac{\boldsymbol{\epsilon}(\boldsymbol{u})}{1 + A\,|\boldsymbol{\sigma}|^B}. \tag{2.3}$$

Using this formulation, the elastic property of the Neo-Hookean model is conserved for small strains, but allow to obtain smaller values of the extra-stress when the deformations become larger. An additional nonlinear relation is introduced by taking the norm of the extra-stress tensor to the power B, thus this term is taken explicitly in the time discretisation. In Figure 2.10, the stress-strain curves for $A = 10^{-7}$ and two different value of B in equation 2.3 are displayed. Visual convergence to the exact stress-strain curve is observed for $B = 1.4$.

In order to test large deformations for the tensile test, a rubber material is used instead of steel. In [POV^{+}12] a stretch ratio L/L_0 of 2.5 is considered, while the deformation of steel does not exceed 1.1, showing the difference between ductile and brittle material as explained in the introduction. The tensile specimen used in [POV^{+}12] is replicated
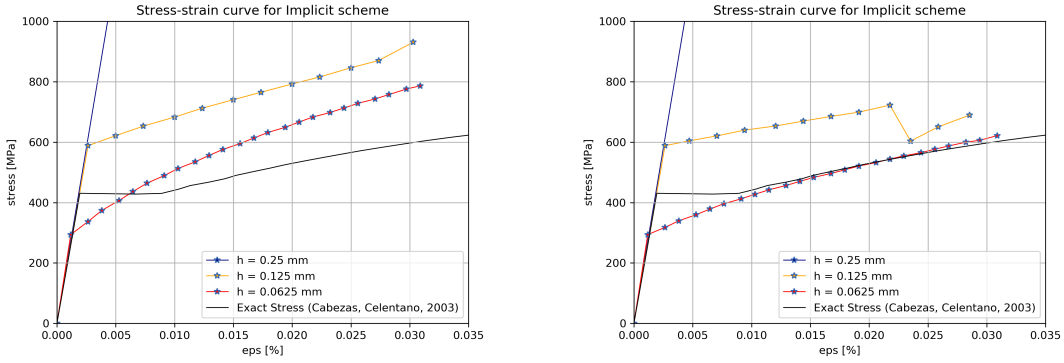
Figure 2.10 – Tensile test. Stress-strain curve for alternative constitutive equation for $A = 10^{-7}$. Left: $B = 1.35$. Right: $B = 1.4$.

here and the results are shown in Figure 2.11. The used parameters are $\rho = 940$ kg/m^3, $\eta_s = 0$ Pa s, $\eta_p = 2 \cdot 10^5$ Pa s, $\lambda = 0.5$ s and $\alpha = 0$, corresponding to a Young modulus of $E = 1.2$ MPa. One simulation has been run with $\Delta t = 0.8$ s with final time $T = 12$ s, the cell grid size is $h = 0.6$mm and FE mesh diameter is $H = 4$ mm. The velocity imposed is not linear anymore in order to obtain a constant strain rate in time [POV$^+$12] so $\boldsymbol{u}_{\text{imp}} = (0, 0, \pm \alpha L_0 e^{\alpha t})$ m/s, with $\alpha = 0.01$ and L_0 being the initial length of the tensile specimen. The nonlinear terms of the simulation lead to unstability of the numerical scheme and thus are removed to compute the simulation. It allows the tensile to obtain an elongation ratio of near 1.3, see Figure 2.11.
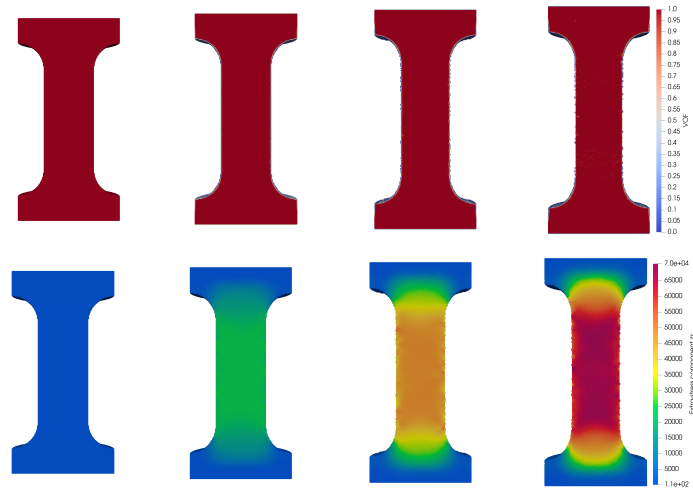

Figure 2.11 – Tensile test. Rubber material traction profile. Top: the characteristic function φ. Bottom: the extra-stress component $\boldsymbol{\sigma}_{zz}$. From left to right: $t = 0, 4, 8, 12$ s.

2.2.2 Euler-Bernoulli beam

The goal is now to achieve beam deformations and validate results using the Euler-Bernoulli beam theory [BC09, JM13, BL19, TBMG20]. A beam is defined as a structure with a length that is proportionally much larger than the size of its cross section. The assumption of the Euler-Bernoulli beam theory is that, when bending moment is applied, the cross-sectional area is infinitely rigid, thus not deformable. Furthermore the cross-sectional area remains normal to the deformed axis of the beam, as shown in Figure 2.12.
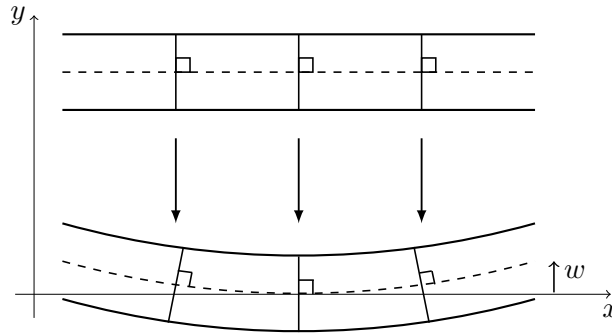

Figure 2.12 – Euler-Bernoulli beam assumption. Small displacement are allowed and the cross-section area is not deformed. The cross-section remains normal to the deformed axis of the beam.

From these assumptions, we compute a set of equations for the beam for a set of boundary conditions. The complete stationary sets of equations can be found in [Pas08]. Let $w(x,t)$ be the deformation in the Oy axis of a given point x in the Ox axis on the beam at time t, see Figure 2.12. The equation reads

$$\frac{\partial^2 w}{\partial t^2} + \frac{EI}{\rho A}\frac{\partial^4 w}{\partial x^4} = f, \tag{2.4}$$

where f denotes external forces. Here E is the Young modulus of the beam material, I is the section area momentum, ρ is the density and A is the section area. In the case of a cantilever beam, the left-hand side is fixed and the right-hand side is free. Thus, the initial and boundary conditions are:

$$\omega(0,t) = 0, \quad \frac{\partial w}{\partial x}(0,t) = 0, \quad \frac{\partial^2 w}{\partial x^2}(L,t) = 0, \quad \frac{\partial^3 w}{\partial x^3}(L,t) = 0,$$
$$w(x,0) = 0, \qquad \frac{\partial w}{\partial t}(x,0) = v_0(x). \tag{2.5}$$

Using the change of variable $w(x,t) = X(x)T(t)$ and $f = 0$ we obtain the following set

61

of equations:

$$T''(t) + \omega^2 T(t) = 0, \tag{2.6}$$

$$X^{(4)}(x) - \beta^4 X(x) = 0, \tag{2.7}$$

where $\beta^4 = \frac{\rho A}{EI} \omega^2$ and ω represents the different frequencies of the beam deformations. We obtain

$$T(t) = a\sin(\omega t) + b\cos(\omega t), \tag{2.8}$$

$$X(x) = C_1 \sin(\beta x) + C_2 \cos(\beta x) + C_3 \sinh(\beta x) + C_4 \cosh(\beta x), \tag{2.9}$$

where the constants are determined from boundary conditions. More precisely the following system is obtained:

$$\begin{pmatrix} 0 & 1 & 0 & 1 \\ \beta & 0 & \beta & 0 \\ -\beta^2 \sin(\beta L) & -\beta^2 \cos(\beta L) & \beta^2 \sinh(\beta L) & \beta^2 \cosh(\beta L) \\ -\beta^3 \cos(\beta L) & \beta^3 \sin(\beta L) & \beta^3 \cosh(\beta L) & \beta^3 \sinh(\beta L) \end{pmatrix} \begin{pmatrix} C_1 \\ C_2 \\ C_3 \\ C_4 \end{pmatrix} = \begin{pmatrix} 0 \\ 0 \\ 0 \\ 0 \end{pmatrix}.$$

A non-trivial solution is obtained when the kernel dimension is non-zero. We recover the oscillations frequencies of the beam for $n > 0$:

$$\beta_n = \frac{(2n-1)\pi}{2L}, \quad \omega_n = \sqrt{\frac{EI}{\rho A}} \beta_n^2 = \sqrt{\frac{EI}{\rho A}} \left(\frac{(2n-1)\pi}{2L} \right)^2.$$

From (2.5) we recover the following solution:

$$w(x,t) = \sum_{n=1}^{+\infty} c_n \sin(\omega_n t) \phi_n(x), \tag{2.10}$$

where

$$\phi_n(x) = (\cosh(\beta_n x) - \cos(\beta_n x)) - \sigma_n(\sinh(\beta_n x) - \sin(\beta_n x)),$$

with

$$\sigma_n = \frac{\sinh(\beta_n L) - \sin(\beta_n L)}{\cos(\beta_n L) + \cosh(\beta_n L)}.$$

The parameters c_n are the Fourier coefficients for the function v_0 in the orthonormal basis $\{\phi_n\}$. In our experiment we chose $v_0 = C\phi_1$, $C \in \mathbb{R}$. This allows the beam to oscillate only in its principal frequency and to recover a simple formula for the final solution, thanks to Fourier theory. The solution hence becomes:

$$w(x,t) = (C/\omega_1)\sin(\omega_1 t)\phi_1(x),$$

and is illustrated in Figure 2.13. It is called a cantilever beam and we use no-slip boundary conditions on the left part of the cavity. No force is applied but an initial

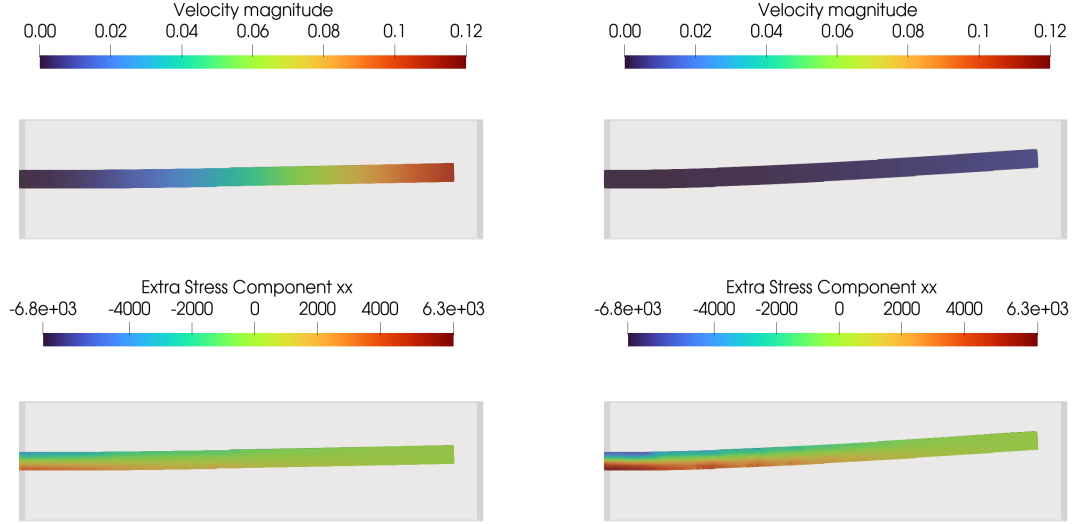velocity $v_0(x) = 0.06 \cdot \phi_1(x)$ gives the impulsion for the deformation of the elastic solid.

Figure 2.13 – Euler-Bernoulli cantilever beam dynamic. Left: Time $t = 0.1$ s. Right: Time $t = 0.3$ s. Top: Velocity magnitude $\|\boldsymbol{u}\|$. Bottom: Extra-stress coefficient $\boldsymbol{\sigma}_{xx}$.

Simulations were done for two different sizes of cross-section length $r = 0.06$ m and $r = 0.12$ m in a cavity $\Lambda = [0, 1.6]$ m$\times[0, 0.6]$ m. The simulations are computed in pseudo 2D instead of 2D, in the sense that the variables are constant along the third dimension. The cavity becomes $\Lambda = [0, 1.6]$ m$\times[0, 0.6]$ m$\times[0, 0.1]$ m, the initial velocity in the $\mathcal{O}z$ component is zero and free-slip boundary conditions are applied on the domain boundary $\partial\Lambda$. This difference in computation is made easier by the cfsFlow software and only slightly impact the computational time without impacting the simulation precision. Only the implicit scheme has been applied for these simulations. Three meshes and times steps have been used to prove convergence to the exact solution. In the coarse settings, the time step is $\Delta t = 0.075$ s with final time $T = 1.5$ s, the cell grid size is $h = 6.25$ mm and the average finite element diameter is $H = 20$ mm. The finer settings are obtained by dividing the discretisation parameters by two. The RAM memory and CPU time to compute the simulations are summarised in the following table:

	$r = 0.06$ m			$r = 0.12$ m	
h [mm]	memory [GB]	CPU time [h]	h [mm]	memory [GB]	CPU time [h]
6.25	0.29	0.013	6.25	0.46	0.025
3.125	1.23	0.119	3.125	2.37	0.254
1.562	8.1	1.37	1.562	16.42	3.86

In Figure 2.14, convergence can be observed with respect to the exact solution computed with the Euler-Bernoulli beam theory. A discrepancy between the numerical results

and the Euler-Bernoulli beam model can be observed for the larger value of r, since the Euler-Bernoulli beam theory can no longer be applied. However, the visual convergence is still observed. When the beam velocity reaches its maximum deformation and the velocity is close to zero, the CFL number (1.15) becomes small and interpolation errors are observed. Thus the time step cannot be taken arbitrarily small.
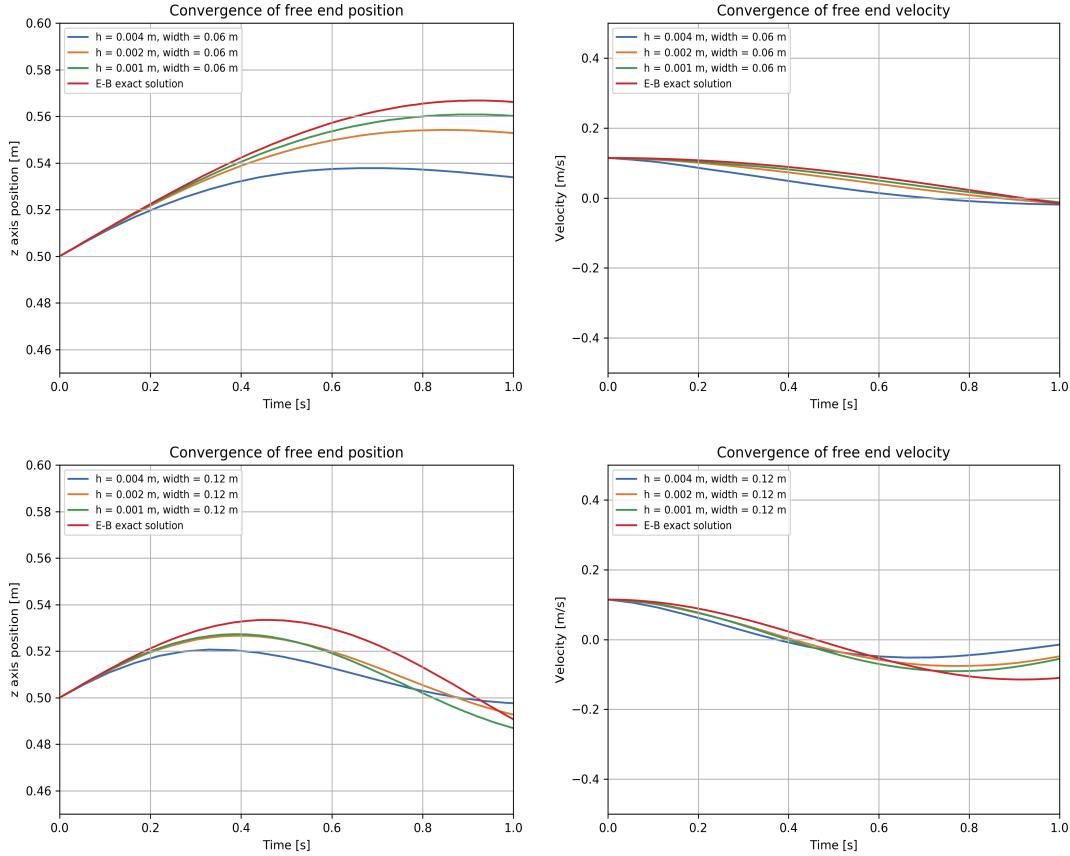
Figure 2.14 – Euler-Bernoulli beam. The numerical approximation is monitored at the free-end of the beam. Convergence of the monitored point compared with an exact solution computed with Euler-Bernoulli beam theory. Top: $r = 0.06$ m. Bottom: $r = 0.12$ m. Left: Position $w(L, t)$. Right: Velocity $\frac{\partial}{\partial t} w(L, t)$.

2.2.3 Buckling experiment

Our goal is now to reproduce a buckling phenomena, that is the deformation of an axially compressed bar when the exerted force P reaches a certain threshold. It is determined by the so-called Euler buckling load, found out by Euler in 1744:

$$P = \frac{\pi^2 EI}{(kL)^2},\tag{2.11}$$

where E and I are the Young modulus and section area moment as defined previously, L is the length of the bar and k is a parameter depending on the number of degrees of freedom of the end point where the load is applied. For instance, $k = 1$ implies that the extremities are fixed but the angular moment is free ($\omega(0, t) = 0$, $\frac{\partial w}{\partial x}(0, t)$ free) and $k = 0.5$ when both degrees of freedom are fixed ($\omega(0, t) = 0$, $\frac{\partial w}{\partial x}(0, t) = 0$). The full derivation of the Euler buckling load (2.11) can be found in [BL19].

The goal of this experiment is to estimate the Euler buckling load threshold. Two different radii for the cross section $r = \{2, 4\}$ mm are used in order to modify the section moment I (see equation (2.4)). The length of the gage section of the initial elastic domains is 200 mm aand re illustrated in Figure 2.15. The computational domain Λ is a cylinder of radius 30 mm and length 240 mm.
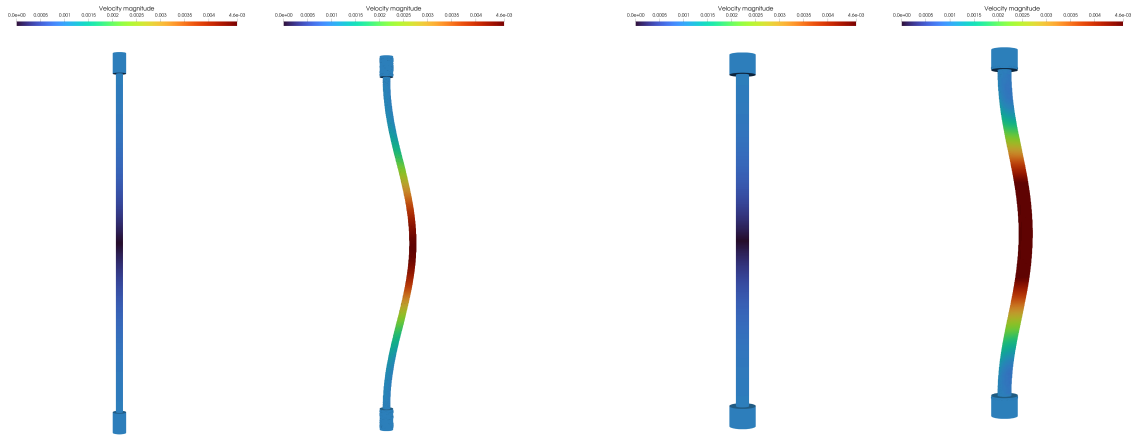
Figure 2.15 – Buckling experiment. Initial ($t = 0$) position and position after buckling. Left: small radius $r = 2$ mm at time $t = 0.5$ s. Right: large radius $r = 4$ mm at time $t = 1$ s.

As for the traction experiment, the force applied on the shoulders (both ends) of the specimen is simulated using imposed velocity. Only the implicit scheme was applied for this experiment as for the Euler-Bernoulli beam experiment. Shoulders are moved vertically on Oz axis at constant speed $\boldsymbol{u}_{\mathrm{imp}} = (0, 0, -1)$ mm/s for the top shoulder, applied by imposing velocity as previously. The convergence study consists in three different mesh sizes and time steps. In the coarser case, the time step is $\Delta t = 0.4$ s with final time $T = 2$ s, the cell grid size is $h = 0.8$ mm and the minimum element diameter is $H = 2.5$ mm, thus the CFL constant (1.15) is equal to 0.5. The RAM memory and CPU time to compute the simulations are summarised in the following table:

r = 2 mm			r = 4 mm		
h [mm]	memory [GB]	CPU time [h]	h [mm]	memory [GB]	CPU time [h]
0.8	0.92	0.007	0.8	0.94	0.008
0.4	7.06	0.056	0.4	7.15	0.08
0.2	55.64	0.7	0.2	56.42	1.2

In order to capture the moment when the bar buckles, the variables values are monitored at the bar center $(0, 0, 0)$. In Figure 2.16 the stress and pressure are visualised as in the tensile test experiment and the quantity $\tilde{\boldsymbol{\sigma}}_{zz} = -p + \boldsymbol{\sigma}_{zz}$ is represented with respect to time. The buckling moment is observed when the stress $\tilde{\boldsymbol{\sigma}}_{zz}$ suddenly decreases. The relative error with the theoretical value (2.11) is reported in Figure 2.17. The moment when the bar buckles is a phenomena happening in an extremely small amount of time. The time step Δt of the simulation was taken as small as possible, but the CFL number must be kept larger than 0.2 to avoid excessive interpolation errors.
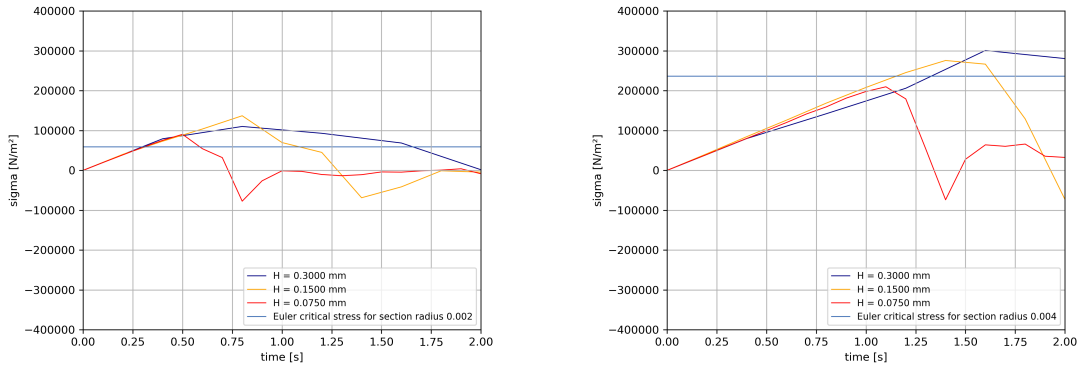
Figure 2.16 – Buckling experiment. Stress with respect to time. Buckling occurs when the stress suddenly decreases. The theoretical Euler buckling load is displayed as a horizontal threshold. Left: small radius $r = 2$ mm. Right: large radius $r = 4$ mm.

These last numerical experiments are based on engineering test cases and allow to validate numerically our numerical scheme using the implicit scheme.

2.3 Signorini boundary conditions and machining experiments

In the two last numerical experiments of this chapter, the potential of our model is exploited. Signorini boundary conditions are imposed instead of free slip boundary conditions in order to make it leave the boundary. Then, we put the emphasis on the potential of the numerical model and present a machining experiment.
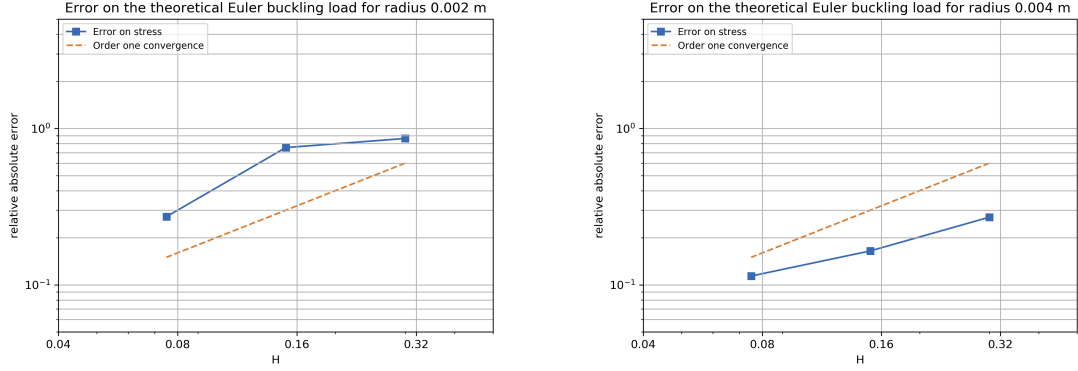
Figure 2.17 – Buckling experiment. Relative error of the stress on the column at buckling with the Euler buckling load with order one convergence curve. Left: small radius $r = 2$ mm. Right: large radius $r = 4$ mm.

2.3.1 Bouncing elastic ball

In this experiment, a ball-shaped elastic solid ($\alpha = 0, \eta_s = 0$) is dropped in a cavity with a given initial velocity $\boldsymbol{u}_0$ and extra-stress tensor $\boldsymbol{\sigma}_0$. It enters in contact with the bottom of the cavity before bouncing back upwards. For this experiment, we need to define Signorini boundary conditions [Sig33]. They define a set of boundary conditions for an elastic solid to collide with a frictionless rigid surface. Let us denote by $\boldsymbol{n}$ the unit outer normal of $\partial\Lambda$ and $\boldsymbol{t}$ are all unitary vector orthogonal to $\boldsymbol{n}$. The normal and tangent force are respectively defined as $\boldsymbol{T_n} = (-p\boldsymbol{n} + (2\eta_s\boldsymbol{\epsilon}(\boldsymbol{u}) + \boldsymbol{\sigma})\boldsymbol{n}) \cdot \boldsymbol{n}$ and $\boldsymbol{T_t} = (-p\boldsymbol{n} + (2\eta_s\boldsymbol{\epsilon}(\boldsymbol{u}) + \boldsymbol{\sigma})\boldsymbol{n}) \cdot \boldsymbol{t}$. The Signorini boundary conditions read

$$\boldsymbol{T_t} = 0, \quad \boldsymbol{T_n} \leq 0, \quad \boldsymbol{u} \cdot \boldsymbol{n} \leq 0, \quad (\boldsymbol{u} \cdot \boldsymbol{n})\boldsymbol{T_n} = 0. \tag{2.12}$$

Details can be found in [KO88, BBRS05], where a variational Lagrangian formulation of the problem has been investigated. A different approach is taken here in order to take into account the Eulerian formulation of the problem. The goal is to allow the material to detach from the boundary in order to bounce upwards.

The algorithm goes as follows: after the prediction step of the splitting algorithm, the functions $\varphi^n, \boldsymbol{u}_H^{n-\frac{1}{2}}, \boldsymbol{\sigma}_H^{n-\frac{1}{2}}$ have been computed on the structured grid and interpolated on the FE mesh. We compute a continuous piecewise linear FE approximation $\boldsymbol{T}_{\boldsymbol{n},H}^{n-1}$ of $\boldsymbol{T_n}$ at intermediate time step $n - \frac{1}{2}$ on the boundary of the domain. In this purpose, we compute $\boldsymbol{D}_H^{n-\frac{1}{2}} = \pi_H(\boldsymbol{\epsilon}(\boldsymbol{u}_H^{n-\frac{1}{2}}))$ on the space of piecewise $\mathbb{P}^1$ finite element, using (1.27a). Hence we obtain $\boldsymbol{T}_H^{n-1} = 2\eta_s\boldsymbol{D}_H^{n-\frac{1}{2}} + \boldsymbol{\sigma}_H^{n-\frac{1}{2}} - p_H^{n-1}\boldsymbol{I}$ and $\boldsymbol{T}_{\boldsymbol{n},H}^{n-1} = (\boldsymbol{T}_H^{n-1}\boldsymbol{n}) \cdot \boldsymbol{n}$ for each vertex on the boundary of the domain. Then, on each vertex of the mesh

- If $\boldsymbol{T}_{\boldsymbol{n},H}^{n-1} < 0$, then according to (2.12), $\boldsymbol{u}_H^n \cdot \boldsymbol{n}$ must be set to 0.

- Else, the normal stress $\boldsymbol{T}_{\boldsymbol{n},H}^{n} = (2\eta_s\boldsymbol{\epsilon}(\boldsymbol{u}_H^n) + \boldsymbol{\sigma}_H^n)\boldsymbol{n} - p\boldsymbol{n}$ will be set to $\boldsymbol{0}$ in the correction step, so that the total force is $\boldsymbol{0}$.

The elastic ball is placed in a cavity $\Lambda = [0, 0.4]^2 \text{ m}^2 \times [0, 0.3]$ m, with the mass center situated at $(0.2, 0.2, 0.15)$ m. The ball has radius $r = 0.08$ m is initialized with velocity $\boldsymbol{u}_0 = (0, 0, -0.1)$ m/s, extra-stress $\boldsymbol{\sigma}_0 = \boldsymbol{0}$. It is only subjected to gravity forces. The parameters are $\rho = 1100 \text{ kg}/m^3$, $\lambda = 10^{-2}$s and $\eta_p = 10^2$ Pa s. Three sets of discretisation parameters is used. In the coarse case, the time step is $\Delta t = 0.024$ s with final time $T = 0.4$ s, the cell grid size is $h = 0.004$ m and the FE mesh size is $H = 0.02$ m. The elastic material deforms itself when hitting the bottom of the cavity and its elastic energy is transformed back into upgoing velocity when moving back up. In Figure 2.18, the evolution of the barycenter of the characteristic function φ in time is presented for both numerical schemes. We can observe that both EVSS and implicit schemes provide us similar results. In Figure 2.19, screenshots of the elastic material evolution is shown using the implicit scheme.
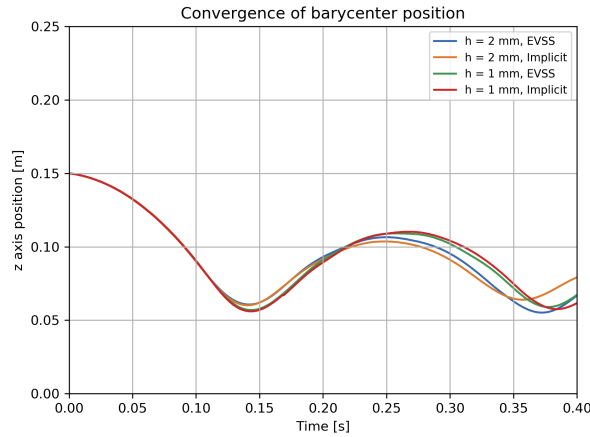
Figure 2.18 – Bouncing elastic ball. Convergence of mass center position for the EVSS and implicit schemes.

In Figure 2.20, the algorithm is illustrated for two different time steps. The nodes where the normal component of the force is negative are displayed. The velocity has now a negative normal component and the ball leaves the boundary on the next time step. In Figure 2.21, the values of the pressure and the normal component of the body surface force $\boldsymbol{T}_{H,\boldsymbol{n}}^{n}$ have been monitored through time on the boundary at position $(0.2, 0.2, 0)$. Their value are zero before the elastic solid is in contact with the bottom surface. Instabilities arise when the ball touches and leaves the bottom when using the EVSS, which shows another advantages of the implicit scheme.
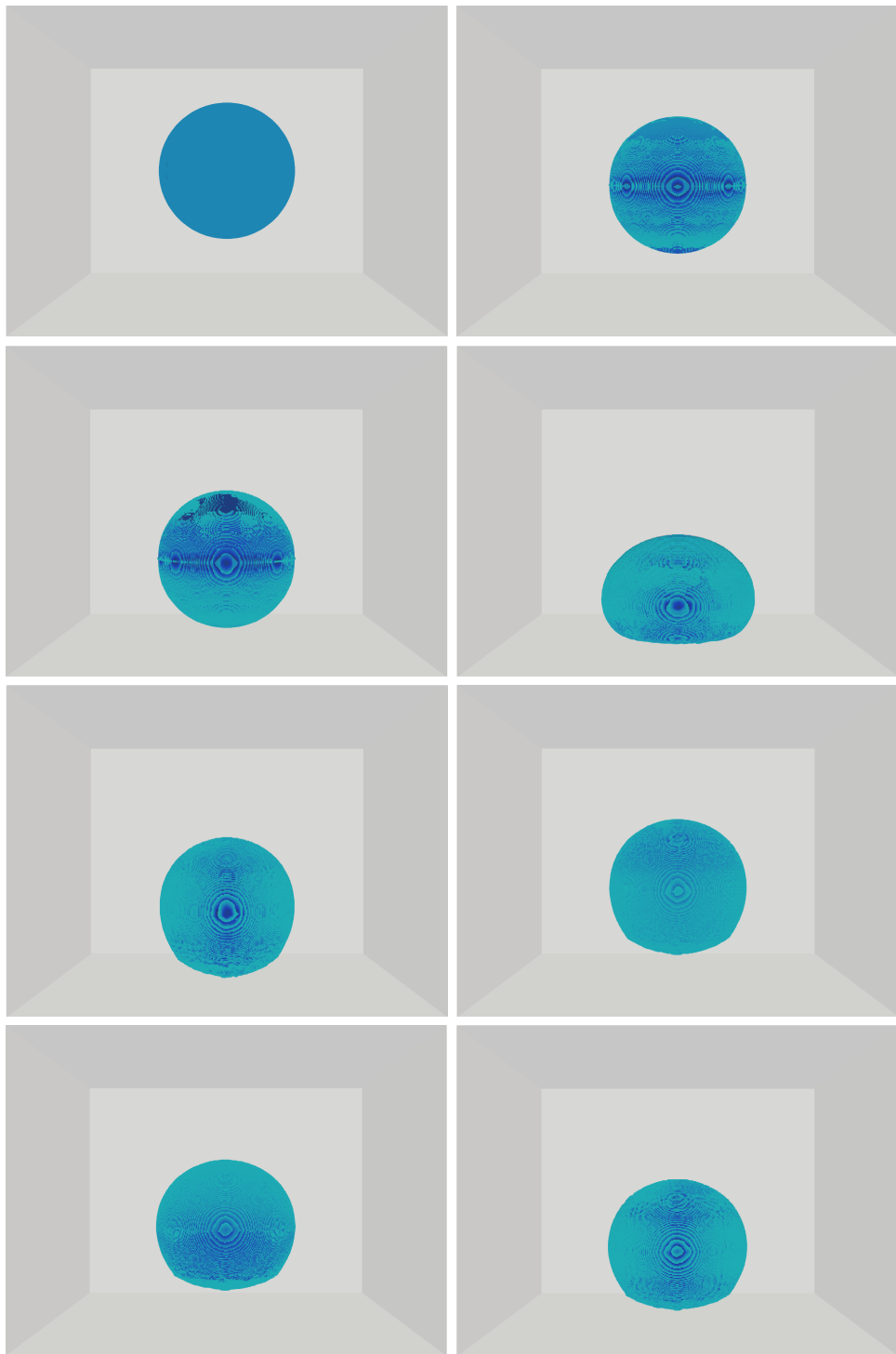
Figure 2.19 – Bouncing elastic ball. Simulation of an incompressible neo-Hookean elastic ball of radius $r = 0.08$ m hitting the bottom of a box, only subject to gravitational force. Signorini boundary conditions are used and the ball bounces against the surface. From left to right, top to bottom: $t = 0, 0.048, 0.096, 0.144, 0.192, 0.24, 0.288, 0.336$ s.
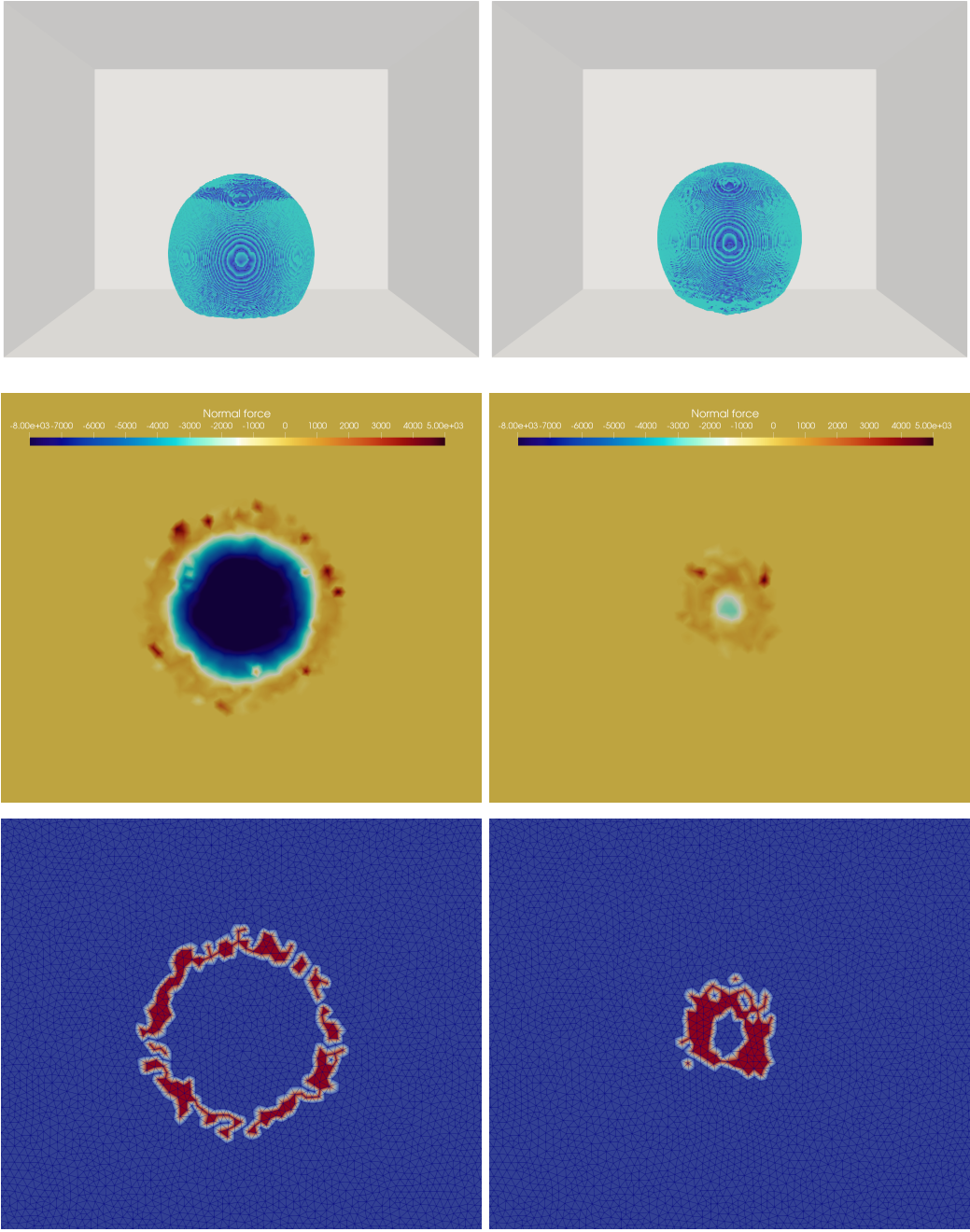
Figure 2.20 – Bouncing elastic ball. Simulation of an incompressible neo-Hookean elastic ball of radius $r = 0.08$ m hitting the bottom of a box, only subject to gravitational force. Signorini boundary conditions are used. The ball is pushed upwards. Top: Snapshots of characteristic function ($\varphi = 1$ in the blue region). Middle: normal force at the bottom. Bottom: nodes where velocity has a negative normal component. Left: $t = 0.168$ s. Right: $t = 0.192$ s.
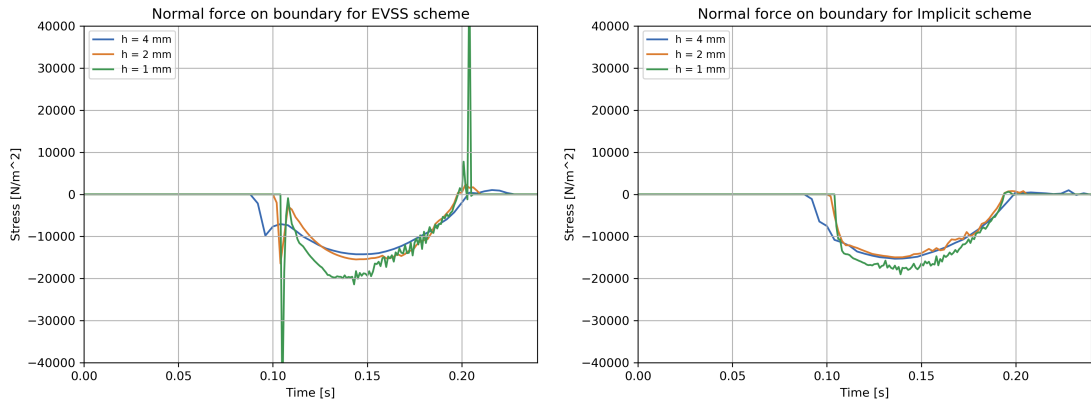
Figure 2.21 – Bouncing elastic ball. Evolution of the force on boundary at position $(0.2, 0.2, 0)$ for three different mesh sizes. Left: EVSS scheme. Right: implicit scheme.

2.3.2 Machining simulation

Finally a steel machining type experiment is presented. The goal is to cut into a piece of steel to give it a specific shape. In Arrazola et.al [AÖ10], a finite element simulation of chip formation process is presented, see Figure 2.22, where the model is discretised using an Arbitrary-Lagrangian-Eulerian method. We would like to reproduce such machining simulations using our own model, which allows large deformations and topology.
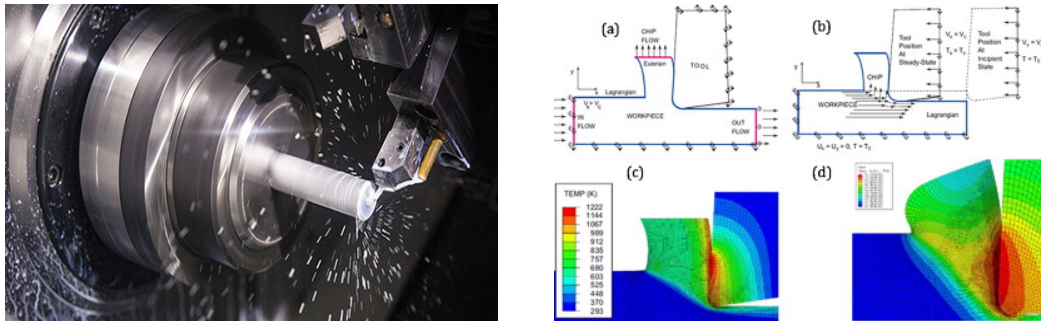
Figure 2.22 – Left: steel machining. Right: machining simulation figures extracted from [AÖ10].

A first test case is investigated, where an elastic solid $(\alpha = 0, \lambda > 0, \eta_s = 0)$ models the steel work with a free surface using model (1.1). This test case investigates the large deformation of the elastic solid when it is split in half. The visual convergence and the stability of the numerical scheme on this simplified test case is shown. A pseudo-2D simulation is applied here as described in section 2.2.2. The steel is injected in a rectangular domain $\Lambda = [0, 0.05]$ m $\times [0, 0.04]$ m $\times [0, 0.001]$ m with a notch modelling the rigid tool. The inflow boundary corresponds to the surface $\{0.015 \leq x \leq 0.035; y = 0.04\}$. In this numerical experiment, the set of parameters is $\rho = 7500$ kg/m^3, $\lambda = 10^{-3}$ s

$\eta_s = 0$ Pa s, $\eta_p = 2 \cdot 10^5$ Pa s and $\alpha = 0$. The use of large value of the ratio η_p / λ allows to obtain the Young modulus of steel. The coarser discretisation configuration is $H = 1$ mm, $h = 0.25$ mm and $\Delta t = 0.5$ ms. Finer meshes are then obtained by dividing discretisation parameters by two. The steel is injected at the top of the domain at speed $\boldsymbol{u} = (0, -1, 0)$ m/s. Free-slip boundary conditions are applied for the pseudo-D direction and in the notch boundaries, and an outflow let the material flow out of the domain when it reaches the bottom. Results are shown in Figure 2.23 for the finer mesh. The material flows in the cavity and is cut by the notch in the center corner of the domain, creating a singularity of the solution. The Figure 2.24 shows the visual convergence of the approximated characteristic function φ.
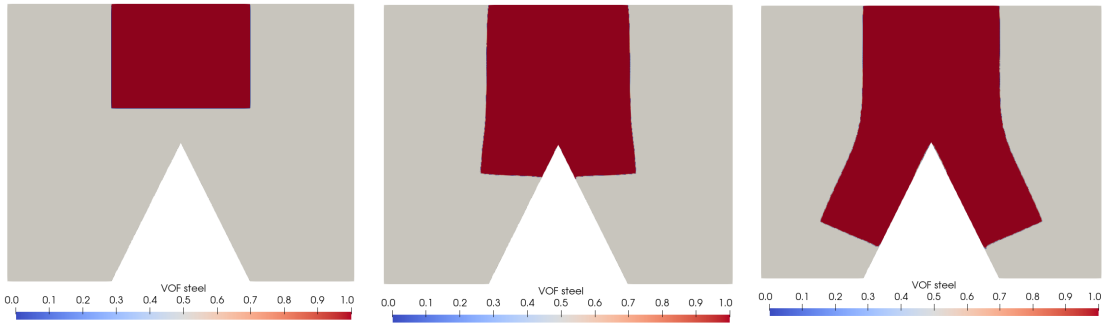
Figure 2.23 – Machining simulation. Simplified 2D test case for implicit scheme. Extra-stress component $\boldsymbol{\sigma}_{yy}$. From left to right: $t = 0.01, 0.025, 0.035$ s.
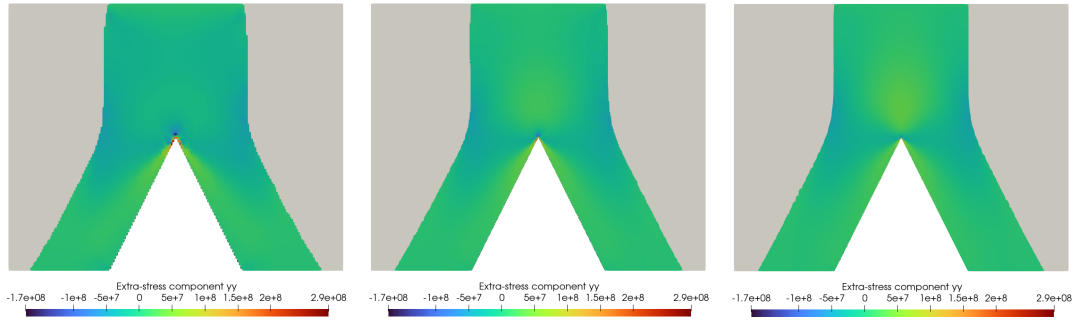
Figure 2.24 – Machining simulation. Simplified 2D test case for implicit scheme. Extra-stress component $\boldsymbol{\sigma}_{yy}$ at time $t = 0.05$ s. From left to right: $H = 1, 0.5$ and 0.25 mm.

Our implicit time discretisation scheme (1.25) has been used rather than the EVSS scheme (1.24). Using a large value of the parameter η_p in the hyperbolic case $\alpha = 0$ yields utterly large errors in simulations using the EVSS scheme, as mentioned in Remark 1.5.2 in section 1.5. In Figure 2.25, two simulations using the EVSS and implicit schemes are presented. The same parameters as previously have been used except for the two different values of the parameters $\eta_p = \{2 \cdot 10^5, 2 \cdot 10^7\}$ and $\lambda = \{10^{-3}, 10^{-1}\}$. Their ratio remains $\eta_p / \lambda = 2 \cdot 10^7$ Pa. The difference on the approximated characteristic function φ

and extra-stress tensor $\boldsymbol{\sigma}$ is too large between both simulations, which motivates the use of the implicit scheme for machining simulation.
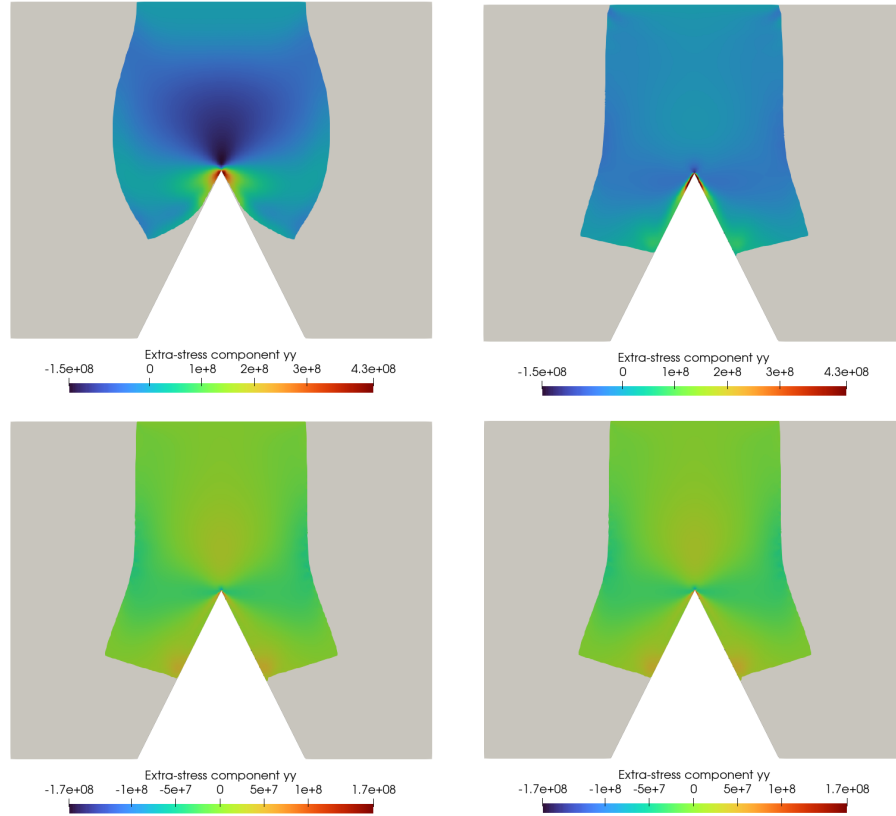
Figure 2.25 – Machining simulation. Simplified test case. Illustration of the issue raised by the ratio η_p/λ at $t = 0.03$ s. Left: elastic simulation for $\eta_p = 2 \cdot 10^7$ Pa s, $\lambda = 10^{-1}$ s. Right: elastic simulation for $\eta_p = 2 \cdot 10^5$ Pa s, $\lambda = 10^{-3}$ s. Top: EVSS scheme. Bottom: implicit scheme.

Finally, a more sophisticated simulation is presented. The tool is still modelled by a notch in the 3D domain but is shaped to form a realistic case. The set of parameters is $\rho = 7500$ kg/m^3, $\lambda = 10^{-3}$ s and $\eta_p = 2 \cdot 10^5$ Pa s. As previously mentioned, the use of the EVSS scheme is avoided here, in order to ensure a realistic numerical result. The results are presented in Figure 2.26. A chip is formed and allows to cut our material. Although no change of topology is performed, large deformation of the piece of steel is obtained.
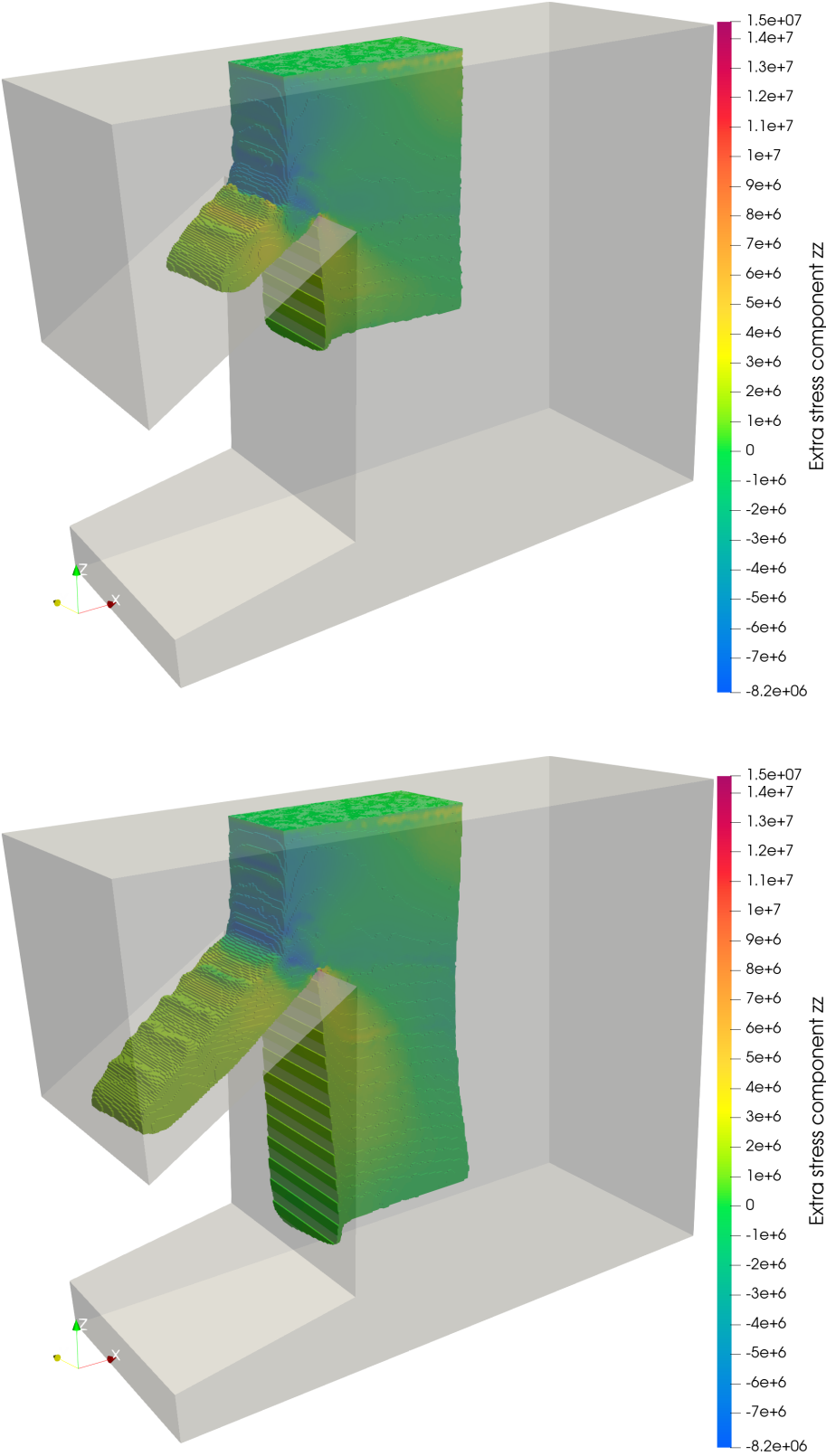
Figure 2.26 – Machining simulation. Extra-stress tensor coefficient $\boldsymbol{\sigma}_{zz}$ on small grid. Top: $t = 0.2$ s. Bottom: $t = 0.3$ s.

3 Numerical modelling of multiple incompressible viscoelastic free-surface flows

The goal is to extend the model in [JBCP14], corresponding to multiple incompressible and immiscible Newtonian flows to the viscoelastic and elastic case. This allows to consider fluid-fluid, fluid-structure and structure-structure interactions.

In this chapter, the model is presented first. The numerical approximation is then described, the implicit scheme of chapter 1 being applied to the multiphase formulation. Stability estimates of the time stepping schemes are then presented.

3.1   The mathematical model

The goal is to model the interaction of $L > 1$ phases, which rheologies range from incompressible Newtonian or Oldroyd-B fluids to incompressible Neo-Hookean elastic solids. The materials are considered isothermal, incompressible and immiscible. Consider a bounded cavity $\Lambda \subset \mathbb{R}^3$ and let $\varphi_\ell : \Lambda \times [0,T] \to \{0,1\}$ be the characteristic functions for each material $\ell = 1, \ldots, L$. The domain containing material ℓ is then defined as equal to 1 in material ℓ and 0 outside. They define the subdomains

$$\Omega_\ell(t) = \{\boldsymbol{x} \in \Lambda; \varphi_\ell(\boldsymbol{x},t) = 1\},$$

for $\ell = 1, \ldots, L$, $\forall t \in [0,T]$. Since the materials are considered immiscible, the subdomains $\Omega_\ell(t)$, $\ell = 1, \ldots, L$ do not intersect $\forall t \in [0,T]$. Hence, defining $\varphi : \Lambda \times [0,T] \to [0,1]$ as $\varphi = \sum_{\ell=1}^{L} \varphi_\ell$, the complete material domain is defined as

$$\Omega(t) = \{\boldsymbol{x} \in \Lambda; \varphi(\boldsymbol{x},t) = 1\} = \bigcup_{\ell=1}^{L} \Omega_\ell(t).$$

The space-time domain containing the material is defined as in chapter 1 as $\mathcal{Q}_T = \{(x,t) \in \Lambda \times (0,T); x \in \Omega(t), 0 < t < T\}$.

Consider the notations of chapter 1. Let $\Omega_0 = \Omega(0) = \bigcup_{\ell=1}^{L} \Omega_\ell(0)$ be the initial configuration and $\boldsymbol{x} : \Omega_0 \times [0, T] \to \Lambda$ be the Lagrangian description of the displacement of the fluids. The displacement of a particle $\boldsymbol{X} \in \Omega_0$ after deformation at time t is defined via the velocity of the deformation $\boldsymbol{u}$ using equation (1.2), see Figure 3.1.
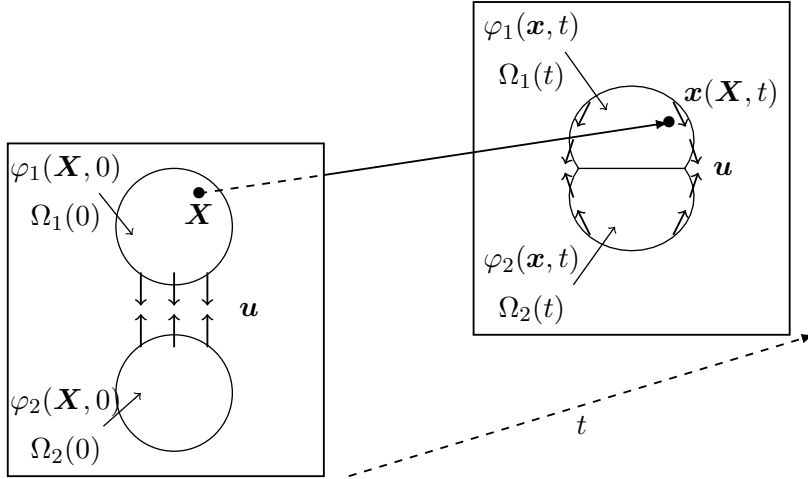
Figure 3.1 – Sketch of multiple materials deformation.

The material particles $\boldsymbol{X} \in \Omega_\ell(0)$ are transported to the position $\boldsymbol{x}(\boldsymbol{X}, t)$, with the material velocity $\boldsymbol{u}$, the characteristics functions ℓ satisfy in the sense of distributions:

$$\frac{\partial \varphi_\ell}{\partial t} + (\boldsymbol{u} \cdot \nabla) \varphi_\ell = 0, \quad \ell = 1, \dots, L, \quad \text{in } \Lambda \times [0, T]. \tag{3.1}$$

Thus, the characteristic functions satisfy for $\ell = 1, \dots, L$ and for all $\boldsymbol{X} \in \Omega_\ell(0)$:

$$\varphi_\ell(\boldsymbol{x}(\boldsymbol{X}, t), t) = \varphi_\ell(\boldsymbol{X}, 0). \tag{3.2}$$

By summing the equation (3.2) over $\ell = 1, \dots, L$, we obtain that the characteristic function φ satisfies the transport equation in the weak sense:

$$\frac{\partial \varphi}{\partial t} + (\boldsymbol{u} \cdot \nabla) \varphi = 0, \quad \text{in } \Lambda \times [0, T]. \tag{3.3}$$

Hence, it also satisfies $\varphi(\boldsymbol{x}(\boldsymbol{X}, t), t) = \varphi(\boldsymbol{X}, 0)$. In the computational domain, the velocity field $\boldsymbol{u} : \mathcal{Q}_T \to \mathbb{R}^3$, the pressure field $p : \mathcal{Q}_T \to \mathbb{R}$, the symmetric extra-stress tensor field $\boldsymbol{\sigma} : \mathcal{Q}_T \to \mathbb{R}^{3 \times 3}$ satisfy:

$$\rho\left(\frac{\partial \boldsymbol{u}}{\partial t} + (\boldsymbol{u}\cdot\nabla)\boldsymbol{u}\right) - \nabla\cdot(2\eta_s\boldsymbol{\epsilon}(\boldsymbol{u})) + \nabla p - \nabla\cdot\boldsymbol{\sigma} = \rho\boldsymbol{g}, \qquad \text{in } \mathcal{Q}_T, \qquad (3.4\text{a})$$

$$\nabla\cdot\boldsymbol{u} = 0, \qquad \text{in } \mathcal{Q}_T, \qquad (3.4\text{b})$$

$$\alpha\boldsymbol{\sigma} + \lambda\left(\frac{\partial\boldsymbol{\sigma}}{\partial t} + (\boldsymbol{u}\cdot\nabla)\boldsymbol{\sigma} - \nabla\boldsymbol{u}\boldsymbol{\sigma} - \boldsymbol{\sigma}\nabla\boldsymbol{u}^T\right) = 2\eta_p\boldsymbol{\epsilon}(\boldsymbol{u}), \qquad \text{in } \mathcal{Q}_T, \qquad (3.4\text{c})$$

where the parameters $\rho, \eta_s, \eta_p, \lambda, \alpha$ are piecewise constant in space, with a discontinuity at the interfaces. For instance, ρ_ℓ denotes the constant density of phase ℓ, $\ell = 1, \ldots, L$, and the density ρ is then defined with respect to the characteristic functions as

$$\rho = \sum_{\ell=1}^{L} \rho_\ell \varphi_\ell. \qquad (3.5)$$

The definition is analogous for the remaining parameters $\eta_s, \eta_p, \lambda, \alpha$. The material number ℓ determines:

1. an incompressible Newtonian fluid if $\alpha_\ell = 1$, $\lambda_\ell = 0$,

2. an incompressible Oldroyd-B viscoelastic fluid if $\alpha_\ell = 1$, $\lambda_\ell > 0$,

3. or an incompressible Neo-Hookean elastic solid if $\alpha_\ell = 0$, $\eta_{s,\ell} = 0$ and $\lambda_\ell > 0$.

At initial time $t = 0$, the material ℓ region is defined as $\Omega_{\ell,0} = \{\boldsymbol{x} \in \Lambda; \varphi_\ell(\boldsymbol{x}, 0) = 1\}$, for $\ell = 1, \ldots, L$ and the computational domain $\Omega_0 = \bigcup_{\ell=1}^{L} \Omega_{\ell,0}$. The initial velocity field $\boldsymbol{u}_0 = \boldsymbol{u}(\cdot, 0)$ and extra-stress tensor $\boldsymbol{\sigma}_0 = \boldsymbol{\sigma}(\cdot, 0)$ are prescribed in Ω_0. On $\partial\Lambda$ either zero tangent force (free slip) ($\boldsymbol{u}\cdot\boldsymbol{n} = 0$, $\boldsymbol{\sigma}\boldsymbol{n}\cdot\boldsymbol{t} = 0$), zero normal force ($\boldsymbol{u}\cdot\boldsymbol{t} = 0$, $\boldsymbol{\sigma}\boldsymbol{n}\cdot\boldsymbol{n} = 0$), no slip ($\boldsymbol{u} = \boldsymbol{0}$) or Signorini boundary conditions (2.12) can be prescribed. Finally, as in section 1.1, in case of inflow boundary conditions the velocity and extra stress must be prescribed at the inflow boundary: $\boldsymbol{u} = \boldsymbol{u}_{\mathbf{in}}$ and $\boldsymbol{\sigma} = \boldsymbol{\sigma}_{\mathbf{in}}$ on $\Gamma_{\text{in}} = \{\boldsymbol{x} \in \partial\Lambda; (\boldsymbol{u}\cdot\boldsymbol{n})(\boldsymbol{x}, t) < 0\}$.

For $0 \leq t \leq T$, the free surface at time t is defined as $\partial\Omega(t)\backslash\partial\Lambda$. The boundary conditions prescribed on the free surface corresponds to the no external forces condition, that is $(-p\boldsymbol{I} + 2\eta_s(\varphi)\boldsymbol{\epsilon}(\boldsymbol{u})) + \boldsymbol{\sigma})\cdot\boldsymbol{n} = 0$, where $\boldsymbol{n}$ is the unit outer normal of the free surface. Since the parameters $\rho, \eta_s, \eta_p, \lambda, \alpha$ are piecewise constant in space, the equation (3.4a) has to be understood in the weak sense and the conditions on the interface $\Gamma_{i,j}(t)$ between two subdomains $\Omega_i(t)$ and $\Omega_j(t)$, for $0 \leq t \leq T$, are:

$$[\boldsymbol{u}] = 0, \qquad (3.6)$$

$$[(2\eta_s\boldsymbol{\epsilon}(\boldsymbol{u}) + \boldsymbol{\sigma})\boldsymbol{n} - p\boldsymbol{n}] = \boldsymbol{0}, \qquad (3.7)$$

where the brackets $[\cdot]$ denotes the jump of the variables across the interface $\Gamma_{i,j}(t)$. The jump of the force at the interface is derived from the momentum equation (3.4a), while

the velocity continuity is needed to write the weak formulation of (3.4), see for instance [QV99]. Similar conditions are obtained for the coupling of viscid and inviscid Stokes equations [QLV91] or in fluid-structure interactions ($\eta_{s,1} = 0, \eta_{s,2} > 0$) [DR06, Ric13].

Should surface tension forces apply on the interface Γ_{ij}, then additional forces terms must be added in (3.4a) and the interface condition becomes [Kat86, TELB06]:
$[(2\eta_s \boldsymbol{\epsilon}(\boldsymbol{u}) + \boldsymbol{\sigma})\boldsymbol{n} - p\boldsymbol{n}] = \boldsymbol{F}_s$. The vector $\boldsymbol{F}_s$ denotes forces acting at the interface. Surface tension forces are not considered here. For further informations, the reader can refer to [Dav83, AMW98, Cab06].

Remark 3.1.1. The equations (3.5) and (3.2) gives the total mass conservation since for every particle $\boldsymbol{X} \in \Omega_0$:

$$\rho(\boldsymbol{X}, 0) = \sum_{\ell=1}^{L} \rho_\ell \varphi_\ell(\boldsymbol{X}, 0) = \sum_{\ell=1}^{L} \rho_\ell \varphi_\ell(\boldsymbol{x}(\boldsymbol{X}, t), t)) = \rho(\boldsymbol{x}(\boldsymbol{X}, t), t).$$

$\square$

3.2 Time discretisation: an order one splitting scheme for multiphase problem

Similarly as in the case $L = 1$, an order one splitting algorithm is applied to solve the system of equations (3.4). Hence, the advection and diffusion terms are splitted and solved separately. Let Δt be the time step, N be the number of time steps, $\Delta t = T/N$ and $t^n = n\Delta t$, $n = 0, 1, \ldots, N$. Let $n \geq 1$ and assume that at time t^{n-1}, the approximated volume fraction $\varphi_\ell^{n-1} : \Lambda \to \mathbb{R}$ are known, $\ell = 1, \ldots, L$. The approximated computational domain is defined by $\Omega^{n-1} = \{\boldsymbol{x} \in \Lambda; \varphi^{n-1}(\boldsymbol{x}) = 1\}$. Let $\boldsymbol{u}^{n-1} : \Omega^{n-1} \to \mathbb{R}^3$ and $\boldsymbol{\sigma}^{n-1} : \Omega^{n-1} \to \mathbb{R}^{3\times 3}$ be the approximation of the velocity $\boldsymbol{u}(t^{n-1})$ and extra-stress tensor $\boldsymbol{\sigma}(t^{n-1})$ respectively. During the prediction step, the set of advection equations from t^{n-1} to t^n in Λ is solved:
Find $\psi_\ell : \Lambda \times [t^{n-1}, t^n] \to \{0, 1\}$, $\ell = 1, \ldots, L$, $\boldsymbol{v} : \Lambda \times [t^{n-1}, t^n] \to \mathbb{R}^3$ and $\boldsymbol{\tau} : \Lambda \times [t^{n-1}, t^n] \to \mathbb{R}^{3\times 3}$ such that:

$$\frac{\partial \boldsymbol{v}}{\partial t} + (\boldsymbol{v} \cdot \nabla)\boldsymbol{v} = \boldsymbol{0}, \tag{3.8a}$$

$$\frac{\partial \boldsymbol{\tau}}{\partial t} + (\boldsymbol{v} \cdot \nabla)\boldsymbol{\tau} = \boldsymbol{0}, \tag{3.8b}$$

$$\frac{\partial \psi_\ell}{\partial t} + (\boldsymbol{v} \cdot \nabla)\psi_\ell = 0, \quad \ell = 1, \ldots, L, \tag{3.8c}$$

with initial conditions

$$\boldsymbol{v}(t^{n-1}) = \boldsymbol{u}^{n-1}, \quad \boldsymbol{\tau}(t^{n-1}) = \boldsymbol{\sigma}^{n-1}, \quad \psi_\ell(t^{n-1}) = \varphi_\ell^{n-1}, \quad \ell = 1, \ldots, L.$$

3.2. Time discretisation: an order one splitting scheme for multiphase problem

Dirichlet boundary conditions for the system of equations (3.8) are only prescribed if inflow boundary conditions are applied on Γ_{in}. Analogously as for $L = 1$, the system of equations (3.8) is solved exactly using the method of characteristics. Let us denote by $\boldsymbol{u}^{n-\frac{1}{2}}, \boldsymbol{\sigma}^{n-\frac{1}{2}}, \varphi_\ell^n$ the solutions at time t^n of the system (1.12). The method of characteristics yields for $\boldsymbol{X} \in \Omega^{n-1}$:

$$\boldsymbol{u}^{n-\frac{1}{2}}(\boldsymbol{X} + \Delta t \boldsymbol{u}^{n-1}(\boldsymbol{X})) = \boldsymbol{u}^{n-1}(\boldsymbol{X}), \tag{3.9a}$$

$$\boldsymbol{\sigma}^{n-\frac{1}{2}}(\boldsymbol{X} + \Delta t \boldsymbol{u}^{n-1}(\boldsymbol{X})) = \boldsymbol{\sigma}^{n-1}(\boldsymbol{X}), \tag{3.9b}$$

$$\varphi_\ell^n(\boldsymbol{X} + \Delta t \boldsymbol{u}^{n-1}(\boldsymbol{X})) = \varphi_\ell^{n-1}(\boldsymbol{X}), \quad \ell = 1, \dots, L. \tag{3.9c}$$

The variables $\varphi_\ell^n, \ell = 1, \dots, L$, solutions of the transport equations (3.8c) at time t^n, determine the updated subdomains $\Omega_\ell^n = \{\boldsymbol{x} \in \Lambda; \varphi_\ell^n(\boldsymbol{x}) = 1\}$. Moreover the total characteristic function $\varphi^n = \sum_{\ell=1}^L \varphi_\ell^n$ is updated and the computational domain is defined by $\Omega^n = \{\boldsymbol{x} \in \Lambda; \varphi^n(\boldsymbol{x}) = 1\} = \bigcup_{\ell=1}^L \Omega_\ell^n$. The parameters are updated at time $t = t^n$ as

$$f^n = \sum_{\ell=1}^L f_\ell \varphi_\ell^n, \tag{3.10}$$

for $f = \rho, \eta_s, \eta_p, \lambda, \alpha$. Then, the correction step consists in solving the remaining system of diffusive equations:
Find $\boldsymbol{v} : \Omega^n \times [t^{n-1}, t^n] \to \mathbb{R}^3$, $q : \Omega^n \times [t^{n-1}, t^n] \to \mathbb{R}$ and $\boldsymbol{\tau} : \Omega^n \times [t^{n-1}, t^n] \to \mathbb{R}^{3 \times 3}$ satisfying

$$\rho^n \frac{\partial \boldsymbol{v}}{\partial t} - \nabla \cdot (2\eta_s^n \boldsymbol{\epsilon}(\boldsymbol{v})) + \nabla q - \nabla \cdot \boldsymbol{\tau} = \rho^n \boldsymbol{g}, \tag{3.11a}$$

$$\nabla \cdot \boldsymbol{v} = 0, \tag{3.11b}$$

$$\alpha^n \boldsymbol{\tau} + \lambda^n \left(\frac{\partial \boldsymbol{\tau}}{\partial t} - \nabla \boldsymbol{v} \boldsymbol{\tau} - \boldsymbol{\tau} \nabla \boldsymbol{v}^T \right) = 2\eta_p^n \boldsymbol{\epsilon}(\boldsymbol{v}), \tag{3.11c}$$

with the initial conditions $\boldsymbol{v}(t^{n-1}) = \boldsymbol{u}^{n-\frac{1}{2}}$ and $\boldsymbol{\tau}(t^{n-1}) = \boldsymbol{\sigma}^{n-\frac{1}{2}}$ and the associated boundary conditions discussed previsouly in section 3.1. The parameters $\rho^n, \eta_s^n, \lambda^n, \eta_p^n, \alpha^n$ are approximations based on the characteristic functions φ_ℓ^n. The approximation of velocity, pressure and extra-stress at time t^n are then updated by $\boldsymbol{u}^n = \boldsymbol{v}(t^n)$, $p^n = q(t^n)$ and $\boldsymbol{\sigma}^n = \boldsymbol{\tau}(t^n)$. A sketch of the main steps of the splitting algorithm is illustrated in Figure 3.2.
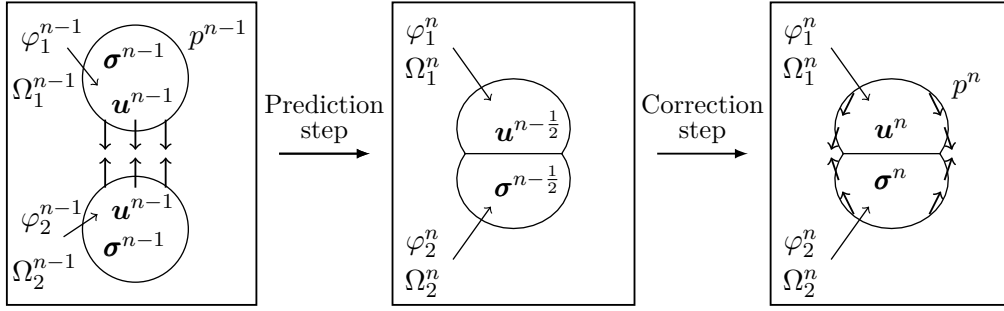
Figure 3.2 – Sketch of the main steps of splitting algorithm. In the prediction step, each fluid domain Ω_ℓ is updated by solving (3.9c) for the characteristic function φ_ℓ^n, $\ell = 1, \ldots, L$. The velocity and extra-stress tensor are first transported by solving (3.9a) and (3.9b), then updated to $\boldsymbol{u}^n$ and $\boldsymbol{\sigma}^n$ during the correction step, by solving (3.11).

3.3 Space discretisation: Two-grid approach

3.3.1 Prediction step: multiphase algorithms on a structured grid

The space discretization relies on the same two-grid approach of chapter 1. The method of characteristics is used to solve the advection equations (3.8) and the formulas are given by (3.9). A cell C_{ijk} with cell barycenter $\boldsymbol{x}_{ijk}$ is defined to be active when $\exists \ell \in \{1, \ldots, L\}$ such that $\varphi_{\ell,ijk}^n > 0$. Its content is transported with the vector $\Delta t \boldsymbol{u}_{ijk}^{n-1}$. This implies an ordering $\ell = 1, \ldots, L$ of the phase to be transported, but this does not have a major influence on the numerical results. A multiphase version of the SLIC and decompression algorithms are used in order to respectively reduce numerical diffusion and deal with overfilling. The multiphase version of SLIC is analogous to the algorithm presented in chapter 1. The amount of material ℓ in the cell C_{ijk} at time t^{n-1} is denoted $\varphi_{\ell,ijk}^{n-1}$ and is pushed towards the edge with fully filled neighbour cell. Whenever there are $m > 1$ different phases in an interface cell, they are respectively pushed towards the fully filled neighbour cells, see Figure 3.3.

The multiphase version of the decompression algorithm deals with overfilled cells where $\varphi_{ijk}^n = \sum_{\ell=1}^{L} \varphi_{\ell,ijk}^n > 1$. The excess of material in each phase is subtracted from overfilled cells and redistributed to the partially filled neighbour cells. Algorithm 1 used in this thesis has been presented in [JBCP14]. When a cell is overfilled, the leftovers are stored in a buffer in order to be redistributed. The excess of each phase is computed in order to keep the ratio of all phases in the cell. Then, a loop is applied on the cells partially filled. They are filled once again by respecting the ratio between the phases.

In some specific cases it is of interest to consider each phase separately, see Algorithm 2. Here, the first loop of the decompression algorithm is applied first on the phases in
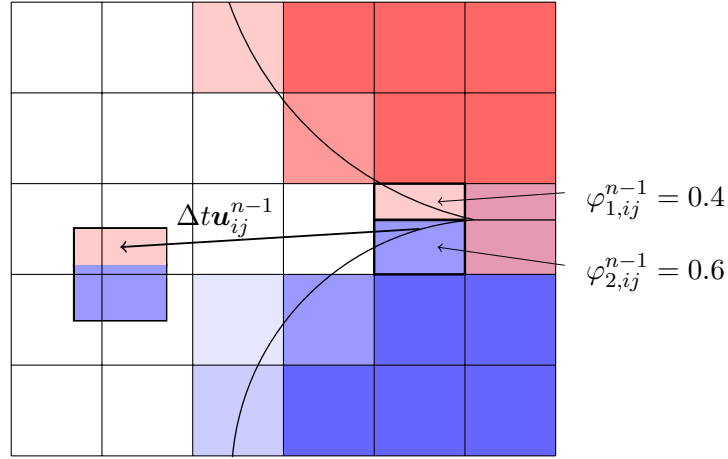
Figure 3.3 – Multiphase SLIC algorithm. The red cells have $\varphi_{1,ij}^{n-1}$ values equal to 1 and the blue cells have $\varphi_{2,ij}^{n-1}$ values equal to 1. The cells at the interface are partially filled by each phase. Consider one having 40% of phase 1 and 60% of phase 2. It is first compressed toward filled cells, then the characteristic functions are transported.

the redistribution process [SA]. It is of particular interest when a phase is immersed in another one. It asks for a specific treatment in order to ensure the VOF from either the immersed or the immersing phase to be redistributed in priority. An empirical analysis of the performance of these decompression algorithms is tackled in section 4.3.

Algorithm 1 Decompression algorithm for multiple phases [JBCP14]

$\quad$ **for** $\ell = 1, \ldots, L$ and all cells such that $\varphi_{ijk}^n > 1$ (in decreasing order) **do**

$\qquad e_{\ell,ijk} \leftarrow (\varphi_{ijk}^n - 1)\varphi_{\ell,ijk}^n / \varphi_{ijk}^n \qquad\qquad$ ▷ Compute excess ratio w.r.t. each phase.

$\qquad \varphi_{\ell,ijk}^n \leftarrow \varphi_{\ell,ijk}^n - e_{\ell,ijk}, \qquad\qquad$ ▷ Update the VOF for each phase in the cell.

$\qquad \mathcal{B}_\ell \leftarrow \mathcal{B}_\ell + e_{\ell,ijk}, \qquad\qquad\qquad$ ▷ Store the VOF excess for each phase.

$\quad$ **for** all cells such that $0 < \varphi_{\ell,ijk}^n < 1$ (in decreasing order) **do**

$\qquad$ **for** each phase $\ell = 1, \ldots, L$ **do**

$\qquad\quad$ **if** $\mathcal{B}_\ell > 0$ **then**

$\qquad\qquad r_{\ell,ijk} \leftarrow (1 - \varphi_{ijk}^n)\varphi_{\ell,ijk}^n / \varphi_{ijk}^n \qquad$ ▷ Compute the relative VOF void.

$\qquad\qquad \varphi_{\ell,ijk}^n \leftarrow \varphi_{\ell,ijk}^n + r_{\ell,ijk}, \qquad\qquad$ ▷ Update the VOF for each phase.

$\qquad\qquad \mathcal{B}_\ell \leftarrow \mathcal{B}_\ell - r_{\ell,ijk}, \qquad\qquad\qquad$ ▷ Update the buffer.

$\quad$ **if** $\exists \ell \in \{1, \ldots, L\}$ such that $\mathcal{B}_\ell > 0$ **then**

$\qquad$ Distribute the remaining excess to closest neighbour partially filled cells. If not possible, store for the next iteration.

3.3.2 Interpolation algorithms

Let $H > 0$ and $\mathcal{T}_H$ be a triangulation of the cavity Λ of maximum diameter $H > 0$. In order to compute the correction step, the characteristic function φ_{ijk}^{n-1} is interpolated

---

Algorithm 2 Decompression algorithm for multiple phases with phases priority

---

    for $\ell = 1, \ldots, L$ and all cells such that $\varphi_{\ell,ijk}^n > 1$ (in decreasing order) **do**

        $e_{\ell,ijk} \leftarrow (\varphi_{ijk}^n - 1)\varphi_{\ell,ijk}^n / \varphi_{ijk}^n$

        $\varphi_{\ell,ijk}^n \leftarrow \varphi_{\ell,ijk}^n - e_{\ell,ijk},$ ▷ The first step of buffer filling is kept unchanged.

        $\mathcal{B}_\ell \leftarrow \mathcal{B}_\ell + e_{\ell,ijk},$

    for each phase $\ell = 1, \ldots, L$ **do**   ▷ The loop on phases is here done first.

        for all cells such that $0 < \varphi_{\ell,ijk}^n < 1$ (in decreasing order) **do**

            if $\mathcal{B}_\ell > 0$ **then**

                $r_{\ell,ijk} \leftarrow (1 - \varphi_{ijk}^n)\varphi_{\ell,ijk}^n / \varphi_{ijk}^n$ ▷ Compute the relative VOF void.

                $\varphi_{\ell,ijk}^n \leftarrow \varphi_{\ell,ijk}^n + r_{\ell,ijk},$ ▷ Update the VOF for each phase.

                $\mathcal{B}_\ell \leftarrow \mathcal{B}_\ell - r_{\ell,ijk},$ ▷ Update the buffer.

    if $\exists \ell \in \{1, \ldots, L\}$ such that $\mathcal{B}_\ell > 0$ **then**

        Distribute the remaining excess to closest neighbour partially filled cells. If not possible, store for the next iteration.

---

from the cell grid to the FE mesh $\mathcal{T}_H$ via an L^2 projection. The interpolation operator uses the same equation (1.16) as for the case $L = 1$. The active FE region is then defined as

$$\Omega_H^n = \{K \in \mathcal{T}_H : \exists P \in \{P_i^K\}_{i=1}^4 \text{ vertices of } K \text{ such that } \varphi_H^n(P) \geq 0.5\}. \tag{3.12}$$

The intermediate velocity $\boldsymbol{u}_{ijk}^{n-\frac{1}{2}}$ and extra-stress tensor $\boldsymbol{\sigma}_{ijk}^{n-\frac{1}{2}}$ are similarly interpolated on the FE mesh using the interpolation equations (1.18), see Remark 1.4.1, section 1.4.2.

The set of parameters $f^n = \rho^n, \eta_s^n, \eta_p^n, \lambda^n, \alpha^n$ are then interpolated on the FE mesh, where their value f_H^n is piecewise constant. They depend on the values of the characteristic functions $\varphi_{\ell,ijk}^n$, $\ell = 1, \ldots, L$, on each cell C_{ijk}. Thus two different approaches are available for the interpolation, as illustrated in Figure 3.4.

1. One possibility is to do the interpolation of each characteristic functions $\varphi_{\ell,ijk}^n$, $\ell = 1, \ldots, L$ on the FE mesh. Then we compute their values for all $K \in \mathcal{T}_H$ using an L^2-interpolation:

$$f_H^n|_K = \frac{1}{4} \sum_{i=1}^4 \frac{\displaystyle\sum_{\ell=1}^L f_\ell \varphi_{\ell,H}^n(P_i^K)}{\displaystyle\sum_{\ell=1}^L \varphi_{\ell,H}^n(P_i^K)}, \tag{3.13}$$

    where P_i^K are the four nodes of the element K.

2. The second way to compute these parameters are to calculate first their values on

each cell grid by using the formula

$$f_{ijk}^n = \frac{\displaystyle\sum_{\ell=1}^{L} f_\ell \varphi_{\ell,ijk}^n}{\displaystyle\sum_{\ell=1}^{L} \varphi_{\ell,ijk}^n}, \tag{3.14}$$

for $f = \rho, \eta_s, \eta_p, \lambda, \alpha$ and then interpolate the results onto the FE mesh, using the same interpolation formula as previously applied to the characteristic function. They are then interpolated from the nodes to the elements by an L^2-projection formula.

Numerical experiments have shown that no fundamental difference in the numerical results can be observed. Thus, the second approach is applied in our numerical computations since it has the advantages of not looping on the cells for each phase.
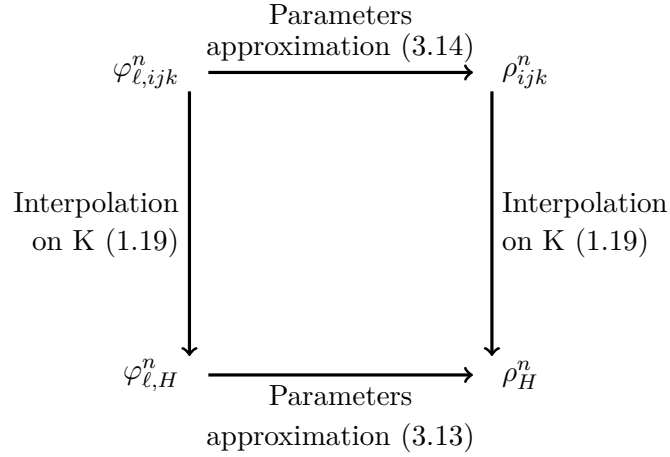
Figure 3.4 – Interpolation algorithm from cells grid to FE mesh. Both strategies are considered. First the parameters are evaluated on the cells and then interpolated on the FE mesh. The second choice is to interpolate the characteristic functions on the FE mesh and approximate the parameters in a second step.

3.3.3 Correction step: finite elements

Consider now the FE discretization of the system of equations (3.11). Consider the triangulation $\mathcal{T}_H$ and the active domain Ω_H^n defined in (3.12). From the continuity conditions at the interface (3.6),(3.7), no specific treatment on the FE space have to be taken into account. Then, the considered piecewise linear FE spaces are the same as considered for $L = 1$ and as defined in (1.26). Both time discretisations of the correction step presented in chapter 1 are adapted for the time discretization of the system (3.11). For the EVSS scheme, the stabilization tensor $\boldsymbol{D}_H^{n-\frac{1}{2}} \in \boldsymbol{T}_H^n$ is computed

using the equation (1.27a) and the problem reads:

Find $\boldsymbol{u}_H^n \in \boldsymbol{V}_H^n$, $p_H^n \in Q_H^n$ such that

$$\int_{\Omega_H^n} \rho_H^n \frac{\boldsymbol{u}_H^n - \boldsymbol{u}_H^{n-\frac{1}{2}}}{\Delta t} \cdot \boldsymbol{v}_H \; \mathrm{d}\boldsymbol{x} + \int_{\Omega_H^n} 2(\eta_{s,H}^n + \eta_{p,H}^n)\boldsymbol{\epsilon}(\boldsymbol{u}_H^n) : \boldsymbol{\epsilon}(\boldsymbol{v}_H) \; \mathrm{d}\boldsymbol{x} - \int_{\Omega_H^n} p_H^n (\nabla \cdot \boldsymbol{v}_H) \; \mathrm{d}\boldsymbol{x}$$

$$= \int_{\Omega_H^n} (2\eta_{p,H}^n \boldsymbol{D}_H^{n-\frac{1}{2}} - \boldsymbol{\sigma}_H^{n-\frac{1}{2}}) : \boldsymbol{\epsilon}(\boldsymbol{v}_H) \; \mathrm{d}\boldsymbol{x} + \int_{\Omega_H^n} \rho_H^n \boldsymbol{g} \cdot \boldsymbol{v}_H \; \mathrm{d}\boldsymbol{x}, \qquad \forall \boldsymbol{v}_H \in \boldsymbol{V}_H^n, \quad (3.15\text{a})$$

$$\int_{\Omega_H^n} (\nabla \cdot \boldsymbol{u}_H^n) q_H \; \mathrm{d}\boldsymbol{x}$$

$$+ \sum_{\substack{K \in \mathcal{T}_H \\ K \subset \Omega_H^n}} \alpha_K \int_K \left(\nabla p_H^n - \nabla \cdot \boldsymbol{\sigma}_H^{n-\frac{1}{2}} - \rho_H^n \boldsymbol{g} \right) \cdot \nabla q_H \; \mathrm{d}\boldsymbol{x} = 0, \qquad \forall q_H \in Q_H^n, \qquad (3.15\text{b})$$

and in the next step we solve the weak formulation of the Oldroyd-B equation to recover the extra-stress tensor $\boldsymbol{\sigma}_H^n \in \boldsymbol{T}_H^n$ such that:

$$\int_{\Omega_H^n} \boldsymbol{\sigma}_H^n : \boldsymbol{\tau}_H \; \mathrm{d}\boldsymbol{x} = \int_{\Omega_H^n} \frac{\lambda_H^n}{\lambda_H^n + \alpha_H^n \Delta t} \boldsymbol{\sigma}_H^{n-\frac{1}{2}} : \boldsymbol{\tau}_H \; \mathrm{d}\boldsymbol{x}$$

$$+ \int_{\Omega_H^n} \frac{\lambda_H^n \Delta t}{\lambda_H^n + \alpha_H^n \Delta t} (\nabla \boldsymbol{u}_H^n \boldsymbol{\sigma}_H^{n-\frac{1}{2}} + \boldsymbol{\sigma}_H^{n-\frac{1}{2}} (\nabla \boldsymbol{u}_H^n)^T) : \boldsymbol{\tau}_H \; \mathrm{d}\boldsymbol{x} \qquad (3.15\text{c})$$

$$+ \int_{\Omega_H^n} \frac{2\eta_{p,H}^n \Delta t}{\lambda_H^n + \alpha_H^n \Delta t} \boldsymbol{\epsilon}(\boldsymbol{u}_H^n) : \boldsymbol{\tau}_H \; \mathrm{d}\boldsymbol{x}, \quad \forall \boldsymbol{\tau}_H \in \boldsymbol{T}_H^n.$$

The local stabilization coefficients α_k are defined by

$$\alpha_K = \begin{cases} \dfrac{|K|^{\frac{2}{3}}}{12(\eta_{s,H}^n + \eta_{p,H}^n)} & \text{if } Re_K \leq 3, \\[4mm] \dfrac{|K|^{\frac{2}{3}}}{4Re_K(\eta_{s,H}^n + \eta_{p,H}^n)} & \text{otherwise,} \end{cases} \quad , \quad Re_K = \frac{\rho |K|^{\frac{1}{3}} \max_{\boldsymbol{x} \in K} |\boldsymbol{u}_H^{n-\frac{1}{2}}(\boldsymbol{x})|}{2(\eta_{s,H}^n + \eta_{p,H}^n)}.$$

The implicit numerical scheme for time discretization (1.28) is adapted here for multiphase flows. The finite element approximations of the velocity $\boldsymbol{u}_H^n$ and of the pressure p_H^n are computed by solving:

Find $\boldsymbol{u}_H^n \in \boldsymbol{V}_H^n$, $p_H^n \in Q_H^n$ such that

$$
\int_{\Omega_H^n} \rho_H^n \frac{\boldsymbol{u}_H^n - \boldsymbol{u}_H^{n-\frac{1}{2}}}{\Delta t} \cdot \boldsymbol{v}_H \; \mathrm{d}\boldsymbol{x} + \int_{\Omega_H^n} 2 \left(\eta_{s,H}^n + \frac{\eta_{p,H}^n \Delta t}{\lambda_H^n + \alpha_H^n \Delta t} \right) \boldsymbol{\epsilon}(\boldsymbol{u}_H^n) : \boldsymbol{\epsilon}(\boldsymbol{v}_H) \; \mathrm{d}\boldsymbol{x}
$$

$$
- \int_{\Omega_H^n} p_H^n (\nabla \cdot \boldsymbol{v}_H) \; \mathrm{d}\boldsymbol{x} = \int_{\Omega_H^n} \rho_H^n \boldsymbol{g} \cdot \boldsymbol{v}_H \; \mathrm{d}\boldsymbol{x} - \int_{\Omega_H^n} \frac{\lambda_H^n}{\lambda_H^n + \alpha_H^n \Delta t} \boldsymbol{\sigma}_H^{n-\frac{1}{2}} : \boldsymbol{\epsilon}(\boldsymbol{v}_H) \; \mathrm{d}\boldsymbol{x} \quad (3.16\text{a})
$$

$$
- \int_{\Omega_H^n} \frac{\lambda_H^n \Delta t}{\lambda_H^n + \alpha_H^n \Delta t} (\nabla \boldsymbol{u}_H^{n-\frac{1}{2}} \boldsymbol{\sigma}_H^{n-\frac{1}{2}} + \boldsymbol{\sigma}_H^{n-\frac{1}{2}} (\nabla \boldsymbol{u}_H^{n-\frac{1}{2}})^T) : \boldsymbol{\epsilon}(\boldsymbol{v}_H) \; \mathrm{d}\boldsymbol{x}, \qquad \forall \boldsymbol{v}_H \in \boldsymbol{V}_H^n,
$$

$$
\int_{\Omega_H^n} (\nabla \cdot \boldsymbol{u}_H^n) q_H \; \mathrm{d}\boldsymbol{x} \qquad\qquad\qquad (3.16\text{b})
$$

$$
+ \sum_{\substack{K \in \mathcal{T}_H \\ K \subset \Omega_H^n}} \alpha_K \int_K \left(\nabla p_H^n - \frac{\lambda_H^n}{\lambda_H^n + \alpha_H^n \Delta t} \nabla \cdot \boldsymbol{\sigma}_H^{n-\frac{1}{2}} - \rho_H^n \boldsymbol{g} \right) \cdot \nabla q_H \; \mathrm{d}\boldsymbol{x} = 0, \;\; \forall q_H \in Q_H^n.
$$

Similarly as for the EVSS scheme, we solve the weak formulation of the Oldroyd-B equation (3.15c) to recover the extra-stress tensor $\boldsymbol{\sigma}_H^n \in \boldsymbol{T}_H$. Similarly, the coefficients α_K are defined as:

$$
\alpha_K = \begin{cases} \dfrac{|K|^{\frac{2}{3}}}{12(\eta_{s,H}^n + \eta_{p,H}^n \frac{\Delta t}{\lambda_H^n + \alpha_H^n \Delta t})} & \text{if } Re_K \leq 3 \\[4ex] \dfrac{|K|^{\frac{2}{3}}}{4 Re_K (\eta_{s,H}^n + \eta_{p,H}^n \frac{\Delta t}{\lambda_H^n + \alpha_H^n \Delta t})} & \text{else,} \end{cases} \quad , \quad Re_K = \frac{\rho |K|^{\frac{1}{3}} \max_{\boldsymbol{x} \in K} |\boldsymbol{u}_H^{n-\frac{1}{2}}(\boldsymbol{x})|}{2(\eta_{s,H}^n + \eta_{p,H}^n \frac{\Delta t}{\lambda_H^n + \alpha_H^n \Delta t})}.
$$

3.4 Stability and convergence study of linear system

In this section, the stability analysis done in chapter 1 is carried for $L > 1$. The analysis is applied for completely filled cavity ($\varphi(\boldsymbol{x}, t) = 1$, for all $\boldsymbol{x} \in \Lambda$ and for all $t \in [0, T]$). The additional issue is to deal with the interfaces between Ω_i and Ω_j, $i, j = 1, \ldots, L$ and the advection terms are removed. The goal is to find a priori estimate for a simplified analytical model. Then, we recover a similar result in the discrete case.

3.4.1 Analysis of a simplified multiphase model

Stability estimates for a simplification of the model (3.4) are now studied. The nonlinear terms in the Oldroyd-B equation (3.4c) and the external forces are removed, and a completely filled cavity is considered ($\varphi = 1$ and $\Lambda = \Omega(t) = \Omega$, for $0 \leq t \leq T$). Furthermore, we assume the characteristic functions to be constant in time: $\varphi_\ell(\boldsymbol{x}, t) = \varphi_\ell(\boldsymbol{x}, 0)$, $\boldsymbol{x} \in \Omega$, $t \in [0, T]$ and $\ell = 1, \ldots, L$. The weak formulation of the simplified problem reads in $\Omega \times [0, T]$:

$$\int_\Omega \rho \frac{\partial \boldsymbol{u}}{\partial t} \cdot \boldsymbol{v} \; \mathrm{d}\boldsymbol{x} + \int_\Omega (2\eta_s \boldsymbol{\epsilon}(\boldsymbol{u}) + \boldsymbol{\sigma}) : \boldsymbol{\epsilon}(\boldsymbol{v}) \; \mathrm{d}\boldsymbol{x} \qquad (3.17\mathrm{a})$$

$$- \int_\Omega p(\nabla \cdot \boldsymbol{v}) \; \mathrm{d}\boldsymbol{x} = \boldsymbol{0}, \; \forall \boldsymbol{v} \in H_0^1(\Omega)^3,$$

$$\int_\Omega (\nabla \cdot \boldsymbol{u}) q \; \mathrm{d}\boldsymbol{x} = 0, \; \forall q \in L_0^2(\Omega), \qquad (3.17\mathrm{b})$$

$$\int_\Omega \alpha \boldsymbol{\sigma} : \boldsymbol{\tau} \; \mathrm{d}\boldsymbol{x} + \int_\Omega \lambda \frac{\partial \boldsymbol{\sigma}}{\partial t} : \boldsymbol{\tau} \; \mathrm{d}\boldsymbol{x} - \int_\Omega 2\eta_p \boldsymbol{\epsilon}(\boldsymbol{u}) : \boldsymbol{\tau} \; \mathrm{d}\boldsymbol{x} = \boldsymbol{0}, \; \forall \boldsymbol{\tau} \in L^2(\Omega)^{3\times 3}. \qquad (3.17\mathrm{c})$$

The parameters $f = \rho, \eta_s, \eta_p, \lambda, \alpha$ are piecewise constant and defined as in (3.5): $f = \sum_{\ell=1}^{L} f_\ell \varphi_\ell$. Finally, homogeneous Dirichlet boundary conditions apply: $\boldsymbol{u} = 0$ on $\partial\Omega$.

Using $\boldsymbol{v} = \boldsymbol{u}$ in (3.17a), $q = p$ in (3.17b) and $\boldsymbol{\tau} = \frac{1}{2\eta_p}\boldsymbol{\sigma}$ in (3.17c) ($\eta_{p,\ell} > 0$, $\ell = 1, \ldots, L$), we find, for $0 < t < T$:

$$\frac{\mathrm{d}}{\mathrm{d}t} \left(\int_\Omega \frac{\rho}{2} |\boldsymbol{u}|^2 \; \mathrm{d}\boldsymbol{x} \right) + \int_\Omega 2\eta_s |\boldsymbol{\epsilon}(\boldsymbol{u})|^2 + \boldsymbol{\sigma} : \boldsymbol{\epsilon}(\boldsymbol{u}) \; \mathrm{d}\boldsymbol{x} - \int_\Omega p(\nabla \cdot \boldsymbol{u}) = \boldsymbol{0},$$

$$\int_\Omega p(\nabla \cdot \boldsymbol{u}) = 0,$$

$$\frac{\mathrm{d}}{\mathrm{d}t} \left(\int_\Omega \frac{\lambda}{4\eta_p} |\boldsymbol{\sigma}|^2 \; \mathrm{d}\boldsymbol{x} \right) + \int_\Omega \frac{\alpha}{2\eta_p} |\boldsymbol{\sigma}|^2 \; \mathrm{d}\boldsymbol{x} - \int_\Omega \boldsymbol{\sigma} : \boldsymbol{\epsilon}(\boldsymbol{u}) \; \mathrm{d}\boldsymbol{x} = \boldsymbol{0},$$

since the characteristic functions are constant in time, so $\frac{\partial}{\partial t} f = 0$, for $f = \rho, \eta_s, \eta_p, \lambda, \alpha$. Finally, we obtain

$$\frac{\mathrm{d}}{\mathrm{d}t} \int_\Omega \left(\rho |\boldsymbol{u}|^2 + \frac{\lambda}{2\eta_p} |\boldsymbol{\sigma}|^2 \right) \; \mathrm{d}\boldsymbol{x} + \int_\Omega 4\eta_s |\boldsymbol{\epsilon}(\boldsymbol{u})|^2 + \frac{\alpha}{\eta_p} |\boldsymbol{\sigma}|^2 \; \mathrm{d}\boldsymbol{x} = 0. \qquad (3.18)$$

The equation (3.18) is analogous to the a priori estimate (1.32) proved for the case $L = 1$. As previously, an alternative stability result must be obtained when $\eta_{\ell,s} = 0$ for any $\ell = 1, \ldots, L$, in order to bound the velocity gradient $\boldsymbol{\epsilon}(\boldsymbol{u})$. However, since the parameters are now piecewise constant, only the case $\alpha_\ell = 0$, $\ell = 1, \ldots, L$ is treated. When $\alpha_\ell = 0$, $\ell = 1, \ldots, L$, the strong form of the system (3.17) reads

$$\rho \frac{\partial \boldsymbol{u}}{\partial t} - \nabla \cdot (2\eta_s \boldsymbol{\epsilon}(\boldsymbol{u}) + \boldsymbol{\sigma}) + \nabla p = 0, \qquad (3.19\mathrm{a})$$

$$\nabla \cdot \boldsymbol{u} = 0, \qquad (3.19\mathrm{b})$$

$$\frac{\partial \boldsymbol{\sigma}}{\partial t} = \frac{2\eta_p}{\lambda} \boldsymbol{\epsilon}(\boldsymbol{u}). \qquad (3.19\mathrm{c})$$

Since $\alpha_\ell = 0$, we then must have $\lambda_\ell > 0$, $\ell = 1, \ldots, L$. Otherwise only a trivial solution would be obtained for the velocity ($0 = 2\eta_p \boldsymbol{\epsilon}(\boldsymbol{u})$). By taking the time derivative of

(3.19a), we can substitute (3.19c) into the result and it yields

$$\rho \frac{\partial^2 \boldsymbol{u}}{\partial t^2} - \nabla \cdot \left(2\eta_s \boldsymbol{\epsilon} \left(\frac{\partial \boldsymbol{u}}{\partial t} \right) + \frac{2\eta_p}{\lambda} \boldsymbol{\epsilon}(\boldsymbol{u}) \right) + \nabla \frac{\partial p}{\partial t} = 0,$$

since $\frac{\partial f}{\partial t} = 0$, for $f = \rho, \eta_s, \eta_p, \lambda, \alpha$. Taking the scalar product with $\frac{\partial \boldsymbol{u}}{\partial t}$ and integrate over Ω yields

$$\frac{\mathrm{d}}{\mathrm{d}t} \left(\int_\Omega \rho \left| \frac{\partial \boldsymbol{u}}{\partial t} \right|^2 + \frac{2\eta_p}{\lambda} |\boldsymbol{\epsilon}(\boldsymbol{u})|^2 \, \mathrm{d}\boldsymbol{x} \right) + \int_\Omega 2\eta_s \left| \boldsymbol{\epsilon} \left(\frac{\partial \boldsymbol{u}}{\partial t} \right) \right|^2 \, \mathrm{d}\boldsymbol{x} = 0. \tag{3.20}$$

3.4.2 Analysis of a simplified model for the discretisation in time

Now, let us consider the implicit discretisation in time for the simplified system (3.17). Since the characteristic functions φ_ℓ^n are constant in time, we still consider piecewise constant parameters $\rho, \eta_s, \eta_p, \lambda, \alpha$. The weak formulation of the problem reads: For $n = 1, \ldots, N$, find $\boldsymbol{u}^n$, p^n and $\boldsymbol{\sigma}^n$ in Ω such that

$$\int_\Omega \rho \frac{\boldsymbol{u}^n - \boldsymbol{u}^{n-1}}{\Delta t} \cdot \boldsymbol{v} \, \mathrm{d}\boldsymbol{x} + \int_\Omega (2\eta_s \boldsymbol{\epsilon}(\boldsymbol{u}^n) + \boldsymbol{\sigma}^n) : \boldsymbol{\epsilon}(\boldsymbol{v}) \, \mathrm{d}\boldsymbol{x} \tag{3.21a}$$

$$- \int_\Omega p^n (\nabla \cdot \boldsymbol{u}^n) \, \mathrm{d}\boldsymbol{x} = \boldsymbol{0}, \quad \forall \boldsymbol{v} \in H_0^1(\Omega)^3,$$

$$\int_\Omega (\nabla \cdot \boldsymbol{u}^n) q \, \mathrm{d}\boldsymbol{x} = 0, \quad \forall q \in L_0^2(\Omega), \tag{3.21b}$$

$$\int_\Omega \alpha \boldsymbol{\sigma}^n : \boldsymbol{\tau} \, \mathrm{d}\boldsymbol{x} + \int_\Omega \lambda \left(\frac{\boldsymbol{\sigma}^n - \boldsymbol{\sigma}^{n-1}}{\Delta t} \right) : \boldsymbol{\tau} \, \mathrm{d}\boldsymbol{x} \tag{3.21c}$$

$$- \int_\Omega 2\eta_p \boldsymbol{\epsilon}(\boldsymbol{u}^n) : \boldsymbol{\tau} \, \mathrm{d}\boldsymbol{x} = 0, \quad \forall \boldsymbol{\tau} \in L^2(\Omega)^{3 \times 3}.$$

The weak formulation (3.21) implies the interface conditions $[(2\eta_s \boldsymbol{\epsilon}(\boldsymbol{u}^n) + \boldsymbol{\sigma}^n - p^n \boldsymbol{I})\boldsymbol{n}] = \boldsymbol{0}$ and $[\boldsymbol{u}^n] = 0$, for $n = 1, \ldots, N$. By using $\boldsymbol{v} = \boldsymbol{u}^n$ in (3.21a) and $\boldsymbol{\tau} = \boldsymbol{\sigma}^n$ in (3.21c), we find

$$\int_\Omega \frac{\rho}{2} |\boldsymbol{u}^n|^2 + \frac{\rho}{2} |\boldsymbol{u}^n - \boldsymbol{u}^{n-1}|^2 \, \mathrm{d}\boldsymbol{x} + \Delta t \int_\Omega 2\eta_s |\boldsymbol{\epsilon}(\boldsymbol{u}^n)|^2 + \boldsymbol{\sigma}^n : \boldsymbol{\epsilon}(\boldsymbol{u}^n) \, \mathrm{d}\boldsymbol{x} - \Delta t \int_\Omega p^n (\nabla \cdot \boldsymbol{u}^n) \, \mathrm{d}\boldsymbol{x}$$

$$= \int_\Omega \frac{\rho}{2} |\boldsymbol{u}^{n-1}|^2 \, \mathrm{d}\boldsymbol{x}.$$

$$\int_\Omega \frac{\lambda}{4\eta_p} |\boldsymbol{\sigma}^n|^2 + \frac{\lambda}{4\eta_p} |\boldsymbol{\sigma}^n - \boldsymbol{\sigma}^{n-1}|^2 \, \mathrm{d}\boldsymbol{x} + \Delta t \int_\Omega \frac{\alpha}{2\eta_p} |\boldsymbol{\sigma}^n|^2 \, \mathrm{d}\boldsymbol{x}$$

$$= \int_\Omega \frac{\lambda}{4\eta_p} |\boldsymbol{\sigma}^{n-1}|^2 \, \mathrm{d}\boldsymbol{x} + \Delta t \int_\Omega \boldsymbol{\sigma}^n : \boldsymbol{\epsilon}(\boldsymbol{u}^n) \, \mathrm{d}\boldsymbol{x}.$$

This yields by summing the two previous equations and removing the pressure terms using (3.21b):

$$\int_\Omega \left(\rho|\boldsymbol{u}^n|^2 + \frac{\lambda}{2\eta_p}|\boldsymbol{\sigma}^n|^2 \right) \, \mathrm{d}\boldsymbol{x} + \int_\Omega \left(\rho|\boldsymbol{u}^n - \boldsymbol{u}^{n-1}|^2 + \frac{\lambda}{2\eta_p}|\boldsymbol{\sigma}^n - \boldsymbol{\sigma}^{n-1}|^2 \right) \, \mathrm{d}\boldsymbol{x}$$

$$+ \Delta t \int_\Omega \left(4\eta_s\boldsymbol{\epsilon}(\boldsymbol{u}^n) + \frac{\alpha}{\eta_p}|\boldsymbol{\sigma}^n|^2 \right) \, \mathrm{d}\boldsymbol{x}$$

$$= \int_\Omega \left(\rho|\boldsymbol{u}^{n-1}|^2 + \frac{\lambda}{2\eta_p}|\boldsymbol{\sigma}^{n-1}|^2 \right) \, \mathrm{d}\boldsymbol{x}$$

This is the multiphase counterpart of the result (1.40). Now we want to compute an estimate which gives an upper bound of $\boldsymbol{\epsilon}(\boldsymbol{u}^n)$ in the case $\alpha_\ell = 0$, $\ell = 1,\ldots,L$. The strong form of (3.21) yields for $n = 0,\ldots,N-1$:

$$\rho\frac{\boldsymbol{u}^{n+1} - \boldsymbol{u}^n}{\Delta t} - \nabla \cdot (2\eta_s\boldsymbol{\epsilon}(\boldsymbol{u}^{n+1}) + \boldsymbol{\sigma}^{n+1}) + \nabla p^{n+1} = 0, \qquad (3.22\mathrm{a})$$

$$\nabla \cdot \boldsymbol{u}^{n+1} = 0, \qquad (3.22\mathrm{b})$$

$$\frac{\boldsymbol{\sigma}^{n+1} - \boldsymbol{\sigma}^n}{\Delta t} = \frac{2\eta_p}{\lambda}\boldsymbol{\epsilon}(\boldsymbol{u}^{n+1}). \qquad (3.22\mathrm{c})$$

Take the difference between two consecutive steps of (3.22a) and substitute (3.22c) into the result yields:

$$\rho\frac{\boldsymbol{u}^{n+1} - 2\boldsymbol{u}^n + \boldsymbol{u}^{n-1}}{\Delta t} - \nabla \cdot \left(2\eta_s\boldsymbol{\epsilon}(\boldsymbol{u}^{n+1} - \boldsymbol{u}^n) + \boldsymbol{\sigma}^{n+1} - \boldsymbol{\sigma}^n \right) + \nabla(p^{n+1} - p^n) = 0.$$

Take the scalar product of the result with $\dfrac{\boldsymbol{u}^{n+1} - \boldsymbol{u}^n}{\Delta t}$ and integrate over Ω. Since the interface conditions are true for $n = 0, 1, \ldots, N$, we have $[(2\eta_s\boldsymbol{\epsilon}(\boldsymbol{u}^{n+1} - \boldsymbol{u}^n) + \boldsymbol{\sigma}^{n+1} - \boldsymbol{\sigma}^n - (p^{n+1} - p^n)\boldsymbol{I})\boldsymbol{n}] = \boldsymbol{0}$ and $[\boldsymbol{u}^{n+1} - \boldsymbol{u}^n] = \boldsymbol{0}$, for $n = 0,\ldots,N-1$. Thus, the diffusion terms read

$$-\frac{1}{\Delta t}\int_\Omega (\boldsymbol{u}^{n+1} - \boldsymbol{u}^n) \cdot (\nabla \cdot \left(2\eta_s\boldsymbol{\epsilon}(\boldsymbol{u}^{n+1} - \boldsymbol{u}^n) + \boldsymbol{\sigma}^{n+1} - \boldsymbol{\sigma}^n \right) + \nabla(p^{n+1} - p^n)) \, \mathrm{d}\boldsymbol{x}$$

$$= -\frac{1}{\Delta t}\sum_{\ell=1}^L \int_{\Omega_\ell} (\boldsymbol{u}^{n+1} - \boldsymbol{u}^n) \cdot (\nabla \cdot \left(2\eta_{s,\ell}\boldsymbol{\epsilon}(\boldsymbol{u}^{n+1} - \boldsymbol{u}^n) + \boldsymbol{\sigma}^{n+1} - \boldsymbol{\sigma}^n \right) + \nabla(p^{n+1} - p^n)) \, \mathrm{d}\boldsymbol{x}$$

$$= \frac{1}{\Delta t}\sum_{\ell=1}^L \int_{\Omega_\ell} (2\eta_{s,\ell}\boldsymbol{\epsilon}(\boldsymbol{u}^{n+1} - \boldsymbol{u}^n) + \boldsymbol{\sigma}^{n+1} - \boldsymbol{\sigma}^n - (p^{n+1} - p^n)\boldsymbol{I}) : (\boldsymbol{\epsilon}(\boldsymbol{u}^{n+1} - \boldsymbol{u}^n) \, \mathrm{d}\boldsymbol{x}$$

$$- \frac{1}{\Delta t}\sum_{\ell=1}^L \int_{\partial\Omega_\ell} (\boldsymbol{u}^{n+1} - \boldsymbol{u}^n) \cdot (2\eta_{s,\ell}\boldsymbol{\epsilon}(\boldsymbol{u}^{n+1} - \boldsymbol{u}^n) + \boldsymbol{\sigma}^{n+1} - \boldsymbol{\sigma}^n + (p^{n+1} - p^n)\boldsymbol{I})\boldsymbol{n} \, \mathrm{d}\boldsymbol{S}$$

$$= \frac{1}{\Delta t}\int_\Omega 2\eta_s|\boldsymbol{\epsilon}(\boldsymbol{u}^{n+1} - \boldsymbol{u}^n)|^2 + (\boldsymbol{\sigma}^{n+1} - \boldsymbol{\sigma}^n) : \boldsymbol{\epsilon}(\boldsymbol{u}^{n+1} - \boldsymbol{u}^n) \, \mathrm{d}\boldsymbol{x},$$

where the pressure terms and surface integrals cancel out respectively using equation (3.21b) and the interface conditions previously highlighted. By taking the tensor product of (3.21c) with $\boldsymbol{\epsilon}(\boldsymbol{u}^{n+1} - \boldsymbol{u}^n)$ and integrate over Ω, we find

$$\frac{1}{\Delta t} \int_{\Omega} (\boldsymbol{\sigma}^{n+1} - \boldsymbol{\sigma}^n) : \boldsymbol{\epsilon}(\boldsymbol{u}^{n+1} - \boldsymbol{u}^n) \, \mathrm{d}\boldsymbol{x} = \int_{\Omega} \frac{2\eta_p}{\lambda} \boldsymbol{\epsilon}(\boldsymbol{u}^{n+1}) : \boldsymbol{\epsilon}(\boldsymbol{u}^{n+1} - \boldsymbol{u}^n) \, \mathrm{d}\boldsymbol{x}$$

It yields by summing the results:

$$\int_{\Omega} \frac{\rho}{2} \left| \frac{\boldsymbol{u}^{n+1} - \boldsymbol{u}^n}{\Delta t} \right|^2 \mathrm{d}\boldsymbol{x} + \int_{\Omega} \frac{\rho}{2} \left| \frac{\boldsymbol{u}^{n+1} - 2\boldsymbol{u}^n + \boldsymbol{u}^{n-1}}{\Delta t} \right|^2 \mathrm{d}\boldsymbol{x} + \int_{\Omega} \frac{\eta_p}{\lambda} |\boldsymbol{\epsilon}(\boldsymbol{u}^{n+1})|^2 \, \mathrm{d}\boldsymbol{x}$$

$$+ \int_{\Omega} \frac{2\eta_p}{\lambda} |\boldsymbol{\epsilon}(\boldsymbol{u}^{n+1} - \boldsymbol{u}^n)|^2 \, \mathrm{d}\boldsymbol{x} + \Delta t \int_{\Omega} 2\eta_s \left| \boldsymbol{\epsilon}\left(\frac{\boldsymbol{u}^{n+1} - \boldsymbol{u}^n}{\Delta t} \right) \right|^2 \mathrm{d}\boldsymbol{x}$$

$$= \int_{\Omega} \frac{\rho\lambda}{2} \left| \frac{\boldsymbol{u}^n - \boldsymbol{u}^{n-1}}{\Delta t} \right|^2 \mathrm{d}\boldsymbol{x} + \int_{\Omega} \frac{\eta_p}{\lambda} |\boldsymbol{\epsilon}(\boldsymbol{u}^n)|^2 \, \mathrm{d}\boldsymbol{x}.$$

Summing from $n = 0$ to $n = N - 1$, it yields the discrete counterpart of (3.20):

$$\int_{\Omega} \rho \left| \frac{\boldsymbol{u}^N - \boldsymbol{u}^{N-1}}{\Delta t} \right|^2 \mathrm{d}\boldsymbol{x} + \int_{\Omega} \frac{2\eta_p}{\lambda} |\boldsymbol{\epsilon}(\boldsymbol{u}^N)|^2 \, \mathrm{d}\boldsymbol{x} + \Delta t \sum_{n=0}^{N-1} \int_{\Omega} 4\eta_s \left| \boldsymbol{\epsilon}\left(\frac{\boldsymbol{u}^{n+1} - \boldsymbol{u}^n}{\Delta t} \right) \right|^2 \mathrm{d}\boldsymbol{x}$$

$$\leq \int_{\Omega} \rho \left| \frac{\boldsymbol{u}^1 - \boldsymbol{u}^0}{\Delta t} \right|^2 \mathrm{d}\boldsymbol{x} + \int_{\Omega} \frac{2\eta_p}{\lambda} |\boldsymbol{\epsilon}(\boldsymbol{u}^1)|^2 \, \mathrm{d}\boldsymbol{x}.$$

It also correspond to the multiple phases counterpart of the a priori estimate (1.41) in the case $\alpha = 0$. Numerical experiments are presented in the next chapter.

4 Numerical experiments of multiple incompressible viscoelastic free-surface flows

In this chapter, validation of the multiphase model is presented. First, the collision between elastic structures is studied. Two sets of parameters are used, and the convergence of both time discretisation schemes is analysed. Both elastic material split after collision, thus changes of topology are observed and explained.

A simulation of multiple incompressible Newtonian and viscoelastic flows is provided. A viscoelastic droplet is immersed in a Newtonian fluid and flows in a constricted tube. Convergence of the numerical scheme is shown and compared to the numerical results of a referenced article [ZIM17].

Fluid-structure interaction is investigated. First, an elastic material falls in a Newtonian fluid due to gravity. It deforms but never touches the boundary of the cavity, extending a result in [Hil07]. The performances of the different decompression algorithms are compared. A shock absorber experiment is then proposed, where three different phases are involved. An elastic material, immersed in a viscoelastic fluid is enveloped in a mechanical hull. The influence of the relaxation time parameter is studied.

4.1   Collision between two elastic materials

We address the interaction between structures by considering two incompressible Neo-Hookean phases. Two ball-shaped solids collide into each other, inducing large deformations. The two subdomains then split, inducing a change of topology of the computational domain. We present a 3D simulation, where the variables are constant in the $\mathcal{O}z$ axis. The cavity $\Lambda = [-0.43, 0.35]$ m$\times[-0.14, 0.14]$ m$\times[0, 0.02]$ m is considered. The two different materials are defined by their initial subdomains $\Omega_{1,0} = \{(x,y) \in \Lambda; (x+0.135)^2 + y^2 < 0.01\}$ and $\Omega_{2,0} = \{(x,y) \in \Lambda; (x-0.135)^2 + y^2 < 0.01\}$, thus $\varphi_1(\boldsymbol{x}, 0) = 1$ for $\boldsymbol{x} \in \Omega_{1,0}$ and zero elsewhere, and $\varphi_2(\boldsymbol{x}, 0) = 1$ for $\boldsymbol{x} \in \Omega_{2,0}$ and zero elsewhere. The surrounding air is modelled as vacuum and the free surfaces are determined by the characteristic function

$\varphi = \varphi_1 + \varphi_2$. The phases are initialised with the same velocity $\boldsymbol{u}_0 = (\pm 10, 0)$ m/s in opposite directions. In Figure 4.1, the position and velocity of both phases are displayed at initial time $t = 0$ and time $t = 4.3$ ms slightly after the collision. Free-slip boundary conditions are applied on the domain boundary $\partial \Lambda$.
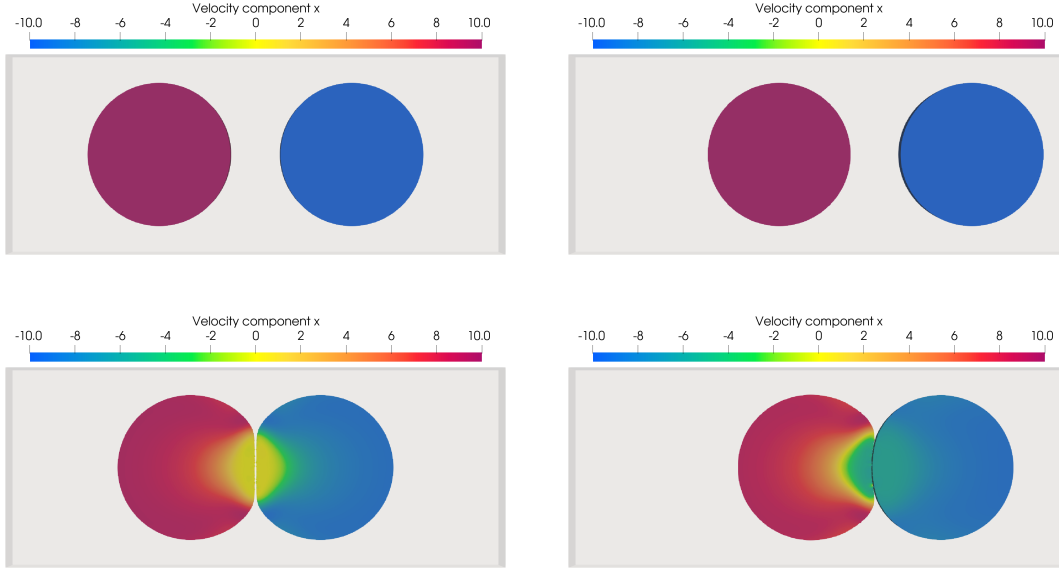
Figure 4.1 – Colliding elastic balls. The component along the axis $\mathcal{O}x$ (horizontal) of the velocity $\boldsymbol{u}_x$ is displayed. Top: initial time $t = 0$ ms. Bottom: deformed materials at $t = 4.3$ ms. Left: P1 set of parameters for phase 2. Right: $P2$ set of parameters for phase 2.

The material corresponding to φ_1 has the following set of parameters: $\rho_1 = 1000$ kg/m^3, $\eta_{s,1} = 0$ Pa s, $\eta_{p,1} = 2 \cdot 10^4$ Pa s, $\lambda_1 = 0.01$ s and $\alpha_1 = 0$. It corresponds to an incompressible Neo-Hookean solid with an analogous density and Young modulus as rubber. Two sets of parameters have been chosen for the second material in order to run different simulations:

P1: In the first setting, the two phases correspond to the same material ($f_1 = f_2$, for $f = \rho, \eta_s, \eta_p, \lambda, \alpha$) and we expect to observe symmetry in our numerical computations.

P2: In the second setting, the material is more dense ($\rho_2 = 2000$ kg/m^3) and more rigid ($\eta_{p,2} = 10^5$ Pa s), where the other parameters remain identical ($\eta_{s,1} = \eta_{s,2}$, $\lambda_1 = \lambda_2$ and $\alpha_1 = \alpha_2$). The second phase being more dense, it has more momentum than the first phase.

Both EVSS (3.15) and implicit (3.16) schemes are applied to run the simulations. In the coarse settings, the time step is $\Delta t = 0.538$ ms with final time $T = 21.5$ ms, the cell grid

size is $h = 4.375$ mm and the average finite element diameter is $H = 15$ mm. In Figures 4.2 and 4.3, the velocity component $\boldsymbol{u}_x$ of the barycenter of each phase is monitored through time. In Figure 4.2, the set of parameters P1 is used, where the parameters are the same for each phase. We can observe that the symmetry of the curves is obtained for both schemes, by multiplying the value of the curve by -1. The elastic effects makes the phases bounces off each other and the velocity becomes negative smoothly. The symmetry is broken in Figure 4.3, when the second set of parameters is used. The less dense material is pulled backward with a velocity norm close to its original one, while the more dense loses movement energy. We can notice that the material gets a positive velocity at $t = 9$ ms for the implicit scheme, while it is almost stopped for the EVSS scheme.

Figure 4.2 – Colliding elastic balls. Horizontal velocity $\boldsymbol{u}_x$ of the barycenter of each phase for $0 \leq t \leq 9$ ms for the first set of parameters P1. Top: EVSS scheme (3.15). Bottom: implicit scheme (3.16). Left: First phase. Right: Second phase.

The exact solution for this problem is not known. Nevertheless, convergence is observed for the implicit scheme (3.16) for both sets of parameters P1 and P2. Here, the EVSS scheme (3.15) is less accurate. As mentioned in Remark 1.5.2 for $L = 1$, the EVSS scheme is less accurate if η_p is larger than one. Furthermore, let us consider the kinetic and elastic energy (1.67) defined in section 1.7. Since $\alpha_\ell = \eta_{s,\ell} = 0$, $\ell = 1, 2$, it yields
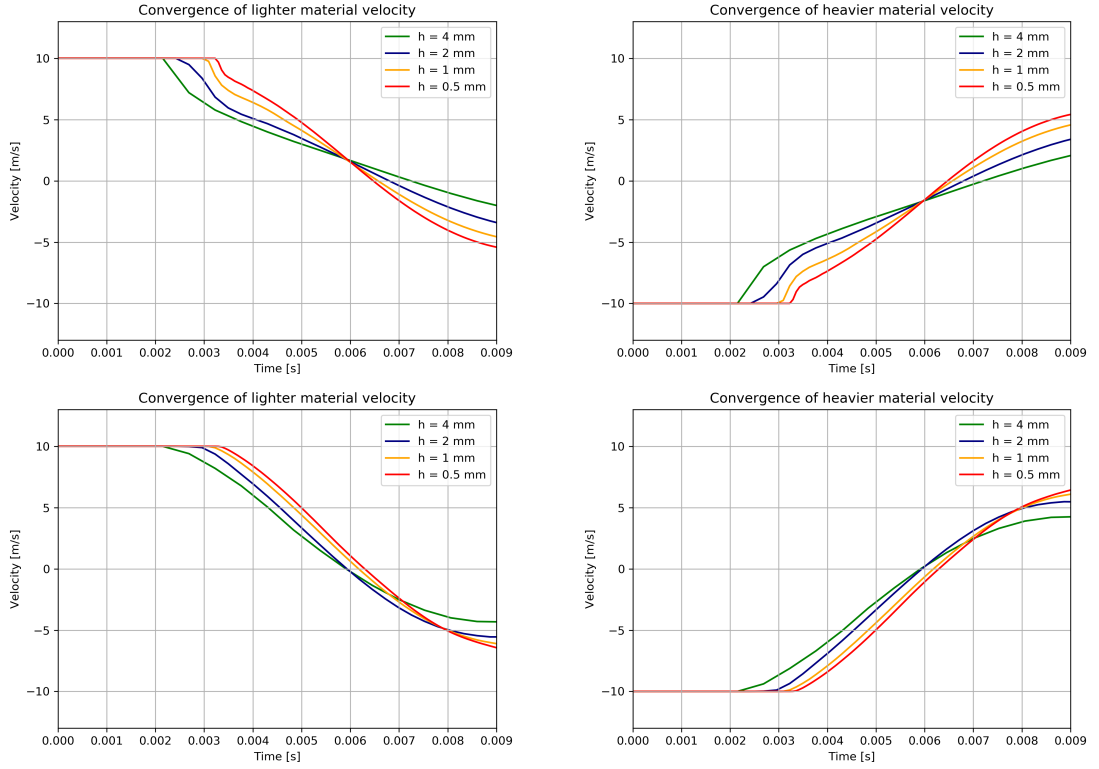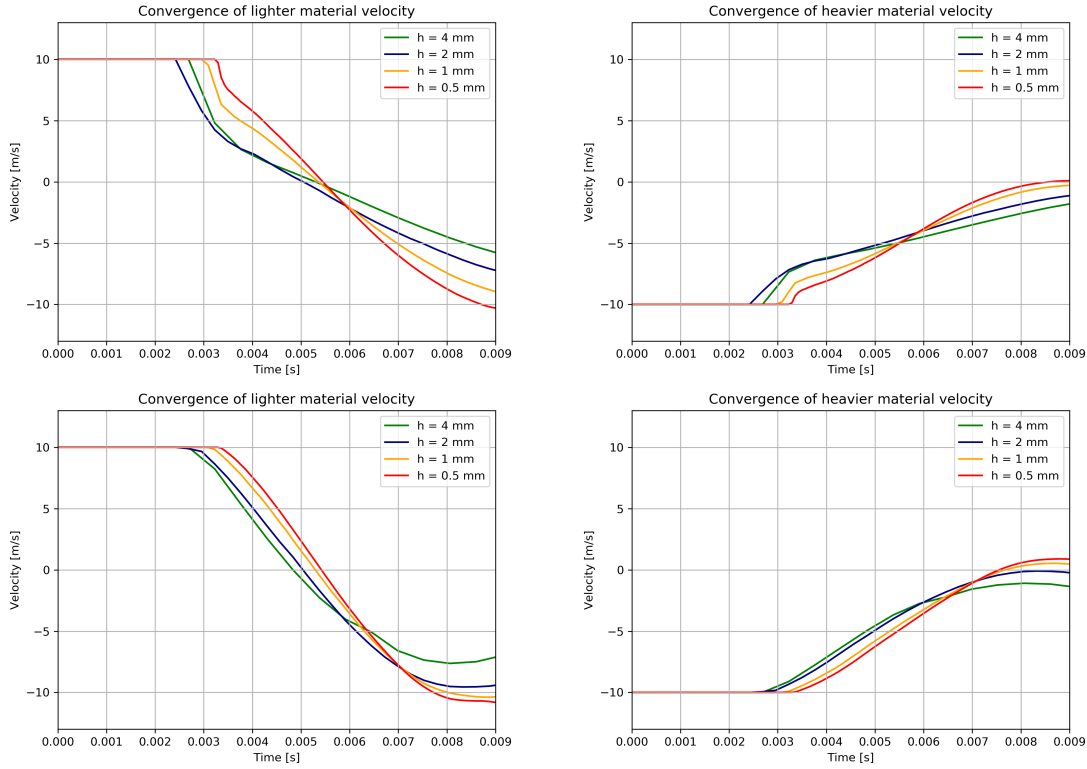
Figure 4.3 – Colliding elastic balls. Horizontal velocity $\boldsymbol{u}_x$ of the barycenter of each phase for $0 \le t \le 9$ ms for the second set of parameters P2. Top: EVSS scheme (3.15). Bottom: implicit scheme (3.16). Left: First phase. Right: Second phase.

$E^n = \int_{\Omega^n} \left(\rho |\boldsymbol{u}_H^n|^2 + \frac{\lambda}{2\eta_p} |\boldsymbol{\sigma}_H^n|^2 \right) \, \mathrm{d}\boldsymbol{x}$, $n = 0, 1, \ldots, N$. The evolution of E^n is displayed in Figure 4.4. Even though the convergence of this quantity is not guaranteed, we can observe that the energy of the EVSS scheme decreases strongly when the balls collide, while it remains smooth using the implicit scheme.

Finally, the different set of parameters in a simulation affect the condition number of the linear system, solved using the GMRES algorithm with an ILU preconditioner. In Figure 4.5, the number of iterations of the GMRES solver is displayed for the simulation for both sets of parameters P1 and P2 in the case $h = 1$ mm for both schemes. It shows that the linear system computed with the EVSS scheme requires more iterations than the one for the implicit scheme. As expected, we notice that the use of two phases with different parameters (P2) than only one set of parameters for both phases (P1) implies a worse conditioning of the linear system. The RAM memory and CPU time to compute the simulations for the implicit scheme are summarised in the following table:
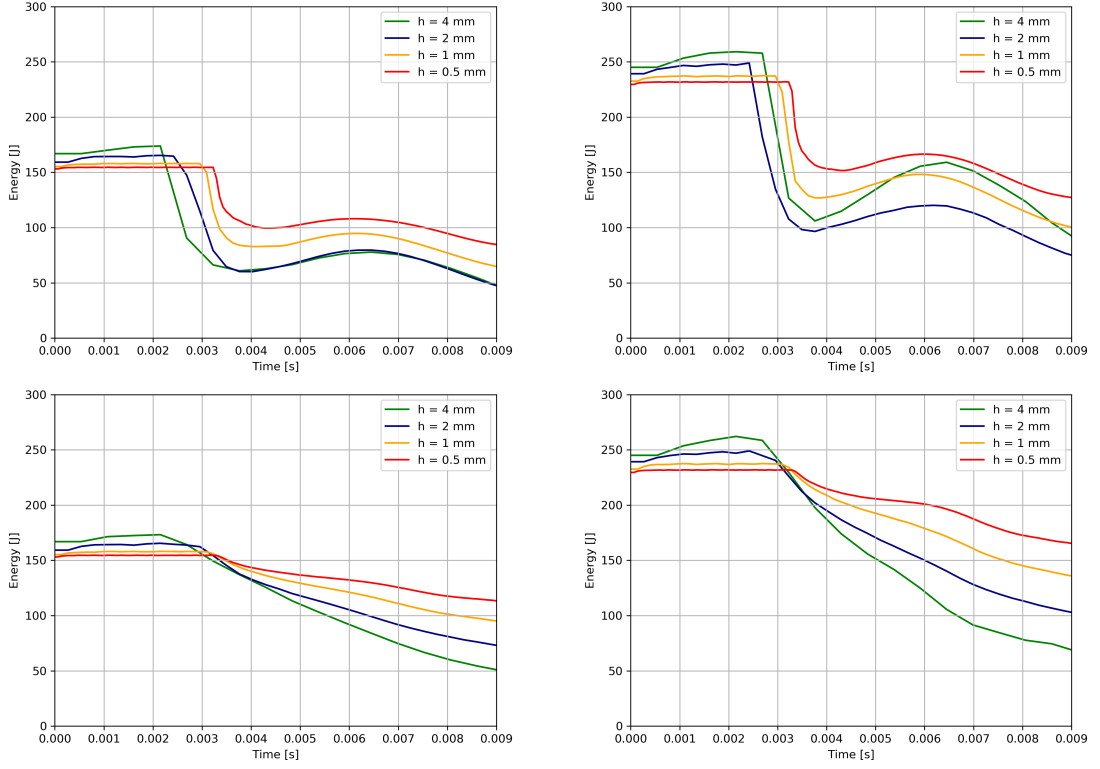
Figure 4.4 – Colliding elastic balls. Kinetic and elastic energy evolution. Top: EVSS scheme (3.15). Bottom: implicit scheme (3.16). Left: P1 set of parameters. Right: P2 set of parameters.

	Set of parameters P1			Set of parameters P2	
h [mm]	memory [GB]	CPU time [h]	h [mm]	memory [GB]	CPU time [h]
4.375	0.14	0.015	4.375	0.141	0.015
2.2	0.676	0.189	2.2	0.67	0.192
1.1	4.041	3.32	1.1	4.254	3.36
0.55	31.5	66.48	0.55	32.84	67.89

The velocity $\boldsymbol{u}$ and extra-stress tensor $\boldsymbol{\sigma}$ are monitored on the horizontal axis along the line $\mathcal{O}x$ ($y = 0, z = 0.01$) at time $t = 4.3$ ms, when the shock has happened and the phases are deforming. In Figure 4.6, the profile of velocity is displayed for both set of parameters for the implicit scheme (3.16). The convergence is observed for both sets of parameters P1 and P2 as well. The symmetry is indeed obtained for the first set of parameters P1. In Figure 4.7, the component xx of extra-stress $\boldsymbol{\sigma}_{h,xx}^{n}$ is displayed along the $\mathcal{O}x$ axis. The momentum is higher in the second set of parameters P2, as well as the consequent force around the interface.

In order to validate the multiphase model (3.4), with respect to the unified model for $L = 1$ (1.1), a numerical experiment using the numerical framework presented in chapter
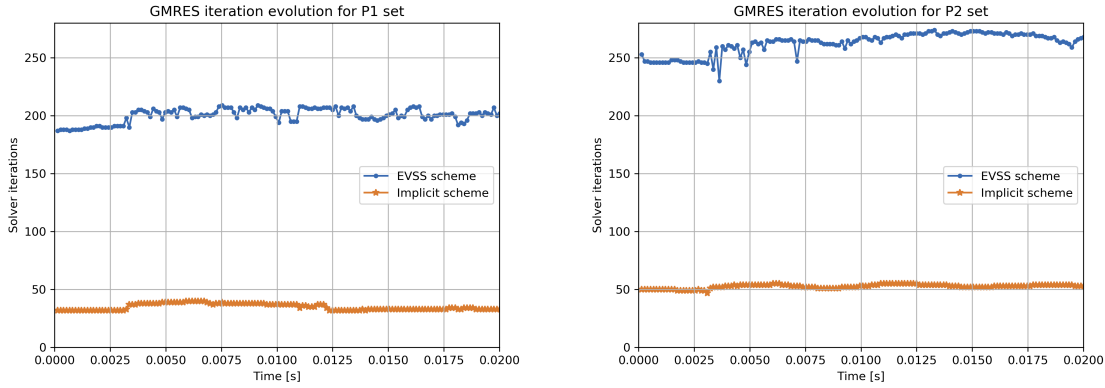
Figure 4.5 – Colliding elastic balls. Comparison of GMRES iterations between schemes EVSS scheme (3.15) implicit scheme (3.16). Left: P1 set of parameters. Right: P2 set of parameters.
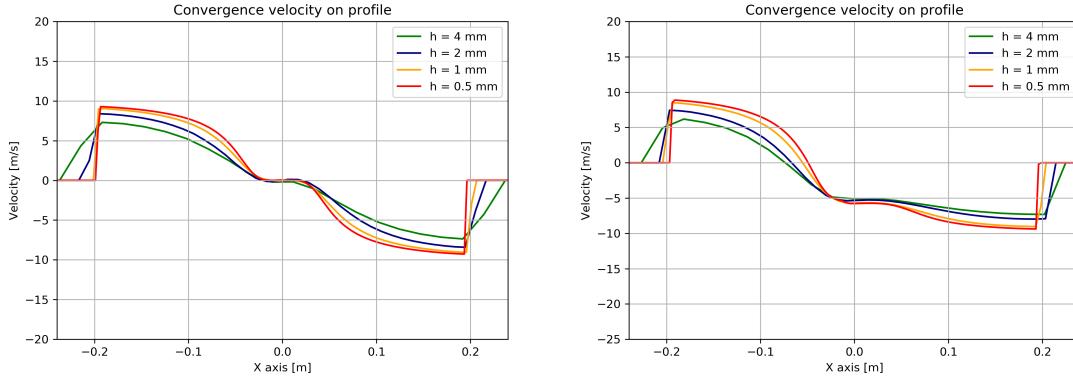
Figure 4.6 – Colliding elastic balls. Velocity $\boldsymbol{u}_x$ along the axis $\mathcal{O}x$ at time $t = 4.3$ ms for the implicit scheme (3.16). Left: first set of parameters for φ_2. Right: second set of parameters for φ_2.

1 is run using the same parameters for each phase, that is the set of parameters P1, using the implicit scheme (1.28) for the model using one phase, and the implicit scheme (3.16) for the multiphase model. In Figure 4.8, the profile of velocity is displayed for both numerical models for two different time steps. The profile of the velocity remains identical for both numerical framework until the materials split. In the second figure, the material just splitted and the velocity is large. Small differences can be spotted in this case. This can be explained by the difference in the numerical algorithms applied to take into account the multiple phases.

In Figure 4.9 the profile of the velocity on cells are displayed at time $t = 17.2$ ms for the set of parameters P1. The momentum of both materials allows the phases to split, changing the topology of the domain $\Omega(t)$. The continuity condition of the velocity on the interface (3.6) should not allow this change of topology. It is a numerical artefact,
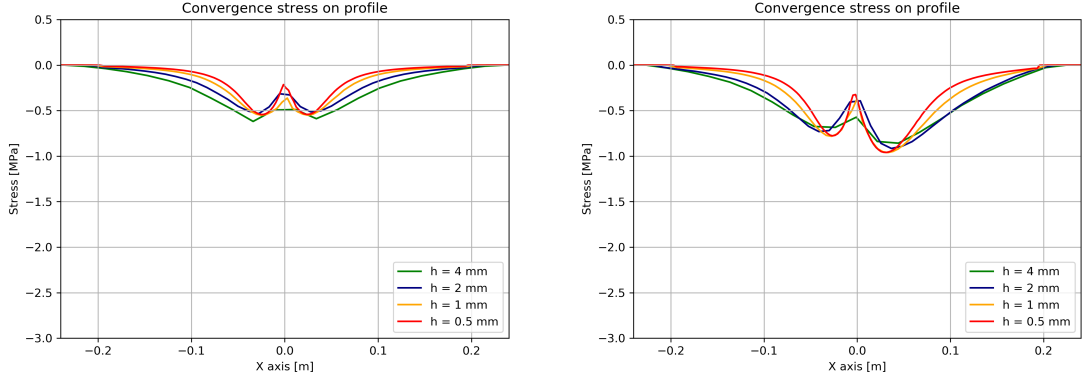
Figure 4.7 – Colliding elastic balls. Component xx of extra-stress $\boldsymbol{\sigma}_{xx}$ along the axis $\mathcal{O}x$ ($y = 0, z = 0.01$) at time $t = 4.3$ ms for the implicit scheme (3.16). Left: first set of parameters for φ_2. Right: second set of parameters for φ_2.
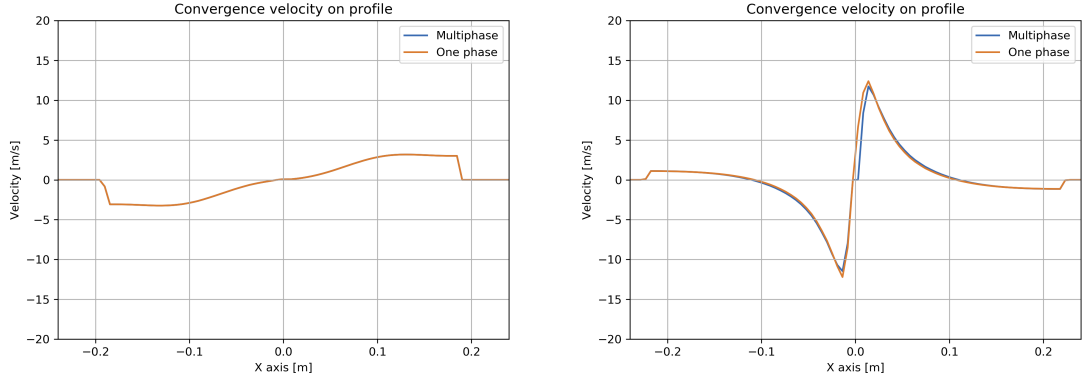
Figure 4.8 – Colliding elastic balls. Velocity $\boldsymbol{u}_x$ along the axis $\mathcal{O}x$ for the implicit scheme (3.16) using the unified model (1.1) and the multiphase model (3.4) for the set of parameters P1. Left: $t = 7$ ms . Right: $t = 14$ ms.

due to the method of characteristics and the SLIC and decompression algorithms. If the gradient of the velocity is large enough at the interface, the VOF on cells is transported because the velocity is not zero. We can notice this splitting on the monitored velocity when a gap is obtained between both phases. Thus, topology change is obtained for $h < 8$ mm with the implicit scheme and for $h < 2$ mm for the EVSS scheme.

This change of topology was not obtained for the second set of parameters P2 for both numerical schemes, and the phases remained glued to each other due to the continuity of the velocity. In Figure 4.10, 3D simulations are computed for both sets of parameters P1 and P2, using the implicit scheme (3.16). The cavity $\Lambda = [-0.43, 0.35]$ m$\times[-0.14, 0.14]$ m$\times[-0.14, 0.14]$ m is now considered. The two different materials are now spheres and defined by their initial subdomains $\Omega_{1,0} = \{(x, y) \in \Lambda; (x + 0.135)^2 + y^2 + z^2 < 0.01\}$ and $\Omega_{2,0} = \{(x, y) \in \Lambda; (x - 0.135)^2 + y^2 + z^2 < 0.01\}$.

97
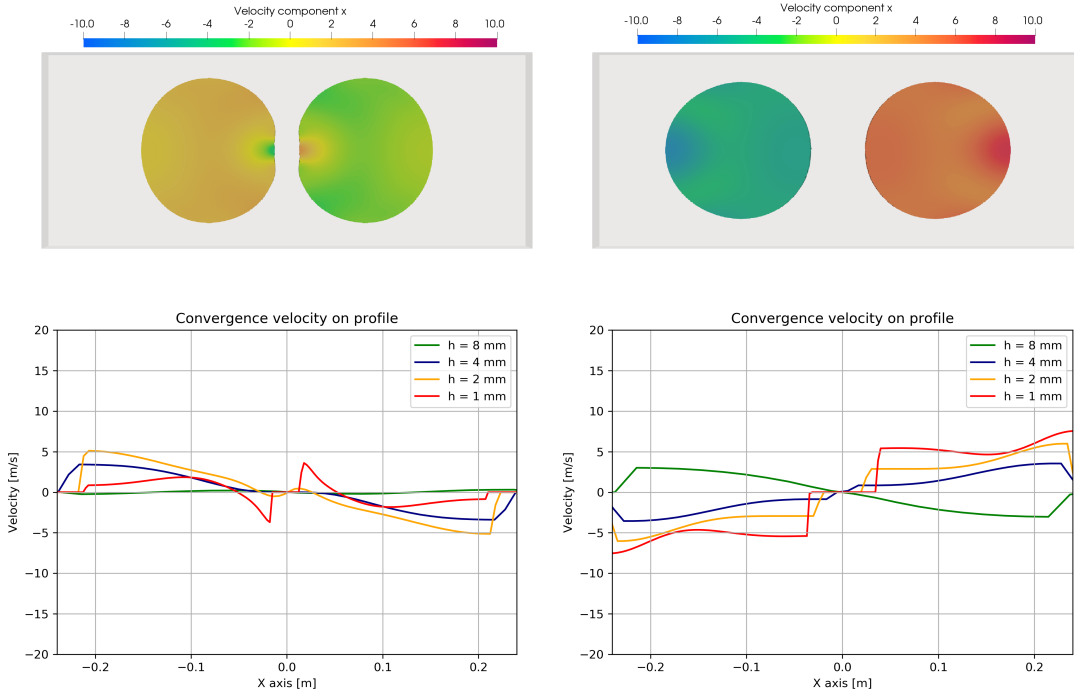
Figure 4.9 – Colliding elastic balls. Change of topology appear when velocity is equal to 0 on graph. Top: Velocity $\boldsymbol{u}_x$ along the axis $\mathcal{O}x$ at time $t = 17.2$ ms. Bottom: Velocity $\boldsymbol{u}_x$ on cells. Left: EVSS scheme (3.15). Right: implicit scheme (3.16).

Small defects on the surface of the first material ($\varphi_1 = 1$) can be observed. They are due to SLIC and decompression algorithms, designed for a fluid numerical scheme. In this case, the materials are splitted for both sets of parameters P1 and P2. Since this phenomenon is a numerical artefact, the momentum of the balls decreases. Indeed, the continuity of the velocity at the interface implies that the heavy material holds back the light one.

Nevertheless, a change of topology is expected as a physical reality: two rubber balls colliding with each other then repel each other. The mathematical framework that we use unfortunately does not allow us to reproduce this result. Our thoughts on future work on the problem are the following. In chapter 2, Signorini boundary conditions (2.12) are imposed on the boundary of the cavity in order to let the ball bouncing upwards, where the normal force $\boldsymbol{T}_{n,H}^{n-1} = (\boldsymbol{T}_H^{n-1}\boldsymbol{n}) \cdot \boldsymbol{n} = ((2\eta_s \boldsymbol{D}_H^{n-\frac{1}{2}} + \boldsymbol{\sigma}_H^{n-\frac{1}{2}})\boldsymbol{n} - p_H^{n-1}\boldsymbol{n}) \cdot \boldsymbol{n}$ is computed on the domain boundary. A similar condition as the Signorini boundary conditions could thus be imposed at the interface. If $\boldsymbol{T}_{n,H}^{n-1} > 0$, the materials tend to split. In this particular case, the continuity condition must be artificially broken. The algorithm would rely on removing cells in active regions, in order to break the contact between the materials. It would result in a discontinuity in the velocity which would allow to separate the materials, although yielding a loss of mass. This is future work.
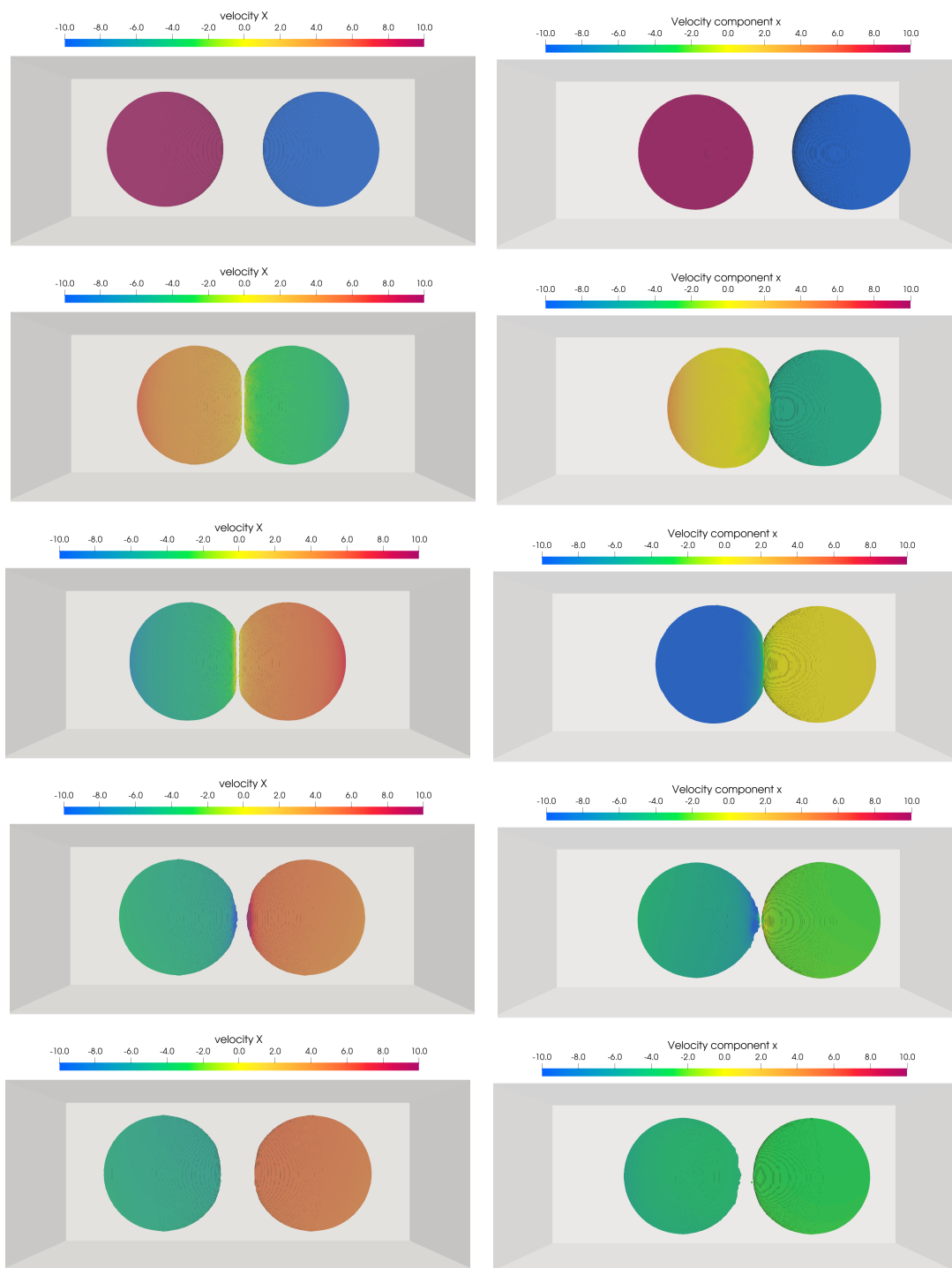
Figure 4.10 – Colliding elastic balls. Velocity $\boldsymbol{u}_x$ for the two phases, specified by the characteristic functions φ_1 (left) and φ_2 (right). From top to bottom: $t = 0, 6, 8, 12, 16$ ms. Left: first set of parameters for φ_2. Right: second set of parameters for φ_2.

4.2 Interactions between Newtonian and Oldroyd-B fluids

In this section, we consider the flow of multiple Oldroyd-B viscoelastic fluids. To validate our model, the numerical experiments in [ZIM17] are reproduced. In this article, a viscoelastic droplet is immersed in a Newtonian fluid, flowing in a constricted tube, see Figure 4.11. Several necks are presented in [ZIM17], the sharp-edged neck in the tube has been chosen here, since our numerical scheme can capture the singularity (see machining experiment, in section 2.3.2).

x
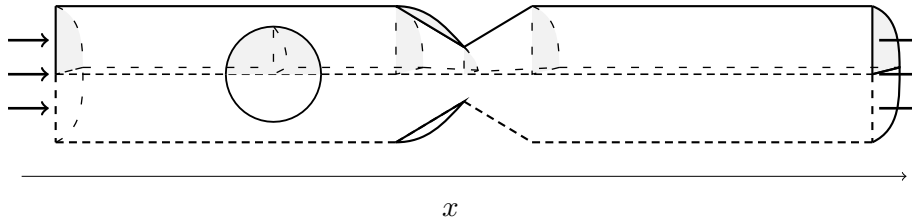
Figure 4.11 – Constricted tube. Sketch of the numerical experiment. A viscoelastic droplet is immersed in a Newtonian flow, with inflow on the left and outflow on the right. Half of the pipe is presented, but numerical simulations are computed on a quarter of the pipe. It preserves the symmetry of the experiment and earns computational time.

The cavity is a cylinder of length $L = 12$ m and of radius $R = 1$ m. The neck has length $2R = 2$ m and height $0.6R = 0.6$ m. The axial symmetry of the simulation allow to only simulate one quarter of the cylinder, see Figure 4.12. Thus, the cavity Λ is a subdomain of the rectangular domain $[-6, 6]$ m$\times[0, 1]^2$ m^2. An inflow is set on the surface $\{x = -6\}$, with a parabolic profile for the velocity $\boldsymbol{u}_{\text{in}} = V(1 - (y^2 + z^2), 0, 0)$, where V is a Reynolds dependent parameter. An outflow is set on the opposite side boundary, where we impose zero-force on the boundary. Free-slip boundary conditions are set on the surface $\{y = 0\}$ and $\{z = 0\}$ on the symmetry axes and no-slip boundary condition are set on the remaining curved boundaries. A Newtonian fluid, characterised by the function φ_1, flows in the domain and carries the viscoelastic droplet away, characterised by the function φ_2. The non-dimensional parameters used in [ZIM17] are

$$Re = \frac{5\rho_1 V R}{2(\mu_{s,1} + \mu_{p,1})} = 10, \quad Wi = \frac{\lambda_2 V}{R} = 1,$$

respectively defining the Reynolds and Weissenberg numbers and

$$\beta = \frac{\mu_{s,2}}{\mu_{s,2} + \mu_{p,2}} = 0.5, \quad \theta = \frac{\mu_{s,2} + \mu_{p,2}}{\mu_{s,1} + \mu_{p,1}} = 2, \quad \alpha = \frac{\rho_2}{\rho_1} = 1,$$

being the solvent viscosity, viscosity and density ratios. This yields the following set of parameters: for a radius $R = 1$ m, a velocity $V = 1$ m/s, the Newtonian fluid has the parameters $\rho_1 = 1$ kg/m^3, $\mu_{s,1} = 0$ Pa s, $\mu_{p,1} = 0.25$ Pa s, $\lambda_1 = 0$ s and $\alpha_1 = 1$.

The Oldroyd-B viscoelastic fluid has the parameters $\rho_2 = 1$ kg/m^3, $\mu_{s,2} = 0.25$ Pa s, $\mu_{p,2} = 0.25$ Pa s, $\lambda_2 = 1$ s and $\alpha_2 = 1$.
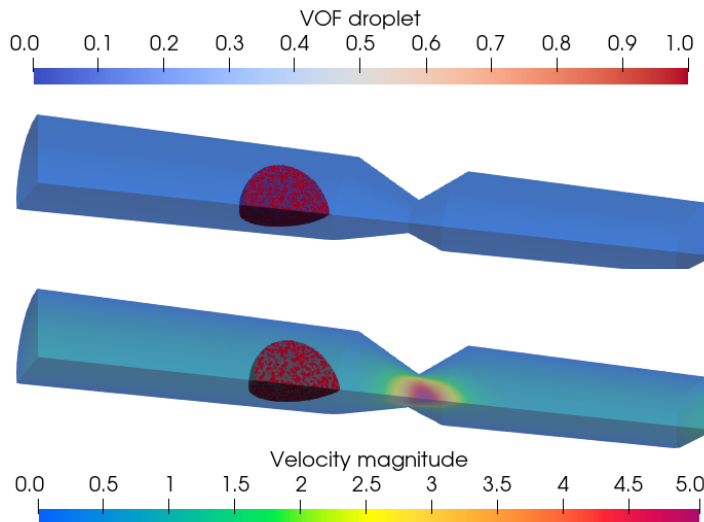
Figure 4.12 – Constricted tube. Velocity in the FE mesh and characteristic function φ_2 for the viscoelastic droplet. Top: $t = 0$. Bottom: $t = 0.5$ s.

A first numerical simulation is computed in order to test the convergence of the velocity and pressure. Four mesh sizes are used, where the coarser settings are the following: the average FE mesh diameter is $H = 0.2$ m, and more precision is imposed at the neck with $H = 0.1$ m. The grid cell diameter is $h = 0.05$ m and the time step is $\Delta t = 0.008$ s. The initial viscoelastic droplet is $\Omega_{2,0} = \{\boldsymbol{x} = (x, y, z) \in \Lambda; \|\boldsymbol{x} - (-2.8, 0, 0)\| < 0.7\}$. The simulation is stopped when a laminar flow is obtained, thus at a final time $T = 0.5$ s. In Figure 4.13, the profile of the velocity component $\boldsymbol{u}_x$ and the pressure p along the axis $\mathcal{O}x$ is displayed at final time T. Convergence of the results are obtained, with a lower precision on the pressure.

For the next numerical experiment, the initial viscoelastic droplet is $\Omega_{2,0} = \{\boldsymbol{x} = (x, y, z) \in \Lambda; \|\boldsymbol{x} - (-2, 0, 0)\| < 0.7\}$. The initial velocity $\boldsymbol{u}_0$ and the initial extra-stress tensor $\boldsymbol{\sigma}_0$ are the solutions of the previous numerical results in Figure 4.12. In Figure 4.14 (top), the solution for $h = 0.012$ m is displayed. The VOF function is similar to the results in [ZIM17] up to $t = 0.7$ s. The results become different after that time. In our simulations, the droplet is slowed down at the neck. Furthermore, the velocity of the flow is larger at the center of the cylinder and especially at the neck where the pressure quickly decreases. Thus, the droplet is sped up at its center (at the symmetry axes) and starts to hollow out in the middle when it passes through the neck. It eventually develops a tail at the end of the simulation.
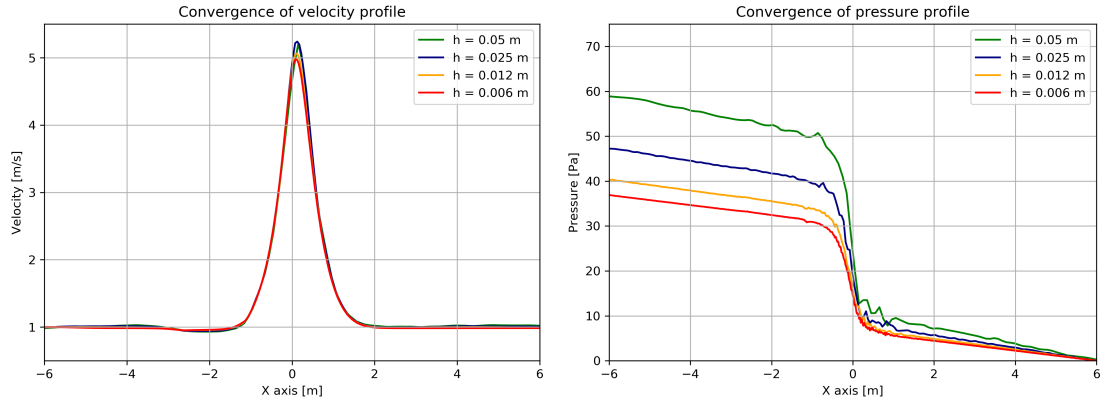
Figure 4.13 – Constricted tube. Simulation of two phases flows without free surface. Profile monitoring along the axis $\mathcal{O}x$ at time $t = 0.3$ s. Left: Velocity component $\boldsymbol{u}_x$. Right: Pressure p.

In order to tackle this problem, a simulation with an increased viscosity ($\mu_{s,2} = \mu_{p,2} = 2$) is performed in Figure 4.14 (bottom). The hole at the extremity here does not form but it grows a tail anyway. Furthermore, the simulation is slowed down even more. The constitutive equation for the extra-stress tensor in [ZIM17] uses a FENE-CR model, but has a sufficiently low effect on the viscoelastic droplet in order for us to compare our results. Indeed, this model implies finite extensibility of the dumbells, for maximum elongation L_0. But this parameter is here taken to be very high, implying a behaviour close to an Oldroyd-B fluid.

Finally, the addition of surface tension in the model of [ZIM17] has a real impact on the droplet. Indeed, it is controlled by the capillary number $C_a = (\mu_{s,1} + \mu_{p,1})V/\sigma$, where σ denotes the surface tension coefficient. In their simulation, this number is taken very low and implies a strong effect of the surface tension. It is further motivated by the tail growing at the end of the droplet, which would be prevented by a strong force at the interface. Finally, a study on the effect of the capillary number has been carried on in [ZIM17], which shows that the droplet is hollowing out when the capillary number increases (no surface tension is obtained when the limit goes to infinity). In order to take into account the surface tension in our model, the algorithm would rely on a similar approach as in [CHMP21], where the mesh is adapted to fit on the free surfaces and on the multiphase interface, corresponding to the nodes where $0 \leq \varphi_{\ell,H}, \varphi_{m,H} < 1$, $\ell \neq m$ for at least two phases $\ell, m = \{1, \ldots, N\}$. A convolution smoothing $\nabla\tilde{\varphi}_\ell$ of the characteristic function φ_ℓ is applied in order to compute $\boldsymbol{n} = \nabla\tilde{\varphi}_\ell / \|\nabla\tilde{\varphi}_\ell\|$ and the mean curvature $k = \nabla \cdot (\nabla\tilde{\varphi}_\ell / \|\nabla\tilde{\varphi}_\ell\|)$ [Cab06]. This is future work.
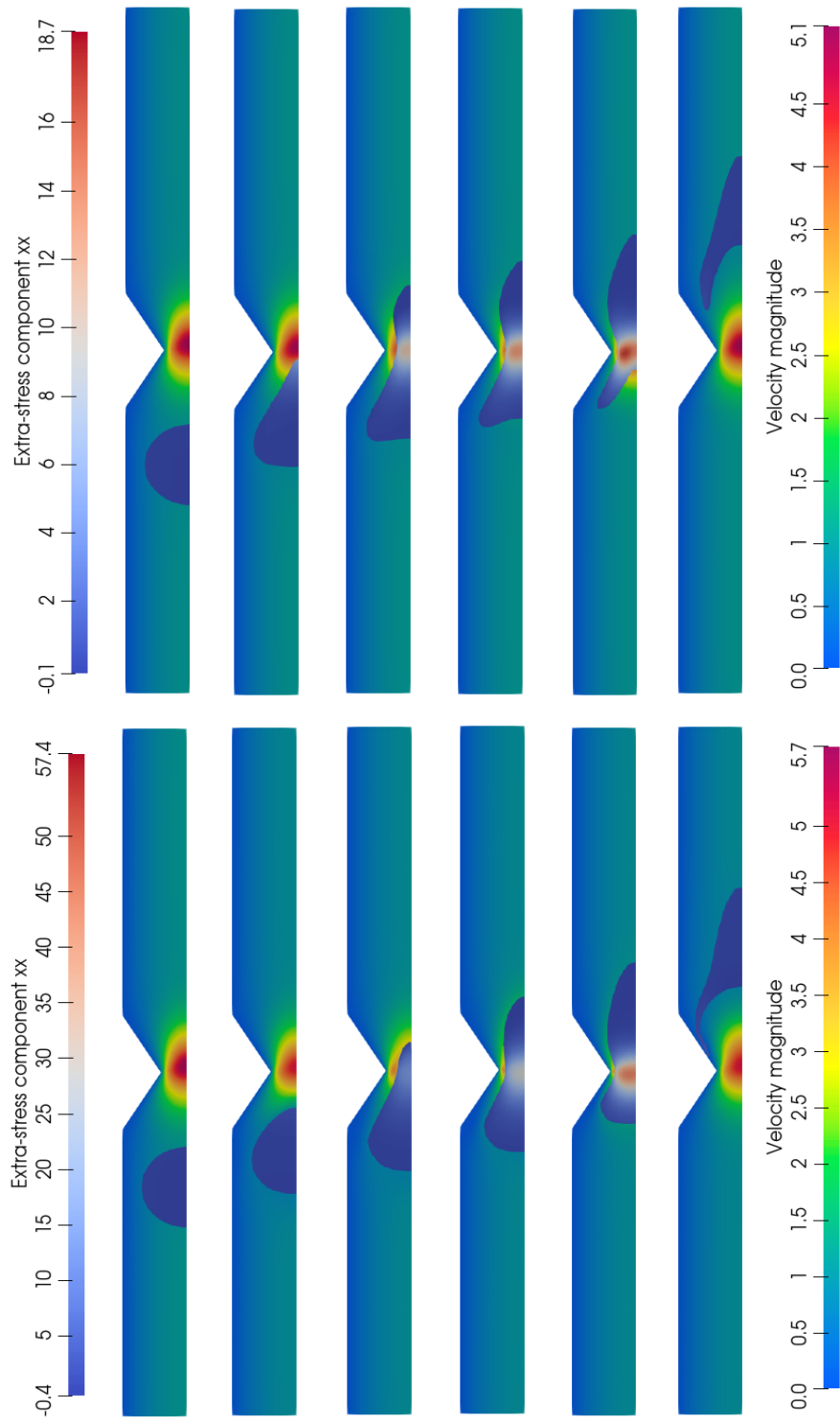
Figure 4.14 – Constricted tube. Velocity in the FE mesh and extra-stress component $\boldsymbol{\sigma}_{zz}$ for the viscoelastic droplet on cells. Top: $\eta_{s,2} = \eta_{p,2} = 0.25$. Bottom: $\eta_{s,2} = \eta_{p,2} = 2$. From left to right: $t = 0, 0.75, 1.25, 1.625, 2.125, 3.5$ s.

4.3   Lack of collision of a deformable elastic disk immersed in a Newtonian fluid

Consider a cavity $\Lambda \in \mathbb{R}^2$, filled with a Newtonian fluid and containing an immersed rigid body, with the shape of a disk. Gravity forces then drive the material towards the bottom of the cavity. In [Hil07], it is proved that the body never touches the bottom of the cavity. This lack of collision between the material and the boundary was reproduced numerically in [DPW21], where a space-time adaptive algorithm catches the pressure peak observed when the material reaches the boundary of the domain. For a deformable elastic material, bouncing upwards was observed in [GSST22], for an Eulerian formulation of the Fluid-Structure Interaction model. The goal of this experiment is to benchmark our numerical solver with the result in [GSST22]. Furthermore, the influence of the rigidity of the elastic disk is studied.

Similarly as in section 4.1, pseudo 2D simulations are considered. Consider the domain $\Lambda = [-0.6, 0.6] \text{ m} \times [0, 0.9] \text{ m} \times [0, 0.02] \text{ m}$ and an incompressible Neo-Hookean elastic disk. The immersed incompressible Newtonian fluid domain is characterised by the function φ_1. The parameters are $\rho_1 = 1 \text{ kg/m}^3$, $\eta_{s,1} = 0.2 \text{ Pa s}$, $\eta_{p,1} = 0 \text{ Pa s}$, $\lambda_1 = 0 \text{ s}$ and $\alpha_1 = 1$. The incompressible Neo-Hookean material phase is initialised in the subdomain $\Omega_{2,0} = \{(x, y, z) \in \Lambda; x^2 + (y - 0.3)^2 < 10^{-2}\}$, with the parameters $\rho_2 = 1001 \text{ kg / m}^3$, $\eta_{s,2} = 0 \text{ Pa s}$, $\lambda_2 = 0.01 \text{ s}$ and $\alpha_2 = 0$. Two different values are used for the parameter $\eta_{p,2} \in \{50, 500\} \text{ Pa s}$. This yields a shear modulus parameter of the elastic material of $\{5, 50\} \text{ kPa}$. No external forces are considered and the initial velocity is $\boldsymbol{u}_0 = (0, -0.5, 0) \text{ m/s}$ in $\Omega_{1,0}$ and $(0, 0, 0) \text{ m/s}$ in $\Omega_{2,0}$. The solution is smoothed by the correction step at the first iteration. Three mesh sizes are considered for the convergence study. In the coarse settings, the maximum diameter of the FE mesh is $H = 28 \text{ mm}$ and is reduced to $H = 5 \text{ mm}$ near the boundary in order to better capture the pressure at the bottom of the domain. The grid cells diameter is $h = 5 \text{ mm}$ and the time step is $\Delta t = 0.0045 \text{ s}$. The results are displayed in Figure 4.15 for both values of $\eta_{p,2}$, when the pressure at the bottom of the cavity is maximum and at the end of the simulation. We can observe larger deformations of the elastic disk for the softer material.

In Figure 4.16, the evolution of the position of the bottom of the disk in time is shown for the soft material ($\eta_{p,2} = 50 \text{ Pa s}$) and the more rigid one ($\eta_{p,2} = 500 \text{ Pa s}$). In both cases, we can observe convergence of the curves and the elastic disk does not touch the bottom of the cavity. The snapshots on the FE mesh and on the cells grid in Figure 4.17 are captured at $t = 0.3 \text{ s}$ for $\eta_{p,2} = 50 \text{ Pa s}$ and at $t = 0.23 \text{ s}$ for $\eta_{p,2} = 500 \text{ Pa s}$, where the peak of pressure is observed. Several mesh nodes in the fluid between the disk and the boundary shows that the disk does not touch the boundary.
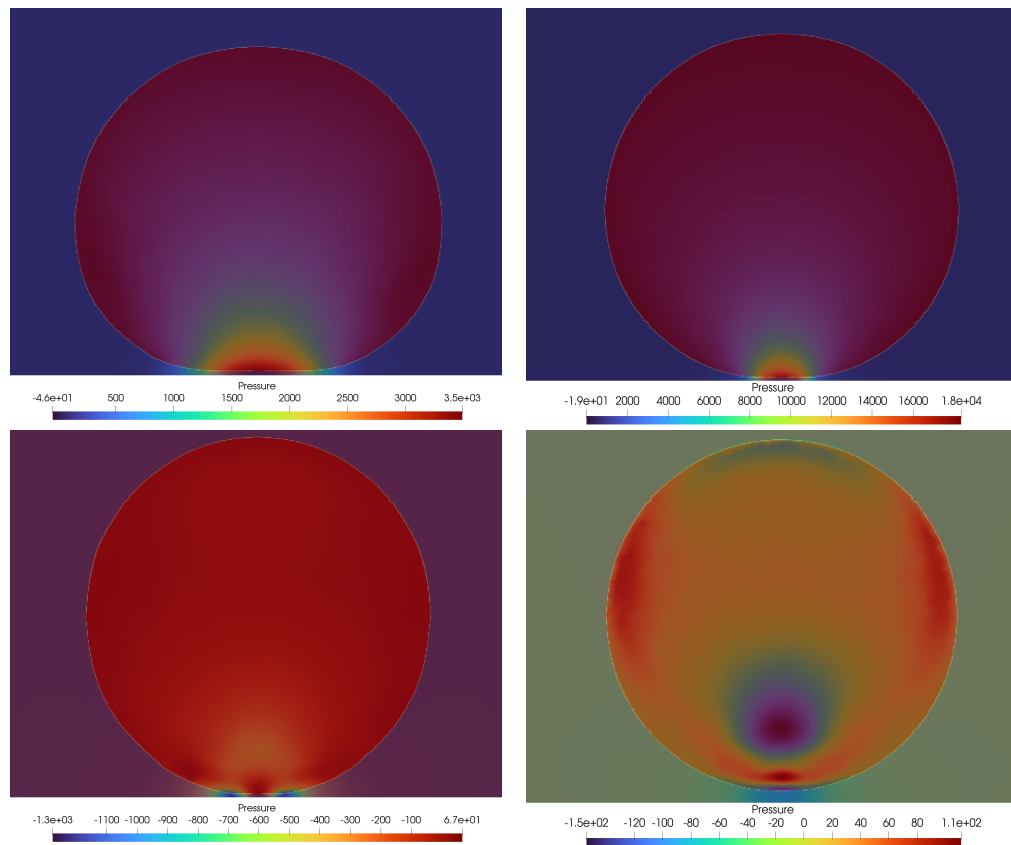
Figure 4.15 – Lack of collision. Pressure at the bottom on FE and VOF disk on cells. Top: pressure peak time. Left: $\eta_{p,2} = 50$ Pa s at $t = 0.3$ s. Right: $\eta_{p,2} = 500$ Pa s at $t = 0.23$ s. Bottom: Depression when bouncing back. Left: $\eta_{p,2} = 50$ Pa s at $t = 0.5$ s. Right: $\eta_{p,2} = 500$ Pa s at $t = 0.4$ s.
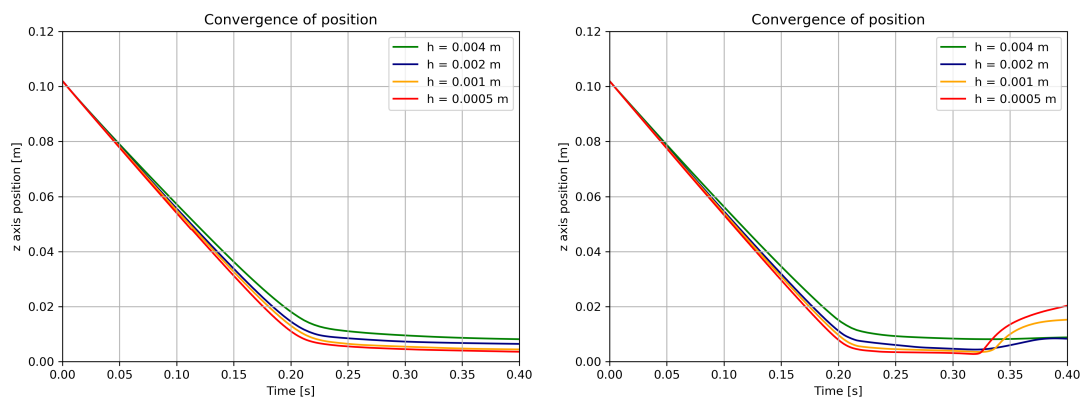
Figure 4.16 – Lack of collision. Evolution of the bottom of the disk. Left: $\eta_{p,2} = 50$ Pa s. Right: $\eta_{p,2} = 500$ Pa s.
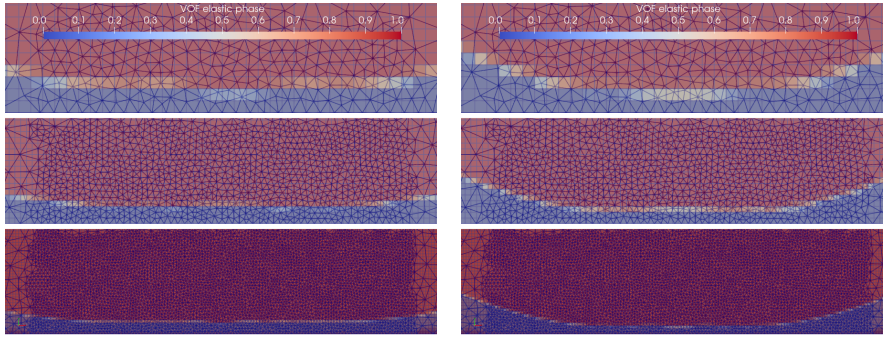
Figure 4.17 – Lack of collision. FE mesh and grid convergence for VOF of the disk, at the time corresponding to the maximum pressure peak and $h = 0.004, 0.002, 0.001$ m. Left: $\eta_{p,2} = 50$ Pa s at $t = 0.3$ s. Right: $\eta_{p,2} = 500$ Pa s at $t = 0.25$ s.

In Figure 4.18, we can see that the pressure peak at the bottom of the cavity is slightly higher that the maximum amount obtained in [GSST22] for $\eta_{p,2} = 500$ Pa s. It is better caught for a sufficiently small mesh size and time step. The peak pressure is smaller for the more soft material, since the bottom is more deformed and flattened, which increases the surface of contact and decreases the maximum pressure. Furthermore, we can observe that the elastic material bounce upwards and a depression appears between the bottom of the disk and the boundary of the cavity.
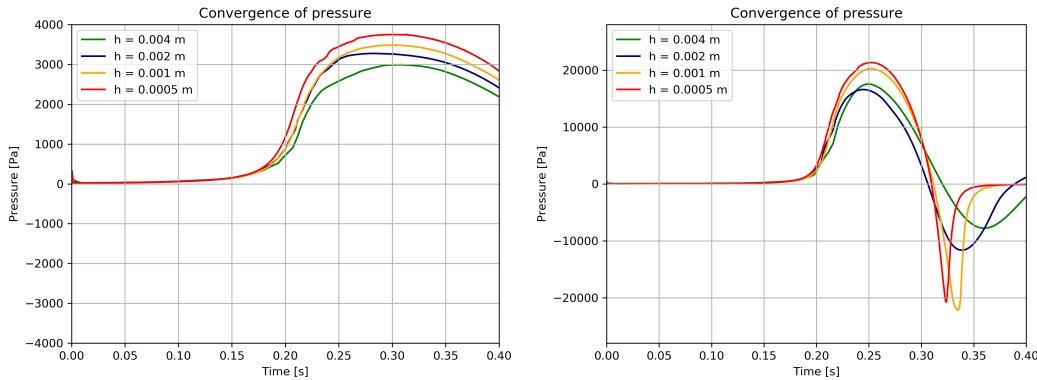
Figure 4.18 – Lack of collision. Evolution of the pressure p at position $(0, 0.002)$. Left: $\eta_{p,2} = 50$ Pa s. Right: $\eta_{p,2} = 500$ Pa s.

In Figure 4.19, the velocity field in the computational domain is displayed at time $t = 0.2$ s and $t = 0.3$ s for $\eta_{s,2} = 500$ Pa s. The velocity is constant in the disk as long as the pressure peak does not form. The boundary layer induced by the fluid incompressibility can be seen. Then, the disk bounces upwards due to elastic effects. Thus, the velocity vortex in the fluid, induced by the disk movement, is inverted.

Finally, the GMRES iterations needed to solve the linear system are displayed in Figure

4.3. Lack of collision of a deformable elastic disk immersed in a Newtonian fluid
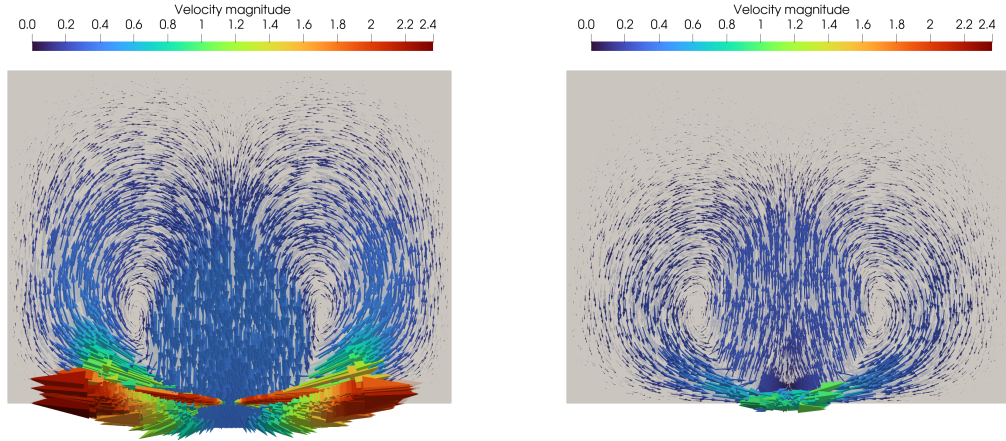
Figure 4.19 – Lack of collision. Simulation of two phases flows without free surface for $\eta_{p,2} = 500$ Pa s. Velocity field $\boldsymbol{u}$. Left: $t = 0.2$ s. Right: $t = 0.3$ s.

4.20. The number of iterations doubles each time the time and space discretisation is divided by two. They also are slightly higher for a bigger value of $\eta_{p,2}$. Together with the numerical experiment in section 4.1, it confirms that a higher discrepancy between the parameters increases the number of iterations of the algorithm. Although, this difference is kept relatively small. The RAM memory and CPU time to compute the simulations for the implicit scheme are summarised in the following table:

	$\eta_{s,2} = 50$ Pa s			$\eta_{s,2} = 500$ Pa s	
h [mm]	memory [GB]	CPU time [h]	h [mm]	memory [GB]	CPU time [h]
5	0.517	0.235	5	0.506	0.236
2.5	2.009	2.09	2.5	2.041	2.16
1.25	8.415	31.44	1.25	8.157	29.52
0.625	38.03	472.24	0.625	40.72	459.12

The results we provided are harder to obtain for a larger value of $\eta_{p,2}$, thus a more rigid material, and when gravity forces are considered. The pressure peak becomes larger and asks for higher order precision to obtain the result, as reached with a space-time adaptive algorithm like in [DPW21]. Thus, we consider the settings of the numerical experiment in [DPW21] for a deformable elastic solid, whose rigidity is slightly larger than the previous experiment. Consider the domain $\Lambda = [-0.05, 0.05]$ m$\times[0, 0.08]$ m$\times[0, 0.005]$ m and an incompressible Neo-Hookean elastic disk. The immersed incompressible Newtonian fluid domain is characterised by the function φ_1. The parameters are $\rho_1 = 1000$ kg/m^3, $\eta_{s,1} = 1$ Pa s, $\eta_{p,1} = 0$ Pa s, $\lambda_1 = 0$ s and $\alpha_1 = 1$. The incompressible Neo-Hookean material phase is initialised in the subdomain $\Omega_{2,0} = \{(x, y) \in \Lambda; x^2 + (y - 0.035)^2 < 10^{-4}\}$, with the parameters $\rho_2 = 10000$ kg / m^3, $\eta_{s,2} = 0$ Pa s, $\eta_{p,2} = 1500$ Pa s, $\lambda_2 = 0.01$ s and $\alpha_2 = 0$. The velocity is initialised to $\boldsymbol{u}_0 = (0, -0.1)$ m/s in $\Omega_{1,0}$ and $(0, 0)$ m/s in $\Omega_{2,0}$. In the coarse settings, the maximum diameter of the FE mesh is $H = 2.8$ mm and
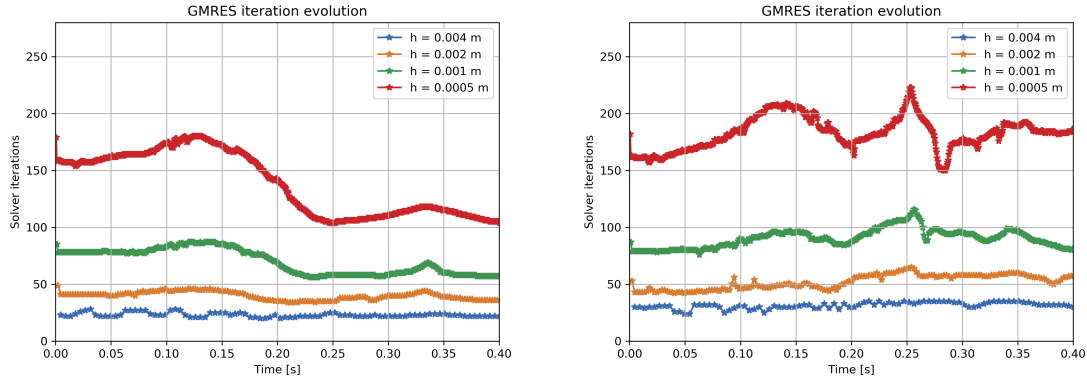
Figure 4.20 – Lack of collision. Comparison of GMRES iterations between both set of parameters. Left: $\eta_{p,2} = 50$ Pa s. Right: $\eta_{p,2} = 500$ Pa s.

is reduced to $H = 0.4$ mm near the boundary in order to better capture the pressure at the bottom. The grid cells diameter is $h = 0.4$ mm and the time step is $\Delta t = 0.0015$ s. The position of the bottom of the disk is displayed on Figure 4.21. From the curves convergence, it shows that the disk stops at approximately 0.2 mm of the boundary. In Figure 4.22, we can see that the pressure peak observed between the disk and the bottom of the cavity is larger for a more rigid disk. In our results, a discrepancy for the velocity and pressure, is observed between the discretisation parameters. The larger between the parameter values in each phase, the larger the discrepancy and the larger the loss of accuracy of the numerical scheme.
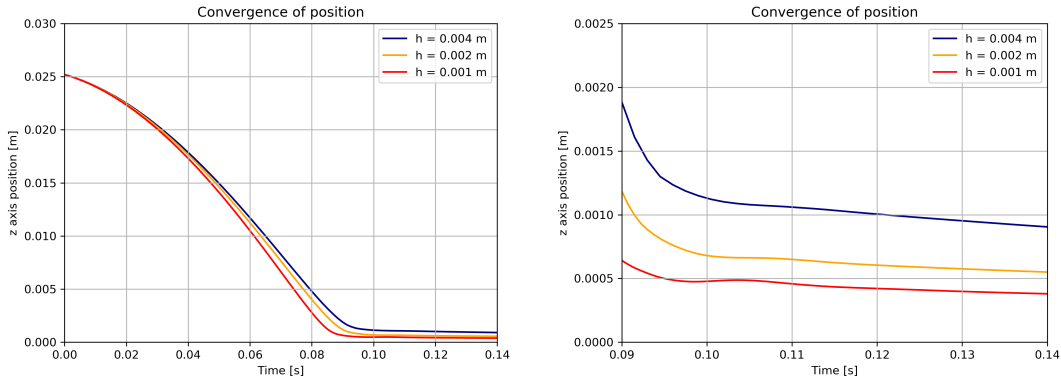
Figure 4.21 – Lack of collision. Left: Evolution of the bottom of the disk. Right: zoom from $t = 0.09$ s to 0.14 s.

In Figure 4.23, the efficiency of the decompression Algorithms 1 and 2 are compared. In the bottom pictures, the amount of fluid which could not be distributed, and hence kept in stock, is displayed with respect to time. This amount is significantly larger for the Algorithm 1. Thus, we notice an optimised efficiency of the decompression algorithm for multiphase simulations when we first loop on the phases instead of the cells, as applied
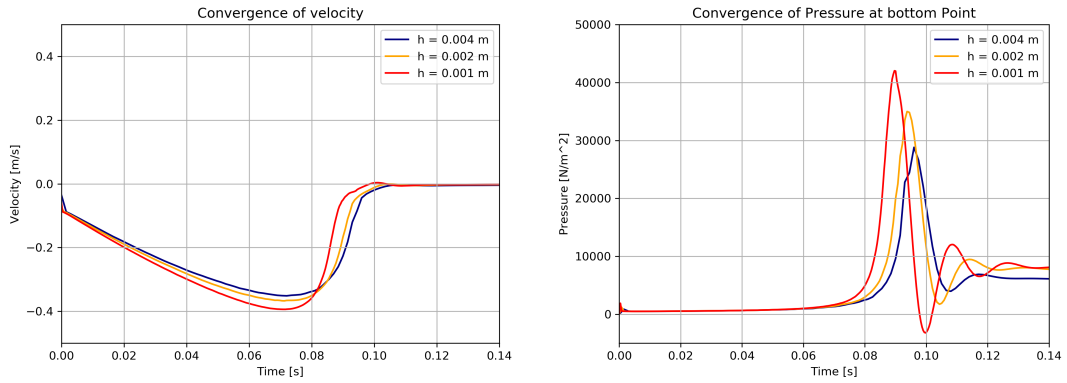
Figure 4.22 – Lack of collision. Left: Velocity of the bottom point of the disk. Right: Evolution of the pressure p at position $(0, 0.002)$.

in Algorithm 2. However, this difference is smaller when the phases are not immersed into one another. This occurs in particular when the set of parameters is very different between the phases and the velocity gradient is large at the interface.
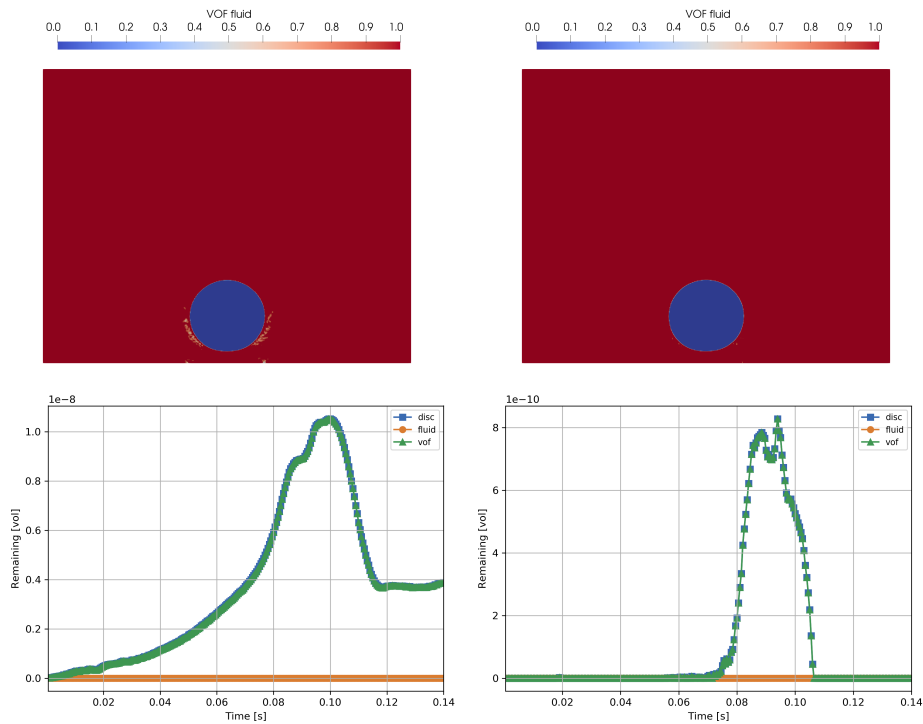
Figure 4.23 – Lack of collision. Comparison between both decompression algorithms. Top: VOF characteristic function φ at time $t = 0.1$ s. Bottom: Evolution of remaining VOF in the buffer. In orange (fluid), VOF of phase 1, in blue (disc), VOF of phase 2 and in green (vof), total VOF φ. Left: Algorithm 1. Right: Algorithm 2.

4.4   Shock absorber

For this next numerical experiment, consider a fragile mechanism immersed in an Oldroyd-B viscoelastic fluid, protected by a hull, see Figure 4.24. The goal is to investigate the shock absorption of the viscoelastic fluid, in order to protect the inner mechanism.
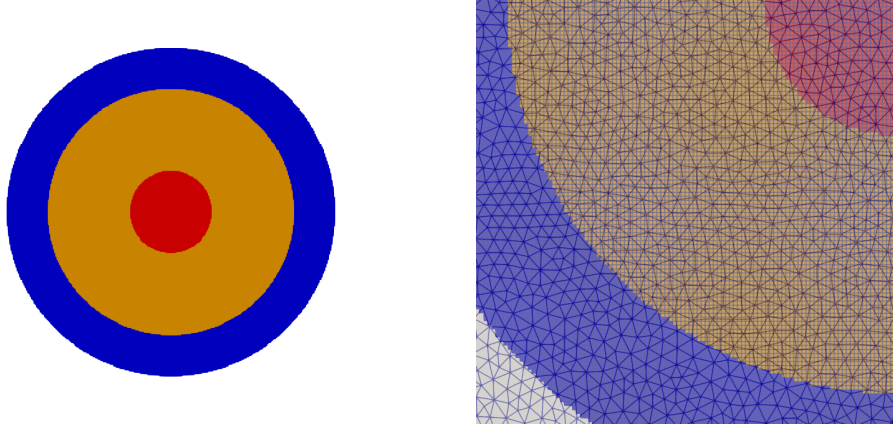
Figure 4.24 – Shock absorber. Characterisation of the different phases. In blue: hull as an elastic solid, characterised by the function φ_1 with a free-surface. In orange: shock absorber viscoelastic fluid, characterised by the function φ_2. In red: mechanism as an elastic solid, characterised by the function φ_3.

The simulation has the following settings. Consider a 3D cavity $\Lambda = [-0.05, 0.05]^2$ m$^2 \times [0, 0.1]$ m, where three different phases are considered. First, the mechanical hull is modelled as an incompressible Neo-Hookean solid, being enough soft to allow deformations. Its initial subdomain is $\Omega_{1,0} = \{(x, y) \in \mathbb{R}^2; 9 \cdot 10^{-4} < x^2 + (y - 0.046)^2 < 1.6 \cdot 10^{-3}\}$ and its set of parameters is $\rho_1 = 3000$ kg/m^3, $\eta_{s,1} = 0$ Pa s, $\eta_{p,1} = 10^4$ Pa s, $\lambda_1 = 10^{-2}$ s and $\alpha_1 = 0$. The shock absorber is an incompressible Oldroyd-B viscoelastic fluid, with initial subdomain $\Omega_{2,0} = \{(x, y) \in \mathbb{R}^2; 10^{-4} < x^2 + (y - 0.046)^2 < 9 \cdot 10^{-4}\}$ and its set of parameters is $\rho_2 = 900$ kg/m^3, $\eta_{s,2} = 0.4$ Pa s, $\eta_{p,2} = 1.6$ Pa s and $\alpha_2 = 1$. The role of the parameter λ_2 is studied and takes values in $\{0, 10^{-4}, 10^{-3}\}$. Finally, the mechanism is modelled as an incompressible Neo-Hookean solid, with initial subdomain $\Omega_3(0) = \{(x, y) \in \mathbb{R}^2; x^2 + (y - 0.046)^2 < 10^{-4}\}$. The parameters are $\rho_3 = 1500$ kg/m^3, $\eta_{s,3} = 0$ Pa s, $\eta_{p,3} = 10^3$ Pa s and $\alpha_3 = 0$. These set of parameters do not correspond to specific materials. For the numerical settings, the average diameter of the FE mesh is $H = 1$ mm. The grid cells diameter is $h = 0.3$ mm and the time step is $\Delta t = 0.0002$ s.

In order to observe the influence of the immersing fluid on the mechanism, the pressure p and the extra-stress tensor $\boldsymbol{\sigma}$ are monitored along the trajectory of the center of the disk characterised by the function φ_3, that is $\boldsymbol{x}_{\text{cen}} = (0, 0, 0.046)$. In Figure 4.26, the influence of the relaxation time of the viscoelastic fluid is compared. First, the position

of the mass center $\boldsymbol{x}_{\text{cen}}$ bounces upwards, due to the elasticity of the mechanical hull. But it is influenced by the Oldroyd-B fluid, relatively to the relaxation time and the time lapse of the shock. Now, we can observe that the force applied on the mechanism is lightly influenced by the relaxation time of the viscoelastic fluid λ_2. The elastic effect indeed yields a higher pressure on the mechanism than a Newtonian fluid. However, for a lower value of λ_2, the curves reaches the same peak, but the elastic effects are relaxed faster and reaches zero a bit faster.
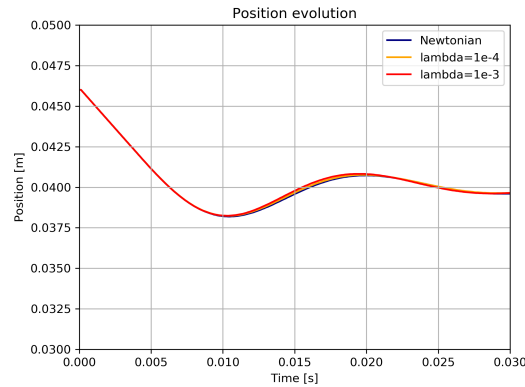
Figure 4.25 – Shock absorber. Evolution of the position of the center of the mechanism over time, transported with the materials.
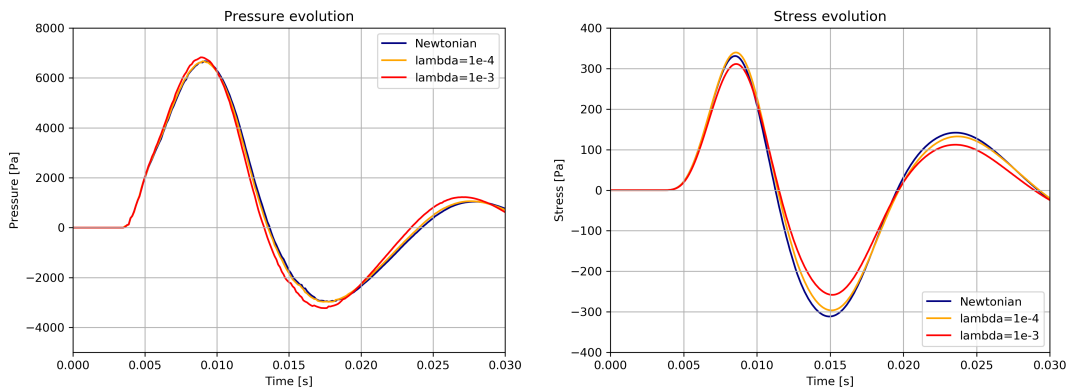
Figure 4.26 – Shock absorber. Evolution of different components at the center of the mechanism (characterised by φ_3) over time, transported with the materials. Left: Evolution of the pressure p. Right: Evolution of the stress component zz.

In Figure 4.27 and 4.28, the norm of the velocity $\boldsymbol{u}$ and the extra-stress component $\boldsymbol{\sigma}_{yy}$ are displayed respectively at two different time t. At time $t = 0.01$ s, the hull collided against the boundary, but the pressure peak appears at $t = 0.0135$ s, due to the elastic momentum. We can already witness a major influence of the relaxation time λ on the results. The viscoelastic effects imply instabilities in the flow within the hull when

the shock happen. On the right side of Figure 4.27, the snapshots are taken at time $t = 0.024$ s, where the pressure has relaxed. In Figure 4.28, we observe that the hull has absorbed most of the shock, and the viscoelastic fluid has a small impact.
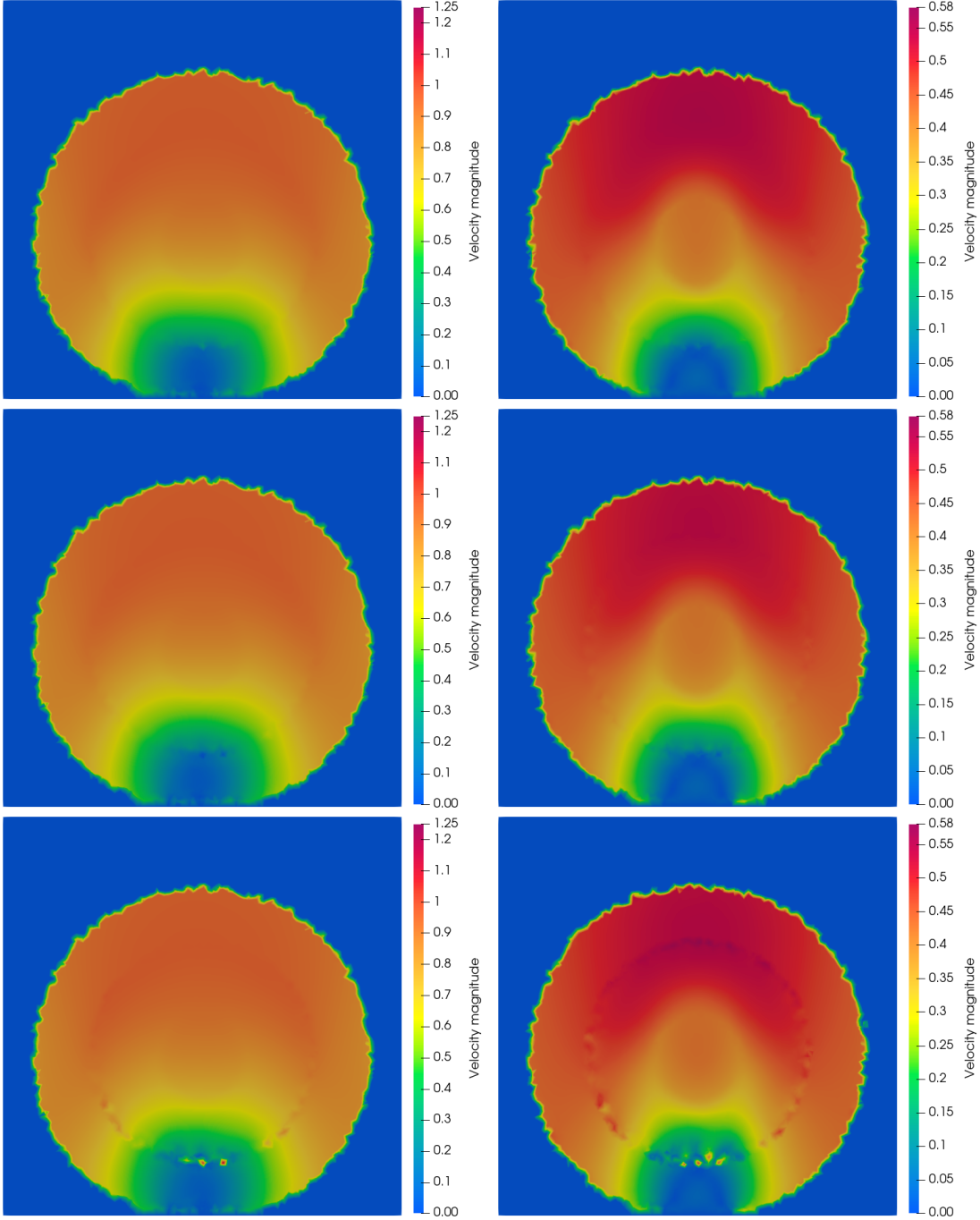
Figure 4.27 – Shock-absorber. Velocity magnitude $\|\boldsymbol{u}\|$. From top to bottom: $\lambda = 0, 10^{-4}, 10^{-3}$. Left: $t = 0.006$ s. Right: $t = 0.015$ s.
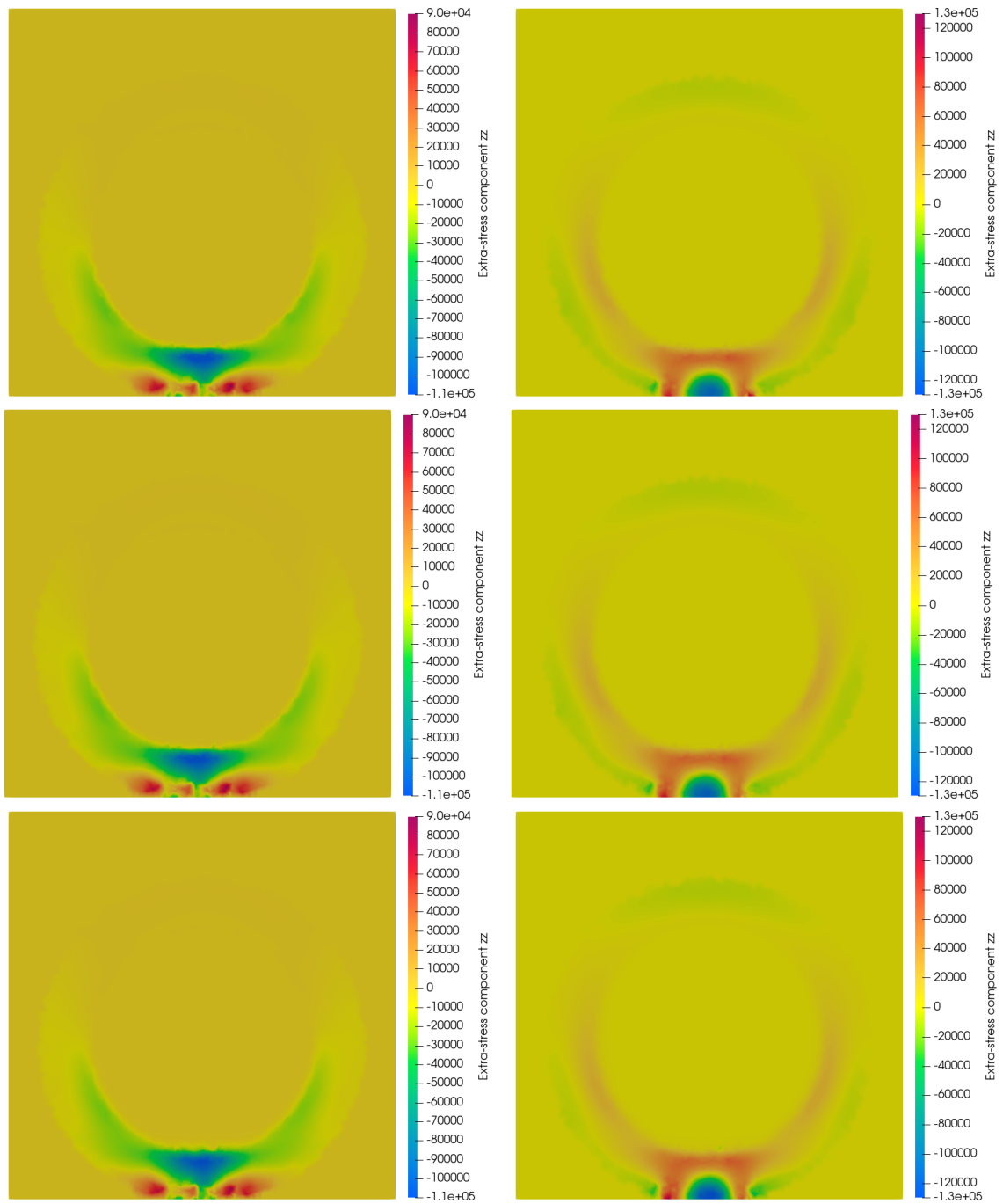
Figure 4.28 – Shock-absorber. Extra-stress component $\boldsymbol{\sigma}_{yy}$. From top to bottom: $\lambda = 0, 10^{-4}, 10^{-3}$. Left: $t = 0.006$ s. Right: $t = 0.015$ s.

5 Extension to weakly compressible free surface flows

The system of equations (1.1) shows limitations in the modelling of physical phenomena. The incompressible condition, leading to the divergence free condition $\nabla \cdot \boldsymbol{u} = 0$ allows a simplified mathematical analysis, but is a strong hypothesis of the fluid nature [LL89]. This also concerns viscoelastic fluids, whose density is also variable in time and space. Acoustic waves appear in fluids when considering compressible effects, which yield a more complex model.

The Poisson ratio ν in continuum mechanics is a key parameter, since almost all elastic materials cannot be considered as incompressible. Exceptions exist, like rubber, which has a Poisson ratio close to $\nu = 0.5$ and is considered nearly incompressible. Our elastic material deformation model is formulated using Eulerian coordinates. The goal is to obtain large deformations. However, the Neo-Hookean model has the particularity to only model small strain and the plastic deformation of the material is not involved. Thus the main advantage of the Eulerian formulation is missed and an extension of the model must be considered. Multiple constitutive laws can be found in continuum mechanics [RBJ97], but the two most popular are the Neo-Hookean and the St-Venant-Kirchhoff models [DR06, LSKG$^+$20]. The latter implies compressible materials, and this issue is first tackled.

First, a mathematical framework from literature is presented for the modelling of weakly compressible Newtonian and viscoelastic fluids. Then, we present a new model for the deformation of compressible elastic materials, extending the incompressible model (1.1). It is based on a compressible Neo-Hookean model, formulated in Eulerian coordinates. This formulation allows us to build up a unified model for the simulation of weakly compressible viscous and elastic flows. The numerical approximation of the model (1.1) is extended to weakly compressible flows and we present a numerical experiment.

5.1 Model extension: from incompressible flows to weakly compressible materials

In this section, we will consider the extension of the model (1.1) to compressible Newtonian and viscoelastic fluids ($\alpha = 1$) and use a compressible version of the Neo-Hookean material to extend the elastic deformations model ($\alpha = 0$). The derivation of the system of equations describes the two different types of phases. For more details, we refer to [LL89] for a complete mathematical analysis on fluid dynamics. The analogous mathematical background as in chapter 1 is considered: let Λ be a cavity of $\mathbb{R}^3$ in which a fluid is contained and let $T > 0$ be the final time of the simulation. Let $\varphi : \Lambda \times [0, T] \to \{0, 1\}$ be the volume fraction of fluid. It is equal to 1 in the fluid and 0 in the surrounding vacuum. Thus the function φ denotes the characteristic function of the liquid region, which is denoted by $\Omega(t) = \{\boldsymbol{x} \in \Lambda; \varphi(x, t) = 1\}$ for $0 \leq t \leq T$, and the space-time domain containing the fluid is denoted by $\mathcal{Q}_T = \{(\boldsymbol{x}, t) \in \Lambda \times (0, T); \boldsymbol{x} \in \Omega(t)\}$.

The characteristic function φ is transported with the fluid, for a velocity field $\boldsymbol{u}$ such that $\nabla \cdot \boldsymbol{u} \neq 0$. Hence, similarly as before, it satisfies $\varphi(\boldsymbol{x}(\boldsymbol{X}, t), t) = \varphi(\boldsymbol{X}, 0)$, for $\boldsymbol{X} \in \Omega_0$, where the characteristic lines $\boldsymbol{x}(\boldsymbol{X}, t)$ solves $\frac{\mathrm{d}}{\mathrm{d}t}\boldsymbol{x}(\boldsymbol{X}, t) = \boldsymbol{u}(\boldsymbol{x}(\boldsymbol{X}, t), t)$. It is equivalent to the equation (1.1a) in the sense of distributions.

5.1.1 Model extension for weakly compressible Newtonian fluids

The acoustic waves are fluctuations of pressure, travelling at a velocity called the speed of sound c. They take place in compressible flows and are initiated by the variations of the density. The Mach number $Ma = u/c$, where u determines the maximum velocity of the fluid, allows to determine the relative velocity of these waves compared to the fluid velocity. The incompressibility condition is retrieved for a Mach number $Ma \to 0$, where density can be considered constant. Weakly compressible flows refer to flows with a small Mach number and having low compressible effects [WKB04]. This allows to treat a simplified system of equations, which is presented here based on the work of [Bru99, BKW06]. Furthermore, we can consider pressure-based Navier-Stokes equations in order to apply the numerical scheme presented in chapter 1.

Consider a weakly compressible fluid at initial state in Ω_0, with density ρ_0 and viscosity $\eta_{s,0}$. We define $\rho, \eta_s : \mathcal{Q}_T \to \mathbb{R}$ being the density and viscosity in the fluid region. In the fluid region, the velocity field $\boldsymbol{u} : \mathcal{Q}_T \to \mathbb{R}^3$, a pressure field $p : \mathcal{Q}_T \to \mathbb{R}$ and the density

5.1. Model extension: from incompressible flows to weakly compressible materials

$\rho : \mathcal{Q}_T \to \mathbb{R}$ satisfy:

$$\rho \left(\frac{\partial \boldsymbol{u}}{\partial t} + (\boldsymbol{u} \cdot \nabla)\boldsymbol{u} \right) - \nabla \cdot \left(2\eta_s \left(\boldsymbol{\epsilon}(\boldsymbol{u}) - \frac{1}{3}(\nabla \cdot \boldsymbol{u})\boldsymbol{I} \right) \right) + \nabla p = \rho \boldsymbol{g}, \tag{5.1a}$$

$$\frac{\partial p}{\partial t} + (\boldsymbol{u} \cdot \nabla)p + \rho c^2 (\nabla \cdot \boldsymbol{u}) = 0, \tag{5.1b}$$

$$\rho = \frac{m}{c^2}(p + B), \tag{5.1c}$$

where B is a factor with the same dimension as p and m a dimensonless power-index [Bru99, BKW06]. They are further developped later on. The momentum equation (5.1a) denotes the conservation principle

$$\rho \left(\frac{\partial \boldsymbol{u}}{\partial t} + (\boldsymbol{u} \cdot \nabla)\boldsymbol{u} \right) - \nabla \cdot \boldsymbol{T} = \boldsymbol{F}, \tag{5.2}$$

where $\boldsymbol{T}$ denotes the stress tensor and the right-hand side tensor $\boldsymbol{F}$ is the total external forces on the system. For a compressible Newtonian flow, the stress tensor becomes [LL89, TBE$^+$01]

$$\boldsymbol{T} = -\tilde{p}\boldsymbol{I} + 2\eta_s\boldsymbol{\epsilon}(\boldsymbol{u}) + \left(k_s - \frac{2\eta_s}{3} \right)(\nabla \cdot \boldsymbol{u})\boldsymbol{I}, \tag{5.3}$$

where $\tilde{p}$ here denotes the pressure. The parameter k_s is known as the bulk viscosity, describing the effects of volume change on velocity diffusion. The Stokes hypothesis states that $k_s = 0$ [GeH95]. But we can also get rid of the parameters by considering $p := -\frac{1}{3}\text{tr}(\boldsymbol{T})$, which is the so-called augmented pressure. From (5.3) it yields

$$p = \tilde{p} - k_s \nabla \cdot \boldsymbol{u}. \tag{5.4}$$

Thus, the tensor becomes

$$\boldsymbol{T} = -p\boldsymbol{I} + 2\eta_s\boldsymbol{\epsilon}(\boldsymbol{u}) - \frac{2\eta_s}{3}(\nabla \cdot \boldsymbol{u})\boldsymbol{I}. \tag{5.5}$$

To close the system of equations for a Newtonian weakly compressible fluid with free surface flows, an equation of state describing the thermodynamic state of the system must be defined. We consider an isentropic system, defining an adiabatic and reversible system. In an isentropic system, the Tait equation of state can be applied to link the pressure with the density [Bru99, BKW06]:

$$\frac{p + B}{p_0 + B} = \left(\frac{\rho}{\rho_0} \right)^m, \tag{5.6}$$

where p is the augmented pressure, p_0, ρ_0 are the values of the augmented pressure and density at rest, B is a dimensionless factor ratio. By assuming the system to be isentropic, the speed of sound c (i.e. the velocity at which pressure waves travels) can be determined

by the relation [Bru99, BKW06]

$$c^2 = \frac{\partial p}{\partial \rho} = \frac{p_0 + B}{\rho_0} m \left(\frac{\rho}{\rho_0} \right)^{m-1} = \frac{m(p + B)}{\rho} \tag{5.7}$$

and yields the equation (5.1c). The parameters B and m are dependent on the fluid. Since we consider weakly compressible flows, we assume very small changes of density and we can assume the speed of sound to be constant in space and time [SY88, YA21]. In this case, and considering an isentropic system, the energy can be assumed to remain constant, and the equation for the evolution of the energy does not need to be treated [Bru99, BKW06, MJB$^+$13]. Despite a lack in generality, this assumption allows to consider a smaller set of equations. Finally, the continuity equation reads:

$$\frac{\partial \rho}{\partial t} + \nabla \cdot (\rho \boldsymbol{u}) = 0. \tag{5.8}$$

From (5.7), we obtain

$$0 = \frac{\partial \rho}{\partial t} + (\boldsymbol{u} \cdot \nabla)\rho + \rho(\nabla \cdot \boldsymbol{u}) = \frac{1}{c^2} \left(\frac{\partial p}{\partial t} + (\boldsymbol{u} \cdot \nabla)p \right) + \rho(\nabla \cdot \boldsymbol{u})$$

and yields (5.1b). This formulation yields an evolution equation for the pressure, enabled for isentropic weakly compressible flows [Cho68, YA21]. The viscosity in an isentropic system can be considered as linearly dependent of the density. Hence, $\eta_s = \eta_{s,0}(\rho/\rho_0)$.

Remark 5.1.1.   The hypotheses of a constant speed of sound and of constant system energy lacks on physical reality. The presence of friction due to the effect of viscosity yields a decrease in the system energy. However, we can relax these hypotheses by considering an alternative equation of state $p = p(e, \rho)$ in an isothermal system and consider the equation of energy for an isothermal system [TELB06]:

$$\rho \left(\frac{\partial e}{\partial t} + (\boldsymbol{u} \cdot \nabla)e \right) - \left(2\eta_s \left(\boldsymbol{\epsilon}(\boldsymbol{u}) - \frac{1}{3}(\nabla \cdot \boldsymbol{u})\boldsymbol{I} \right) - p\boldsymbol{I} \right) : \nabla \boldsymbol{u} = 0. \tag{5.9}$$

$\square$

5.1.2 Weakly compressible viscoelastic flows

The model for Oldroyd-B weakly compressible viscoelastic flows reads:
Find $\boldsymbol{u} : \mathcal{Q}_T \to \mathbb{R}^3$, $p : \mathcal{Q}_T \to \mathbb{R}$, $\rho : \mathcal{Q}_T \to \mathbb{R}$ and $\boldsymbol{\sigma} : \mathcal{Q}_T \to \mathbb{R}^{3 \times 3}$ satisfy:

$$\rho \left(\frac{\partial \boldsymbol{u}}{\partial t} + (\boldsymbol{u} \cdot \nabla)\boldsymbol{u} \right) - \nabla \cdot \left(2\eta_s \left(\boldsymbol{\epsilon}(\boldsymbol{u}) - \frac{1}{3}(\nabla \cdot \boldsymbol{u})\boldsymbol{I} \right) \right) + \nabla p \tag{5.10a}$$

$$- \nabla \cdot \left(\boldsymbol{\sigma} - \frac{1}{3}\mathrm{tr}(\boldsymbol{\sigma})\boldsymbol{I} \right) = \rho \boldsymbol{g},$$

$$\frac{\partial p}{\partial t} + (\boldsymbol{u} \cdot \nabla)p + \rho c^2 (\nabla \cdot \boldsymbol{u}) = 0, \tag{5.10b}$$

$$\rho = \frac{m}{c^2}(p + B), \tag{5.10c}$$

$$\boldsymbol{\sigma} + \lambda \left(\frac{\partial \boldsymbol{\sigma}}{\partial t} + (\boldsymbol{u} \cdot \nabla)\boldsymbol{\sigma} + (\nabla \cdot \boldsymbol{u})\boldsymbol{\sigma} - \nabla \boldsymbol{u}\boldsymbol{\sigma} - \boldsymbol{\sigma}\nabla \boldsymbol{u}^T \right) = 2\eta_p \boldsymbol{\epsilon}(\boldsymbol{u}). \tag{5.10d}$$

This model was derived in [BKW06, MP19]. Similarly as for the model (1.1), an additional extra-stress tensor models the elastic behaviour:

$$\rho \left(\frac{\partial \boldsymbol{u}}{\partial t} + (\boldsymbol{u} \cdot \nabla)\boldsymbol{u} \right) - \nabla \cdot (\boldsymbol{T} + \boldsymbol{\sigma}) = \rho \boldsymbol{g}, \tag{5.11}$$

where $\boldsymbol{T}$ is described by (5.3) and $\boldsymbol{\sigma}$ is the viscoelastic extra-stress tensor. Using (5.11), the system of equations is not consistent with the weakly compressible Newtonian flows model (5.1). Indeed, when no elastic effect is considered, then the relaxation time λ is equal to 0. We would like the system to model a compressible Newtonian fluid with viscosity $\eta_s + \eta_p$ for $\lambda = 0$. To tackle this problem and similarly as in section (5.1.1), we consider an augmented pressure instead in (5.4), that is $p := \tilde{p} - k_s(\nabla \cdot \boldsymbol{u}) - \frac{1}{3}\mathrm{tr}(\boldsymbol{\sigma})$ [BKW06]. Using this formulation, it yields the momentum equation (5.10a).

The relation between the density and the pressure relies to the state equation (5.6). It is still applied to obtain weakly compressible viscoelastic flow and yields the equations (5.10b) and (5.10c). The viscosity terms η_s, η_p are linearly related to the density and we have $\eta_s = \eta_{s,0}(\rho/\rho_0)$ and $\eta_p = \eta_{p,0}(\rho/\rho_0)$. Finally, as mentioned in the introduction, different constitutive equations can be applied for the viscoelastic extra-stress tensor. Here, the Oldroyd-B model is still applied and the constitutive equation (5.10d) has a supplementary term due to the compressible effects [MP19].

5.1.3 Weakly compressible elastic deformations

Let us recall the notation from (1.1). Consider $\Omega_0 = \Omega(0)$ being the initial configuration of a given material and $\boldsymbol{X} \in \Omega_0$. The Lagrangian formulation of displacement is

$$\boldsymbol{x}(\boldsymbol{X}, t) - \boldsymbol{X} = \int_0^t \boldsymbol{u}(\boldsymbol{x}(\boldsymbol{X}, s), s) \, \mathrm{d}s \tag{5.12}$$

where $\boldsymbol{x}$ is the deformation of $\boldsymbol{X}$ at time t and $\boldsymbol{u}(\boldsymbol{x}, t)$ the deformation velocity at position $\boldsymbol{x}$ and time t in Eulerian coordinates. The deformation gradient tensor in Lagrangian coordinates $\tilde{\boldsymbol{F}} : \Omega_0 \times [0, T] \to \mathbb{R}^{3 \times 3}$ is defined for all $\boldsymbol{X} \in \Omega_0$ by $\tilde{\boldsymbol{F}}_{ij}(\boldsymbol{X}, t) = \dfrac{\partial \boldsymbol{x}_i}{\partial \boldsymbol{X}_j}(\boldsymbol{X}, t)$. We now define $\boldsymbol{F} : \mathcal{Q}_T \to \mathbb{R}^{3 \times 3}$ to be the deformation tensor in Eulerian coordinates as $\boldsymbol{F}(\boldsymbol{x}(\boldsymbol{X}, t), t) = \tilde{\boldsymbol{F}}(\boldsymbol{X}, t)$.

The general system of equations for structure deformations in Eulerian coordinates read: Find $\boldsymbol{u} : \mathcal{Q}_T \to \mathbb{R}^3$ and $\rho : \mathcal{Q}_T \to \mathbb{R}$ which satisfy:

$$\rho \left(\frac{\partial \boldsymbol{u}}{\partial t} + (\boldsymbol{u} \cdot \nabla)\boldsymbol{u} \right) - \nabla \cdot \boldsymbol{C} = \rho \boldsymbol{g}, \tag{5.13a}$$

$$\rho J = \rho_0, \tag{5.13b}$$

where $\boldsymbol{C} = \boldsymbol{C}(\boldsymbol{F})$ denotes the Cauchy stress tensor and $J = \det(\boldsymbol{F})$. The system (5.13) comes together with the deformation equation

$$\frac{\partial \boldsymbol{F}}{\partial t} + (\boldsymbol{u} \cdot \nabla)\boldsymbol{F} = \nabla \boldsymbol{u} \boldsymbol{F}, \tag{5.14}$$

obtained by taking the time and space derivative of (5.12), similarly as in (1.5a). The equation (5.13a) denotes the momentum principle in Eulerian coordinates [Hol02, CMPF17]. Furthermore, the principle of mass conservation reads:

$$\int_{\Omega_0} \rho(\boldsymbol{X}, 0) \, \mathrm{d}\boldsymbol{X} = \int_{\Omega(t)} \rho(\boldsymbol{x}, t) \, \mathrm{d}\boldsymbol{x} = \int_{\Omega_0} \rho(\boldsymbol{x}(\boldsymbol{X}, t), t)\tilde{J}(\boldsymbol{X}, t) \, \mathrm{d}\boldsymbol{X} \tag{5.15}$$

$$= \int_{\Omega_0} \rho(\boldsymbol{x}(\boldsymbol{X}, t), t)J(\boldsymbol{x}(\boldsymbol{X}, t), t) \, \mathrm{d}\boldsymbol{X},$$

where $\tilde{J}(\boldsymbol{X}, t) = \det(\nabla_{\boldsymbol{X}}(\boldsymbol{x}(\boldsymbol{X}, t))) = \det(\tilde{\boldsymbol{F}}(\boldsymbol{X}, t)) = \det(\boldsymbol{F}(\boldsymbol{x}(\boldsymbol{X}, t), t)) = J(\boldsymbol{x}(\boldsymbol{X}, t), t)$. Since the equation (5.15) is true for any subdomains of Ω_0, it yields the equation (5.13b) with $\rho_0 = \rho(\boldsymbol{X}, 0)$.

The constitutive equation for the Cauchy stress tensor of an incompressible Neo-Hookean material is $\boldsymbol{C} = -p\boldsymbol{I} + \mu(\boldsymbol{F}\boldsymbol{F}^T - \boldsymbol{I})$. A simple compressible Neo-Hookean model yields [Ogd97, Hol02, PG15]

$$\boldsymbol{C} = \mu J^{-1}(\boldsymbol{F}\boldsymbol{F}^T - \boldsymbol{I}) + \lambda(J - 1)\boldsymbol{I} \tag{5.16}$$

where μ, λ are the second and first Lamé parameters. Using this formulation and similarly as suggested in [Pic16], we want to obtain an equation for a pressure p and an extra-stress tensor $\boldsymbol{\sigma}$ instead of the deformation gradient tensor $\boldsymbol{F}$ in the system of equations (5.13). Then, we would be able to formulate a unified model for weakly compressible flows, based on the weakly compressible viscoelastic flows model (5.10) and on a parameter α. In this optic, the Cauchy stress tensor can be expressed using the hydrostatic pressure

5.1. Model extension: from incompressible flows to weakly compressible materials

[Hol02, PG15], so we split the Cauchy stress tensor $\boldsymbol{C}$ into $\boldsymbol{C} = \boldsymbol{\sigma} - p\boldsymbol{I}$, with

$$\boldsymbol{\sigma} = \mu J^{-1}(\boldsymbol{F}\boldsymbol{F}^T - \boldsymbol{I}), \tag{5.17}$$

$$p = -\lambda(J - 1). \tag{5.18}$$

Similarly as in Remark 3.1.1 in section 3.1, an equation for the evolution of J, using Lemma A.0.1 in Appendix and (1.4), yields

$$\frac{\mathrm{d}}{\mathrm{d}t} J(\boldsymbol{x}(\boldsymbol{X}, t), t) = J(\boldsymbol{x}(\boldsymbol{X}, t), t)\mathrm{tr}\left(\boldsymbol{F}^{-1}(\boldsymbol{x}(\boldsymbol{X}, t), t)\frac{\mathrm{d}}{\mathrm{d}t}\boldsymbol{F}(\boldsymbol{x}(\boldsymbol{X}, t), t)\right)$$

$$\stackrel{(5.14)}{=} J(\boldsymbol{x}(\boldsymbol{X}, t), t)\mathrm{tr}\left(\boldsymbol{F}^{-1}(\boldsymbol{x}(\boldsymbol{X}, t), t))\nabla_{\boldsymbol{x}}\boldsymbol{u}(\boldsymbol{x}(\boldsymbol{X}, t), t)\boldsymbol{F}(\boldsymbol{x}(\boldsymbol{X}, t), t)\right)$$

$$= J(\boldsymbol{x}(\boldsymbol{X}, t), t)\mathrm{tr}(\nabla_{\boldsymbol{x}}\boldsymbol{u}(\boldsymbol{x}(\boldsymbol{X}, t), t)) = J(\boldsymbol{x}(\boldsymbol{X}, t), t)(\nabla_{\boldsymbol{x}} \cdot \boldsymbol{u}(\boldsymbol{x}(\boldsymbol{X}, t), t)).$$

Thus we have

$$\frac{\partial}{\partial t} J(\boldsymbol{x}(\boldsymbol{X}, t), t) + (\nabla_{\boldsymbol{x}}\boldsymbol{u}(\boldsymbol{x}(\boldsymbol{X}, t), t) \cdot \nabla_{\boldsymbol{x}})J(\boldsymbol{x}(\boldsymbol{X}, t), t) = \frac{\mathrm{d}}{\mathrm{d}t} J(\boldsymbol{x}(\boldsymbol{X}, t), t) \tag{5.19}$$

$$= J(\boldsymbol{x}(\boldsymbol{X}, t), t)(\nabla_{\boldsymbol{x}} \cdot \boldsymbol{u}(\boldsymbol{x}(\boldsymbol{X}, t), t)).$$

From the previous computation, we find for the pressure (5.18):

$$\frac{\mathrm{d}p}{\mathrm{d}t}(\boldsymbol{x}(\boldsymbol{X}, t), t) = \left(\frac{\partial p}{\partial t} + (\boldsymbol{u} \cdot \nabla)p\right)(\boldsymbol{x}(\boldsymbol{X}, t), t) = -\lambda\left(\frac{\partial J}{\partial t} + (\boldsymbol{u} \cdot \nabla)J\right)(\boldsymbol{x}(\boldsymbol{X}, t), t)$$

$$\stackrel{(5.19)}{=} -\lambda(\nabla_{\boldsymbol{x}} \cdot \boldsymbol{u}(\boldsymbol{x}(\boldsymbol{X}, t), t))J \tag{5.20}$$

Now for the extra-stress tensor $\boldsymbol{\sigma}$, taking the convective derivative of (5.17) yields in Eulerian coordinates:

$$\frac{\partial \boldsymbol{\sigma}}{\partial t} + (\boldsymbol{u} \cdot \nabla)\boldsymbol{\sigma} = \mu\left(\frac{\partial J^{-1}}{\partial t} + (\boldsymbol{u} \cdot \nabla)J^{-1}\right)(\boldsymbol{F}\boldsymbol{F}^T - \boldsymbol{I})$$

$$+ \mu J^{-1}\left(\frac{\partial}{\partial t}(\boldsymbol{F}\boldsymbol{F}^T - \boldsymbol{I}) + (\boldsymbol{u} \cdot \nabla)(\boldsymbol{F}\boldsymbol{F}^T - \boldsymbol{I})\right).$$

We have

$$\frac{\partial J^{-1}}{\partial t} + (\boldsymbol{u} \cdot \nabla)J^{-1} = -\frac{1}{J^2}\left(\frac{\partial J}{\partial t} + (\boldsymbol{u} \cdot \nabla)J\right)$$

$$\stackrel{(5.19)}{=} -\frac{1}{J}(\nabla \cdot \boldsymbol{u})$$

and

$$\frac{\partial}{\partial t}(\boldsymbol{F}\boldsymbol{F}^T - \boldsymbol{I}) + (\boldsymbol{u} \cdot \nabla)(\boldsymbol{F}\boldsymbol{F}^T - \boldsymbol{I}) = \left(\frac{\partial}{\partial t}\boldsymbol{F} + (\boldsymbol{u} \cdot \nabla)\boldsymbol{F}\right)\boldsymbol{F}^T + \boldsymbol{F}\left(\frac{\partial}{\partial t}\boldsymbol{F}^T + (\boldsymbol{u} \cdot \nabla)\boldsymbol{F}^T\right)$$

$$= \nabla\boldsymbol{u}\boldsymbol{F}\boldsymbol{F}^T + \boldsymbol{F}\boldsymbol{F}^T\nabla\boldsymbol{u}^T.$$

It yields

$$\frac{\partial\boldsymbol{\sigma}}{\partial t} + (\boldsymbol{u}\cdot\nabla)\boldsymbol{\sigma} = -(\nabla\cdot\boldsymbol{u})\boldsymbol{\sigma} + 2\mu J^{-1}\boldsymbol{\epsilon}(\boldsymbol{u})$$
$$+ \mu J^{-1}\left(\nabla\boldsymbol{u}(\boldsymbol{F}\boldsymbol{F}^T - \boldsymbol{I}) + (\boldsymbol{F}\boldsymbol{F}^T - \boldsymbol{I})\nabla\boldsymbol{u}^T\right).$$

Finally we obtain the new equation for the stress $\boldsymbol{\sigma}$:

$$\frac{\partial\boldsymbol{\sigma}}{\partial t} + (\boldsymbol{u}\cdot\nabla)\boldsymbol{\sigma} + (\nabla\cdot\boldsymbol{u})\boldsymbol{\sigma} - \nabla\boldsymbol{u}\boldsymbol{\sigma} - \boldsymbol{\sigma}\nabla\boldsymbol{u}^T = \frac{2\mu}{J}\boldsymbol{\epsilon}(\boldsymbol{u}). \tag{5.21}$$

Using the momentum equation (5.13a), the final model for compressible elastic deformation yields:
Find $\boldsymbol{u} : \mathcal{Q}_T \to \mathbb{R}^3$, $p : \mathcal{Q}_T \to \mathbb{R}$, $\rho : \mathcal{Q}_T \to \mathbb{R}$ and $\boldsymbol{\sigma} : \mathcal{Q}_T \to \mathbb{R}^{3\times3}$ which satisfy:

$$\rho\left(\frac{\partial\boldsymbol{u}}{\partial t} + (\boldsymbol{u}\cdot\nabla)\boldsymbol{u}\right) - \nabla\cdot(\boldsymbol{\sigma} - p\boldsymbol{I}) = \rho\boldsymbol{g}, \tag{5.22a}$$

$$\frac{\partial p}{\partial t} + (\boldsymbol{u}\cdot\nabla)p + \frac{\lambda\rho_0}{\rho}(\nabla\cdot\boldsymbol{u}) = 0, \tag{5.22b}$$

$$p = -\lambda\left(\frac{\rho_0}{\rho} - 1\right), \tag{5.22c}$$

$$\frac{\partial\boldsymbol{\sigma}}{\partial t} + (\boldsymbol{u}\cdot\nabla)\boldsymbol{\sigma} + (\nabla\cdot\boldsymbol{u})\boldsymbol{\sigma} - \nabla\boldsymbol{u}\boldsymbol{\sigma} - \boldsymbol{\sigma}\nabla\boldsymbol{u}^T = 2\frac{\rho\mu}{\rho_0}\boldsymbol{\epsilon}(\boldsymbol{u}). \tag{5.22d}$$

The pressure equation (5.22b) is equivalent to (5.20). The equation (5.22c) comes from (5.18) and is analogous to an equation of state, rather close to Tait equation (5.6). From (5.13b), the Lamé parameters $\mu/J = \mu\rho/\rho_0$ and $\lambda J = \lambda\rho_0/\rho_J$ express the modifications due to compressible effects, where μ and λ are the value at incompressible position ($J = 1$).

Remark 5.1.2.   Alternative formulations for the Cauchy-stress tensor exist [PG15], for instance

$$\boldsymbol{T} = J^{-\frac{2}{3}}\left(\boldsymbol{\sigma} - \frac{1}{3}\mathrm{tr}(\boldsymbol{\sigma})\boldsymbol{I}\right) - p\boldsymbol{I},$$

where

$$\boldsymbol{\sigma} = \mu J^{-1}(\boldsymbol{F}\boldsymbol{F}^T - \boldsymbol{I}), \quad p = -\frac{\lambda + \frac{2}{3}\mu}{4}\left(J - \frac{1}{J^3}\right).$$

Similar computations as previously applied yield the following model for compressible elastic deformation:

$$\rho\left(\frac{\partial\boldsymbol{u}}{\partial t} + (\boldsymbol{u}\cdot\nabla)\boldsymbol{u}\right) - \nabla\cdot\left(\left(\frac{\rho_0}{\rho}\right)^{\frac{2}{3}}\left(\boldsymbol{\sigma} - \frac{1}{3}\mathrm{tr}(\boldsymbol{\sigma})\boldsymbol{I}\right)\right) + \nabla p = \rho\boldsymbol{g}, \tag{5.23a}$$

$$\frac{\partial p}{\partial t} + (\boldsymbol{u}\cdot\nabla)p + \left(\frac{1}{4} + \frac{3}{4}\left(\frac{\rho_0}{\rho}\right)^4\right)\left(\lambda + \frac{2}{3}\mu\right)(\nabla\cdot\boldsymbol{u}) = 0. \tag{5.23b}$$

This system of equations is more complicated, but take into account the term $-\frac{1}{3}\mathrm{tr}(\boldsymbol{\sigma})\boldsymbol{I}$

in the diffusion term, similarly as in the system (5.10). □

5.1.4 Unified model for compressible viscoelastic flows and elastic solid deformation

The goal in this section is to reunite the model for compressible Newtonian and viscoelastic flows, and the model of compressible Neo-Hookean material deformations. In the cavity Λ, the characteristic function $\varphi : \Lambda \times [0, T] \to \{0, 1\}$ satisfy

$$\frac{\partial \varphi}{\partial t} + (\boldsymbol{u} \cdot \nabla)\varphi = 0 \tag{5.24a}$$

in the weak sense. Then, in the fluid domain, the unified model reads: Find $\boldsymbol{u} : \mathcal{Q}_T \to \mathbb{R}^3$, $p : \mathcal{Q}_T \to \mathbb{R}$, $\rho : \mathcal{Q}_T \to \mathbb{R}$ and $\boldsymbol{\sigma} : \mathcal{Q}_T \to \mathbb{R}^{3\times 3}$ satisfy:

$$\rho \left(\frac{\partial \boldsymbol{u}}{\partial t} + (\boldsymbol{u} \cdot \nabla)\boldsymbol{u} \right) - \nabla \cdot \left(2\eta_s \left(\boldsymbol{\epsilon}(\boldsymbol{u}) - \frac{1}{3}(\nabla \cdot \boldsymbol{u})\boldsymbol{I} \right) \right) + \nabla p \tag{5.24b}$$

$$- \nabla \cdot \left(\boldsymbol{\sigma} - \frac{\alpha}{3}\mathrm{tr}(\boldsymbol{\sigma})\boldsymbol{I} \right) = \rho \boldsymbol{g},$$

$$\frac{\partial p}{\partial t} + (\boldsymbol{u} \cdot \nabla)p + \beta(\nabla \cdot \boldsymbol{u}) = 0, \tag{5.24c}$$

$$p = p(\rho), \tag{5.24d}$$

$$\alpha\boldsymbol{\sigma} + \lambda \left(\frac{\partial \boldsymbol{\sigma}}{\partial t} + (\boldsymbol{u} \cdot \nabla)\boldsymbol{\sigma} + (\nabla \cdot \boldsymbol{u})\boldsymbol{\sigma} - \nabla\boldsymbol{u}\boldsymbol{\sigma} - \boldsymbol{\sigma}\nabla\boldsymbol{u}^T \right) = 2\eta_p\boldsymbol{\epsilon}(\boldsymbol{u}), \tag{5.24e}$$

where the newly introduced parameter β takes a different value for each rheology and takes physical values, whereas the parameter α has a numerical meaning and is adimensional. Furthermore, it controls the compressible effects, in the sense that the limit $\beta \to \infty$ gives back the incompressible system. Initial conditions $\boldsymbol{u}(\cdot, 0) = \boldsymbol{u}_0$, $p(\cdot, 0) = p_0$, $\rho(\cdot, 0) = \rho_0$ and $\boldsymbol{\sigma}(\cdot, 0) = \boldsymbol{\sigma}_0$ are prescribed. The boundary conditions on the cavity Λ are similar as described in chapter 1. The condition on the free-surface on $\partial\Omega \backslash \partial\Lambda$ is:

$$\left(2\eta_s\boldsymbol{\epsilon}(\boldsymbol{u}) - \frac{1}{3}(\nabla \cdot \boldsymbol{u})\boldsymbol{I} \right)\boldsymbol{n} - p\boldsymbol{n} + \left(\boldsymbol{\sigma} - \frac{\alpha}{3}\mathrm{tr}(\boldsymbol{\sigma})\boldsymbol{I} \right)\boldsymbol{n} = 0.$$

The equation of state (5.24d) is dependent on the material, whether it concerns a fluid (Tait equation (5.6)) or a solid (hydrostatic pressure (5.18)). The parameters η_s, η_p are linearly dependent on the density: $\eta_s = \eta_{s,0}\rho/\rho_0$ and $\eta_p = \eta_{p,0}\rho/\rho_0$. This yields the three different cases previously obtained for the different sets of parameters:

1. When $\alpha = 1, \lambda = 0$, we recover the system of equation of weakly compressible Newtonian flows. The equation (5.24e) becomes $\boldsymbol{\sigma} = 2\eta_p\boldsymbol{\epsilon}(\boldsymbol{u})$. We recover the system of equations (5.1), for the viscosity parameter $\eta_s + \eta_p$. In this case, the additional parameter β corresponds to ρc^2. The equation of state must be the

equation (5.1c).

2. When $\alpha = 1$ and $\lambda > 0$, we recover the system of equation (5.10) modelling the flow of weakly compressible Oldroyd-B viscoelastic fluid. Similarly as for the Newtonian fluids, we have $\beta = \rho c^2$.

3. Finally, for $\alpha = 0$ and $\eta_s = 0$, we recover the system (5.22) for the deformation of compressible Neo-Hookean elastic solids. The parameters become $\beta = \lambda \rho_0 / \rho$ and $\mu \rho / \rho_0 = \eta_p / \lambda = \eta_{p,0} \rho / (\lambda \rho_0)$.

The addition of the continuity equation (5.8) adds an extra nonlinearity in equations (5.24b) and (5.24c) (β is dependent on ρ). To the best of our knowledge, the well-posedness of any three systems of equations listed above has not been proved. Indeed, no maximum principle can be obtained for the density ρ in the compressible Navier-Stokes equations (5.1) or compressible solid deformations (5.22). For these reasons, we dismiss the continuity equations (5.8) and take

$$\rho(\boldsymbol{x}, t) = \rho_0 \in \mathbb{R}_+, \qquad \forall (\boldsymbol{x}, t) \in \mathcal{Q}_T. \tag{5.25}$$

This simplification has already been applied in [SY88, YA21] for Newtonian compressible flows. By applying constant parameters instead of new variables, we have better hopes to find stability estimates for this model in a future work. Apart from the lack of physical interpretation, the model still shows some advantages. Pressure waves are implied by the equation (5.24c). It allows to treat acoustic waves in the material. Furthermore, the divergence of the velocity is not equal to zero any more, and this implies changes of the total volume. It also implies that the state equation is no longer needed to close our system of equations and that all parameters $\rho, \eta_s, \beta, \alpha, \lambda$ and η_p are now constant.

Finally, when α and η_s are equal to 0, this simplification allows to use the system (5.23) in Remark 5.1.2 instead of the original system of equations (5.22), which was preferred for its simplicity. Indeed, the equation (5.24b) now becomes

$$\rho \left(\frac{\partial \boldsymbol{u}}{\partial t} + (\boldsymbol{u} \cdot \nabla) \boldsymbol{u} \right) - \nabla \cdot \left(2\eta_s \left(\boldsymbol{\epsilon}(\boldsymbol{u}) - \frac{1}{3} (\nabla \cdot \boldsymbol{u}) \boldsymbol{I} \right) \right) + \nabla p - \nabla \cdot \left(\boldsymbol{\sigma} - \frac{1}{3} \mathrm{tr}(\boldsymbol{\sigma}) \boldsymbol{I} \right) = \rho \boldsymbol{g}$$

and is now equivalent to (5.23a) for $\eta_s = 0$ and $\rho = \rho_0$. In equation (5.23b), the parameter β is now equal to $\lambda + \frac{2}{3}\mu$ in the point 3. above, when α and η_s are equal to 0 and we model a compressible Neo-Hookean material.

5.2   Numerical approximation for compressible flows

In this section, we address the numerical approximation of the system of equations (5.24). Our goal is to apply the same numerical scheme used in the incompressible case (1.1).

Thus, the splitting algorithm is applied to the system and we recover a prediction and correction step. The specificities brought by the compressible case are then tackled.

5.2.1 Numerical approximation of the characteristic function for compressible flows

The discretisation of the characteristic function in the VOF method is usually performed with the finite volume method [dNKM07, Dum13, MJB+13]. Our goal in this section is to apply the method of characteristics (1.13) to the compressible flow to the characteristic function φ and the variables $\boldsymbol{u}$ and $\boldsymbol{\sigma}$ in the prediction step..

Let Δt be the time step, N be the number of time steps, $T = N\Delta t$ and $t^n = n\Delta t$, $n = 0, 1, \ldots, N$. Let us assume that at time t^{n-1}, the approximated volume fraction $\varphi^{n-1} : \Lambda \to \mathbb{R}$ and the approximated velocity field $\boldsymbol{u}^{n-1} : \Omega^{n-1} \to \mathbb{R}^3$ are known, where $\Omega^{n-1} = \{\boldsymbol{x} \in \Lambda; \varphi^{n-1}(\boldsymbol{x}) = 1\}$. Consider the characteristic lines $\boldsymbol{x} : \Omega^{n-1} \times [t^{n-1}, t^n] \to \Lambda$, which satisfy the condition

$$\frac{\mathrm{d}}{\mathrm{d}t}\boldsymbol{x}(\boldsymbol{X}, t) = \boldsymbol{u}(\boldsymbol{x}(\boldsymbol{X}, t), t), \tag{5.26}$$

for all $(\boldsymbol{X}, t) \in \Omega^{n-1} \times [t^{n-1}, t^n]$. Let $h > 0$ and consider a grid made of cubic cells C_{ijk} of size h, with barycenter $\boldsymbol{x}_{ijk}$. Let φ_{ijk}^{n-1} and $\boldsymbol{u}_{ijk}^{n-1}$ be the approximated value respectively of the functions φ^{n-1} and $\boldsymbol{u}^{n-1}$ on each cell C_{ijk}. These values are transported along the vector $\Delta t \boldsymbol{u}_{ijk}^{n-1}$.

It can be proved in one dimension that the method of characteristics is equivalent to a finite difference method [Cab04]. As illustrated in Figure 1.4, the cells can be considered as particles, with a given value for φ. This function satisfies a transport equation. Since the method of characteristics that we use is a particle method, then it actually solves the conservative form of the transport equation (1.1a):

$$\frac{\partial \varphi}{\partial t} + \nabla \cdot (\varphi \boldsymbol{u}) = 0. \tag{5.27}$$

No proof of this result was found for the best of our knowledge. However, it can be proved that a particle function solve the conservative form of the transport equation [Rav85]. A study of particle method for the advection equation in conservative form can be found in [CEPP14]. Furthermore, a numerical experiment at the end of this section shows an empirical proof of this result.

This issue has no repercussion when the fluid is divergence-free ($\nabla \cdot \boldsymbol{u} = 0$). Indeed, the equation (5.27) yields $\dfrac{\partial \varphi}{\partial t} + (\boldsymbol{u} \cdot \nabla)\varphi + \varphi(\nabla \cdot \boldsymbol{u}) = 0$, which is equivalent to the transport equation (1.1a) in this case. However, considering compressible fluids forces us to apply

a correction to the previously used method of characteristics. For this reason, we use a splitting algorithm again to solve our problem. The initial problem reads:
Find $\varphi : [t^{n-1}, t^n] \times \Lambda \to \{0, 1\}$ such that

$$\frac{\partial \varphi}{\partial t} + (\boldsymbol{u} \cdot \nabla)\varphi = 0.$$

To solve it, we advocate the following splitting algorithm. A first correction equation is solved. It yields:
Find $\varphi : [t^{n-1}, t^n] \times \Lambda \to \{0, 1\}$ such that

$$\frac{\partial \varphi}{\partial t} - \varphi(\nabla \cdot \boldsymbol{u}) = 0, \tag{5.28a}$$

with initial condition $\varphi(t^{n-1}) = \varphi^{n-1}$. The solution is denoted by $\varphi^{n-\frac{1}{2}}$. Finally, we solve the conservative equation:
Find $\varphi : [t^{n-1}, t^n] \times \Lambda \to \{0, 1\}$ such that

$$\frac{\partial \varphi}{\partial t} + \nabla \cdot (\varphi \boldsymbol{u}) = 0, \tag{5.28b}$$

with initial condition $\varphi(t^{n-1}) = \varphi^{n-\frac{1}{2}}$.

At the discrete level, the algorithm to solve (5.28) is the following:

1. The divergence of the velocity $\nabla \cdot \boldsymbol{u}_{ijk}^{n-1}$ is approximated by a piecewise constant function, on each cell of the grid for active cells only. It is computed on the FE mesh and interpolated on the cells using either one of the equations in (1.21).

2. The equation (5.28a) is approximated in each non-empty cell C_{ijk}:
   For all active cells C_{ijk}, find $\tilde{\varphi}_{ijk} : [t^{n-1}, t^n] \to \mathbb{R}_+$ such that:

   $$\frac{\mathrm{d}\tilde{\varphi}_{ijk}}{\mathrm{d}t}(t) - \tilde{\varphi}_{ijk}(t)(\nabla \cdot \boldsymbol{u}_{ijk}^{n-1}) = 0, \tag{5.29}$$

   with the initial condition $\tilde{\varphi}_{ijk}(t^{n-1}) = \varphi_{ijk}^{n-1}$. The equation (5.29) admits an exact solution for each cell C_{ijk}:

   $$\tilde{\varphi}_{ijk}(t) = \varphi_{ijk}^{n-1} \exp((t - t^{n-1})(\nabla \cdot \boldsymbol{u}_{ijk}^{n-1})), \qquad t^{n-1} \leq t \leq t^n.$$

   We denote the new variable to be transported along the characteristics by:

   $$\bar{\varphi}_{ijk}^{n-\frac{1}{2}} := \exp((t^n - t^{n-1})(\nabla \cdot \boldsymbol{u}_{ijk}^{n-1})).$$

3. The SLIC algorithm illustrated in Figure 1.6 must be applied in order to avoid numerical diffusion. However, this algorithm detects a cell to be full if its value is

equal to 1. Hence, we cannot directly transport the newly computed value $\tilde{\varphi}_{ijk}(t^n)$. For this reason, the transport equation (5.28b) is first solved for the characteristic function φ_{ijk}^{n-1} in each cell using the method of characteristics (1.13c), where the SLIC algorithm can be applied. Then, we recover in each cell C_{ijk} the updated value φ_{ijk}^n, and the cell is considered active if $\varphi_{ijk}^n > 0$.

4. Note that $\tilde{\varphi}_{ijk}(t^n) = \varphi_{ijk}^{n-1} \bar{\varphi}_{ijk}^{n-\frac{1}{2}}$, which is the solution at time t^n of the equation (5.29). As described in section 1.4.1, where the weighted velocity $\varphi_{ijk}^{n-1} \boldsymbol{u}_{ijk}^{n-1}$ is transported, the weighted function $\varphi_{ijk}^{n-1} \bar{\varphi}_{ijk}^{n-\frac{1}{2}}$ is transported with the method of characteristics to solve (5.28b). Then, we recover in each updated active cell C_{ijk} the updated value $\bar{\varphi}_{ijk}^n$.

5. The characteristic functions φ_{ijk}^n are then updated with the transported corrected functions $\bar{\varphi}_{ijk}^n$ by $\varphi_{ijk}^n := \varphi_{ijk}^n \bar{\varphi}_{ijk}^n$.

6. The decompression algorithm presented in section 1.4.1 is finally applied. Like in the incompressible case, the overfilled cells and the cells advected out of the domain are treated.

We present a numerical result for an empirical proof of appropriate convergence. Consider a domain $\Lambda = (-6, 0) \times (-1, 1)$ and a velocity $\boldsymbol{u}(\boldsymbol{X}, t) = (-x, 0)$ imposed in $\boldsymbol{X} = (x, y) \in \Lambda$. Thus, it corresponds to a 2D test case, but the flow evolves only in 1D. Now let us define

$$\varphi_0(x, y) = \begin{cases} 1 & \text{if } |x + 5| < 0.5 \\ 0 & \text{otherwise} \end{cases}$$

to define the initial fluid domain .

The equation of the method of characteristics (5.26) yields

$$\boldsymbol{x}(\boldsymbol{X}, t) = \begin{pmatrix} x \exp(-t) \\ y \end{pmatrix}$$

Thus, the equation $\varphi(\boldsymbol{x}(\boldsymbol{X}, t), t) = \varphi(\boldsymbol{X}, 0)$ yields

$$\varphi((x, y), t) = \varphi((x \exp(t), y), 0). \tag{5.30}$$

If we consider that the method of characteristics solves the equation (5.27), we find in a formal computation:

$$\begin{aligned} \frac{\mathrm{d}}{\mathrm{d}t} \varphi(\boldsymbol{x}(\boldsymbol{X}, t), t) &= \frac{\partial}{\partial t} \varphi(\boldsymbol{x}(\boldsymbol{X}, t), t) + (\boldsymbol{u} \cdot \nabla) \varphi(\boldsymbol{x}(\boldsymbol{X}, t), t) \\ &= -(\nabla \cdot \boldsymbol{u}) \varphi(\boldsymbol{x}(\boldsymbol{X}, t), t) \\ &= \varphi(\boldsymbol{x}(\boldsymbol{X}, t), t), \end{aligned}$$

since $\nabla \cdot \boldsymbol{u} = -1$. Hence we obtain

$$\varphi((x, y), t) = \varphi((x \exp(t), y), 0)e^t. \tag{5.31}$$

For the numerical experiment, the coarse discretisation uses the cell size $h = 0.05$ m, a time step $\Delta t = 0.012$ s and final time $T = 0.96$ s. Figures 5.1 and 5.2 illustrate snapshots of the results and convergence results respectively. In the left column, the method of characteristics converges for an order lower than 1 to the solution (5.31), which is the solution of the conservative form (5.27). Whereas in the right column, the correction (5.29) implies a convergence of order $\mathcal{O}(\Delta t + h)$ to the solution (5.30), which is the solution of the initial non-conservative advection equation (1.1a). The numerical diffusion implied by the method of characteristics is reduced using the SLIC algorithm. Since the equation (5.28a) modifes the property $\varphi \in \{0, 1\}$, the decompression algorithm is still to be applied, and does not alter the convergence of the algorithm. The result at the bottom left in Figure 5.1 shows that this latter algorithm cannot be applied if the correction (5.29) is not applied, since the values in each cell of the characteristic function are not between 0 and 1.

5.2.2   Numerical approximation of the complete model

We address now the numerical approximation of the unified model for compressible flows. The splitting algorithm presented in chapter 1 is adapted and the convective terms are solved separately. During the prediction step, the following set of convection equations from t^{n-1} to t^n are solved:

$$\frac{\partial \boldsymbol{v}}{\partial t} + (\boldsymbol{v} \cdot \nabla)\boldsymbol{v} = 0, \tag{5.32a}$$

$$\frac{\partial q}{\partial t} + (\boldsymbol{v} \cdot \nabla)q = 0, \tag{5.32b}$$

$$\frac{\partial \boldsymbol{\tau}}{\partial t} + \nabla \cdot (\boldsymbol{\tau} \otimes \boldsymbol{v}) = 0, \tag{5.32c}$$

$$\frac{\partial \psi}{\partial t} + (\boldsymbol{v} \cdot \nabla)\psi = 0, \tag{5.32d}$$

with initial conditions

$$\boldsymbol{v}(t^{n-1}) = \boldsymbol{u}^{n-1}, \quad q(t^{n-1}) = p^{n-1}, \quad \boldsymbol{\tau}(t^{n-1}) = \boldsymbol{\sigma}^{n-1}, \quad \psi(t^{n-1}) = \varphi^{n-1},$$

respectively. The computational domain is then updated, $\Omega^n = \{\boldsymbol{x} \in \Lambda; \varphi^n(\boldsymbol{x}) = 1\}$. The correction step then consists in finding $\boldsymbol{v} : \Omega^n \times [t^{n-1}, t^n] \to \mathbb{R}^3$, $q : \Omega^n \times [t^{n-1}, t^n] \to \mathbb{R}$ and $\boldsymbol{\tau} : \Omega^n \times [t^{n-1}, t^n] \to \mathbb{R}^{3 \times 3}$ which satisfy
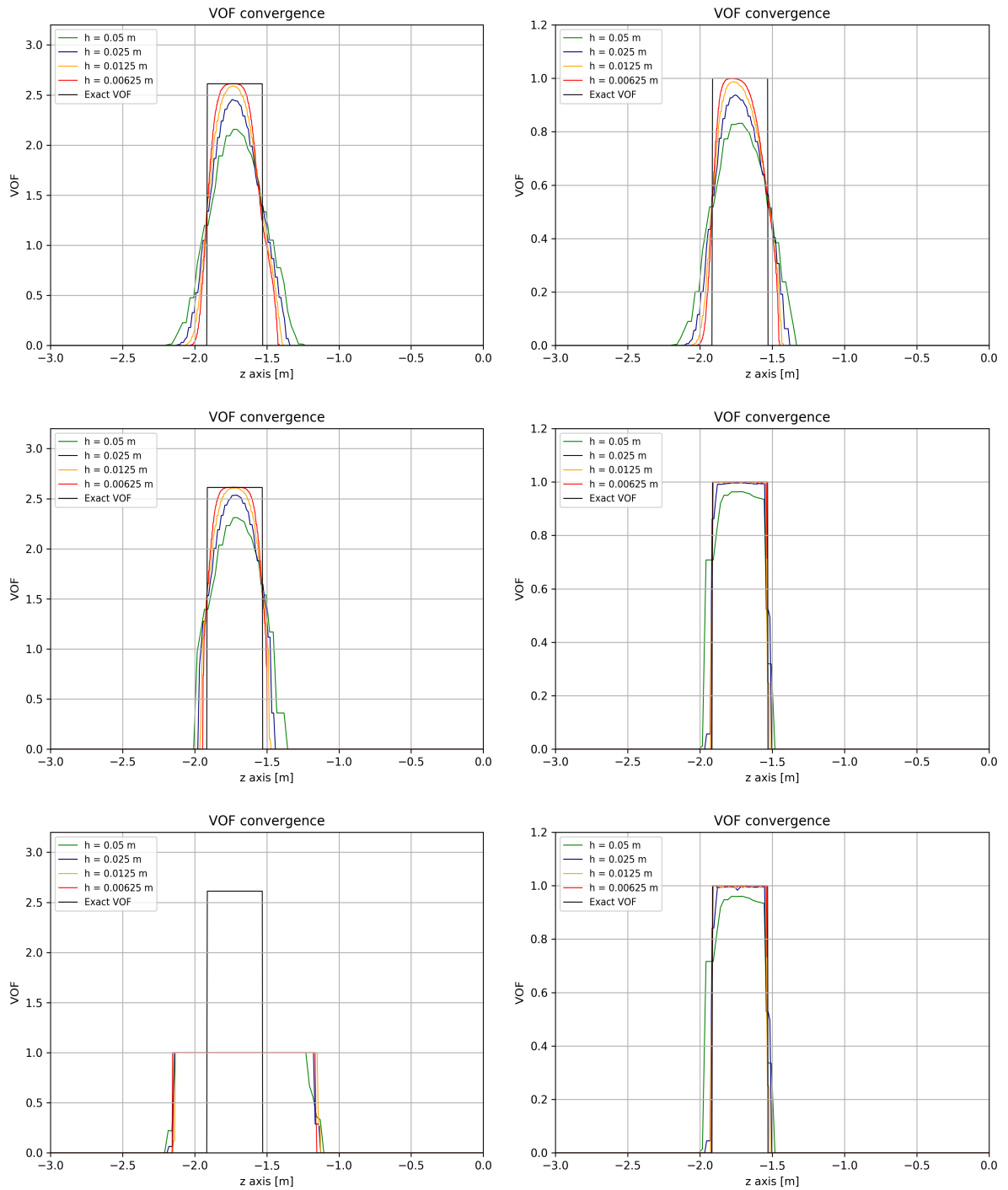
Figure 5.1 – Profiles of φ at time $t = 1$ for four different mesh sizes and the exact solution. Left: the correction (5.28a) is not applied. Right: the correction (5.28a) is applied. Top: no SLIC and decompression algorithm. Middle: SLIC applied without decompression. Bottom: SLIC and decompression
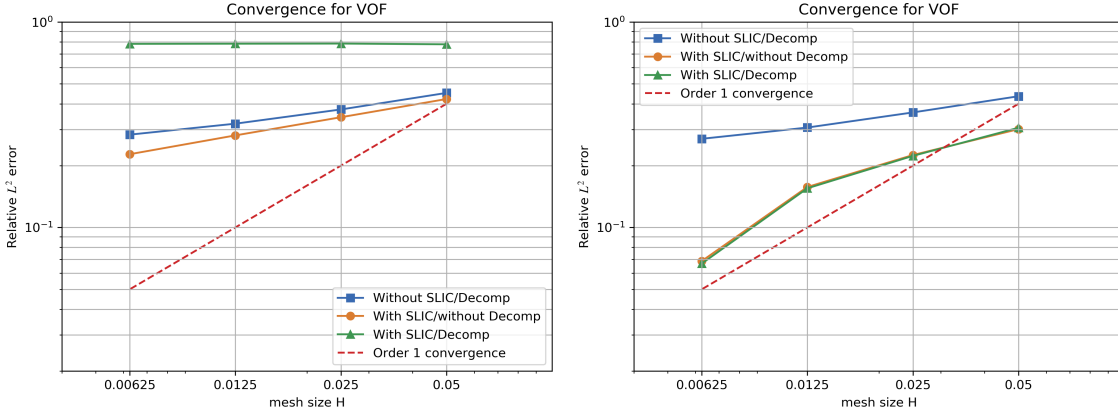
Figure 5.2 – Relative error $\|\varphi(t_n) - \varphi^n\|_{L^2(\Omega)} / \|\varphi(t_n)\|_{L^2(\Omega)}$ at time $t = 1$ for four different mesh sizes. Left: the correction (5.28a) is not applied. Right: the correction (5.28a) is applied.

$$\rho\frac{\partial \boldsymbol{v}}{\partial t} - \nabla \cdot \left(2\eta_s\left(\boldsymbol{\epsilon}(\boldsymbol{v}) - \frac{1}{3}(\nabla \cdot \boldsymbol{v})\boldsymbol{I}\right)\right) + \nabla q - \nabla \cdot \left(\boldsymbol{\tau} - \frac{1}{3}\mathrm{tr}(\boldsymbol{\tau})\boldsymbol{I}\right) = \rho\boldsymbol{g}, \qquad (5.33a)$$

$$\frac{\partial q}{\partial t} + \beta(\nabla \cdot \boldsymbol{v}) = 0, \qquad (5.33b)$$

$$\alpha\boldsymbol{\tau} + \lambda\left(\frac{\partial \boldsymbol{\tau}}{\partial t} - \nabla\boldsymbol{v}\boldsymbol{\tau} - \boldsymbol{\tau}\nabla\boldsymbol{v}^T\right) = 2\eta_p\boldsymbol{\epsilon}(\boldsymbol{v}), \qquad (5.33c)$$

with initial conditions $\boldsymbol{v}(t^{n-1}) = \boldsymbol{u}^{n-\frac{1}{2}}$, $q(t^{n-1}) = p^{n-\frac{1}{2}}$ and $\boldsymbol{\tau}(t^{n-1})) = \boldsymbol{\sigma}^{n-\frac{1}{2}}$ and boundary conditions discussed previously. The approximation of velocity, pressure and extra-stress at time t^n are then updated by $\boldsymbol{u}^n = \boldsymbol{v}(t^n)$, $p^n = q(t^n)$ and $\boldsymbol{\sigma}^n = \boldsymbol{\tau}(t^n)$.

The method of characteristics (1.13) is applied to solve the system of equations (5.32). As previously analysed, the method solves the conservative transport equations:

$$\frac{\partial \boldsymbol{v}}{\partial t} + \nabla \cdot (\boldsymbol{v} \otimes \boldsymbol{v}) = 0, \qquad (5.34a)$$

$$\frac{\partial q}{\partial t} + \nabla \cdot (q\boldsymbol{v}) = 0, \qquad (5.34b)$$

$$\frac{\partial \boldsymbol{\tau}}{\partial t} + \nabla \cdot (\boldsymbol{\tau} \otimes \boldsymbol{v}) = 0, \qquad (5.34c)$$

$$\frac{\partial \psi}{\partial t} + \nabla \cdot (\psi\boldsymbol{v}) = 0, \qquad (5.34d)$$

Hence, it allows to solve (5.32c) exactly but a correction has to be made for the remaining equations (5.32a),(5.32b),(5.32d). Now, let $h > 0$ and consider a grid made of cubic cells C_{ijk} of size h, with barycenter $\boldsymbol{x}_{ijk}$. Let φ_{ijk}^{n-1} and $\boldsymbol{u}_{ijk}^{n-1}$ be the approximated value respectively of the functions φ^{n-1} and $\boldsymbol{u}^{n-1}$ on each cell C_{ijk}. The algorithm

presented earlier for the characteristic function equation (5.32d) is similarly applied to the equations (5.32a) and (5.32b). Hence, we solve in each non-empty cell C_{ijk} the approximated equations in $[t^{n-1}, t^n]$:

$$\frac{\mathrm{d}\tilde{\boldsymbol{v}}_{ijk}}{\mathrm{d}t}(t) - \tilde{\boldsymbol{v}}_{ijk}(t)(\nabla \cdot \boldsymbol{u}_{ijk}^{n-1}) = 0, \tag{5.35a}$$

$$\frac{\mathrm{d}\tilde{q}_{ijk}}{\mathrm{d}t}(t) - \tilde{q}_{ijk}(t)(\nabla \cdot \boldsymbol{u}_{ijk}^{n-1}) = 0, \tag{5.35b}$$

$$\frac{\mathrm{d}\tilde{\psi}_{ijk}}{\mathrm{d}t}(t) - \tilde{\psi}_{ijk}(t)(\nabla \cdot \boldsymbol{u}_{ijk}^{n-1}) = 0, \tag{5.35c}$$

with the initial conditions $\tilde{\boldsymbol{v}}_{ijk}(t^{n-1}) = \boldsymbol{u}_{ijk}^{n-1}, \tilde{q}_{ijk}(t^{n-1}) = p_{ijk}^{n-1}$ and $\tilde{\psi}_{ijk}(t^{n-1}) = \varphi_{ijk}^{n-1}$. These equations are solved exactly in each cell C_{ijk} at time t^n:

$$\tilde{\boldsymbol{v}}_{ijk}^{n-\frac{1}{2}} := \tilde{\boldsymbol{v}}_{ijk}(t^n) = \boldsymbol{u}_{ijk}^{n-1}\bar{\psi}_{ijk}^{n-\frac{1}{2}},$$

$$\tilde{q}_{ijk}^{n-\frac{1}{2}} := \tilde{q}_{ijk}(t^n) = p_{ijk}^{n-1}\bar{\psi}_{ijk}^{n-\frac{1}{2}},$$

$$\tilde{\psi}_{ijk}^{n-\frac{1}{2}} := \tilde{\psi}_{ijk}(t^n) = \varphi_{ijk}^{n-1}\bar{\psi}_{ijk}^{n-\frac{1}{2}},$$

where $\bar{\psi}_{ijk}^{n-\frac{1}{2}} = \exp((t^n - t^{n-1})(\nabla \cdot \boldsymbol{u}_{ijk}^{n-1}))$, similarly as in the previous section 5.2.1.

Now, we use the method of characteristics to transport the non-corrected characteristic function φ_{ijk}^{n-1}. We obtain the updated characteristic function φ_{ijk}^n. Then, the function $\varphi_{ijk}^{n-1}\bar{\psi}_{ijk}^{n-\frac{1}{2}}$ is transported by the method of characteristics, which solves the equation (5.34c) and we obtain the updated values ψ_{ijk}^n in each active cell. The characteristic function φ_{ijk}^n at time t^n is updated as $\varphi_{ijk}^n := \varphi_{ijk}^n\psi_{ijk}^n$. This part is similar as explained in section 5.2.1. Then, as motivated in chapter 1, the method of characteristics is used on $\varphi_{ijk}^{n-1}\tilde{\boldsymbol{v}}_{ijk}^{n-\frac{1}{2}}$ to obtain the velocity $\boldsymbol{u}_{ijk}^{n-\frac{1}{2}}$ and on $\varphi_{ijk}^{n-1}\tilde{q}_{ijk}^{n-\frac{1}{2}}$ to obtain the pressure $p_{ijk}^{n-\frac{1}{2}}$. The extra-stress $\boldsymbol{\sigma}_{ijk}^{n-\frac{1}{2}}$ is then recovered on the cells using the method of characteristics.

Consider now the FE discretization of the system of equations (5.36d). Let $H > 0$ and $\mathcal{T}_H$ be a triangulation of the cavity Λ of maximum diameter H. The characteristic function φ_{ijk}^n is interpolated on the FE mesh and allows to define the computational domain Ω_H^n, similarly as in section 1.4.2. Let $\boldsymbol{V}_H^n \subset (\mathcal{C}^0(\overline{\Omega_H^n}))^3$, $Q_H^n \subset \mathcal{C}^0(\overline{\Omega_H^n})$ and $\boldsymbol{T}_H^n \subset (\mathcal{C}^0(\overline{\Omega_H^n}))^{3\times3}$ be the piecewise linear FE spaces considered in section 1.4.3, with the definition (1.26). The velocity $\boldsymbol{u}_H^{n-\frac{1}{2}} \in \boldsymbol{V}_H^n$, the pressure $p_H^{n-\frac{1}{2}} \in Q_H^n$ and the extra-stress $\boldsymbol{\sigma}_H^{n-\frac{1}{2}} \in \boldsymbol{T}_H^n$ are obtained from interpolating the functions from the structured grid to FE mesh using equation (1.18).

The implicit scheme previously applied to the incompressible scheme is adapted here for the system of equations (5.33) of the correction step. Consider the semi-implicit time

discretisation of the correction step system of equations in Ω^n:

$$\rho \frac{\boldsymbol{u}^n - \boldsymbol{u}^{n-\frac{1}{2}}}{\Delta t} - \nabla \cdot \left(2\eta_s \left(\boldsymbol{\epsilon}(\boldsymbol{u}^n) - \frac{1}{3}(\nabla \cdot \boldsymbol{u}^n)\boldsymbol{I} \right) \right) \tag{5.36a}$$

$$+ \nabla p^n - \nabla \cdot \left(\boldsymbol{\sigma}^n - \frac{1}{3}\mathrm{tr}(\boldsymbol{\sigma}^n)\boldsymbol{I} \right) = \rho \boldsymbol{g},$$

$$\frac{1}{\beta}\frac{p^n - p^{n-\frac{1}{2}}}{\Delta t} + \nabla \cdot \boldsymbol{u}^n = 0, \tag{5.36b}$$

$$\alpha \boldsymbol{\sigma}^n + \lambda \left(\frac{\boldsymbol{\sigma}^n - \boldsymbol{\sigma}^{n-\frac{1}{2}}}{\Delta t} - \nabla \boldsymbol{u}^{n-\frac{1}{2}} \boldsymbol{\sigma}^{n-\frac{1}{2}} - \boldsymbol{\sigma}^{n-\frac{1}{2}} (\nabla \boldsymbol{u}^{n-\frac{1}{2}})^T \right) = 2\eta_p \boldsymbol{\epsilon}(\boldsymbol{u}^n). \tag{5.36c}$$

Similarly as in equation (1.25d) we can explicit $\boldsymbol{\sigma}^n$ from (5.36c) and insert it in (5.36a) to decouple the computation of $(\boldsymbol{u}^n, p^n)$ and $\boldsymbol{\sigma}^n$. Thus, we first find $\boldsymbol{u}^n : \Omega^n \to \mathbb{R}^3$ and $p^n : \Omega^n \to \mathbb{R}$ such that

$$\rho \frac{\boldsymbol{u}^n - \boldsymbol{u}^{n-\frac{1}{2}}}{\Delta t} - \nabla \cdot \left(2 \left(\eta_s + \frac{\eta_p \Delta t}{\lambda + \alpha \Delta t} \right) \left(\boldsymbol{\epsilon}(\boldsymbol{u}^n) - \frac{1}{3}\nabla \cdot \boldsymbol{u}^n \right) \boldsymbol{I} \right) + \nabla p^n$$

$$= \frac{\lambda}{\lambda + \alpha \Delta t} \left(\nabla \cdot \boldsymbol{\sigma}^{n-\frac{1}{2}} - \frac{1}{3}\nabla \left(\mathrm{tr}(\boldsymbol{\sigma}^{n-\frac{1}{2}}) \right) \right) \tag{5.36d}$$

$$+ \frac{\lambda \Delta t}{\lambda + \alpha \Delta t} \left(\nabla \cdot (\nabla \boldsymbol{u}^{n-\frac{1}{2}} \boldsymbol{\sigma}^{n-\frac{1}{2}} + \boldsymbol{\sigma}^{n-\frac{1}{2}} (\nabla \boldsymbol{u}^{n-\frac{1}{2}})^T) + \frac{2}{3}\nabla \left(\nabla \boldsymbol{u}^{n-\frac{1}{2}} : \boldsymbol{\sigma}^{n-\frac{1}{2}} \right) \right) + \rho \boldsymbol{g}.$$

and then $\boldsymbol{\sigma}^n : \Omega^n \to \mathbb{R}^{3\times 3}$ satisfying (5.36c).

Hence, the FE discretisation of the correction step (5.33) reads:
Find $\boldsymbol{u}_H^n \in \boldsymbol{V}_H^n$, $p_H^n \in Q_H^n$ such that

$$\int_{\Omega_H^n} \rho \frac{\boldsymbol{u}_H^n - \boldsymbol{u}_H^{n-\frac{1}{2}}}{\Delta t} \cdot \boldsymbol{v}_H \, \mathrm{d}\boldsymbol{x} + \int_{\Omega_H^n} 2 \left(\eta_s + \frac{\eta_p \Delta t}{\lambda + \alpha \Delta t} \right) \boldsymbol{\epsilon}(\boldsymbol{u}_H^n) : \boldsymbol{\epsilon}(\boldsymbol{v}_H) \, \mathrm{d}\boldsymbol{x}$$

$$- \int_{\Omega_H^n} \frac{2}{3} \left(\eta_s + \frac{\eta_p \Delta t}{\lambda + \alpha \Delta t} \right) (\nabla \cdot \boldsymbol{u}_H^n)(\nabla \cdot \boldsymbol{v}_H) \, \mathrm{d}\boldsymbol{x} - \int_{\Omega_H^n} p_H^n \nabla \cdot \boldsymbol{v}_H \, \mathrm{d}\boldsymbol{x} \tag{5.37a}$$

$$= \int_{\Omega_H^n} \rho \boldsymbol{g} \cdot \boldsymbol{v}_H \, \mathrm{d}\boldsymbol{x} - \int_{\Omega_H^n} \frac{\lambda}{\lambda + \alpha \Delta t} \left(\boldsymbol{\sigma}_H^{n-\frac{1}{2}} : \boldsymbol{\epsilon}(\boldsymbol{v}_H) - \frac{1}{3}\mathrm{tr}(\boldsymbol{\sigma}_H^{n-\frac{1}{2}})(\nabla \cdot \boldsymbol{v}_H) \right) \, \mathrm{d}\boldsymbol{x}$$

$$- \int_{\Omega_H^n} \frac{\lambda \Delta t}{\lambda + \alpha \Delta t} \left(\left(\nabla \boldsymbol{u}_H^{n-\frac{1}{2}} \boldsymbol{\sigma}_H^{n-\frac{1}{2}} + \boldsymbol{\sigma}_H^{n-\frac{1}{2}} (\nabla \boldsymbol{u}_H^{n-\frac{1}{2}})^T \right) : \boldsymbol{\epsilon}(\boldsymbol{v}_H) \right.$$

$$\left. - \frac{2}{3} \left(\nabla \boldsymbol{u}_H^{n-\frac{1}{2}} : \boldsymbol{\sigma}_H^{n-\frac{1}{2}} \right) (\nabla \cdot \boldsymbol{v}_H) \right) \, \mathrm{d}\boldsymbol{x}, \qquad\qquad \forall \boldsymbol{v}_H \in \boldsymbol{V}_H^n,$$

$$\int_{\Omega_H^n} (\nabla \cdot \boldsymbol{u}_H^n) q_H \, \mathrm{d}\boldsymbol{x} + \int_{\Omega_H^n} \frac{1}{\beta} \frac{p_H^n - p_H^{n-\frac{1}{2}}}{\Delta t} q_H \, \mathrm{d}\boldsymbol{x} = 0, \qquad \forall q_H \in Q_H^n. \tag{5.37b}$$

Then, we solve the weak formulation of the Oldroyd-B equation to recover the extra-stress

tensor $\boldsymbol{\sigma}_H^n \in \boldsymbol{T}_H^n$, which is actually similar as the equation (1.27d).

The initial velocity $\boldsymbol{u}_H^0$, pressure p_H^0 and extra-stress tensor $\boldsymbol{\sigma}_H^0$ are interpolated onto $\boldsymbol{V}_H^0$. However, depending on the initial pressure, oscillations can be observed and never decrease due to the wave nature of the equation. In [YA21], the pressure was initialised by solving a Poisson equation $\nabla p = \rho \boldsymbol{g}$ in order to suppress the oscillations. The pressure p_H^0 can be computed by relying on the following stationary Stokes problem:

$$
\begin{aligned}
\int_{\Omega_H^0} p_H^0 \nabla \cdot \boldsymbol{v}_H \; \mathrm{d}\boldsymbol{x} \;\; &= \int_{\Omega_H^0} \rho \boldsymbol{g} \cdot \boldsymbol{v}_H \; \mathrm{d}\boldsymbol{x} - \int_{\Omega_H^0} 2\eta_s \boldsymbol{\epsilon}(\boldsymbol{u}_H^0) : \boldsymbol{\epsilon}(\boldsymbol{v}_H) \; \mathrm{d}\boldsymbol{x} \\
&\quad + \frac{2\eta_s}{3} \int_{\Omega_H^n} (\nabla \cdot \boldsymbol{u}_H^0)(\nabla \cdot \boldsymbol{v}_H) \; \mathrm{d}\boldsymbol{x} \\
&\quad - \int_{\Omega_H^0} \boldsymbol{\sigma}_H^0 : \boldsymbol{\epsilon}(\boldsymbol{v}_H) \; \mathrm{d}\boldsymbol{x} \\
&\quad + \frac{1}{3} \int_{\Omega_H^n} \mathrm{tr}(\boldsymbol{\sigma}_H^0)(\nabla \cdot \boldsymbol{v}_H) \; \mathrm{d}\boldsymbol{x}, \quad \forall \boldsymbol{v}_H \in \boldsymbol{V}_H^0.
\end{aligned}
\tag{5.38}
$$

5.3 Numerical simulation for volume changing

In this section, we only address the case $\alpha = \eta_s = 0$, corresponding to the deformation of a compressible Neo-Hookean material. It corresponds to a tensile test experiment, similarly as developped in section 2.2.1 for rubber material. Indeed, the main motivation of taking into account compressible effect is first to extend the model to improve the result obtained in chapter 2. Validation results for the numerical model for weakly compressible Newtonian and viscoelastic flows are still to be obtained.

Rubber is nearly incompressible and its Poisson ratio is close to 0.5. Consider the unified model (5.24) for compressible Neo-Hookean solid, that is for $\alpha = 0$ and $\eta_s = 0$. The parameter β now corresponds to the first Lamé parameter λ. Consider the settings of the rubber traction experiments, where the velocity is imposed on the shoulders of the tensile. The mesh sizes and physical parameters remain the same: $H = 4$ mm, $h = 0.6$ mm, $\Delta t = 0.8$ s, $\rho = 940$ kg/m^3, $\eta_p = 2 \cdot 10^5$ Pa s. The parameter β controls the change of volume, thus the simulations are computed for values of β in $\{10^6, 10^7, 10^8\}$ Pa s. The initial pressure p_0 is here initialised to 0 and the extra-stress tensor $\boldsymbol{\sigma}_0 = \boldsymbol{0}$. The initial velocity is smoothed: $\boldsymbol{u}_0 = (0, 0, 2 \cdot 10^{-4} \tanh(80z))$.

In Figure 5.3, the pressure p and extra-stress component $\boldsymbol{\sigma}_{zz}$ are monitored along the axis $\mathcal{O}z$ in the axial direction of the tensile specimen, at the time corresponding to 0.1% relative elongation. Visual convergence is observed. In Figure 5.4, a comparison of the force $\boldsymbol{\sigma}_{zz} - p$ profile for the different values of the parameter β. As we can expect from equation (5.24c), the pressure becomes smaller for a larger value of β. Finally, Figure 5.4 shows the evolution of the total volume $\int_\Lambda \varphi(\boldsymbol{x}, t) \; \mathrm{d}\boldsymbol{x}$ over time. The conservation

of the total mass is not anymore respected due to the mass equation (5.24c) and the numerical correction on the prediction step (5.29). A smaller value of β induces a larger compressibility and we obtain a larger change in volume for $\beta = 10^6$ Pa s.
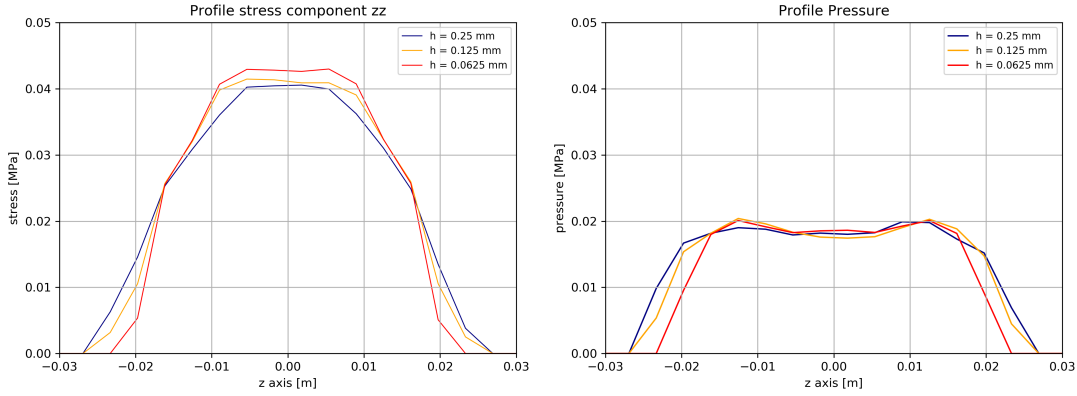
Figure 5.3 – Compressible model. Profile along the axis $\mathcal{O}z$ at time $t = 8$ s and strain 0.1% for $\beta = 10^6$ Pa s. Left: Extra-stress component $\boldsymbol{\sigma}_{zz}$. Right: Pressure p.
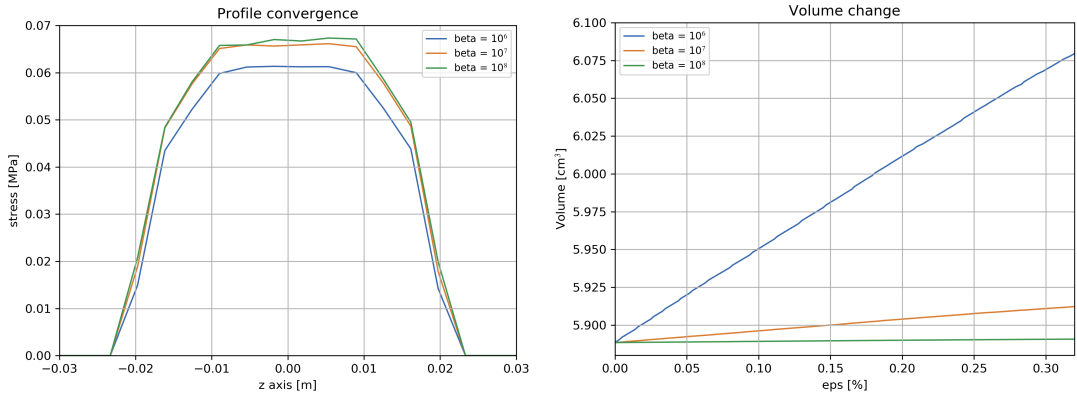
Figure 5.4 – Compressible model. Finer discretisation parameters. Left: Component z of total force $\boldsymbol{\sigma}_{zz} - p$ profile at time $t = 8$ s and strain 0.1%. Right: Evolution of total VOF volume with respect to strain.

■ Conclusion

The numerical framework proposed in [Mar00, BCP06] has been adapted to the unified model of [Pic16] for the simulation of incompressible Newtonian and viscoelastic fluids and incompressible Neo-Hookean elastic solid free-surface flows. An alternative time discretisation of the diffusive part of the system was proposed and study on a simplified system of equations. The unconditional stability of this implicit scheme and convergence of the system energy was proved. The performance of the alternative time discretisation has been tested on numerical experiments and shown to be superior to the EVSS scheme, previously applied on Oldroyd-B model. The numerical validation of the incompressible Neo-Hookean elastic model was carried on a set of numerical experiments based on engineering applications. Finally, an algorithm applying the Signorini boundary conditions on the system of equations was proposed and tested.

Then, we proposed a multiphase formulation of the previous system of equations, allowing to model the interactions of multiple incompressible Newtonian and viscoelastic fluids and incompressible Neo-Hookean elastic solids. The model is based on a VOF method suggested by [JBCP14]. The numerical approximation of the system of equations was adapted to the alternative rheology of the model by the application of the previously used time discretisations of the diffusive terms. The performances of this new model were tested on different numerical experiments, exhibiting its accuracy and flexibility. Indeed, the number of phases to be simulated is not restricted and the method of characteristics is a robust tool to handle their movements. Also, the model allows the simulation of multiple rheologies using the same set of equations for a straightforward formulation, letting us tackle a large panel of problems.

An extension to weakly compressible flows was proposed in order to improve the modelling of physical problems. A compressible unified model was obtained, as well as a complementary numerical framework, in order to take into account the compressible effects. Indeed, an additional splitting algorithm for the transport equations allowed to tackle the issue brought by the method of characteristics in compressible flows.

Future work is split on different axes:

135

- The a priori estimates for the simplified multiphase model are not complete. A multi-domain formulation of the simplified problem could allow to obtain multiphase counterpart of the general results obtain in chapter 1 for $N = 1$.

- The interface conditions between the phases in the multiphase formulation can be relaxed and would allow the modelling of surface tension. This additional feature would improve the results for the simulation of mutliple fluids flows, for instance in the numerical experiment in section 4.2. Together with a different viscoelastic constitutive equation (FENE or Giesekus), these extensions would allow the validation of our fluid model with respect to the literature review. Furthermore, the algorithm proposed in section 4.1 can be implemented and tested for the simulation of analogous Signorini boundary conditions on multiphase interface.

- Proper validation of the unified compressible model must be carried on. Compressible extension to multiphase compressible flows is allowed by our formulation and would bring an additional extension to the multiphase formulation we suggested.

- Finally, extension to order two schemes should be investigated. This could be done using the order two Strang splitting scheme. A Crank-Nicolson time discretisation of the correction step should also be applied. Then, a higher order interface reconstruction should be investigated.

Et si tu crois que c'est fini, ...

attends!

— Celine

A Appendix A: Useful results

Lemma A.0.1 (Jacobi's formula [MN19], Theorem 8.1)**.** Let $n > 1$ and $A : \mathbb{R} \to \mathbb{R}^{n \times n}$ be an invertible differential matrix function. Then it holds

$$\frac{\mathrm{d}}{\mathrm{d}t} \det(A(t)) = \mathrm{tr}\left(\mathrm{adj}(A(t))\frac{\mathrm{d}A(t)}{\mathrm{d}t}\right)$$
$$= \det(A(t))\mathrm{tr}\left(A(t)^{-1}\frac{\mathrm{d}A(t)}{\mathrm{d}t}\right)$$

Theorem A.0.1 (Reynold's transport theorem [Hol02])**.** Let $T > 0$ and $\Omega_0 \subset \mathbb{R}^3$. Let $\boldsymbol{x} : [0,T] \times \Omega_0 \to \mathbb{R}^3$ a particle displacement function, defining for all $t \in (0,T)$ a domain $\Omega(t) = \{\boldsymbol{x} \in \mathbb{R}^3; \exists \boldsymbol{X} \in \Omega_0 \text{ such that } \boldsymbol{x} = \varphi(\boldsymbol{X}, t)\}$. We also define the space-time domain $\mathcal{Q}_T = \{(\boldsymbol{x}, t) \in \mathbb{R}^3 \times [0,T]; \boldsymbol{x} \in \Omega(t)\}$ and $\boldsymbol{n}(\boldsymbol{x}, t)$ be the normal of the boundary $\partial\Omega(t)$ at $\boldsymbol{x}$. Now, let $f : \mathcal{Q}_T \to \mathbb{R}$. Then, the following formula holds:

$$\frac{\mathrm{d}}{\mathrm{d}t}\left(\int_{\Omega(t)} f \, \mathrm{d}\boldsymbol{x}\right) = \int_{\Omega(t)} \frac{\partial f}{\partial t} \, \mathrm{d}\boldsymbol{x} + \int_{\partial\Omega(t)} (\boldsymbol{u} \cdot \boldsymbol{n})f \, \mathrm{d}\boldsymbol{S}, \tag{A.1}$$

where $\frac{\partial}{\partial t}\boldsymbol{x}(\boldsymbol{X}, t) = \boldsymbol{u}(\boldsymbol{x}(\boldsymbol{X}, t), t)$ denotes the interface velocity.

Lemma A.0.2 (A first discrete Grönwall's Lemma [Dub20])**.** Let $N \geq 1$ be an integer. Let $a_n, \gamma_n, 0 \leq n \leq N$ and $b_n, c_n, \mu_n, 1 \leq n \leq N$ be non-negative numbers such that

$$a_m - a_{m-1} + b_m \leq \gamma_{m-1}a_{m-1} + \mu_m a_m + c_m, \quad \forall 1 \leq m \leq N.$$

Assume that $\mu_n < 1$ for all $1 \leq n \leq N$. Then

$$a_m^2 + \sum_{n=1}^m b_n \leq \left(a_0 + \sum_{n=1}^m c_n\right) + \exp\left(\sum_{n=0}^{m-1} \gamma_n\right)\exp\left(\sum_{n=1}^m \frac{\mu_n}{1-\mu_n}\right), \quad \forall 1 \leq m \leq N.$$

Lemma A.0.3 (Corollary of Grönwall's Lemma)**.** Let $N \geq 1$ be an integer. Let a_n, b_n, c_n, μ_n be non-negative numbers for all $0 \leq n \leq N$ such that

$$a_n^2 + b_n \leq a_{n-1}^2 + \mu_n a_n + c_n, \quad \forall 1 \leq m \leq N. \tag{A.2}$$

Appendix A. Appendix A: Useful results

Then

$$a_m^2 + \sum_{n=1}^m b_n \leq \exp(1)\left(a_0^2 + \sum_{n=1}^m c_n + \frac{N+1}{4}\sum_{n=1}^m \mu_n^2\right), \quad \forall 1 \leq m \leq N. \qquad \text{(A.3)}$$

Proof. We have from Young's inequality:

$$a_n^2 - a_{n-1}^2 + b_n \leq \mu_n a_n + c_n \leq \frac{\epsilon}{2}\mu_n^2 + \frac{1}{2\epsilon}a_n^2 + c_n, \qquad \text{(A.4)}$$

for any $\epsilon > 0$. Using Lemma A.0.2, we find

$$a_m^2 + \sum_{n=1}^m b_n \leq \left(a_0^2 + \sum_{n=1}^m \frac{1}{2\epsilon}\mu_n^2 + \sum_{n=1}^m c_n\right)\exp\left(m\frac{\epsilon}{2-\epsilon}\right).$$

For $\epsilon = 2/(N+1) < 2$, we find

$$\exp\left(m\frac{2/(N+1)}{2 - 2/(N+1)}\right) \leq \exp\left(N\frac{2/(N+1)}{2 - 2/(N+1)}\right) = \exp(1).$$

■

B | Appendix B: Validation of interpolation methods between cells and finite elements

Two interpolation methods were presented in section 1 to interpolate the variables from the structured grid to unstructured FE mesh. We want to compare the convergence of the L^2-interpolation method (1.20) and the weighted distance method (1.18). Convergence is checked starting for a domain $\Lambda = [-0.14, 0.14] \times [-0.14, 0.14]$ with a characteristic function $\varphi_0(\boldsymbol{x}) = \{\boldsymbol{x} = (x, y) \in \Lambda; x^2 + y^2 < 0.005\}$ and initial velocity $\boldsymbol{u}_0(\boldsymbol{x}) = 16 * (1 - y^2)$. The coarse setting corresponds to $H = 0.015$ m, $h = 0.0045$ m and $\Delta t = 0.0016$ s. Finer meshes are then obtained by dividing the discretisation parameters by two, keeping the CFL number constant. The velocity is interpolated from one mesh to the other until $T = 0.0192$ s. The expected convergence is divided by the number of time steps and for $CFL = \Delta t/h$ and $R = H/h$ yields $\|\boldsymbol{u}_H(t) - \boldsymbol{u}_{H,0}\|_{L^2(\Omega)} \leq C(h^2 + H^2)(T/\Delta t) = (CT(1 + R^2)/CFL)h$. In Figure B.1, the order 1 convergence is recovered for both interpolation method. However, the weighted distance method (Steiner) performs better than the L^2-interpolation method (Maronnier) and were thus used in our computations.
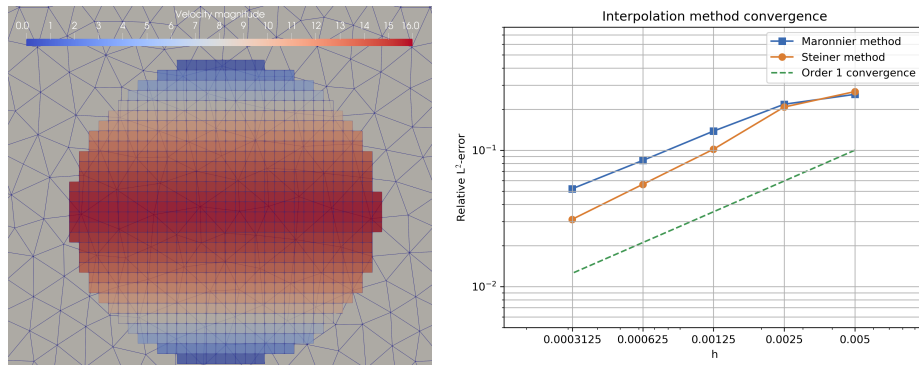
Figure B.1 – Convergence of interpolation method. Left: Active cells and FE mesh, the velocity is displayed on the cells. Right: Convergence graphs for Maronnier's (1.20) and Steiner's (1.18) interpolation methods.

C Appendix C: Additional proofs

C.1 Proof of Proposition 1.5.3

Proof. Let $e_{\boldsymbol{u}}^n = \boldsymbol{u}(t^n) - \boldsymbol{u}^n$, $e_p^n = p(t^n) - p^n$ and $e_{\boldsymbol{\sigma}}^n = \boldsymbol{\sigma}(t^n) - \boldsymbol{\sigma}^n$. From Taylor expansion we obtain from (1.29) at time t^n:

$$\int_\Omega \rho \frac{\boldsymbol{u}(t^n) - \boldsymbol{u}(t^{n-1})}{\Delta t} \cdot \boldsymbol{v} \, \mathrm{d}\boldsymbol{x} + \int_\Omega 2\eta_s \boldsymbol{\epsilon}(\boldsymbol{u}(t^n)) : \boldsymbol{\epsilon}(\boldsymbol{v}) \, \mathrm{d}\boldsymbol{x} - \int_\Omega p(t^n)(\nabla \cdot \boldsymbol{v}) \, \mathrm{d}\boldsymbol{x} \qquad \text{(C.1)}$$

$$+ \int_\Omega \boldsymbol{\sigma}(t^n) : \boldsymbol{\epsilon}(\boldsymbol{v}) \, \mathrm{d}\boldsymbol{x} + \frac{\rho}{\Delta t} \int_{t^{n-1}}^{t^n} \left[\int_t^{t^n} \left(\int_\Omega \frac{\partial^2 \boldsymbol{u}}{\partial t^2}(s) \cdot \boldsymbol{v} \, \mathrm{d}\boldsymbol{x} \right) \mathrm{d}s \right] \mathrm{d}t = 0, \quad \forall \boldsymbol{v} \in H_0^1(\Omega),$$

$$\int_\Omega q \nabla \cdot \boldsymbol{u}(t^n) \, \mathrm{d}\boldsymbol{x} = 0, \quad \forall q \in L_0^2(\Omega),$$

$$\int_\Omega \alpha \boldsymbol{\sigma}(t^n) : \boldsymbol{\tau} \, \mathrm{d}\boldsymbol{x} + \int_\Omega \lambda \frac{\boldsymbol{\sigma}(t^n) - \boldsymbol{\sigma}(t^{n-1})}{\Delta t} : \boldsymbol{\tau} \, \mathrm{d}\boldsymbol{x} - \int_\Omega 2\eta_p \boldsymbol{\epsilon}(\boldsymbol{u}(t^n)) : \boldsymbol{\tau} \, \mathrm{d}\boldsymbol{x}$$

$$+ \frac{\lambda}{\Delta t} \int_{t^{n-1}}^{t^n} \left[\int_t^{t^n} \left(\int_\Omega \frac{\partial^2 \boldsymbol{\sigma}}{\partial t^2}(s) : \boldsymbol{\tau} \, \mathrm{d}\boldsymbol{x} \right) \mathrm{d}s \right] \mathrm{d}t = 0, \quad \forall \boldsymbol{\tau} \in L^2(\Omega)^{3\times 3}.$$

Taking the difference between the previous equations and the weak formulation for the implicit scheme (1.42) and it yields:

$$\int_\Omega \rho \frac{e_{\boldsymbol{u}}^n - e_{\boldsymbol{u}}^{n-1}}{\Delta t} \cdot \boldsymbol{v} \, \mathrm{d}x + \int_\Omega 2\eta_s \boldsymbol{\epsilon}(e_{\boldsymbol{u}}^n) : \boldsymbol{\epsilon}(\boldsymbol{v}) \, \mathrm{d}x - \int e_p^n \nabla \cdot \boldsymbol{v} \, \mathrm{d}x \qquad \text{(C.2)}$$

$$+ \int_\Omega e_{\boldsymbol{\sigma}}^n : \boldsymbol{\epsilon}(\boldsymbol{v}) \, \mathrm{d}x + \frac{\rho}{\Delta t} \int_{t^{n-1}}^{t^n} \left[\int_t^{t^n} \left(\int_\Omega \frac{\partial^2 \boldsymbol{u}}{\partial t^2}(s) \cdot \boldsymbol{v} \, \mathrm{d}\boldsymbol{x} \right) \mathrm{d}s \right] \mathrm{d}t = 0, \quad \forall \boldsymbol{v} \in H_0^1(\Omega),$$

$$\int_\Omega (\nabla \cdot e_{\boldsymbol{u}}^n) q \, \mathrm{d}x = 0, \forall q \in L_0^2(\Omega) \quad \text{(C.3)}$$

$$\int_\Omega \alpha e_{\boldsymbol{\sigma}}^n : \boldsymbol{\tau} \, \mathrm{d}x + \int_\Omega \lambda \frac{e_{\boldsymbol{\sigma}}^n - e_{\boldsymbol{\sigma}}^{n-1}}{\Delta t} : \boldsymbol{\tau} \, \mathrm{d}x - \int_\Omega 2\eta_p \boldsymbol{\epsilon}(e_{\boldsymbol{u}}^n) : \boldsymbol{\tau} \, \mathrm{d}x \qquad \text{(C.4)}$$

$$+ \frac{\lambda}{\Delta t} \int_{t^{n-1}}^{t^n} \left[\int_t^{t^n} \left(\int_\Omega \frac{\partial^2 \boldsymbol{\sigma}}{\partial t^2}(s) : \boldsymbol{\tau} \, \mathrm{d}\boldsymbol{x} \right) \mathrm{d}s \right] \mathrm{d}t = 0, \quad \forall \boldsymbol{\tau} \in L^2(\Omega)^{3\times 3}.$$

We set $\boldsymbol{v} = e_{\boldsymbol{u}}^n$, $q = e_n^p$, $\boldsymbol{\tau} = e_{\boldsymbol{\sigma}}^n$ and use the identity $(a-b)a = \frac{1}{2}\|a\|^2 - \frac{1}{2}\|b\|^2 + \frac{1}{2}\|a-b\|^2$ for $a, b \in \mathbb{R}^3$ (identical identity for $a, b \in \mathbb{R}^{3\times 3}$) to obtain:

$$\frac{\rho}{2\Delta t}\|e_{\boldsymbol{u}}^n\|_{L^2(\Omega)^3}^2 + \frac{\rho}{2\Delta t}\left\|e_{\boldsymbol{u}}^n - e_{\boldsymbol{u}}^{n-1}\right\|_{L^2(\Omega)^3}^2 + 2\eta_s\|\boldsymbol{\epsilon}(e_{\boldsymbol{u}}^n)\|_{L^2(\Omega)^{3\times3}}^2 + \int_\Omega e_{\boldsymbol{\sigma}}^n : \boldsymbol{\epsilon}(e_{\boldsymbol{u}}^n)\,\mathrm{d}x$$

$$= \frac{\rho}{2\Delta t}\left\|e_{\boldsymbol{u}}^{n-1}\right\|_{L^2(\Omega)^3}^2 - \frac{\rho}{\Delta t}\int_{t^{n-1}}^{t^n}\left[\int_t^{t^n}\left(\int_\Omega \frac{\partial^2 \boldsymbol{u}}{\partial t^2}(s)\cdot e_{\boldsymbol{u}}^n\,\mathrm{d}x\right)\mathrm{d}s\right]\mathrm{d}t,$$

$$\left(\frac{\alpha}{2\eta_p} + \frac{\lambda}{4\Delta t\eta_p}\right)\|e_{\boldsymbol{\sigma}}^n\|_{L^2(\Omega)^{3\times3}}^2 + \frac{\lambda}{4\Delta t\eta_p}\left\|e_{\boldsymbol{\sigma}}^n - e_{\boldsymbol{\sigma}}^{n-1}\right\|_{L^2(\Omega)^{3\times3}}^2 - \int_\Omega \boldsymbol{\epsilon}(e_{\boldsymbol{u}}^n) : e_{\boldsymbol{\sigma}}^n\,\mathrm{d}x$$

$$= \frac{\lambda}{4\Delta t\eta_p}\left\|e_{\boldsymbol{\sigma}}^{n-1}\right\|_{L^2(\Omega)^{3\times3}}^2 - \frac{\lambda}{2\eta_p\Delta t}\int_{t^{n-1}}^{t^n}\left[\int_t^{t^n}\left(\int_\Omega \frac{\partial^2 \boldsymbol{\sigma}}{\partial t^2}(s) : e_{\boldsymbol{\sigma}}^n\,\mathrm{d}x\right)\mathrm{d}s\right]\mathrm{d}t.$$

By using Cauchy-Schwarz inequality we find:

$$-\frac{\rho}{\Delta t}\int_{t^{n-1}}^{t^n}\left[\int_t^{t^n}\left(\int_\Omega \frac{\partial^2 \boldsymbol{u}}{\partial t^2}(s)\cdot e_{\boldsymbol{u}}^n\,\mathrm{d}x\right)\mathrm{d}s\right]\mathrm{d}t \leq \frac{\rho}{\Delta t}\|e_{\boldsymbol{u}}^n\|_{L^2(\Omega)^3}\int_{t^{n-1}}^{t^n}\left(\int_t^{t^n}\left\|\frac{\partial^2 \boldsymbol{u}}{\partial t^2}(s)\right\|_{L^2(\Omega)^3}\mathrm{d}s\right)\mathrm{d}t$$

$$\leq \rho\|e_{\boldsymbol{u}}^n\|_{L^2(\Omega)^3}\int_{t^{n-1}}^{t^n}\left\|\frac{\partial^2 \boldsymbol{u}}{\partial t^2}(t)\right\|_{L^2(\Omega)^3}\mathrm{d}t$$

$$\leq \rho\sqrt{\Delta t}\|e_{\boldsymbol{u}}^n\|_{L^2(\Omega)^3}\left(\int_{t^{n-1}}^{t^n}\left\|\frac{\partial^2 \boldsymbol{u}}{\partial t^2}(s)\right\|_{L^2(\Omega)^3}^2\mathrm{d}t\right)^{\frac{1}{2}}.$$

We similarly obtain

$$-\frac{\lambda}{2\eta_p\Delta t}\int_{t^{n-1}}^{t^n}\left[\int_t^{t^n}\left(\int_\Omega \frac{\partial^2 \boldsymbol{\sigma}}{\partial t^2}(s) : e_{\boldsymbol{\sigma}}^n\,\mathrm{d}x\right)\mathrm{d}s\right]\mathrm{d}t \leq \frac{\lambda}{2\eta_p}\sqrt{\Delta t}\|e_{\boldsymbol{\sigma}}^n\|_{L^2(\Omega)^{3\times3}}\left(\int_{t^{n-1}}^{t^n}\left\|\frac{\partial^2 \boldsymbol{\sigma}}{\partial t^2}(s)\right\|_{L^2(\Omega)^{3\times3}}^2\mathrm{d}t\right)^{\frac{1}{2}}.$$

Thus it yields

$$\left(\rho\|e_{\boldsymbol{u}}^n\|_{L^2(\Omega)^3}^2 + \frac{\lambda}{2\eta_p}\|e_{\boldsymbol{\sigma}}^n\|_{L^2(\Omega)^{3\times3}}^2\right) + \Delta t\left(4\eta_s\|\boldsymbol{\epsilon}(e_{\boldsymbol{u}}^n)\|_{L^2(\Omega)^{3\times3}}^2 + \frac{\alpha}{\eta_p}\|e_{\boldsymbol{\sigma}}^n\|_{L^2(\Omega)^{3\times3}}^2\right)$$

$$\leq \left(\rho\left\|e_{\boldsymbol{u}}^{n-1}\right\|_{L^2(\Omega)^3}^2 + \frac{\lambda}{2\eta_p}\left\|e_{\boldsymbol{\sigma}}^{n-1}\right\|_{L^2(\Omega)^{3\times3}}^2\right) + \left(\rho\|e_{\boldsymbol{u}}^n\|_{L^2(\Omega)^3}^2 + \frac{\lambda}{2\eta_p}\|e_{\boldsymbol{\sigma}}^n\|_{L^2(\Omega)^{3\times3}}^2\right)^{\frac{1}{2}}$$

$$\left[\left(\rho\Delta t^3\int_{t^{n-1}}^{t^n}\left\|\frac{\partial^2 \boldsymbol{u}}{\partial t^2}(s)\right\|_{L^2(\Omega)^3}^2\mathrm{d}t\right)^{\frac{1}{2}} + \left(\frac{\lambda}{2\eta_p}\Delta t^3\int_{t^{n-1}}^{t^n}\left\|\frac{\partial^2 \boldsymbol{\sigma}}{\partial t^2}(s)\right\|_{L^2(\Omega)^{3\times3}}^2\mathrm{d}t\right)^{\frac{1}{2}}\right].$$

Define for $n = 0, \ldots, N$:

- $a_n = \left(\rho\|e_{\boldsymbol{u}}^n\|_{L^2(\Omega)^3}^2 + \frac{\lambda}{2\eta_p}\|e_{\boldsymbol{\sigma}}^n\|_{L^2(\Omega)^{3\times3}}^2\right)^{\frac{1}{2}},$

- $b_n = \Delta t \left(4\eta_s \|\boldsymbol{\epsilon}(e_{\boldsymbol{u}}^n)\|_{L^2(\Omega)^{3\times3}}^2 + \dfrac{\alpha}{\eta_p} \|e_{\boldsymbol{\sigma}}^n\|_{L^2(\Omega)^{3\times3}}^2 \right)$,

- $\mu_n = \left[\left(\rho \Delta t^3 \displaystyle\int_{t^{n-1}}^{t^n} \left\| \dfrac{\partial^2 \boldsymbol{u}}{\partial t^2}(s) \right\|_{L^2(\Omega)^3}^2 \, \mathrm{d}t \right)^{\frac{1}{2}} + \left(\dfrac{\lambda}{2\eta_p} \Delta t^3 \displaystyle\int_{t^{n-1}}^{t^n} \left\| \dfrac{\partial^2 \boldsymbol{\sigma}}{\partial t^2}(s) \right\|_{L^2(\Omega)^{3\times3}}^2 \, \mathrm{d}t \right)^{\frac{1}{2}} \right]$,

- $c_n = 0$.

Applying Lemma A.0.3, it yields for $N + 1 \le \frac{2}{\Delta t}$:

$$\rho \left\| e_{\boldsymbol{u}}^N \right\|_{L^2(\Omega)^3}^2 + \frac{\lambda}{2\eta_p} \left\| e_{\boldsymbol{\sigma}}^N \right\|_{L^2(\Omega)^{3\times3}}^2 + \sum_{n=1}^N \Delta t \left(4\eta_s \|\boldsymbol{\epsilon}(e_{\boldsymbol{u}}^n)\|_{L^2(\Omega)^{3\times3}}^2 + \frac{\alpha}{\eta_p} \|e_{\boldsymbol{\sigma}}^n\|_{L^2(\Omega)^{3\times3}}^2 \right)$$

$$\le \Delta t^2 \left(\rho \int_0^T \left\| \frac{\partial^2 \boldsymbol{u}}{\partial t^2}(s) \right\|_{L^2(\Omega)^3}^2 \, \mathrm{d}t + \frac{\lambda}{2\eta_p} \int_0^T \left\| \frac{\partial^2 \boldsymbol{\sigma}}{\partial t^2}(s) \right\|_{L^2(\Omega)^{3\times3}}^2 \, \mathrm{d}t \right).$$

which concludes the proof. ∎

C.2 Proof of Proposition 1.5.4

Proof. Let us use the previous notations of section C.1 and, for $n = 0, \dots, N-1$:

$$\langle \boldsymbol{R}_{\boldsymbol{u}}^n, \boldsymbol{v} \rangle = \int_{t^{n-1}}^{t^n} \left[\int_t^{t^n} \left(\int_\Omega \frac{\partial^2 \boldsymbol{u}}{\partial t^2}(s) \cdot \boldsymbol{v} \, \mathrm{d}\boldsymbol{x} \right) \mathrm{d}s \right] \mathrm{d}t, \tag{C.5}$$

$$\langle \boldsymbol{R}_{\boldsymbol{\sigma}}^n, \boldsymbol{\sigma} \rangle = \int_{t^{n-1}}^{t^n} \left[\int_t^{t^n} \left(\int_\Omega \frac{\partial^2 \boldsymbol{\sigma}}{\partial t^2}(s) : \boldsymbol{\tau} \, \mathrm{d}\boldsymbol{x} \right) \mathrm{d}s \right] \mathrm{d}t. \tag{C.6}$$

Taking the difference between two time steps of the equation (C.1) yields

$$\int_\Omega \rho \frac{\boldsymbol{u}(t^{n+1}) - 2\boldsymbol{u}(t^n) + \boldsymbol{u}(t^{n-1})}{\Delta t} \cdot \boldsymbol{v} \, \mathrm{d}\boldsymbol{x} + \int_\Omega 2\eta_s \boldsymbol{\epsilon}(\boldsymbol{u}(t^{n+1}) - \boldsymbol{u}(t^n)) : \boldsymbol{\epsilon}(\boldsymbol{v}) \, \mathrm{d}\boldsymbol{x}$$

$$- \int_\Omega (p(t^{n+1}) - p(t^n))(\nabla \cdot \boldsymbol{v}) \, \mathrm{d}\boldsymbol{x} + \int_\Omega (\boldsymbol{\sigma}(t^{n+1}) - \boldsymbol{\sigma}(t^n)) : \boldsymbol{\epsilon}(\boldsymbol{v}) \, \mathrm{d}\boldsymbol{x}$$

$$+ \frac{\rho}{\Delta t} \langle \boldsymbol{R}_{\boldsymbol{u}}^{n+1} - \boldsymbol{R}_{\boldsymbol{u}}^n, \boldsymbol{v} \rangle = 0, \qquad \forall \boldsymbol{v} \in H_0^1(\Omega).$$

The difference between two time steps of the implicit scheme yields the equation (1.44). Taking the difference with the latter equation and multiply by $\frac{\lambda}{\Delta t}$ yields

$$\int_\Omega \rho\lambda \frac{e_{\boldsymbol{u}}^{n+1} - 2e_{\boldsymbol{u}}^n + e_{\boldsymbol{u}}^{n-1}}{\Delta t^2} \cdot \boldsymbol{v} \, \mathrm{d}\boldsymbol{x} + \int_\Omega 2\eta_s \lambda \boldsymbol{\epsilon}\left(\frac{e_{\boldsymbol{u}}^{n+1} - e_{\boldsymbol{u}}^n}{\Delta t} \right) : \boldsymbol{\epsilon}(\boldsymbol{v}) \, \mathrm{d}\boldsymbol{x}$$

$$- \int_\Omega \lambda \left(\frac{e_p^{n+1} - e_p^n}{\Delta t} \right) (\nabla \cdot \boldsymbol{v}) \, \mathrm{d}\boldsymbol{x} + \int_\Omega \lambda \left(\frac{e_{\boldsymbol{\sigma}}^{n+1} - e_{\boldsymbol{\sigma}}^n}{\Delta t} \right) : \boldsymbol{\epsilon}(\boldsymbol{v}) \, \mathrm{d}\boldsymbol{x}$$

$$+ \frac{\rho\lambda}{\Delta t^2} \langle \boldsymbol{R}_{\boldsymbol{u}}^{n+1} - \boldsymbol{R}_{\boldsymbol{u}}^n, \boldsymbol{v} \rangle = 0, \qquad \forall \boldsymbol{v} \in H_0^1(\Omega).$$

Appendix C. Appendix C: Additional proofs

Using the equation (C.3), we can remove the pressure error terms. Add α times the equation (C.2) to obtain:

$$
\int_\Omega \rho\lambda \frac{e_{\boldsymbol{u}}^{n+1} - 2e_{\boldsymbol{u}}^n + e_{\boldsymbol{u}}^{n-1}}{\Delta t^2} \cdot \boldsymbol{v}\,\mathrm{d}\boldsymbol{x} + \int_\Omega 2\eta_s\lambda\boldsymbol{\epsilon}\left(\frac{e_{\boldsymbol{u}}^{n+1} - e_{\boldsymbol{u}}^n}{\Delta t}\right) : \boldsymbol{\epsilon}(\boldsymbol{v})\,\mathrm{d}\boldsymbol{x} + \int_\Omega \rho\alpha\left(\frac{e_{\boldsymbol{u}}^{n+1} - e_{\boldsymbol{u}}^n}{\Delta t}\right) \cdot \boldsymbol{v}\,\mathrm{d}\boldsymbol{x}
$$

$$
+ \int_\Omega 2\eta_s\alpha\boldsymbol{\epsilon}(e_{\boldsymbol{u}}^{n+1}) : \boldsymbol{\epsilon}(\boldsymbol{v})\,\mathrm{d}\boldsymbol{x} + \int_\Omega \left(\alpha e_{\boldsymbol{\sigma}}^{n+1} + \lambda\left(\frac{e_{\boldsymbol{\sigma}}^{n+1} - e_{\boldsymbol{\sigma}}^n}{\Delta t}\right)\right) : \boldsymbol{\epsilon}(\boldsymbol{v})\,\mathrm{d}\boldsymbol{x}
$$

$$
+ \frac{\rho\lambda}{\Delta t^2}\langle \boldsymbol{R}_{\boldsymbol{u}}^{n+1} - \boldsymbol{R}_{\boldsymbol{u}}^n, \boldsymbol{v}\rangle + \frac{\rho\alpha}{\Delta t}\langle \boldsymbol{R}_{\boldsymbol{u}}^{n+1}, \boldsymbol{v}\rangle = 0.
$$

Using $\boldsymbol{\tau} = \boldsymbol{\epsilon}(\boldsymbol{v})$ in (C.4), the error terms for the extra-stress are cancelled out and we find:

$$
\int_\Omega \rho\lambda \frac{e_{\boldsymbol{u}}^{n+1} - 2e_{\boldsymbol{u}}^n + e_{\boldsymbol{u}}^{n-1}}{\Delta t} \cdot \boldsymbol{v}\,\mathrm{d}\boldsymbol{x} + \int_\Omega 2\eta_s\lambda\boldsymbol{\epsilon}\left(\frac{e_{\boldsymbol{u}}^{n+1} - e_{\boldsymbol{u}}^n}{\Delta t}\right) : \boldsymbol{\epsilon}(\boldsymbol{v})\,\mathrm{d}\boldsymbol{x} + \int_\Omega \rho\alpha\left(\frac{e_{\boldsymbol{u}}^{n+1} - e_{\boldsymbol{u}}^n}{\Delta t}\right) \cdot \boldsymbol{v}\,\mathrm{d}\boldsymbol{x}
$$

$$
+ \int_\Omega 2(\eta_s\alpha + \eta_p)\boldsymbol{\epsilon}(e_{\boldsymbol{u}}^{n+1}) : \boldsymbol{\epsilon}(\boldsymbol{v})\,\mathrm{d}\boldsymbol{x}
$$

$$
+ \frac{\rho\lambda}{\Delta t^2}\langle \boldsymbol{R}_{\boldsymbol{u}}^{n+1} - \boldsymbol{R}_{\boldsymbol{u}}^n, \boldsymbol{v}\rangle + \frac{\rho\alpha}{\Delta t}\langle \boldsymbol{R}_{\boldsymbol{u}}^{n+1}, \boldsymbol{v}\rangle + \frac{\lambda}{\Delta t}\langle \boldsymbol{R}_{\boldsymbol{\sigma}}^{n+1}, \boldsymbol{\epsilon}(\boldsymbol{v})\rangle = 0.
$$

For $\boldsymbol{v} = e_{\boldsymbol{u}}^{n+1} - e_{\boldsymbol{u}}^n$, we find:

$$
\int_\Omega \frac{\rho\lambda}{2}\left|\frac{e_{\boldsymbol{u}}^{n+1} - e_{\boldsymbol{u}}^n}{\Delta t^2}\right|^2 + \frac{\rho\lambda}{2}\left|\frac{e_{\boldsymbol{u}}^{n+1} - 2e_{\boldsymbol{u}}^n + e_{\boldsymbol{u}}^{n-1}}{\Delta t}\right|^2\,\mathrm{d}\boldsymbol{x}
$$

$$
+ \int_\Omega (\eta_s\alpha + \eta_p)|\boldsymbol{\epsilon}(e_{\boldsymbol{u}}^{n+1})|^2 + (\eta_s\alpha + \eta_p)|\boldsymbol{\epsilon}(e_{\boldsymbol{u}}^{n+1} - e_{\boldsymbol{u}}^n)|^2\,\mathrm{d}\boldsymbol{x}
$$

$$
+ \Delta t\int_\Omega \rho\alpha\left|\frac{e_{\boldsymbol{u}}^{n+1} - e_{\boldsymbol{u}}^n}{\Delta t}\right|^2 + 2\eta_s\lambda\left|\boldsymbol{\epsilon}\left(\frac{e_{\boldsymbol{u}}^{n+1} - e_{\boldsymbol{u}}^n}{\Delta t}\right)\right|^2\,\mathrm{d}\boldsymbol{x}
$$

$$
= \int_\Omega \frac{\rho\lambda}{2}\left|\frac{e_{\boldsymbol{u}}^n - e_{\boldsymbol{u}}^{n-1}}{\Delta t}\right|^2\,\mathrm{d}\boldsymbol{x} + \int_\Omega (\eta_s\alpha + \eta_p)|\boldsymbol{\epsilon}(e_{\boldsymbol{u}}^n)|^2\,\mathrm{d}\boldsymbol{x}
$$

$$
- \frac{\rho\lambda}{\Delta t^2}\langle \boldsymbol{R}_{\boldsymbol{u}}^{n+1} - \boldsymbol{R}_{\boldsymbol{u}}^n, e_{\boldsymbol{u}}^{n+1} - e_{\boldsymbol{u}}^n\rangle
$$

$$
- \frac{\rho\alpha}{\Delta t}\langle \boldsymbol{R}_{\boldsymbol{u}}^{n+1}, e_{\boldsymbol{u}}^{n+1} - e_{\boldsymbol{u}}^n\rangle - \frac{\lambda}{\Delta t}\langle \boldsymbol{R}_{\boldsymbol{\sigma}}^{n+1}, \boldsymbol{\epsilon}(e_{\boldsymbol{u}}^{n+1} - e_{\boldsymbol{u}}^n)\rangle.
$$

We have

$$-\frac{1}{\Delta t^2}\langle \boldsymbol{R_u}^{n+1} - \boldsymbol{R_u}^n, e_{\boldsymbol{u}}^{n+1} - e_{\boldsymbol{u}}^n\rangle$$

$$= \frac{1}{\Delta t}\left(\int_{t^n}^{t^{n+1}}\left[\int_t^{t^{n+1}}\left(\int_\Omega \frac{\partial^2 \boldsymbol{u}}{\partial t^2}(s)\cdot\frac{e_{\boldsymbol{u}}^{n+1} - e_{\boldsymbol{u}}^n}{\Delta t}\,\mathrm{d}\boldsymbol{x}\right)\mathrm{d}s\right]\mathrm{d}t\right.$$

$$\left.-\int_{t^{n-1}}^{t^n}\left[\int_t^{t^n}\left(\int_\Omega \frac{\partial^2 \boldsymbol{u}}{\partial t^2}(s)\cdot\frac{e_{\boldsymbol{u}}^{n+1} - e_{\boldsymbol{u}}^n}{\Delta t}\,\mathrm{d}\boldsymbol{x}\right)\mathrm{d}s\right]\mathrm{d}t\right)$$

$$= \Delta t\left[\int_\Omega \frac{1}{\Delta t}\left(\frac{\partial \boldsymbol{u}}{\partial t}(t^{n+1}) - \frac{\partial \boldsymbol{u}}{\partial t}(t^n)\right)\cdot\frac{e_{\boldsymbol{u}}^{n+1} - e_{\boldsymbol{u}}^n}{\Delta t}\,\mathrm{d}\boldsymbol{x}\right.$$

$$\left.-\int_\Omega \frac{\boldsymbol{u}(t^{n+1}) - 2\boldsymbol{u}(t^n) + \boldsymbol{u}(t^{n-1})}{\Delta t^2}\cdot\frac{e_{\boldsymbol{u}}^{n+1} - e_{\boldsymbol{u}}^n}{\Delta t}\,\mathrm{d}\boldsymbol{x}\right]$$

$$= \Delta t\left[\int_\Omega \frac{1}{2}\left(\frac{\partial^2 \boldsymbol{u}}{\partial t^2}(t^{n+1}) - \frac{\partial^2 \boldsymbol{u}}{\partial t^2}(t^n)\right)\cdot\frac{e_{\boldsymbol{u}}^{n+1} - e_{\boldsymbol{u}}^n}{\Delta t}\,\mathrm{d}\boldsymbol{x}\right.$$

$$+\frac{1}{6}\int_{t^n}^{t^{n+1}}\int_\Omega (t^{n+1} - t)\frac{\partial^3 \boldsymbol{u}}{\partial t^3}(t)\cdot\frac{e_{\boldsymbol{u}}^{n+1} - e_{\boldsymbol{u}}^n}{\Delta t}\,\mathrm{d}\boldsymbol{x}\,\mathrm{d}t$$

$$\left.-\frac{1}{6}\int_{t^{n-1}}^{t^n}\int_\Omega (t^{n+1} - t)\frac{\partial^3 \boldsymbol{u}}{\partial t^3}(t)\cdot\frac{e_{\boldsymbol{u}}^{n+1} - e_{\boldsymbol{u}}^n}{\Delta t}\,\mathrm{d}\boldsymbol{x}\,\mathrm{d}t\right]$$

$$\leq \left(\frac{\Delta t^{\frac{3}{2}}}{2} + \frac{\Delta t^2}{6}\right)\left\|\frac{e_{\boldsymbol{u}}^{n+1} - e_{\boldsymbol{u}}^n}{\Delta t}\right\|_{L^2(\Omega)^3}\left(\int_{t^{n-1}}^{t^{n+1}}\left\|\frac{\partial^3 \boldsymbol{u}}{\partial t^3}(t)\right\|_{L^2(\Omega)^3}^2\,\mathrm{d}t\right)^{\frac{1}{2}}.$$

The following terms are bounded as the following:

$$\bullet\ -\frac{\rho\alpha}{\Delta t}\langle \boldsymbol{R_u}^{n+1}, e_{\boldsymbol{u}}^{n+1} - e_{\boldsymbol{u}}^n\rangle = -\rho\alpha\int_{t^n}^{t^{n+1}}\left[\int_t^{t^{n+1}}\left(\int_\Omega \frac{\partial^2 \boldsymbol{u}}{\partial t^2}(s)\cdot\left(\frac{e_{\boldsymbol{u}}^{n+1} - e_{\boldsymbol{u}}^n}{\Delta t}\right)\mathrm{d}\boldsymbol{x}\right)\mathrm{d}s\right]\mathrm{d}t$$

$$\leq \alpha\rho\left\|\frac{e_{\boldsymbol{u}}^{n+1} - e_{\boldsymbol{u}}^n}{\Delta t}\right\|_{L^2(\Omega)^3}\int_{t^n}^{t^{n+1}}\left(\int_t^{t^{n+1}}\left\|\frac{\partial^2 \boldsymbol{u}}{\partial t^2}(s)\right\|_{L^2(\Omega)^3}\,\mathrm{d}s\right)\mathrm{d}t$$

$$\leq \alpha\rho\Delta t^{\frac{3}{2}}\left\|\frac{e_{\boldsymbol{u}}^{n+1} - e_{\boldsymbol{u}}^n}{\Delta t}\right\|_{L^2(\Omega)^3}\left(\int_t^{t^{n+1}}\left\|\frac{\partial^2 \boldsymbol{u}}{\partial t^2}(s)\right\|_{L^2(\Omega)^3}^2\,\mathrm{d}s\right)^{\frac{1}{2}}$$

$$\leq \frac{\alpha\rho\Delta t^2}{2}\int_{t^{n-1}}^{t^n}\left\|\frac{\partial^2 \boldsymbol{u}}{\partial t^2}(t)\right\|_{L^2(\Omega)^3}^2\,\mathrm{d}t + \frac{\alpha\rho\Delta t}{2}\left\|\frac{e_{\boldsymbol{u}}^{n+1} - e_{\boldsymbol{u}}^n}{\Delta t}\right\|_{L^2(\Omega)^3}^2,$$

Appendix C. Appendix C: Additional proofs

$\bullet \ -\dfrac{\lambda}{\Delta t}\langle \boldsymbol{R}_{\boldsymbol{\sigma}}^{n+1}, \boldsymbol{\epsilon}(e_{\boldsymbol{u}}^{n+1} - e_{\boldsymbol{u}}^n)\rangle = -\lambda \displaystyle\int_{t^n}^{t^{n+1}} \left[\int_t^{t^{n+1}} \left(\int_\Omega \dfrac{\partial^2 \boldsymbol{\sigma}}{\partial t^2}(s) : \boldsymbol{\epsilon}\left(\dfrac{e_{\boldsymbol{u}}^{n+1} - e_{\boldsymbol{u}}^n}{\Delta t} \right) \, d\boldsymbol{x} \right) \, ds \right] \, dt$

$= \lambda \displaystyle\int_{t^n}^{t^{n+1}} \left[\int_t^{t^{n+1}} \left(\int_\Omega \dfrac{\partial^2}{\partial t^2}(\nabla \cdot \boldsymbol{\sigma})(s) : \left(\dfrac{e_{\boldsymbol{u}}^{n+1} - e_{\boldsymbol{u}}^n}{\Delta t} \right) \, d\boldsymbol{x} \right) \, ds \right] \, dt$

$\leq \lambda \left\| \dfrac{e_{\boldsymbol{u}}^{n+1} - e_{\boldsymbol{u}}^n}{\Delta t} \right\|_{L^2(\Omega)^{3\times 3}} \displaystyle\int_{t^n}^{t^{n+1}} \left(\int_t^{t^{n+1}} \left\| \dfrac{\partial^2}{\partial t^2}(\nabla \cdot \boldsymbol{\sigma})(s) \right\|_{L^2(\Omega)^{3\times 3}} \, ds \right) \, dt$

$\leq \rho\lambda \left\| \dfrac{e_{\boldsymbol{u}}^{n+1} - e_{\boldsymbol{u}}^n}{\Delta t} \right\|_{L^2(\Omega)^{3\times 3}} \left(\Delta t^3 \displaystyle\int_{t^n}^{t^{n+1}} \left\| \dfrac{\partial^2}{\partial t^2}(\nabla \cdot \boldsymbol{\sigma})(s) \right\|_{L^2(\Omega)^{3\times 3}}^2 \, ds \right)^{\frac{1}{2}}.$

Finally, we obtain for $n = 1, \ldots, N-1$:

$\rho\lambda \left\| \dfrac{e_{\boldsymbol{u}}^{n+1} - e_{\boldsymbol{u}}^n}{\Delta t} \right\|_{L^2(\Omega)^3}^2 + 2(\eta_s\alpha + \eta_p)\left\| \boldsymbol{\epsilon}(e_{\boldsymbol{u}}^{n+1}) \right\|_{L^2(\Omega)^{3\times 3}}^2$

$+ \Delta t \left(\rho\alpha \left\| \dfrac{e_{\boldsymbol{u}}^{n+1} - e_{\boldsymbol{u}}^n}{\Delta t} \right\|_{L^2(\Omega)^3}^2 + 4\eta_s \left\| \boldsymbol{\epsilon}\left(\dfrac{e_{\boldsymbol{u}}^{n+1} - e_{\boldsymbol{u}}^n}{\Delta t} \right) \right\|_{L^2(\Omega)^{3\times 3}}^2 \right)$

$\leq \rho\lambda \left\| \dfrac{e_{\boldsymbol{u}}^n - e_{\boldsymbol{u}}^{n-1}}{\Delta t} \right\|_{L^2(\Omega)^3}^2 + 2(\eta_s\alpha + \eta_p)\|\boldsymbol{\epsilon}(e_{\boldsymbol{u}}^n)\|_{L^2(\Omega)^{3\times 3}}^2 + \alpha\rho\Delta t^2 \displaystyle\int_{t^{n-1}}^{t^n} \left\| \dfrac{\partial^2 \boldsymbol{u}}{\partial t^2}(t) \right\|_{L^2(\Omega)^3}^2 \, dt$

$+ \sqrt{2} \left(\rho\lambda \left\| \dfrac{e_{\boldsymbol{u}}^{n+1} - e_{\boldsymbol{u}}^n}{\Delta t} \right\|_{L^2(\Omega)^3}^2 + 2(\eta_s\alpha + \eta_p)\left\| \boldsymbol{\epsilon}(e_{\boldsymbol{u}}^{n+1}) \right\|_{L^2(\Omega)^{3\times 3}}^2 \right)^{\frac{1}{2}}$

$\left[\left(\dfrac{\Delta t^{\frac{3}{2}}}{2} + \dfrac{\Delta t^2}{6} \right) \left(\displaystyle\int_{t^{n-1}}^{t^{n+1}} \left\| \dfrac{\partial^3 \boldsymbol{u}}{\partial t^3}(t) \right\|_{L^2(\Omega)^3}^2 \, dt \right)^{\frac{1}{2}} + \Delta t^{\frac{3}{2}} \left(\displaystyle\int_{t^n}^{t^{n+1}} \left\| \dfrac{\partial^2}{\partial t^2}(\nabla \cdot \boldsymbol{\sigma})(s) \right\|_{L^2(\Omega)^{3\times 3}}^2 \, ds \right)^{\frac{1}{2}} \right].$

Define for $n = 0, \ldots, N-1$:

- $a_n = \left(\rho\lambda \left\| \dfrac{e_{\boldsymbol{u}}^{n+1} - e_{\boldsymbol{u}}^n}{\Delta t} \right\|_{L^2(\Omega)^3}^2 + 2(\eta_s\alpha + \eta_p)\left\| \boldsymbol{\epsilon}(e_{\boldsymbol{u}}^{n+1}) \right\|_{L^2(\Omega)^{3\times 3}}^2 \right)^{\frac{1}{2}},$

- $b_n = \Delta t \left(\rho\alpha \left\| \dfrac{e_{\boldsymbol{u}}^n - e_{\boldsymbol{u}}^{n-1}}{\Delta t} \right\|_{L^2(\Omega)^3}^2 + 4\eta_s \left\| \boldsymbol{\epsilon}\left(\dfrac{e_{\boldsymbol{u}}^n - e_{\boldsymbol{u}}^{n-1}}{\Delta t} \right) \right\|_{L^2(\Omega)^{3\times 3}}^2 \right),$

- $\mu_n = \Delta t^{\frac{3}{2}} \left[\left(\displaystyle\int_{t^{n-1}}^{t^{n+1}} \left\| \dfrac{\partial^3 \boldsymbol{u}}{\partial t^3}(t) \right\|_{L^2(\Omega)^3}^2 \, dt \right)^{\frac{1}{2}} + \left(\int_{t^n}^{t^{n+1}} \left\| \dfrac{\partial^2}{\partial t^2}(\nabla \cdot \boldsymbol{\sigma})(s) \right\|_{L^2(\Omega)^{3\times 3}}^2 \, ds \right)^{\frac{1}{2}} \right] +$
  $\mathcal{O}(\Delta t^2),$

- $c_n = \alpha\rho\Delta t^2 \displaystyle\int_{t^{n-1}}^{t^n} \left\| \dfrac{\partial^2 \boldsymbol{u}}{\partial t^2}(t) \right\|_{L^2(\Omega)^3}^2 \, dt.$

Applying Lemma A.0.3, it yields for $N + 1 \leq \frac{2}{\Delta t}$:

$$\rho \lambda \left\| \frac{e_{\boldsymbol{u}}^N - e_{\boldsymbol{u}}^{N-1}}{\Delta t} \right\|_{L^2(\Omega)^3}^2 + 2(\eta_s \alpha + \eta_p) \left\| \boldsymbol{\epsilon}(e_{\boldsymbol{u}}^N) \right\|_{L^2(\Omega)^{3 \times 3}}^2$$

$$+ \Delta t \sum_{n=1}^{N} \left(\rho \alpha \left\| \frac{e_{\boldsymbol{u}}^n - e_{\boldsymbol{u}}^{n-1}}{\Delta t} \right\|_{L^2(\Omega)^3}^2 + 4\eta_s \left\| \boldsymbol{\epsilon} \left(\frac{e_{\boldsymbol{u}}^n - e_{\boldsymbol{u}}^{n-1}}{\Delta t} \right) \right\|_{L^2(\Omega)^{3 \times 3}}^2 \right)$$

$$\leq \rho \lambda \left\| \frac{e_{\boldsymbol{u}}^1 - e_{\boldsymbol{u}}^0}{\Delta t} \right\|_{L^2(\Omega)^3}^2 + 2(\eta_s \alpha + \eta_p) \left\| \boldsymbol{\epsilon}(e_{\boldsymbol{u}}^1) \right\|_{L^2(\Omega)^{3 \times 3}}^2$$

$$+ C \Delta t^2 \left[\alpha \rho \int_0^T \left\| \frac{\partial^2 \boldsymbol{u}}{\partial t^2}(t) \right\|_{L^2(\Omega)^3}^2 \, \mathrm{d}t + \int_0^T \left\| \frac{\partial^3 \boldsymbol{u}}{\partial t^3}(t) \right\|_{L^2(\Omega)^3}^2 \, \mathrm{d}t \right.$$

$$\left. + \int_0^T \left\| \frac{\partial^2}{\partial t^2}(\nabla \cdot \boldsymbol{\sigma})(t) \right\|_{L^2(\Omega)^{3 \times 3}}^2 \, \mathrm{d}t \right] + \mathcal{O}(\Delta t^3),$$

for $C \in \mathbb{R}_+$, which concludes the proof. ∎

C.3 Proof of Proposition 1.7.2

Proof. From EVSS definition and L^2-projection property we have

$$\int_\Omega \boldsymbol{D}_H^{n-1} : \boldsymbol{\epsilon}(\boldsymbol{v}_H) \, \mathrm{d}\boldsymbol{x} = \int_\Omega \boldsymbol{D}_H^{n-1} : \pi_H(\boldsymbol{\epsilon}(\boldsymbol{v}_H)) \, \mathrm{d}\boldsymbol{x} = \int_\Omega \boldsymbol{\epsilon}(\boldsymbol{u}_H^{n-1}) : \pi_H(\boldsymbol{\epsilon}(\boldsymbol{v}_H)) \, \mathrm{d}\boldsymbol{x}.$$

Using $\boldsymbol{v}_H = \boldsymbol{u}_H^n + \boldsymbol{u}_H^{n-1}$ in in (1.63b) and $\boldsymbol{\tau}_H = \boldsymbol{\sigma}_H^n + \boldsymbol{\sigma}_H^{n-1}$ in (1.63d) we find:

$$\int_\Omega \frac{\rho}{\Delta t}(|\boldsymbol{u}_H^n|^2 - |\boldsymbol{u}_H^{n-1}|^2) \, \mathrm{d}\boldsymbol{x} + \int_\Omega 2(\eta_s + \eta_p)|\boldsymbol{\epsilon}(\boldsymbol{u}_H^n)|^2 \, \mathrm{d}\boldsymbol{x} + \int_\Omega 2(\eta_s + \eta_p)\boldsymbol{\epsilon}(\boldsymbol{u}_H^n) : \boldsymbol{\epsilon}(\boldsymbol{u}_H^{n-1}) \, \mathrm{d}\boldsymbol{x}$$

$$- \int_\Omega p_H^n \nabla \cdot (\boldsymbol{u}_H^n + \boldsymbol{u}_H^{n-1}) \, \mathrm{d}\boldsymbol{x} + \int_\Omega \boldsymbol{\sigma}_H^{n-1} : \boldsymbol{\epsilon}(\boldsymbol{u}_H^{n-1}) \, \mathrm{d}\boldsymbol{x}$$

$$- \int_\Omega 2\eta_p \boldsymbol{\epsilon}(\boldsymbol{u}_H^{n-1}) : (\pi_H(\boldsymbol{\epsilon}(\boldsymbol{u}_H^n)) + \pi_H(\boldsymbol{\epsilon}(\boldsymbol{u}_H^{n-1}))) \, \mathrm{d}\boldsymbol{x} + \int_\Omega \boldsymbol{\sigma}_H^{n-1} : \boldsymbol{\epsilon}(\boldsymbol{u}_H^n) \, \mathrm{d}\boldsymbol{x} = 0,$$

$$\int_\Omega \frac{\alpha}{2\eta_p}(|\boldsymbol{\sigma}_H^n|^2 + \boldsymbol{\sigma}_H^n : \boldsymbol{\sigma}_H^{n-1}) \mathrm{d}\boldsymbol{x} + \int_\Omega \frac{\lambda}{2\eta_p \Delta t}(|\boldsymbol{\sigma}_H^n|^2 - |\boldsymbol{\sigma}_H^{n-1}|^2) \, \mathrm{d}\boldsymbol{x} = \int_\Omega (\boldsymbol{\sigma}_H^n + \boldsymbol{\sigma}_H^{n-1}) : \boldsymbol{\epsilon}(\boldsymbol{u}_H^n) \, \mathrm{d}\boldsymbol{x}.$$

Appendix C. Appendix C: Additional proofs

Since the L^2-projection implies that for $\boldsymbol{\tau} \in L^2(\Omega)^{3\times 3}$, we have $\|\pi_H(\boldsymbol{\tau})\|_{L^2(\Omega)^{3\times 3}} \leq \|\boldsymbol{\tau}\|_{L^2(\Omega)^{3\times 3}}$ and

$$2\eta_p \Delta t \int_\Omega |\boldsymbol{\epsilon}(\boldsymbol{u}_H^n)|^2 + \boldsymbol{\epsilon}(\boldsymbol{u}_H^{n-1}) : \boldsymbol{\epsilon}(\boldsymbol{u}_H^n) - \boldsymbol{\epsilon}(\boldsymbol{u}_H^{n-1}) : (\pi_H(\boldsymbol{\epsilon}(\boldsymbol{u}_H^n)) + \pi_H(\boldsymbol{\epsilon}(\boldsymbol{u}_H^{n-1}))) \, \mathrm{d}\boldsymbol{x}$$

$$= \eta_p \Delta t \int_\Omega |\boldsymbol{\epsilon}(\boldsymbol{u}_H^n)|^2 - |\boldsymbol{\epsilon}(\boldsymbol{u}_H^{n-1})|^2 + |\boldsymbol{\epsilon}(\boldsymbol{u}_H^{n-1}) - \boldsymbol{\epsilon}(\boldsymbol{u}_H^n)|^2 - |\pi_H(\boldsymbol{\epsilon}(\boldsymbol{u}_H^{n-1}))|^2 + |\pi_H(\boldsymbol{\epsilon}(\boldsymbol{u}_H^n))|^2|$$

$$- |\pi_H(\boldsymbol{\epsilon}(\boldsymbol{u}_H^{n-1}) - \boldsymbol{\epsilon}(\boldsymbol{u}_H^n))|^2 \, \mathrm{d}\boldsymbol{x}$$

$$\geq \eta_p \Delta t \int_\Omega |\boldsymbol{\epsilon}(\boldsymbol{u}_H^n)|^2 - |\boldsymbol{\epsilon}(\boldsymbol{u}_H^{n-1})|^2 - |\pi_H(\boldsymbol{\epsilon}(\boldsymbol{u}_H^{n-1}))|^2 + |\pi_H(\boldsymbol{\epsilon}(\boldsymbol{u}_H^n))|^2| \, \mathrm{d}\boldsymbol{x}.$$

Thus, summing the two equations and using the latter, we find

$$\int_\Omega \rho|\boldsymbol{u}_H^n|^2 + \frac{\lambda}{2\eta_p}|\boldsymbol{\sigma}_H^n|^2 \, \mathrm{d}\boldsymbol{x} + \Delta t\left[\int_\Omega (\eta_s + \eta_p)|\boldsymbol{\epsilon}(\boldsymbol{u}_H^n)|^2 + \frac{\alpha}{4\eta_p}|\boldsymbol{\sigma}_H^n|^2 + \eta_p|\pi_H(\boldsymbol{\epsilon}(\boldsymbol{u}_H^n))|^2 \, \mathrm{d}\boldsymbol{x}\right]$$

$$+ \Delta t \sum_{K \in \mathcal{T}_H} \frac{\alpha_K}{2} \int_K |\nabla p_H^n|^2 \, \mathrm{d}\boldsymbol{x} - \Delta t \int_\Omega \boldsymbol{\sigma}_H^n : \boldsymbol{\epsilon}(\boldsymbol{u}_H^n) \, \mathrm{d}\boldsymbol{x}$$

$$\leq \int_\Omega \rho|\boldsymbol{u}_H^{n-1}|^2 + \frac{\lambda}{2\eta_p}|\boldsymbol{\sigma}_H^{n-1}|^2 \, \mathrm{d}\boldsymbol{x} + \Delta t\left[\int_\Omega (\eta_s + \eta_p)|\boldsymbol{\epsilon}(\boldsymbol{u}_H^{n-1})|^2 + \frac{\alpha}{4\eta_p}|\boldsymbol{\sigma}_H^{n-1}|^2\right.$$

$$\left. + \eta_p|\pi_H(\boldsymbol{\epsilon}(\boldsymbol{u}_H^{n-1}))|^2 \, \mathrm{d}\boldsymbol{x}\right] + \Delta t \sum_{K \in \mathcal{T}_H} \frac{\alpha_K}{2} \int_K |\nabla p_H^{n-1}|^2 \, \mathrm{d}\boldsymbol{x} - \Delta t \int_\Omega \boldsymbol{\sigma}_H^{n-1} : \boldsymbol{\epsilon}(\boldsymbol{u}_H^{n-1}) \, \mathrm{d}\boldsymbol{x}$$

$$\leq \cdots \leq \int_\Omega \rho|\boldsymbol{u}_H^0|^2 + \frac{\lambda}{2\eta_p}|\boldsymbol{\sigma}_H^0|^2 \, \mathrm{d}\boldsymbol{x} + \Delta t\left[\int_\Omega (\eta_s + \eta_p)|\boldsymbol{\epsilon}(\boldsymbol{u}_H^n)|^2 + \frac{\alpha}{4\eta_p}|\boldsymbol{\sigma}_H^0|^2\right.$$

$$\left. + \eta_p|\pi_H(\boldsymbol{\epsilon}(\boldsymbol{u}_H^0))|^2 \, \mathrm{d}\boldsymbol{x}\right] + \Delta t \sum_{K \in \mathcal{T}_H} \frac{\alpha_K}{2} \int_K |\nabla p_H^0|^2 \, \mathrm{d}\boldsymbol{x} - \Delta t \int_\Omega \boldsymbol{\sigma}_H^n : \boldsymbol{\epsilon}(\boldsymbol{u}_H^0) \, \mathrm{d}\boldsymbol{x}.$$

Finally, we find by applying

$$\Delta t \int_\Omega \boldsymbol{\sigma}_H^n : \boldsymbol{\epsilon}(\boldsymbol{u}_H^n) \, \mathrm{d}\boldsymbol{x} \leq \Delta t \int_\Omega \eta_p|\boldsymbol{\epsilon}(\boldsymbol{u}_H^n)|^2 \, \mathrm{d}\boldsymbol{x} + \frac{\Delta t}{4\eta_p} \int_\Omega |\boldsymbol{\sigma}_H^n|^2 \, \mathrm{d}\boldsymbol{x}$$

that

$$\int_\Omega \rho|\boldsymbol{u}_H^N|^2 + \frac{2\lambda - \Delta t}{4\eta_p}|\boldsymbol{\sigma}_H^N|^2 \, \mathrm{d}\boldsymbol{x} + \Delta t\left[\int_\Omega \eta_s|\boldsymbol{\epsilon}(\boldsymbol{u}_H^N)|^2 + \frac{\alpha}{4\eta_p}|\boldsymbol{\sigma}_H^N|^2 + \eta_p|\pi_H(\boldsymbol{\epsilon}(\boldsymbol{u}_H^N))|^2 \, \mathrm{d}\boldsymbol{x}\right]$$

$$+ \Delta t \sum_{K \in \mathcal{T}_H} \frac{\alpha_K}{2} \int_K |\nabla p_H^n|^2 \, \mathrm{d}\boldsymbol{x} \leq \int_\Omega \rho|\boldsymbol{u}_H^0|^2 + \frac{\lambda}{2\eta_p}|\boldsymbol{\sigma}_H^0|^2 \, \mathrm{d}\boldsymbol{x}$$

$$+ \Delta t\left[\int_\Omega (\eta_s + \eta_p)|\boldsymbol{\epsilon}(\boldsymbol{u}_H^n)|^2 + \frac{\alpha}{4\eta_p}|\boldsymbol{\sigma}_H^0|^2 \, \mathrm{d}\boldsymbol{x}\right]$$

$$+ \Delta t \sum_{K \in \mathcal{T}_H} \frac{\alpha_K}{2} \int_K |\nabla p_H^0|^2 \, \mathrm{d}\boldsymbol{x} - \Delta t\left[\int_\Omega \boldsymbol{\sigma}_H^n : \boldsymbol{\epsilon}(\boldsymbol{u}_H^0) \, \mathrm{d}\boldsymbol{x}\right]$$

and we obtain the first result.

Next, by applying $\lambda/\Delta t$ the difference between two steps of (1.63b) and adding up α times (1.63b), we find:

$$
\int_\Omega \rho\lambda \left(\frac{\boldsymbol{u}_H^{n+1} - 2\boldsymbol{u}_H^n + \boldsymbol{u}_H^{n-1}}{\Delta t^2} \right) \cdot \boldsymbol{v}_H \ \mathrm{d}\boldsymbol{x} + \int_\Omega 2(\eta_s + \eta_p)\lambda \boldsymbol{\epsilon} \left(\frac{\boldsymbol{u}_H^{n+1} - \boldsymbol{u}_H^n}{\Delta t} \right) : \boldsymbol{\epsilon}(\boldsymbol{v}_H) \ \mathrm{d}\boldsymbol{x}
$$

$$
+ \int_\Omega 2\eta_p(1 - \alpha)\boldsymbol{\epsilon}(\boldsymbol{u}_H^n) : \pi_H(\boldsymbol{\epsilon}(\boldsymbol{v}_H)) \ \mathrm{d}\boldsymbol{x}
$$

$$
+ \int_\Omega \rho\alpha \left(\frac{\boldsymbol{u}_H^{n+1} - \boldsymbol{u}_H^n}{\Delta t} \right) \cdot \boldsymbol{v}_H \ \mathrm{d}\boldsymbol{x} + \int_\Omega 2\alpha(\eta_p + \eta_s)\boldsymbol{\epsilon}(\boldsymbol{u}_H^{n+1}) : \boldsymbol{\epsilon}(\boldsymbol{v}_H) \ \mathrm{d}\boldsymbol{x}
$$

$$
- \int_\Omega \left(\alpha p_H^{n+1} + \lambda \left(\frac{p_H^{n+1} - p_H^n}{\Delta t} \right) \right) (\nabla \cdot \boldsymbol{v}_H) \ \mathrm{d}\boldsymbol{x}
$$

$$
- \int_\Omega 2\eta_p\lambda \boldsymbol{\epsilon} \left(\frac{\boldsymbol{u}_H^n - \boldsymbol{u}_n^{n-1}}{\Delta t} \right) : \pi_H \left(\boldsymbol{\epsilon}(\boldsymbol{v}_H) \right) \ \mathrm{d}\boldsymbol{x} = 0.
$$

For $\alpha = 1$ we set $\boldsymbol{v}_H = \boldsymbol{u}_H^{n+1} - \boldsymbol{u}_H^n$ and it yields

$$
\int_\Omega \frac{\rho\lambda}{2} \left| \frac{\boldsymbol{u}_H^{n+1} - \boldsymbol{u}_H^n}{\Delta t} \right|^2 + \frac{\rho\lambda}{2} \left| \frac{\boldsymbol{u}_H^{n+1} - 2\boldsymbol{u}_H^n + \boldsymbol{u}_H^{n-1}}{\Delta t} \right|^2
$$

$$
+ (\eta_p + \eta_s)(|\boldsymbol{\epsilon}(\boldsymbol{u}_H^{n+1})|^2 + |\boldsymbol{\epsilon}(\boldsymbol{u}_H^{n+1}) - \boldsymbol{\epsilon}(\boldsymbol{u}_H^n)|^2) \ \mathrm{d}\boldsymbol{x}
$$

$$
+ \Delta t \int_\Omega \rho \left| \frac{\boldsymbol{u}_H^{n+1} - \boldsymbol{u}_H^n}{\Delta t} \right|^2 + 2\eta_s\lambda \left| \boldsymbol{\epsilon} \left(\frac{\boldsymbol{u}_H^{n+1} - \boldsymbol{u}_H^n}{\Delta t} \right) \right|^2 \ \mathrm{d}\boldsymbol{x}
$$

$$
+ \sum_{K \in \mathcal{T}_H} \alpha_K \int_K \frac{1}{2} |\nabla p_H^{n+1}|^2 + \left(\frac{\lambda}{\Delta t} + \frac{1}{2} \right) |\nabla p_H^{n+1} - p_H^n|^2 \ \mathrm{d}\boldsymbol{x}
$$

$$
+ \Delta t \int_\Omega 2\eta_p\lambda \left| \boldsymbol{\epsilon} \left(\frac{\boldsymbol{u}_H^{n+1} - \boldsymbol{u}_n^n}{\Delta t} \right) \right|^2 \ \mathrm{d}\boldsymbol{x} - \Delta t \int_\Omega 2\eta_p\lambda \boldsymbol{\epsilon} \left(\frac{\boldsymbol{u}_H^n - \boldsymbol{u}_n^{n-1}}{\Delta t} \right) : \pi_H \left(\boldsymbol{\epsilon} \left(\frac{\boldsymbol{u}_H^{n+1} - \boldsymbol{u}_H^n}{\Delta t} \right) \right) \ \mathrm{d}\boldsymbol{x}
$$

$$
\leq \int_\Omega \frac{\rho\lambda}{2} \left| \frac{\boldsymbol{u}_H^n - \boldsymbol{u}_H^{n-1}}{\Delta t} \right|^2 \ \mathrm{d}\boldsymbol{x} + \int_\Omega (\eta_p + \eta_s)|\boldsymbol{\epsilon}\boldsymbol{u}_H^n)|^2 \ \mathrm{d}\boldsymbol{x} + \sum_{K \in \mathcal{T}_H} \alpha_K \int_K \frac{1}{2} |\nabla p_H^n|^2 \ \mathrm{d}\boldsymbol{x}.
$$

Appendix C. Appendix C: Additional proofs

From

$$\int_\Omega \left| \epsilon\left(\frac{\boldsymbol{u}_H^{n+1} - \boldsymbol{u}_n^n}{\Delta t}\right) \right|^2 - \epsilon\left(\frac{\boldsymbol{u}_H^n - \boldsymbol{u}_n^{n-1}}{\Delta t}\right) : \pi_H\left(\epsilon\left(\frac{\boldsymbol{u}_H^{n+1} - \boldsymbol{u}_n^n}{\Delta t}\right)\right) \, \mathrm{d}\boldsymbol{x}$$

$$\geq \int_\Omega \left| \pi_H\left(\epsilon\left(\frac{\boldsymbol{u}_H^{n+1} - \boldsymbol{u}_H^n}{\Delta t}\right)\right) \right|^2 - \pi_H\left(\epsilon\left(\frac{\boldsymbol{u}_H^n - \boldsymbol{u}_n^{n-1}}{\Delta t}\right)\right) : \pi_H\left(\epsilon\left(\frac{\boldsymbol{u}_H^{n+1} - \boldsymbol{u}_n^n}{\Delta t}\right)\right) \, \mathrm{d}\boldsymbol{x}$$

$$= \int_\Omega \left| \pi_H\left(\epsilon\left(\frac{\boldsymbol{u}_H^{n+1} - \boldsymbol{u}_H^n}{\Delta t}\right)\right) \right|^2 - \left| \pi_H\left(\epsilon\left(\frac{\boldsymbol{u}_H^n - \boldsymbol{u}_H^{n-1}}{\Delta t}\right)\right) \right|^2$$

$$+ \left| \pi_H\left(\epsilon\left(\frac{\boldsymbol{u}_H^{n+1} - 2\boldsymbol{u}_H^n + \boldsymbol{u}_H^{n-1}}{\Delta t}\right)\right) \right|^2 \, \mathrm{d}\boldsymbol{x},$$

summing from $n = 1$ to $n = N - 1$ we obtain the result. Now for $\alpha = 0$, setting $\boldsymbol{v}_H = \boldsymbol{u}_H^{n+1} - \boldsymbol{u}_H^{n-1}$ it yields

$$\int_\Omega \frac{\rho\lambda}{2} \left| \frac{\boldsymbol{u}_H^{n+1} - \boldsymbol{u}_H^n}{\Delta t} \right|^2 + \int_\Omega 2\eta_p \epsilon(\boldsymbol{u}_H^n) : (\pi_H(\epsilon(\boldsymbol{u}_H^{n+1} - \boldsymbol{u}_H^{n-1}))) \, \mathrm{d}\boldsymbol{x}$$

$$+ \Delta t \int_\Omega 2\eta_s \lambda \epsilon\left(\frac{\boldsymbol{u}_H^{n+1} - \boldsymbol{u}_H^n}{\Delta t}\right) : \epsilon\left(\frac{\boldsymbol{u}_H^{n+1} - \boldsymbol{u}_H^{n-1}}{\Delta t}\right) \, \mathrm{d}\boldsymbol{x}$$

$$- \int_\Omega \lambda\left(\frac{p_H^{n+1} - p_H^n}{\Delta t}\right)(\nabla \cdot (\boldsymbol{u}_H^{n+1} - \boldsymbol{u}_H^{n-1})) \, \mathrm{d}\boldsymbol{x}$$

$$+ \Delta t \int_\Omega 2\eta_p \lambda \epsilon\left(\frac{\boldsymbol{u}_H^{n+1} - \boldsymbol{u}_H^n}{\Delta t}\right) : \epsilon\left(\frac{\boldsymbol{u}_H^{n+1} - \boldsymbol{u}_H^{n-1}}{\Delta t}\right) \, \mathrm{d}\boldsymbol{x}$$

$$- \Delta t \int_\Omega 2\eta_p \lambda \epsilon\left(\frac{\boldsymbol{u}_H^n - \boldsymbol{u}_H^{n-1}}{\Delta t}\right) : \pi_H\left(\epsilon\left(\frac{\boldsymbol{u}_H^{n+1} - \boldsymbol{u}_H^{n-1}}{\Delta t}\right)\right) \, \mathrm{d}\boldsymbol{x}$$

$$\leq \int_\Omega \frac{\rho\lambda}{2} \left| \frac{\boldsymbol{u}_H^n - \boldsymbol{u}_H^{n-1}}{\Delta t} \right|^2 \, \mathrm{d}\boldsymbol{x}.$$

The last but one term can be dealt with by applying

$$- \Delta t \int_\Omega 2\eta_p \lambda \epsilon\left(\frac{\boldsymbol{u}_H^n - \boldsymbol{u}_H^{n-1}}{\Delta t}\right) : \pi_H\left(\epsilon\left(\frac{\boldsymbol{u}_H^{n+1} - \boldsymbol{u}_H^{n-1}}{\Delta t}\right)\right) \, \mathrm{d}\boldsymbol{x}$$

$$= - \Delta t \int_\Omega 2\eta_p \lambda \pi_H\left(\epsilon\left(\frac{\boldsymbol{u}_H^n - \boldsymbol{u}_H^{n-1}}{\Delta t}\right)\right) : \pi_H\left(\epsilon\left(\frac{\boldsymbol{u}_H^{n+1} - \boldsymbol{u}_H^{n-1}}{\Delta t}\right)\right) \, \mathrm{d}\boldsymbol{x}$$

$$= \Delta t \int_\Omega \eta_p \lambda \left(\left| \pi_H\left(\epsilon\left(\frac{\boldsymbol{u}_H^{n+1} - \boldsymbol{u}_H^n}{\Delta t}\right)\right) \right|^2 \right.$$

$$\left. - \left| \pi_H\left(\epsilon\left(\frac{\boldsymbol{u}_H^n - \boldsymbol{u}_H^{n-1}}{\Delta t}\right)\right) \right|^2 - \left| \pi_H\left(\epsilon\left(\frac{\boldsymbol{u}_H^{n+1} - \boldsymbol{u}_H^{n-1}}{\Delta t}\right)\right) \right|^2 \right) \, \mathrm{d}\boldsymbol{x}.$$

Also we have

$$
-\int_\Omega \lambda \left(\frac{p_H^{n+1} - p_H^n}{\Delta t} \right) (\nabla \cdot (\boldsymbol{u}_H^{n+1} - \boldsymbol{u}_H^{n-1})) \, \mathrm{d}\boldsymbol{x}
$$

$$
= \Delta t \sum_{K \in \mathcal{T}_H} \frac{\alpha_k \lambda}{2} \int_K \left(\left| \nabla \left(\frac{p_H^{n+1} - p_H^n}{\Delta t} \right) \right|^2 - \left| \nabla \left(\frac{p_H^n - p_H^{n-1}}{\Delta t} \right) \right|^2 \right.
$$

$$
\left. + \left| \nabla \left(\frac{p_H^{n+1} - p_H^{n-1}}{\Delta t} \right) \right|^2 \right) \, \mathrm{d}\boldsymbol{x}.
$$

Finally it yields

$$
\int_\Omega \frac{\rho \lambda}{2} \left| \frac{\boldsymbol{u}_H^{n+1} - \boldsymbol{u}_H^n}{\Delta t} \right|^2 + \int_\Omega \eta_p (|\pi_H(\boldsymbol{\epsilon}(\boldsymbol{u}_H^{n+1}))|^2 + |\pi_H(\boldsymbol{\epsilon}(\boldsymbol{u}_H^n))|^2) \, \mathrm{d}\boldsymbol{x}
$$

$$
+ \Delta t \int_\Omega (\eta_s + \eta_p) \lambda \left| \boldsymbol{\epsilon} \left(\frac{\boldsymbol{u}_H^{n+1} - \boldsymbol{u}_H^n}{\Delta t} \right) \right|^2 \, \mathrm{d}\boldsymbol{x}
$$

$$
+ \Delta t \int_\Omega \eta_p (\lambda - \Delta t) \left| \pi_H \left(\boldsymbol{\epsilon} \left(\frac{\boldsymbol{u}_H^{n+1} - \boldsymbol{u}_H^n}{\Delta t} \right) \right) \right|^2 \, \mathrm{d}\boldsymbol{x}
$$

$$
+ \Delta t \sum_{K \in \mathcal{T}_H} \frac{\alpha_K \lambda}{2} \int_K \left(\left| \nabla \left(\frac{p_H^{n+1} - p_H^n}{\Delta t} \right) \right|^2 + \left| \nabla \left(\frac{p_H^{n+1} - p_H^{n-1}}{\Delta t} \right) \right|^2 \right) \, \mathrm{d}\boldsymbol{x}
$$

$$
\leq \int_\Omega \frac{\rho \lambda}{2} \left| \frac{\boldsymbol{u}_H^n - \boldsymbol{u}_H^{n-1}}{\Delta t} \right|^2 \, \mathrm{d}\boldsymbol{x} + \int_\Omega \eta_p (|\pi_H(\boldsymbol{\epsilon}(\boldsymbol{u}_H^n))|^2 + |\pi_H(\boldsymbol{\epsilon}(\boldsymbol{u}_H^{n-1}))|^2) \, \mathrm{d}\boldsymbol{x}
$$

$$
+ \Delta t \int_\Omega (\eta_s + \eta_p) \lambda \left| \boldsymbol{\epsilon} \left(\frac{\boldsymbol{u}_H^n - \boldsymbol{u}_H^{n-1}}{\Delta t} \right) \right|^2 \, \mathrm{d}\boldsymbol{x}
$$

$$
+ \Delta t \int_\Omega \eta_p (\lambda - \Delta t) \left| \pi_H \left(\boldsymbol{\epsilon} \left(\frac{\boldsymbol{u}_H^n - \boldsymbol{u}_H^{n-1}}{\Delta t} \right) \right) \right|^2 \, \mathrm{d}\boldsymbol{x}
$$

$$
+ \Delta t \sum_{K \in \mathcal{T}_H} \frac{\alpha_K \lambda}{2} \int_K \left| \nabla \left(\frac{p_H^n - p_H^{n-1}}{\Delta t} \right) \right|^2 \, \mathrm{d}\boldsymbol{x}.
$$

For $\Delta t \leq \lambda$, we can sum for $n = 1$ to $N - 1$ and we obtain the result. ∎

Bibliography

[ABD08]   Emmanuel Audusse, Marie-Odile Bristeau, and Astrid Decoene. Numerical simulations of 3D free surface flows by a multilayer Saint-Venant model. *International journal for numerical methods in fluids*, 56(3):331–350, 2008.

[AMW98]   Daniel M Anderson, Geoffrey B McFadden, and Adam A Wheeler. Diffuse-interface methods in fluid mechanics. *Annual review of fluid mechanics*, 30(1):139–165, 1998.

[AÖ10]   Pedro-Jose Arrazola and Tugrul Özel. Investigations on the effects of friction modeling in finite element simulation of machining. *International journal of mechanical sciences*, 52(1):31–42, 2010.

[BAH87]   Robert Byron Bird, Robert Calvin Armstrong, and Ole Hassager. Dynamics of polymeric liquids. Vol. 1: Fluid mechanics. *Polymer International*, 1987.

[BBRS05]   Faker Ben Belgacem, Yves Renard, and Leila Slimane. A mixed formulation for the Signorini problem in nearly incompressible elasticity. *Applied Numerical Mathematics*, 54(1):1–22, 2005.

[BC09]   Olivier Andre Bauchau and James I Craig. *Structural analysis: with applications to aerospace structures*, volume 163. Springer Science & Business Media, 2009.

[BCP06]   Andrea Bonito, Philippe Clément, and Marco Picasso. Mathematical analysis of a simplified Hookean dumbbells model arising from viscoelastic flows. *Journal of Evolution Equations*, 6(3):381–398, 2006.

[BCP11]   Andrea Bonito, Philippe Clément, and Marco Picasso. Viscoelastic flows with complex free surfaces: Numerical analysis and simulation. In *Handbook of Numerical Analysis*, volume 16, pages 305–369. Elsevier, 2011.

[BJS+21]   Changyeob Baek, Paul Johanns, Tomohiko G Sano, Paul Grandgeorge, and Pedro M Reis. Finite element modeling of tight elastic knots. *Journal of Applied Mechanics*, 88(2), 2021.

[BKW06]   Fawzi Belblidia, IJ Keshtiban, and Michael Francis Webster. Stabilised computations for viscoelastic flows under compressible implementations. *Journal of non-newtonian fluid mechanics*, 134(1-3):56–76, 2006.

Bibliography

[BL19]   Anthony Bedford and Kenneth M Liechti. *Mechanics of materials.* Springer Nature, 2019.

[Bon06]   Andrea Bonito. *Analysis and numerical simulation of viscoelastic flows: deterministic and stochastic models.* PhD thesis, EPFL, Lausanne, 2006.

[BPL06]   Andrea Bonito, Marco Picasso, and Manuel Laso. Numerical simulation of 3D viscoelastic flows with free surfaces. *Journal of Computational Physics*, 215(2):691–716, 2006.

[BPS01]   John Bonvin, Marco Picasso, and Rolf Stenberg. GLS and EVSS methods for a three-field stokes problem arising from viscoelastic flows. *Computer Methods in Applied Mechanics and Engineering*, 190(29-30):3893–3914, 2001.

[Bru99]   Emil-Alexandru Brujan. A first-order model for bubble dynamics in a compressible viscoelastic liquid. *Journal of Non-Newtonian Fluid Mechanics*, 84(1):83–103, 1999.

[Cab04]   Alexandre Caboussat. *Analysis and numerical simulation of free surface flows.* PhD thesis, EPFL, Lausanne, 2004.

[Cab06]   Alexandre Caboussat. A numerical method for the simulation of free surface flows with surface tension. *Computers & fluids*, 35(10):1205–1216, 2006.

[CBM11]   Alexandre Caboussat, Sébastien Boyaval, and Alexandre Masserey. On the modeling and simulation of non-hydrostatic dam break flows. *Computing and visualization in science*, 14(8):401–417, 2011.

[CC04]   Eduardo E Cabezas and Diego J Celentano. Experimental and numerical analysis of the tensile test using sheet specimens. *Finite Elements in Analysis and Design*, 40(5-6):555–575, 2004.

[CEPP14]   Georges-Henri Cottet, Jean-Matthieu Etancelin, Franck Pérignon, and Christophe Picard. High order semi-Lagrangian particle methods for transport equations: numerical analysis and implementation issues. *ESAIM: Mathematical Modelling and Numerical Analysis*, 48(4):1029–1060, 2014.

[CGN05]   Paola Causin, Jean-Frédéric Gerbeau, and Fabio Nobile. Added-mass effect in the design of partitioned algorithms for fluid-structure problems. *Computer methods in applied mechanics and engineering*, 194(42-44):4506–4527, 2005.

[CGR16]   Doina Cioranescu, Vivette Girault, and Kumbakonam Ramamani Rajagopal. *Mechanics and mathematics of fluids of the differential type.* Springer, 2016.

[CHMP21]   Alexandre Caboussat, Julien Hess, Alexandre Masserey, and Marco Picasso. Numerical simulation of temperature-driven free surface flows, with application to laser surface melting. In *Proceedings of the 14th World Congress on Computational Mechanics (WCCM) and ECCOMAS Congress 2020*, 01 2021.

[Cho68]   Alexandre Joel Chorin. Numerical solution of the Navier-Stokes equations. *Mathematics of computation*, 22(104):745–762, 1968.

[CM72]   Mario Carrassi and Angelo Morro. A modified Navier-Stokes equation, and its consequences on sound dispersion. *Il Nuovo Cimento B (1971-1996)*, 9(2):321–343, 1972.

[CMPF17]   Massimiliano Cremonesi, Simone Meduri, Umberto Perego, and Attilio Frangi. An explicit Lagrangian finite element method for free-surface weakly compressible flows. *Computational Particle Mechanics*, 4(3):357–369, 2017.

[CR81]   Bruno Carbonaro and Fabio Rosso. Some remarks on a modified fluid dynamics equation. *Rendiconti Del Circolo Matematico Di Palermo*, 30(1):111–122, 1981.

[Dav83]   Stephen Davis. Contact-line problems in fluid mechanics. *Journal of Applied Mechanics, Transactions ASME*, 50(4):977–982, 1983.

[DD05]   Dolores Demarco and Eduardo N Dvorkin. An Eulerian finite element formulation for modelling stationary finite strain elastic deformation processes. *International journal for numerical methods in engineering*, 62(8):1038–1063, 2005.

[DDFQ06]   Simone Deparis, Marco Discacciati, Gilles Fourestey, and Alfio Quarteroni. Fluid-structure algorithms based on Steklov-Poincaré operators. *Computer Methods in Applied Mechanics and Engineering*, 195(41-43):5797–5812, 2006.

[DGN04]   Fabián Duarte, Raúl Gormaz, and Srinivasan Natesan. Arbitrary Lagrangian-Eulerian method for Navier-Stokes equations with moving boundaries. *Computer Methods in Applied Mechanics and Engineering*, 193(45-47):4819–4836, 2004.

[dNKM07]   Detlef de Niem, Ekkehard Kührt, and Uwe Motschmann. A volume-of-fluid method for simulation of compressible axisymmetric multi-material flow. *Computer physics communications*, 176(3):170–190, 2007.

[DPW21]   Samuel Dubuis, Marco Picasso, and Peter Wittwer. A space-time adaptive algorithm to illustrate the lack of collision of a rigid disk falling in an

incompressible fluid. *Computational Methods in Applied Mathematics*, 21(2):317–334, 2021.

[DR06]   Thomas Dunne and Rolf Rannacher. Adaptive finite element approximation of fluid-structure interaction based on an Eulerian variational formulation. In *Fluid-structure interaction*, pages 110–145. Springer, 2006.

[Dub20]   Samuel Dubuis. *Adaptive algorithms for two fluids flows with anisotropic finite elements and order two time discretizations*. PhD thesis, EPFL, Lausanne, 2020.

[Dum13]   Michael Dumbser. A diffuse interface method for complex three-dimensional free surface flows. *Computer Methods in Applied Mechanics and Engineering*, 257:47–64, 2013.

[FGP97]   Michel Fortin, Robert Guénette, and Roger Pierre. Numerical analysis of the modified EVSS method. *Computer methods in applied mechanics and engineering*, 143(1-2):79–95, 1997.

[FGP00]   André Fortin, Robert Guénette, and Roger Pierre. On the discrete EVSS method. *Computer methods in applied mechanics and engineering*, 189(1):121–139, 2000.

[FH93]   Leopoldo P Franca and Thomas JR Hughes. Convergence analyses of Galerkin least-squares methods for symmetric advective-diffusive forms of the Stokes and incompressible Navier-Stokes equations. *Computer Methods in Applied Mechanics and Engineering*, 105(2):285–298, 1993.

[FOA+16]   Rafael A Figueiredo, Cassio M Oishi, Alexandre Afonso, Italo VM Tasso, and José Alberto Cuminato. A two-phase solver for complex fluids: Studies of the Weissenberg effect. *International Journal of Multiphase Flow*, 84:98–115, 2016.

[FPRA09]   Jiannong Fang, Aurèle Parriaux, Martin Rentschler, and Christophe Ancey. Improved SPH methods for simulating free surface flows of viscous fluids. *Applied numerical mathematics*, 59(2):251–271, 2009.

[Fra82]   Richard Franke. Scattered data interpolation: tests of some methods. *Mathematics of computation*, 38(157):181–200, 1982.

[GeH95]   Mohamed Gad-el Hak. Stokes' hypothesis for a newtonian, isotropic fluid. *Journal of Fluids Engineering*, 117(1):3–5, 1995.

[Glo03]   Roland Glowinski. Finite element methods for incompressible viscous flow. *Handbook of numerical analysis*, 9:3–1176, 2003.

[GM77]   Robert A Gingold and Joseph J Monaghan. Smoothed particle hydrodynamics: theory and application to non-spherical stars. *Monthly notices of the royal astronomical society*, 181(3):375–389, 1977.

[GSST22]   Giovanni Gravina, Sebastian Schwarzacher, Ondřej Souček, and Karel Tůma. Contactless rebound of elastic bodies in a viscous incompressible fluid. *Journal of Fluid Mechanics*, 942, 2022.

[He21]   Tao He. Stabilization of a smoothed finite element semi-implicit coupling scheme for viscoelastic fluid-structure interaction. *Journal of Non-Newtonian Fluid Mechanics*, 292:104545, 2021.

[HFK05]   Martien A Hulsen, Raanan Fattal, and Raz Kupferman. Flow of viscoelastic fluids past a cylinder at high Weissenberg number: stabilized simulations using matrix logarithms. *Journal of Non-Newtonian Fluid Mechanics*, 127(1):27–39, 2005.

[Hil07]   Matthieu Hillairet. Lack of collision between solid bodies in a 2D incompressible viscous flow. *Communications in Partial Differential Equations*, 32(9):1345–1371, 2007.

[HLZ81]   Thomas JR Hughes, Wing Kam Liu, and Thomas K Zimmermann. Lagrangian-Eulerian finite element formulation for incompressible viscous flows. *Computer methods in applied mechanics and engineering*, 29(3):329–349, 1981.

[HN81]   Cyril W Hirt and Billy D Nichols. Volume of fluid (VOF) method for the dynamics of free boundaries. *Journal of computational physics*, 39(1):201–225, 1981.

[Hol02]   Gerhard A Holzapfel. Nonlinear solid mechanics: a continuum approach for engineering science. *Meccanica*, 37(4):489–490, 2002.

[HPMR04]   Sangil Hyun, L Pei, Jean-François Molinari, and Mark O Robbins. Finite-element analysis of contact between elastic self-affine surfaces. *Physical review E*, 70(2):026117, 2004.

[IGP22]   Md Rushdie Ibne Islam, Kona Veera Ganesh, and Puneet Kumar Patra. On the equivalence of Eulerian Smoothed Particle Hydrodynamics, Total Lagrangian Smoothed Particle Hydrodynamics and molecular dynamics simulations for solids. *Computer Methods in Applied Mechanics and Engineering*, 391:114591, 2022.

[IZN18]   Alibek Issakhov, Yeldos Zhandaulet, and Aida Nogaeva. Numerical simulation of dam break flow for various forms of the obstacle by VOF method. *International Journal of Multiphase Flow*, 109:191–206, 2018.

Bibliography

[JBCP14]   Nicolas James, Sébastien Boyaval, Alexandre Caboussat, and Marco Picasso. Numerical simulation of 3D free surface flows, with multiple incompressible immiscible phases. Applications to impulse waves. *International Journal for Numerical Methods in Fluids*, 76(12):1004–1024, 2014.

[JCEL07]   Mansoo Joun, Insu Choi, Jaegun Eom, and Mincheol Lee. Finite element analysis of tensile testing with emphasis on necking. *Computational Materials Science*, 41(1):63–69, 2007.

[JEL08]   ManSoo Joun, Jea Gun Eom, and Min Cheol Lee. A new method for acquiring true stress-strain curves over a large range of strains using a tensile test and finite element method. *Mechanics of Materials*, 40(7):586–593, 2008.

[JGB+21]   Paul Johanns, Paul Grandgeorge, Changyeob Baek, Tomohiko G Sano, John H Maddocks, and Pedro M Reis. The shapes of physical trefoil knots. *Extreme Mechanics Letters*, 43:101172, 2021.

[JM13]   Jan B Jonker and Jacob Philippus Meijaard. A geometrically non-linear formulation of a three-dimensional beam element for solving large deflection multibody system problems. *International journal of non-linear mechanics*, 53:63–74, 2013.

[Jou10]   Guillaume Jouvet. *Modélisation, analyse mathématique et simulation numérique de la dynamique des glaciers*. PhD thesis, EPFL, Lausanne, 2010.

[Kat86]   Isao Kataoka. Local instant formulation of two-phase flow. *International Journal of Multiphase Flow*, 12(5):745–758, 1986.

[KKK+05]   Ju Min Kim, Chongyoup Kim, Jeong Ho Kim, Changkwon Chung, Kyung Hyun Ahn, and Seung Jong Lee. High-resolution finite element simulation of 4: 1 planar contraction flow of viscoelastic fluid. *Journal of non-newtonian fluid mechanics*, 129(1):23–37, 2005.

[KO88]   Noboru Kikuchi and John Tinsley Oden. *Contact problems in elasticity: a study of variational inequalities and finite element methods*, volume 8. SIAM, 1988.

[Lar99]   Ronald G Larson. *The structure and rheology of complex fluids*, volume 150. Oxford university press New York, 1999.

[Leb02]   Jean L Leblanc. Rubber-filler interactions and rheological properties in filled compounds. *Progress in polymer science*, 27(4):627–687, 2002.

[LHPCP19]   José-María López-Herrera, Stéphane Popinet, and Alfonso-Arturo Castrejón-Pita. An adaptive solver for viscoelastic incompressible two-phase problems applied to the study of the splashing of weakly viscoelastic droplets. *Journal of Non-Newtonian Fluid Mechanics*, 264:144–158, 2019.

[LHS15]   Kangping Liao, Changhong Hu, and Makoto Sueyoshi. Free surface flow impacting on an elastic structure: Experiment versus numerical simulation. *Applied Ocean Research*, 50:192–208, 2015.

[LL89]   Lev Landau and Evgueni Lifchitz. *Mécanique des fluides*. Ed. Mir, 1989.

[LM00]   Pierre-Louis Lions and Nader Masmoudi. Global solutions for some Oldroyd models of non-newtonian flows. *Chinese Annals of Mathematics*, 21(02):131–146, 2000.

[LO03]   Alexei Lozinski and Robert G Owens. An energy estimate for the Oldroyd-B model: theory and applications. *Journal of non-newtonian fluid mechanics*, 112(2-3):161–176, 2003.

[LOP11]   Alexei Lozinski, Robert G Owens, and Timothy N Phillips. The Langevin and Fokker-Planck equations in polymer rheology. In *Handbook of numerical analysis*, volume 16, pages 211–303. Elsevier, 2011.

[LPS+18]   Viljami Laurmaa, Marco Picasso, Gilles Steiner, Frederic M Evers, and Willi H Hager. Run-up simulation of impulse-generated solitary waves. *Journal of Engineering Mechanics*, 144(2):04017170, 2018.

[LSKG+20]   Andrea La Spina, Martin Kronbichler, Matteo Giacomini, Wolfgang A Wall, and Antonio Huerta. A weakly compressible hybridizable discontinuous Galerkin formulation for fluid-structure interaction problems. *Computer Methods in Applied Mechanics and Engineering*, 372:113392, 2020.

[Mar00]   Vincent Maronnier. *Simulation numérique d'écoulements de fluides incompressibles avec surface libre*. PhD thesis, EPFL, Lausanne, 2000.

[MBY22]   Sarra Maarouf, Christine Bernardi, and Driss Yakoubi. Characteristics/finite element analysis for two incompressible fluid flows with surface tension using level set method. *Computer Methods in Applied Mechanics and Engineering*, 394:114843, 2022.

[MJB+13]   Scott T Miller, Hrvoje Jasak, David A Boger, Eric G Paterson, and Ashish Nedungadi. A pressure-based, compressible, two-phase flow finite volume method for underwater explosions. *Computers & Fluids*, 87:132–143, 2013.

[MN19]   Jan R Magnus and Heinz Neudecker. *Matrix differential calculus with applications in statistics and econometrics*. John Wiley & Sons, 2019.

Bibliography

[MP19]   Alexander T Mackay and Timothy N Phillips. On the derivation of macroscopic models for compressible viscoelastic fluids using the generalized bracket framework. *Journal of Non-Newtonian Fluid Mechanics*, 266:59–71, 2019.

[MPR03]   Vincent Maronnier, Marco Picasso, and Jacques Rappaz. Numerical simulation of three-dimensional free surface flows. *International journal for numerical methods in fluids*, 42(7):697–716, 2003.

[MTF⁺08]   Sean McKee, Murilo F Tomé, Valdemir G Ferreira, José A Cuminato, Antonio Castelo, FS Sousa, and Norberto Mangiavacchi. The MAC method. *Computers & Fluids*, 37(8):907–930, 2008.

[MWY⁺20]   Jingtao Ma, Zhen Wang, John Young, Joseph CS Lai, Yi Sui, and Fang-Bao Tian. An immersed boundary-lattice Boltzmann method for fluid-structure interaction problems involving viscoelastic fluids and complex geometries. *Journal of Computational Physics*, 415:109487, 2020.

[NGA⁺19]   Alireza Naseri, Ignacio Gonzalez, Ahmad Amani, Carlos David Pérez-Segarra, and Assensi Oliva. A second-order time accurate semi-implicit method for fluid-structure interaction problems. *Journal of Fluids and Structures*, 86:135–155, 2019.

[NLCH21]   Ramy Nemer, Aurélien Larcher, Thierry Coupez, and Elie Hachem. Stabilized finite element method for incompressible solid dynamics using an updated Lagrangian formulation. *Computer Methods in Applied Mechanics and Engineering*, 384:113923, 2021.

[NW76]   William F Noh and Paul Woodward. SLIC (simple line interface calculation). In *Proceedings of the fifth international conference on numerical methods in fluid dynamics June 28–July 2, 1976 Twente University, Enschede*, pages 330–340. Springer, 1976.

[Ogd97]   Raymond W Ogden. *Non-linear elastic deformations*. Courier Corporation, 1997.

[OP02]   Robert G Owens and Timothy N Phillips. *Computational rheology*. World Scientific, 2002.

[OR21]   Joseph O'Connor and Benedict D Rogers. A fluid-structure interaction model for free-surface flows and flexible structures using smoothed particle hydrodynamics on a GPU. *Journal of Fluids and Structures*, 104:103312, 2021.

[Pas08]   Jean-Claude Pascal. Vibrations et acoustique 2. *Cours de l'Ecole Nationale Supériere d'Ingénieurs du Mans, Université du Maine*, 2008.

[PG15]   Thomas J Pence and Kun Gou. On compressible versions of the incompressible neo-Hookean material. *Mathematics and Mechanics of Solids*, 20(2):157–182, 2015.

[Pic16]   Marco Picasso. From the free surface flow of a viscoelastic fluid towards the elastic deformation of a solid. *Comptes Rendus Mathematique*, 354(5):543–548, 2016.

[Pir88]   Olivier Pironneau. *Méthodes des éléments finis pour les fluides*. Masson, 1988.

[POV+12]   Jean-Christophe Petiteau, Ramzi Othman, Erwan Verron, Hervé Le Sourne, Jean-François Sigrist, and Guillaume Barras. Uniaxial tension test on rubber at constant true strain rate. In *EPJ Web of Conferences*, volume 26, page 01011. EDP Sciences, 2012.

[PQ05]   Nicola Parolini and Alfio Quarteroni. Mathematical models and numerical simulations for the America's cup. *Computer Methods in Applied Mechanics and Engineering*, 194(9-11):1001–1026, 2005.

[PR01]   Marco Picasso and Jacques Rappaz. Existence, a priori and a posteriori error estimates for a nonlinear three-field problem arising from Oldroyd-B viscoelastic flows. *ESAIM: Mathematical Modelling and Numerical Analysis*, 35(5):879–897, 2001.

[PZ99]   Stéphane Popinet and Stéphane Zaleski. A front-tracking algorithm for accurate representation of surface tension. *International Journal for Numerical Methods in Fluids*, 30(6):775–793, 1999.

[QLV91]   Alfio Maria Quarteroni, Giovanni Sacchi Landriani, and Alberto Valli. Coupling of viscous and inviscid Stokes equations via a domain decomposition method for finite elements. *Numerische Mathematik*, 59:831–859, 1991.

[QV99]   Alfio Quarteroni and Alberto Valli. *Domain Decomposition Methods for Partial Differential Equations*. Oxford University Press, Oxford, UK, 1999.

[RAB90]   Dilip Rajagopalan, Robert C Armstrong, and Robert A Brown. Finite element methods for calculation of steady, viscoelastic flow using constitutive equations with a newtonian viscosity. *Journal of Non-Newtonian Fluid Mechanics*, 36:159–192, 1990.

[Rav85]   Pierre-Arnaud Raviart. An analysis of particle methods. In *Numerical methods in fluid dynamics*, pages 243–324. Springer, 1985.

[RBJ97]   Ronald S Rivlin, Grigory I Barenblatt, and Daniel D Joseph. *Collected papers of RS Rivlin*, volume 1. Springer Science & Business Media, 1997.

Bibliography

[RHC15]   Saswati Roy, Luca Heltai, and Francesco Costanzo. Benchmarking the immersed finite element method for fluid-structure interaction problems. *Computers & Mathematics with Applications*, 69(10):1167–1188, 2015.

[Ric13]   Thomas Richter. A fully Eulerian formulation for fluid-structure-interaction problems. *Journal of Computational Physics*, 233:227–240, 2013.

[RS12a]   Reinhard Racke and Jürgen Saal. Hyperbolic Navier-Stokes equations I: local well-posedness. *Evolution Equations & Control Theory*, 1(1):195, 2012.

[RS12b]   Reinhard Racke and Jürgen Saal. Hyperbolic Navier-Stokes equations II: Global existence of small solutions. *Evolution Equations & Control Theory*, 1(1):217, 2012.

[SA]   YcoorSystems SA. Private communication.

[Set96]   James A Sethian. A fast marching level set method for monotonically advancing fronts. *Proceedings of the National Academy of Sciences*, 93(4):1591–1595, 1996.

[Sig33]   Antonio Signorini. Sopra alcune questioni di statica dei sistemi continui. *Annali della Scuola Normale Superiore di Pisa-Classe di Scienze*, 2(2):231–251, 1933.

[SJK+22] Hugo A Castillo Sánchez, Mihailo R Jovanović, Satish Kumar, Alexander Morozov, V Shankar, Ganesh Subramanian, and Helen J Wilson. Understanding viscoelastic flow instabilities: Oldroyd-B and beyond. *Journal of Non-Newtonian Fluid Mechanics*, page 104742, 2022.

[SLSO08] Paul Allen Stewart, Nathan Lay, Mark Sussman, and Mitsuhiro Ohta. An improved sharp interface method for viscoelastic and viscous two-phase flows. *Journal of Scientific Computing*, 35(1):43–61, 2008.

[STD+96] Michael Schäfer, Stefan Turek, Franz Durst, Egon Krause, and Rolf Rannacher. Benchmark computations of laminar flow around a cylinder. In *Flow simulation with high-performance computers II*, pages 547–566. Springer, 1996.

[Sül88]   Endre Süli. Convergence and nonlinear stability of the Lagrange-Galerkin method for the Navier-Stokes equations. *Numerische Mathematik*, 53(4):459–483, 1988.

[SY88]   Charles CS Song and Mingshun Yuan. A weakly compressible flow model and rapid convergence methods. 1988.

164

[SZ99]   Ruben Scardovelli and Stéphane Zaleski. Direct numerical simulation of free-surface and interfacial flow. *Annual review of fluid mechanics*, 31(1):567–603, 1999.

[TBE+01]   Gretar Tryggvason, Bernard Bunner, Asghar Esmaeeli, Damir Juric, N Al-Rawahi, Warren Tauber, Jaehoon Han, Selman Nas, and Yih Jena Jan. A front-tracking method for the computations of multiphase flow. *Journal of computational physics*, 169(2):708–759, 2001.

[TBMG20]   Alessandro Tasora, Simone Benatti, Dario Mangoni, and Rinaldo Garziera. A geometrically exact isogeometric beam for large displacements and contacts. *Computer Methods in Applied Mechanics and Engineering*, 358:112635, 2020.

[TCM05]   David Trebotich, Phillip Colella, and Gregory Hale Miller. A stable and convergent scheme for viscoelastic flow in contraction channels. *Journal of Computational Physics*, 205(1):315–342, 2005.

[TCM11]   Talia Tokyay, George Constantinescu, and Eckart Meiburg. Lock-exchange gravity currents with a high volume of release propagating over a periodic array of obstacles. *Journal of Fluid Mechanics*, 672:570–605, 2011.

[TELB06]   Gretar Tryggvason, Asghar Esmaeeli, Jiacai Lu, and Souvik Biswas. Direct numerical simulations of gas/liquid multiphase flows. *Fluid dynamics research*, 38(9):660, 2006.

[TK17]   Meral Tuna and Mesut Kirca. Bending, buckling and free vibration analysis of Euler-Bernoulli nanobeams using Eringen's nonlocal integral model via finite element method. *Composite Structures*, 179:269–284, 2017.

[TMC+02]   Murilo F Tomé, Norberto Mangiavacchi, José A Cuminato, Antonio Castelo, and Sean McKee. A finite difference technique for simulating unsteady viscoelastic free surface flows. *Journal of Non-Newtonian Fluid Mechanics*, 106(2-3):61–106, 2002.

[TOG16]   Mohsen Taghizadeh, Hamid R Ovesy, and Seyed Amir Mahdi Ghannadpour. Beam buckling analysis by nonlocal integral elasticity finite element method. *International Journal of Structural Stability and Dynamics*, 16(06):1550015, 2016.

[TS03]   Tayfun Tezduyar and Sunil Sathe. Stabilization parameters in SUPG and PSPG formulations. *Journal of computational and applied mechanics*, 4(1):71–88, 2003.

[VdPSVW05]   Sem P Van der Pijl, A Segal, Kess Vuik, and Pieter Wesseling. A mass-conserving level-set method for modelling of multi-phase flows. *International journal for numerical methods in fluids*, 47(4):339–361, 2005.

Bibliography

[VG20]   Jagannath Venkatesan and Sashikumaar Ganesan. Finite element compu-
           tations of viscoelastic two-phase flows using local projection stabilization.
           International Journal for Numerical Methods in Fluids, 92(8):825–854,
           2020.

[VYS⁺18]   Antonis I Vakis, Vladislav A Yastrebov, Julien Scheibert, et al. Mod-
           eling and simulation in tribology across scales: An overview. *Tribology
           International*, 125:169–199, 2018.

[WKB04]   Michael Francis Webster, IJ Keshtiban, and Fawzi Belblidia. Compu-
           tation of weakly-compressible highly-viscous liquid flows. *Engineering
           computations*, 2004.

[XAX19]   Shixin Xu, Mark Alber, and Zhiliang Xu. Three-phase model of visco-
           elastic incompressible fluid flow and its computational implementation.
           Communications in computational physics, 25(2):586, 2019.

[XOJL12]   Xiaoyang Xu, Jie Ouyang, Tao Jiang, and Qiang Li. Numerical simulation
           of 3D-unsteady viscoelastic free surface flows by improved smoothed parti-
           cle hydrodynamics method. *Journal of Non-Newtonian Fluid Mechanics*,
           177:109–120, 2012.

[YA21]   Kai Yang and Takayuki Aoki. Weakly compressible Navier-Stokes solver
           based on evolving pressure projection method for two-phase flow simula-
           tions. *Journal of Computational Physics*, 431:110113, 2021.

[ZIM17]   Hadi Zolfaghari, Daulet Izbassarov, and Metin Muradoglu. Simulations of
           viscoelastic two-phase flows in complex geometries. *Computers & Fluids*,
           156:548–561, 2017.

[ZL18]   Zhilang Zhang and Moubin Liu. A decoupled finite particle method for
           modeling incompressible flows with free surfaces. *Applied Mathematical
           Modelling*, 60:606–633, 2018.

[ZZ95]   Zhimin Zhang and Jianzhong Zhu. Analysis of the superconvergent patch
           recovery technique and a posteriori error estimator in the finite element
           method (I). *Computer methods in applied mechanics and engineering*,
           123(1-4):173–187, 1995.

[ZZ98]   Zhimin Zhang and Jianzhong Zhu. Analysis of the superconvergent patch
           recovery technique and a posteriori error estimator in the finite element
           method (II). *Computer Methods in Applied Mechanics and Engineering*,
           163(1-4):159–170, 1998.

Léo Aurélio Diserens

16 Rue de la Pontaise, 1018 Lausanne
leo.diserens@epfl.ch

EDUCATION	*Ecole Polytechnique Fédérale de Lausanne (EPFL)*	
	Master in Applied Mathematics	2014 - 2016
	Master thesis under the supervision of Luca Dede' et Andrea Manzoni	
	Title: *Inverse problems in tumor growth modelling*	
	Bachelor in Mathematics	2011 - 2013

COMPUTER SKILLS

Proficient programming skills in C++, Python, R FreeFem++ and Matlab
Good knowledge of Ansys Maxwell
Experience with statistical analysis and visualization using tools such as `numpy`, `scipy`, and `matplotlib`.
Proficient with the use of TeX/LaTeX for document preparation.

WORK EXPERIENCE

Teaching — 2018 - 2022
Teaching assistant in Advanced Numerical Analysis course

Preparation and supervision of exercise sessions, exam preparation

Civil duty — 2016 - 2017
Civil duty completed in Prof. Auwerx laboratory
Life Science section of EPFL. Statistical data analyses workship.

Technical internship — 2015
Internship completed in Fluid Automation System within my applied mathematic master programm.
Creation of an optimisation algorithm in Python langage for Ansys Maxwell software scripting.

PRESENTATIONS

- MATHICSE retreat (Champery, June 2019)
  Talk: Numerical simulation of free-surface viscoelastic flows

- USNCCM16 (Chicago (online), June 2021)
  Talk: Numerical simulation of elastic flows starting from incompressible viscoelastic fluids with free surfaces

- Swiss Numerics (EPFL, September 2021)
  Talk: Numerical simulation of elastic flows starting from incompressible viscoelastic fluids with free surfaces

- CMIS (Chexbres, May 2022)
  Talk: Numerical simulation of multiple phases of incompressible viscous and elastic flows with free surfaces

- CANUM (Evian, June 2022)
  Talk: Numerical simulation of multiple phases of incompressible viscous and elastic flows with free surfaces

- Acisom seminar (Montpellier, November 2022)
  Seminar: Numerical simulation of immiscible incompressible viscous, viscoelastic and elastic multiphase flows

PUBLICATION   *ECCOMAS Congress 2022*
Numerical simulation of multiphase flows with incompressible viscoelastic flows and elastic solids, Alexandre Caboussat, Lo Diserens, Marco Picasso
URL: `https://www.scipedia.com/public/Caboussat_2022a`

ASSOCIATIVE
- PhD student representative   2019 - 2022
  Discuss the school policies, assist to EDMA and SMA meetings, represent the rights of the PhDs at the EPFL.
- Member of SIAM chapter of EPFL   2018 - 2022
  Organisation of conferences and other events for the promotion of academics in industrial world

LANGUAGES
- French: Mother tongue
- English: fluent
- German: B1 - B2 Gymnasium knowledge

INTERESTS   *Sports*: Volley-ball, bike, Judo, tennis.
Mind work: FSJM: math games championship. Chess.